TECHNISCHE UNIVERSITÄT WIEN

DIPLOMARBEIT

Electrochemical properties of $(Nd,Ca)(Fe,Co)O_3$ thin-film electrodes and of porous GDC electrodes

zur Erlangung des akademischen Grades

Diplom-Ingenieur

im Rahmen des Studiums

Chemie und Technologie der Materialien

eingereicht von

Manuel Holzmann
Matrikelnummer 01406632

ausgeführt am Institut für Chemische Technologien und Analytik
der Fakultät für Technische Chemie der Technischen
Universität Wien

Betreuung
Betreuer: Univ.Prof. Dipl.-Phys. Dr.rer.nat. Jürgen Fleig
Mitwirkung: Univ.Ass. Dipl.-Ing. Dr.rer.nat. Andreas Nenning BSc

Wien, 26.11.2020

Signiert von: Manuel Holzmann
Datum: 26.11.2020 17:50:48

Dieses mit einer qualifizierten elektronischen Signatur versehene Dokument hat gemäß Art. 25 Abs. 2 der Verordnung (EU) Nr 910/2014 vom 23. Juli 2014 ("eIDAS-VO") die gleiche Rechtswirkung wie ein handschriftlich unterschriebenes Dokument.

Dieses Dokument ist digital signiert!

Prüfinformation:
Informationen zur Prüfung der elektronischen Signatur finden Sie unter:
www.handy-signatur.at

www.a-trust.at

A-TRUST einfach sicher

(Unterschrift Betreuer/in)

Abstract

In order to sustain the current way of life and to counteract climate change, research on renewable and environmentally friendly ways to generate and store energy is crucial. Solid oxide fuel and electrolysis cells (SOFCs/SOECs) are a promising and efficient way to generate electricity from fuels and vice versa and are already in use for several applications. However, especially the state-of-the-art Ni-YSZ cermets for fuel electrodes suffer disadvantages in terms of carbon deposition and high degradation in electrolysis mode and new materials are therefore of high interest. In this work the electrochemical properties of gadolinium doped ceria (GDC) based porous electrodes and $Nd_{0.6}Ca_{0.4}FeO_3$/$Nd_{0.6}Ca_{0.4}Fe_{0.9}Co_{0.1}O_3$ (NCF/NCFC) thin-film perovskite electrodes were investigated via electrochemical impedance spectroscopy (EIS). Moreover, scanning electron microscopy (SEM) and X-ray photoelectron spectroscopy (XPS) measurements were performed. The manufactured three-layer GDC electrodes show excellent kinetics with an area specific resistance (ASR) of 0.08 Ωcm^2 at 600°C and < 0.02 Ωcm^2 at 800°C in H_2 atmosphere and an active film thickness below 3 µm. Above 700 °C the Arrhenius curve flattens because contributions of gas diffusion become the limiting factor. The particles of the porous GDC layer are found to be rather monodisperse and measure approximately 200 nm in diameter, providing a huge GDC surface area for the oxidation of H_2. Due to the extraordinarily good performance these electrodes were used as counter electrodes for the measurements of the thin-film electrodes. On the NCF and NCFC thin-film electrodes EIS measurements in reducing and oxidizing atmospheres and with applied bias up to ±400 mV were conducted in different measurement setups to investigate ASR, chemical capacitance and potential exsolution behaviour. The NCFC electrodes exhibit a characteristic jump in the current density-overpotential graph, indicating the presence of exsolution of metal particles on the surface. This assumption is backed by SEM and XPS data and the exsolution already happens at OCV in H_2 + H_2O (25 mbar + 28 mbar) atmosphere. For the NCF electrodes no exsolutions can be observed, most likely due to less reducibility of Fe compared to Co. Furthermore, in-plane measurements on finger-structured microelectrodes are discussed with a focus on the ionic and electronic conductivity of the thin-films.

Kurzfassung

Um den derzeitigen Lebensstandard aufrechterhalten zu können und dem Klimawandel entgegenzuwirken, ist die Forschung an erneuerbaren, umweltfreundlichen Möglichkeiten Energie zu erzeugen und zu speichern unabdingbar. Festoxidbrennstoffzellen (SOFCs) sind eine solche Option Energie effizient zu speichern und werden bereits für diverse Anwendungen eingesetzt. Es gibt allerdings immer noch Probleme, oft aufgrund von Materialeigenschaften, welche den Einsatz einschränken. In dieser Arbeit werden die elektrochemischen Eigenschaften von Gd-dotierten CeO_2 (GDC) basierten porösen Elektroden und $Nd_{0.6}Ca_{0.4}FeO_3$/$Nd_{0.6}Ca_{0.4}Fe_{0.9}Co_{0.1}O_3$ (NCF/NCFC) Dünnschichtelektroden mittels elektrochemischer Impedanzspektroskopie analysiert. Weiters wurden SEM und XPS Messungen durchgeführt. Die hergestellten Drei-Schicht-GDC-Elektroden zeigen eine außerordentlich gute Kinetik mit einem flächenbezogenem Polarisationswiderstand von 0.08 Ωcm^2 bei 600°C und < 0.02 Ωcm^2 bei 800°C in H_2 Atmosphäre mit einer aktiven Schichtdicke von unter 3 µm. Im Arrhenius Diagramm ist über 700°C eine Abflachung der Kurve zu erkennen, was auf eine Limitierung durch Gasdiffusion zurückzuführen ist. Die Partikel der porösen GDC Schicht sind einigermaßen monodispers mit einer durchschnittlichen Größe von etwa 200 nm und stellen daher eine große Oberfläche für die Oxidation von H_2 zur Verfügung. Diese GDC basierten Elektroden wurden aufgrund der exzellenten Eigenschaften als Gegenelektroden für die Messungen mit den Dünnschichtelektroden verwendet. An den NCF und NCFC Dünnschichtelektroden wurden Messungen in reduzierenden und oxidierenden Messatmosphären, sowie mit einer angelegten Spannung von bis zu ±400 mV in verschiedenen Messständen durchgeführt, um ASR, chemische Kapazität und das eventuelle Auftreten von Exsolutions zu untersuchen. Bei den NCFC Elektroden ist ein charakteristischer Sprung im Stromdichte-Überspannung-Diagramm erkennbar, welcher auf die Anwesenheit von Metallpartikeln an der Oberfläche hindeutet. Diese Annahme wird durch Daten von SEM und XPS Messungen unterstützt und es zeigt sich, dass sich die Metallpartikel bereits bei Leerlaufspannung in H_2 + H_2O (25 mbar + 28 mbar) Atmosphäre an der Oberfläche bilden. Bei den NCF-Elektroden kann kein solches Verhalten festgestellt werden, höchstwahrscheinlich aufgrund der schwereren Reduzierbarkeit von Fe im Vergleich zu Co. Weiters werden in-plane Messungen an Mikroelektroden mit Fingerstruktur im Bezug auf die ionische und elektronische Leitfähigkeit der Dünnschichten diskutiert.

Table of contents

1. Introduction

It is crucial to supply energy to places all over the world to maintain our civilization and most of the energy is currently generated from fossil fuels like coal, gas and oil. However, these sources of energy are limited and will run low soon. Furthermore, they are a main contributor to greenhouse gas emissions, which lead to global warming and have a strongly negative impact on the environment.[1–3] The consequences of climate change include melting of the glaciers and an associated rise of the sea level, more extreme weather events, declining biodiversity, an increasing number of wildfires and hence are not only harming nature but also cause new challenges to ultimately sustain human life on earth.[3–6]

As a result, the generation of energy in an environmentally friendly and renewable way is one of the biggest topics in research in the current century. Alternative sources of energy include wind power, solar energy, geothermal energy, nuclear energy, biomass, hydroelectric energy and fuel cells.[7–9] However, there are a lot of challenges to overcome before these sources of energy can be used to fully cover the world's energy needs, like the disposal of radioactive waste or regional limitations.[10,11] Hydro power plants for example require the presence of a river and to produce energy from biomass a lot of space is required, which could be also used to plant crops to meet the increasing food demand of our fast growing population.[2] Another problem is that several of these renewable energy sources are of intermittent nature and as a consequence can't steadily supply energy throughout the day to meet the demand or are relatively expensive in their current state. To overcome this problem electrical energy storage systems that can store the electrical energy as long as the demand is low and there is a surplus and convert it back when it is needed can be applied.[9,12,13]

The energy can be stored mechanically, thermally, electrically, or chemically. An example of mechanical energy storage is pumped hydroelectric storage, where the surplus energy is used to pump up water from a lower level to a higher level and when needed the water going back down can produce energy through a turbine. However, construction costs are very high and possible construction places are not readily available.[14] Thermal energy storage uses materials that can store energy thermally over longer periods of time to release it when needed. Electrical energy storage includes capacitors, which store energy electrostatically, can be cycled very well and charged fast but have a rather low energy density and high self-discharge. To store energy chemically batteries or fuel/electrolysis cells can be used. Batteries are a very mature technology and have been used for a long period of time. They consist of one or more electrochemical cells, where ions are transported through an electrolyte from one electrode to another, an electrochemical reaction occurs and the electrons move through an external circuit, thus creating electrical energy during discharge. If the reactions are reversible in a practical way the battery can be recharged by applying a

voltage to the electrodes. Advantages of batteries are their fast response, high energy efficiencies and low self-discharge losses. However, they often contain toxic materials and have too small energy densities for large applications.[12,13]

Fuel cells differ from batteries because unlike them they are an open system and do not need to be recharged since the reactants are mostly supplied to the system in the form of hydrogen or organic substances and oxygen from air. These reactants are converted through an electrochemical reaction into water and the fuel cell produces energy as long as they are available. It is also possible to operate fuel cells in the reverse direction to split water into hydrogen and oxygen using electric energy (electrolysis cells). There are a lot of different types of fuel cells, normally classified according to their electrolyte and fuel, like proton exchange membrane fuel cells, direct methanol fuel cells, phosphoric acid fuel cells, molten carbonate fuel cells and solid oxide fuel cells with their major applications in power generation, energy storage and transportation.[12,15–17] The main advantages compared to conventional heat engines are high energy conversion efficiency, less maintenance because of the lack of moving parts and that they are environmentally friendly because the produced waste product is water if operated with hydrogen.[15,17] However, also the production of the fuel needed must be considered and the generation of hydrogen in a green way, for instance through electrolysis and photocatalytic water splitting, is at a rather early stage of development.[12,17]

Solid oxide fuel cells (SOFCs) are high temperature fuel cells with operating temperatures of 600 to 1000°C that are well suited for power generation applications with capacities up to hundreds of MW. Advantages compared to other fuel cells are that there are less stability issues concerning the electrolyte and that they are resistant to poisoning of carbon monoxide because it is oxidised to carbon dioxide due to the high temperatures. That allows for more flexibility in the fuel selection. Furthermore, the heat produced through operation can be used to power gas turbines and generate even more electricity. The major challenges include, like for most fuel cell types, high costs and a rather low durability. Moreover, there are specific material requirements because of the temperatures needed for operation and the start-up and cool down times are long.[12,16–18]

The currently mostly used materials for SOFCs are yttria-stabilized zirconia (YSZ)/Ni cermet anodes, YSZ as electrolyte and YSZ/$La_{0.8}Sr_{0.2}MnO_3$ (LSM) composites or $La_{0.6}Sr_{0.4}Fe_{0.8}Co_{0.2}O_3$ (LSCF) as cathode.[18–21] While these materials work relatively well there is still much room for improvement. The Ni/YSZ anodes show some major drawbacks, despite their good catalytic activity and electrochemical properties, like the formation of carbon and thus degradation of the anodes. Furthermore, they are vulnerable to sulfur poisoning and consequently rely on fuels with low sulfur contents. Another problem is that

the Ni tends to sinter, which reduces the available triple-phase boundaries and thus also the performance, especially in electrolysis operation.[19,20,22] For the electrolyte, materials with high ionic and very low electronic conductivity are essential. The currently used YSZ has both properties, however, the high sintering temperature is problematic, and impurities tend to accumulate in grain boundaries reducing the ionic conductivity.[19,20,23] The cathode material LSM has good catalytic activity at high temperature and electrical conductivity at 800 to 1000°C. If the temperature gets too high though, it can react with YSZ which greatly reduces performance, and below 800°C the polarization resistance strongly increases. To target all these challenges with currently used materials for SOFCs a lot of research is done with one of the main goals to lower operation temperatures. That would decrease degradation allow for a wider range of possible materials for components like interconnects, which must provide an electrical contact between anode and cathode while dividing reducing and oxidizing atmosphere in SOFC stacks and thus have very rigorous material requirements. Consequently, a lot of research focuses at the moment on novel materials or improvements of already known materials for SOFC systems that exhibit the desired electrochemical properties at lower temperatures and could help to broaden the range of commercial SOFC applications.[19,20]

A widely used tool for characterizing electrode and electrolyte materials for SOFCs is electrochemical impedance spectroscopy (EIS). The impedance is measured over a range of frequencies and the resulting spectra ideally show a series of semicircles that can be assigned to certain reaction steps. In a typical measurement setup four wires on two electrodes are used to compensate the wire impedance. The measured cells are normally symmetrical to make interpretation of the results easier.[24,25] An approach to measure half cells and thus separate the two electrode features to more easily access their properties is the use of a reference electrode in a three-point measurement setup. However, three-point measurements are heavily dependent on the geometry of the cells and position of the reference electrode and unwanted artifacts can occur in the impedance spectra.[25,26]

An interesting material for several applications in SOFCs is gadolinium-doped ceria (GDC). GDC shows promising properties in YSZ/GDC bilayer electrolytes at intermediate temperatures because it has a better ionic conductivity than YSZ at lower temperatures. A disadvantage for the use as an electrolyte is that it is electron conducting in reducing atmospheres, but this phenomenon can be counteracted by applying a bilayer electrolyte with YSZ as an electron blocking layer.[19,27] The use of GDC as an interlayer between the YSZ electrolyte and LSCF electrodes improves the stability and suppresses the formation of $La_2Zr_2O_7$.[28] It has also been applied in impregnated $La_{0.8}Sr_{0.2}Co_{0.8}Ni_{0.2}O_{3-\delta}$ (LSCN) electrodes with a GDC scaffold for reversible solid oxide cells that show a high performance, however,

there are degradation issues that can be linked to the growth of LSCN particles and the corresponding decrease in triple phase boundaries (TPB).[29] Furthermore, there have been studies on Ni/GDC as an anode material. One of its advantages over Ni/YSZ is a lower polarization resistance, which can be attributed to the better ionic conductivity as well as the fact that in reducing conditions GDC is a mixed ionic electronic conductor (MIEC) and consequently the reaction sites are not limited to the TPB.[30] Moreover, Ni/GDC anodes show a much higher tolerance to sulfur compared to Ni/YSZ, probably because of differences in the microstructure after poisoning with sulfur and the MIEC properties of GDC.[31] Another study suggests that the incorporation of iron into Ni/GDC anodes that use dry methane as a fuel and operate at 650°C helps to prevent the deposition of carbon and the associated degradation, due to the oxidation of methane occurring more completely with iron than without, which is of interest because that would allow for methane and possibly other organic fuels to be directly used in intermediate temperature SOFCs without a reforming or purification step.[32]

An emerging and highly promising approach for solid oxide cell applications is the use of perovskite-type materials as fuel electrodes. They are rather tolerable to impurities but their kinetics show room for improvement. A promising way for achieving high catalytic activity is doping the perovskite with catalytically active, easily reducible metals. These metals can be exsolved from their perovskite host in reducing conditions and form nanoparticles on the surface with high catalytic activity. While it is unresolved whether the exsolution of these nanoparticles is reversible, there is clear evidence that these can be reversibly oxidized and reduced by changing the gas phase or application of a bias. This allows to switch from a low activity state to a high activity state and vice versa, potentially enabling to overcome degradation problems of current electrode materials like Ni/YSZ.[33–35] It has been reported that for $La_{0.6}Sr_{0.4}FeO_{3-\delta}$ (LSF) electrodes Fe^0 particles form on the surface in reducing conditions. The presence of these metal particles could be linked to a huge increase in water splitting activity through in-situ XPS studies, making LSF a promising candidate for the use in solid oxide electrolysis cells. Moreover, it has been found that the exsolution of Fe appears to mainly depend on the oxygen partial pressure in the bulk electrode, because the exsolutions could not only be obtained in certain reducing gas atmospheres but also by applying a large enough cathodic overpotential in ultra-high vacuum.[36–38] The exsolution of Fe seems to be accompanied by a phase change from rhombohedral to cubic structure[39] and it has also been shown that by varying the reducing conditions from static to flowing H_2 and by either using pure LSF or Ni-LSF the nature of the exsolutions can be controlled.[40] Furthermore, there has been research done on LSF with partial substitution of Fe with Ni and Cr (LSCFNi), where Fe-Ni alloy nanoparticles are exsolved in reducing conditions, and the activity for methane reforming has been increased greatly compared to the perovskite without Ni.[41,42] A study on

$La_{0.5}Sr_{0.5}Fe_{0.8}Cu_{0.15}Nb_{0.05}O_{3-\delta}$ electrodes that exsolve Cu nanoparticles for intermediate temperature SOFCs indicates excellent properties for fuel oxidation with high coking and sulfur resistance and the ability to regenerate the electrode by redox cycling.[43] To promote the exsolution of nanoparticles from host perovskites it has been proposed to introduce A-site deficiency to destabilize the metal cations on the B-site. Due to oxygen vacancies in reducing atmospheres these A-site deficient perovskites can be regarded as having B-site excess, which favours B exsolution and it has been shown that increasing nanoparticle exsolution occurs with increasing A-site deficiency and the lattice oxygen mobility improves substantially.[33,34,44,45] Another method that has been suggested to promote exsolution is the introduction of a lattice strain, for example by using lattice mismatched substrates, and a correlation between nanoparticle exsolution and lattice strain could be observed.[46] An advantage of exsolutions over catalytically active nanoparticles that are deposited on the surface has been reported to be their increased resistance to coking and particle agglomeration, attributable to the fact that exsolved nanoparticles seem to be pinned to the parent perovskite on their nucleation site.[47–49] Furthermore, exsolutions have been observed to differ in size and surface coverage on different perovskite matrix orientations, introducing a way to tune the nature of the exsolved nanoparticles.[50]

In this thesis the electrochemical properties of porous GDC based electrodes and novel $(Nd,Ca)(Fe,Co)O_3$ thin-film perovskite electrodes with a special focus on exsolution behaviour are investigated using EIS, XPS and other characterisation methods. The influence of temperature and different atmospheres is analysed. Additionally, it is evaluated whether it is possible or not to retrieve sound data for half cells using a three-point impedance measuring setup and samples with a specific geometry.

2. Theoretical background

2.1. SOFC Basics

SOFCs are high temperature fuel cells that normally operate at around 800 to 1000°C. They differ from most other fuel cells due to all their components being in the solid state. The basic working principle of an SOFC is shown in the following figure.

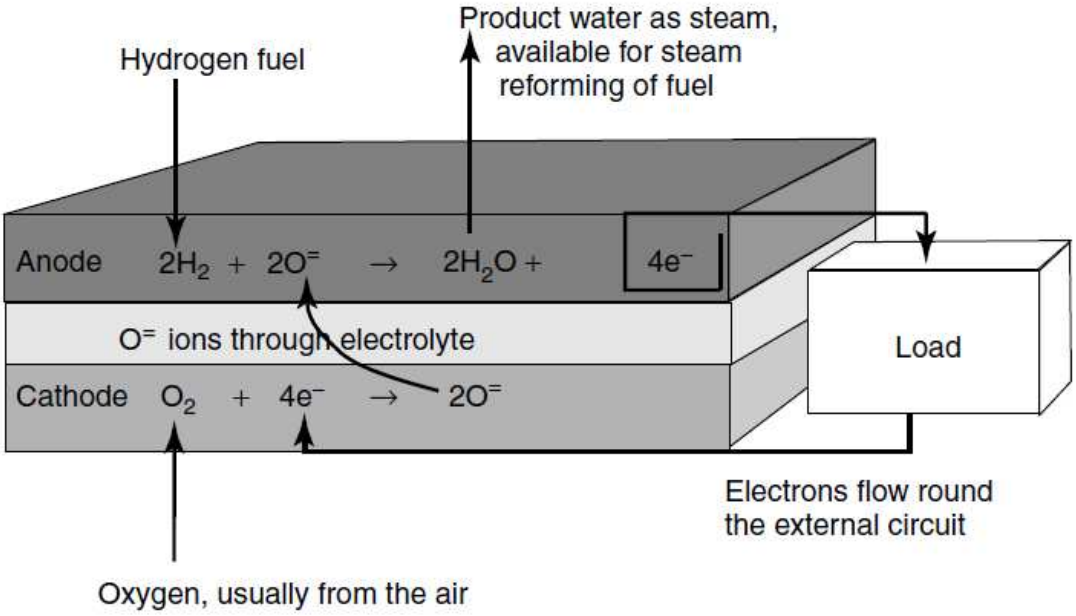

Figure 1: Structure of an SOFC including the half-cell reactions.[51]

An SOFC uses mostly methane as fuel, which reacts with water to hydrogen and CO and the resulting hydrogen gets oxidized at the anode. At the cathode oxygen, normally from air, gets reduced and the oxygen ions are transported through the oxygen conducting solid electrolyte to form water with the hydrogen ions at the anode. The electrons flow through an external circuit. To use SOFCs for commercial applications many of them need to be connected to form stacks and reach the desired power. That is achieved by an interconnect that provides an electrical contact from the anode of one cell to the cathode of the next cells. For practical realization, these stacks are mainly built in either a planar or tubular design, with the planar design being easier to manufacture but needing considerable effort for gas tight sealing, while sealing is not a big problem for the tubular design but manufacturing is more difficult.[51] Due to the lower construction costs and higher power density, a planar stack design is currently favored.[52]

2.2. Electrochemical impedance spectroscopy

Impedance can be defined as the complex electrical resistance and describes the resistance to a current flowing through an electrical circuit. If the circuit only consists of ideal electrical resistors the impedance is equal to the electrical resistance and well defined by Ohm's Law.

$$R = \frac{U}{I} \tag{1}$$

In this case the resistance (R) does not depend on the frequency if an alternating current (AC) signal is applied and voltage (U) and current (I) are in phase, meaning that there is no phase shift between them. However, if there are also capacitors or inductors present in a circuit a phase shift occurs with an ideal capacitor or ideal inductor being completely out of phase with a shift of -90° or +90° respectively. Thus, impedance is used to describe these circuits because it does not only picture the absolute resistance of a system but also captures information on the phase shift. In measurement setups usually a sinusoidal voltage signal $U(t) = U_0 \sin(\omega t)$ expressed as a function of time is applied and the response in form of a current with a phase shift $I(t) = I_0 \sin(\omega t + \varphi)$ is measured. The complex impedance (Z) is defined as the ratio of these two signals:

$$Z = \frac{U(t)}{I(t)} = \frac{U_0 \sin(\omega t)}{I_0 \sin(\omega t + \varphi)} = Z_0 \frac{\sin(\omega t)}{\sin(\omega t + \varphi)} \tag{2}$$

U_0 and I_0 denote the amplitudes of the voltage and current signals, Z_0 the absolute value of the impedance, t the time, ω the angular frequency defined as $\omega = 2\pi f$ with f signifying the frequency and φ labels the phase shift. By using Euler's relationship $e^{j\varphi} = \cos(\varphi) + j \sin(\varphi)$ the voltage and the current response can be written as the complex functions

$$U(t) = U_0 e^{j\omega t} \tag{3}$$

$$I(t) = I_0 e^{j\omega t - j\varphi} \tag{4}$$

and the impedance can be split into a real part Z_{RE} that is in phase with the applied signal and an imaginary part Z_{IM} that is out of phase and the phase shift can be written as the ratio of these two parts:

$$Z = Z_0 e^{j\varphi} = Z_0(\cos(\varphi) + j \sin(\varphi)) = Z_{RE} + jZ_{IM} \tag{5}$$

$$\tan(\varphi) = \frac{Z_{IM}}{Z_{RE}} \tag{6}$$

For practical measurements, the impedance is usually measured in a wide frequency range from mHz to MHz with a rather small amplitude of the input signal, to make sure that $I = f(U)$ is linear. The results are typically plotted in a Nyquist plot or a Bode diagram as shown in Figure 2.[53–55]

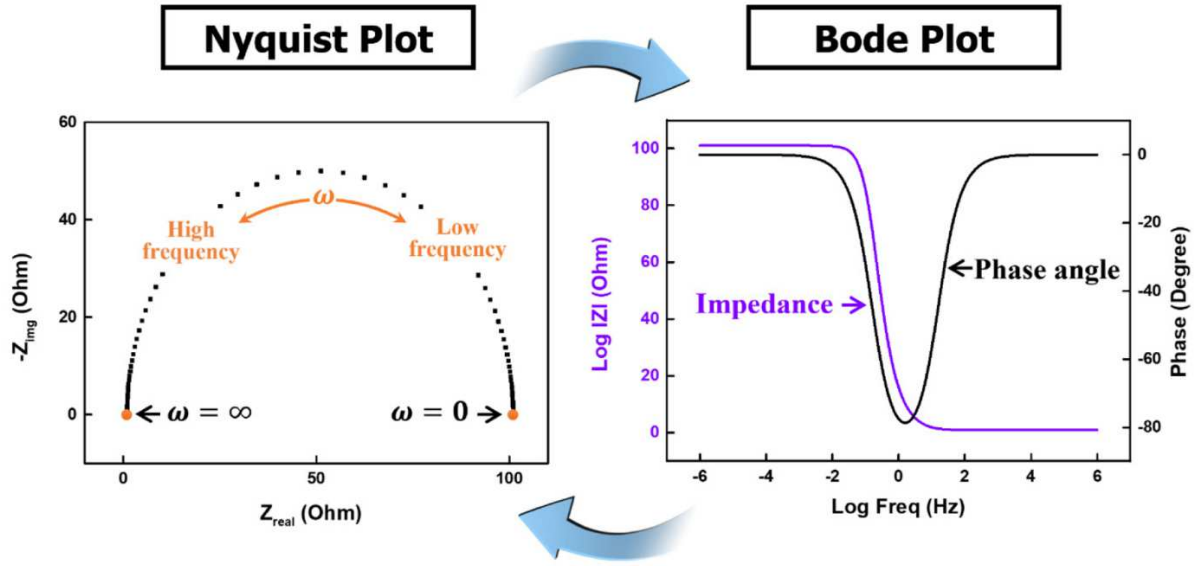

Figure 2: Example of a Nyquist plot (left) and a Bode plot (right) to display the results of impedance measurements.[55]

To obtain information on electrochemical processes, the measured impedance spectra are typically fitted with circuit models that describe the behavior of the electrochemical system. Ideally, these equivalent circuits, consisting of ideal electrical elements like resistors, inductors, capacitors, and some non-ideal elements like constant phase elements (CPE), should describe the electrochemical behavior as precise as possible with a minimum of variables. For solid oxide cells (SOC) semicircle-like features are often measured and fitted with a parallel circuit of a resistor (R) and capacitor (C), where R indicates the resistance of the material and C a chemical or double-layer capacitance. The impedances of a single resistor and capacitor can be expressed as $Z_R = R$ and $Z_C = \frac{1}{j\omega C}$ resulting in an impedance for an RC parallel circuit of $Z_{RC} = \frac{R}{1+j\omega RC}$. Typically, for example when measuring electrodes of SOCs, the semicircle feature of the electrode has a certain offset that can be attributed to the electrolyte and most easily fitted with a resistor in series to the RC parallel circuit yielding for the impedance of the equivalent circuit the following equation:

$$Z = R_s + \frac{R_p}{1 + j\omega R_p C} = R_s + \frac{R_p}{1 + \omega^2 R_p^2 C^2} - \frac{j\omega R_p^2 C}{1 + \omega^2 R_p^2 C^2} = Z_{RE} + jZ_{IM} \qquad (7)$$

The series resistance R_s can be evaluated out of the Nyquist plot (Figure 2) as the high frequency intercept of the semicircle. The polarization resistance R_p parallel to the capacitance C is obtained by subtracting the high frequency intercept on the real axis from

the low frequency intercept, and the capacitance can be calculated by reading the peak angular frequency ω_{peak} out of the Nyquist plot and applying the simple relation $\omega_{peak} = \frac{1}{R_p C}$.

However, most measured features in electrochemical systems do not resemble perfect semicircles and therefore, to improve fitting of real data CPEs can be used parallel to the polarization resistance in the equivalent circuit instead of ideal capacitors. The impedance of a CPE is described as:

$$Z_{CPE} = \frac{1}{T(j\omega)^P} \tag{8}$$

T and P are parameters that do not depend on the frequency and P is a measure for the deviation from an ideal capacitor. If P=1 the CPE acts exactly like an ideal capacitor with T=C. To calculate the capacitance from an equivalent circuit with a resistor parallel to a CPE the following equation can be used:

$$C = (TR_p^{(1-P)})^{\frac{1}{P}} \tag{9}$$

The reason for the non-ideal capacitive behavior can be for example due to surface roughness, non-homogenous electrodes, non-uniform potential and current distribution, porosity, or adsorption processes but to certainly identify the process that is responsible other characterization methods should be applied in addition to EIS, due to impedance spectra offering a lot of different possibilities for interpretation.[53,55–58]

Even without an equivalent circuit model, it is possible to extract useful data from Nyquist plots of in-plane measurements by looking at the intercepts of the features on the x-axis. That allows a first estimation of the ionic and electronic conductivity of an MIEC by taking the inverse value of the low frequency intercept as the electronic conductivity and the inverse value of the high frequency intercept as the total conductivity, both values normalized to the MIEC geometry. Consequently, the ionic conductivity can be calculated by a trivial subtraction of the electronic from the total conductivity. Another way to access the material properties and fit the measured impedance spectra with representative circuit elements is via a transmission line model. Generally, a transmission line model can be applied for fitting of MIECs and consists of one rail that models the electronic transport and one that models the ionic transport through the material. These two rails are coupled over capacitors that describe the chemical capacitance, which is related to the ambipolar diffusion in mixed electronic and ionic conducting materials. Such a transmission line model is shown in Figure 3.

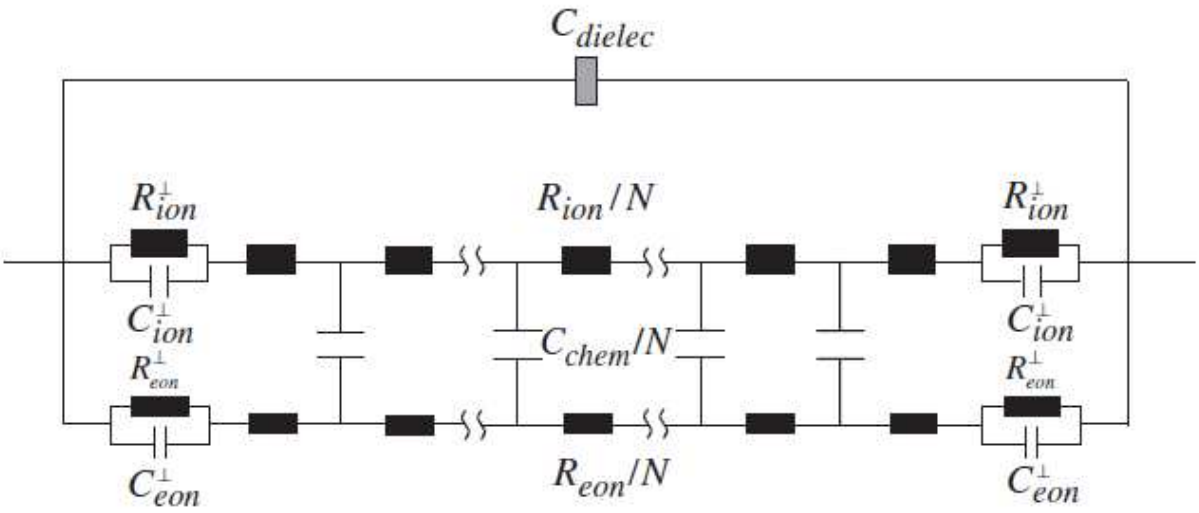

Figure 3: General equivalent circuit of a transmission line model for a MIEC between two electrodes. Reprinted from Ref[59]

In this equivalent circuit the top rail displays the ionic rail with the ionic resistance R_{ion} and the bottom rail the electronic rail with the electronic resistance R_{eon}. As already mentioned, these rails are coupled by the chemical capacitance C_{chem}. N denotes the number of transmission line elements and the RC-parallel circuits on the left and right side of $R_{ion}^{\perp}$, $C_{ion}^{\perp}$ and $R_{eon}^{\perp}$, $C_{eon}^{\perp}$ are the ionic and electronic capacitances and resistances attributed to the electrode-MIEC interface. C_{dielec} describes the double layer capacitance of the bulk MIEC and can be omitted for simplification, due to the normally rather small values that only effect the impedance spectra at very high frequencies.[59–61]

When a mixed conducting film with interdigitating electrode structures is deposited on an ion conducting (e.g. YSZ) substrate, a similar, equivalent circuit can be used to describe both the in-plane impedance as well as the electrochemical impedance, in which the voltage is applied between the current collectors and a counter electrode.

A model based on this general transmission line circuit that has already been used to characterize $SrTi_{0.7}Fe_{0.3}O_{3-\delta}$ anodes with interdigitating current collectors, like the ones used in this study, is shown in Figure 4.

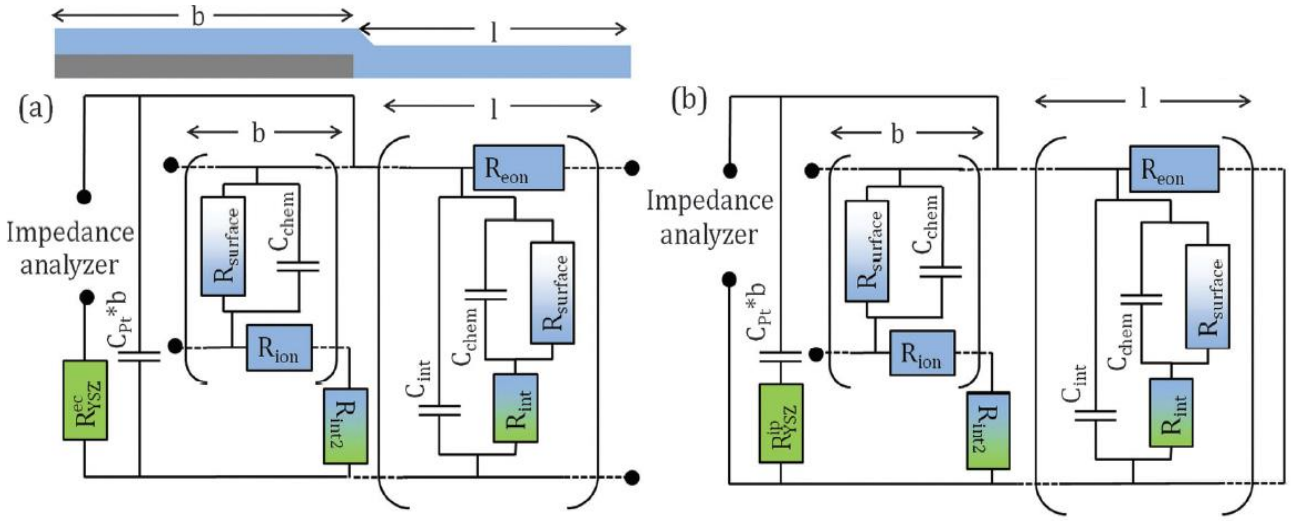

Figure 4: Transmission line model for interdigitating current collectors under a MIEC as displayed on top for (a) electrochemical measurements and (b) in-plane measurements.[62]

In this equivalent circuit $R_{surface}$ is the resistance of the surface reaction with the chemical capacitance of the MIEC C_{chem} parallel. R_{eon} and R_{ion} denote the electronic and ionic sheet resistance of the MIEC. R_{int}, R_{int2} and C_{int} are interfacial resistances and capacities. R^{ip}_{YSZ} is the in-plane resistance of the YSZ electrolyte, R^{ec}_{YSZ} the offset resistance of the electrolyte for electrochemical measurements and C_{Pt} the capacitance of the current collector YSZ interface. An advantage of this model is that electrochemical and in-plane measurements can be performed on the same sample and the resulting spectra are fitted with the same set of parameters, which prevents overparametrization. It takes into account that for example the oxidation of H_2 can occur either on the thin-film above YSZ or above the current collector and that the electrons and oxygen ions have to travel different paths to get to the current collector or the electrolyte, depending on where the reaction took place. The main difference between the model for in-plane and electrochemical measurements is that for the in-plane measurements the transmission line is terminated by a short-circuit, due to the different polarization on two adjacent current collector fingers, while for electrochemical measurements the polarization on all current collector structures on one side of the electrolyte is the same leading to a termination of the transmission line with an open circuit. A more in detail explanation and derivation of the equivalent circuit in Figure 4 has been made by Nenning et al.[62]

To further improve the fitting results the addition shown in Figure 5 could be applied in this work for the electrochemical across-plane measurements. The electrodes consist of finger-type current collectors with electrical contact pads that are roughly as large as the finger structures, shown in Figure 8. These two parts have different electrochemical properties and thus the equivalent circuit also consists of two models in a parallel connection.

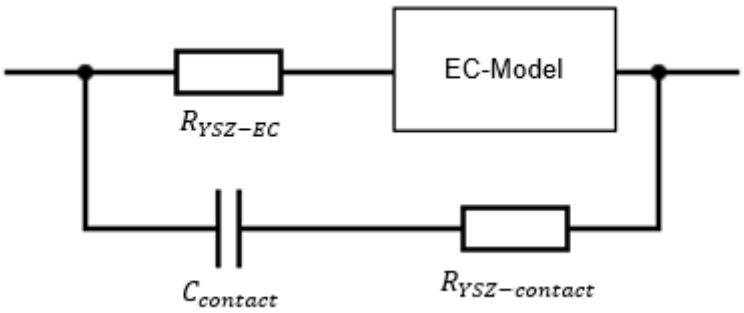

Figure 5: Additional circuit elements to account for an artifact semicircle due to the contact points.

One of the models represents the dielectric coupling of electrolyte and contact pads ($C_{contact}$ and $R_{YSZ-contact}$), and the other line represents the actual MIEC thin-film with interdigitating current collectors (R_{YSZ-EC} and EC-Model). In the Nyquist plots, which will be later shown in the results section, the MIEC model produces the low frequency feature, whereas the contacting pads produce an additional high-frequency feature. EC-Model is the equivalent circuit seen in Figure 4 a).

2.3. Gadolinium-doped ceria (GDC)

Ceria (CeO_2) is a metal oxide with the fluorite structure and has become of interest as electrolyte or electrode material for SOFCs because of its high oxygen ion conductivity if doped with trivalent rare-earth oxides like Sm_2O_3, Gd_2O_3 or Y_2O_3. These dopants form solid solutions with ceria and introduce oxygen vacancies to compensate for the charge difference as written in equation 10 in Kröger-Vink notation.

$$Gd_2O_3 + 2Ce_{Ce}^{x} + O_O^{x} \rightarrow 2Gd'_{Ce} + V_O^{\cdot\cdot} + 2CeO_2 \qquad (10)$$

In reducing atmospheres, the Ce^{4+} ions of ceria or doped ceria can be reduced to Ce^{3+} leading to additional electronic conductivity as shown in the following equation.

$$O_O^{x} + 2Ce_{Ce}^{x} \rightleftharpoons \frac{1}{2}O_2 + V_O^{\cdot\cdot} + 2Ce'_{Ce} \qquad (11)$$

These MIEC properties are a disadvantage for the use as electrolyte material due to leakage currents, but beneficial for ceria-based electrodes. The electronic conduction takes place by small polaron transport with Ce'_{Ce} being the polaron and the electronic conductivity σ_{eon} can therefore be described as follows.

$$\sigma_{eon} = [Ce'_{Ce}]e\mu \qquad (12)$$

e is the electron charge and μ the mobility that depends on the activation energy of small polaron hopping. Furthermore, grain boundaries do not seem to decrease the electronic

conductivity, which could be because the grain boundaries seem to be more easily reduced than the bulk. The ionic conductivity, attributed to oxygen ion hopping in {001} directions between nearest neighbor oxygen sites, on the other hand consists of a contribution from the bulk and from the grain boundaries. Because these contributions are in series the often very badly conducting grain boundaries can significantly lower the overall ionic conductivity. The worse ionic conductivity of the grain boundaries could be due to segregation of the doping ions but also due to amorphous phases occurring because of impurities or micro porosity in the grain boundary region. The trivalent ions that lead to the oxygen vacancies are associated to them and these associations are stronger for smaller ions. However, the activation barrier for oxygen ion hopping is smaller and thus more favorable for smaller trivalent ions, which leads to a tradeoff where ceria doped with either Sm or Gd shows the best ionic conductivity.[63–67]

For application as an SOFC electrode, also the kinetics of surface redox reactions, such as H_2 oxidation/H_2O splitting are of crucial importance. Model studies showed that these redox kinetics are reasonably fast, and happen primarily on the GDC surface, rather than on triple phase boundaries.[68,69] These well-known materials properties of GDC also help in modeling and understanding the impedance of porous GDC anodes.[30]

2.4. $(Nd,Ca)(Fe,Co)O_3$

The rare earth orthoferrite $NdFeO_3$ and its derivates are perovskite-type materials that show promising properties for the application as electrode material in IT-SOFCs. The perovskite structure of these materials is displayed in Figure 6.

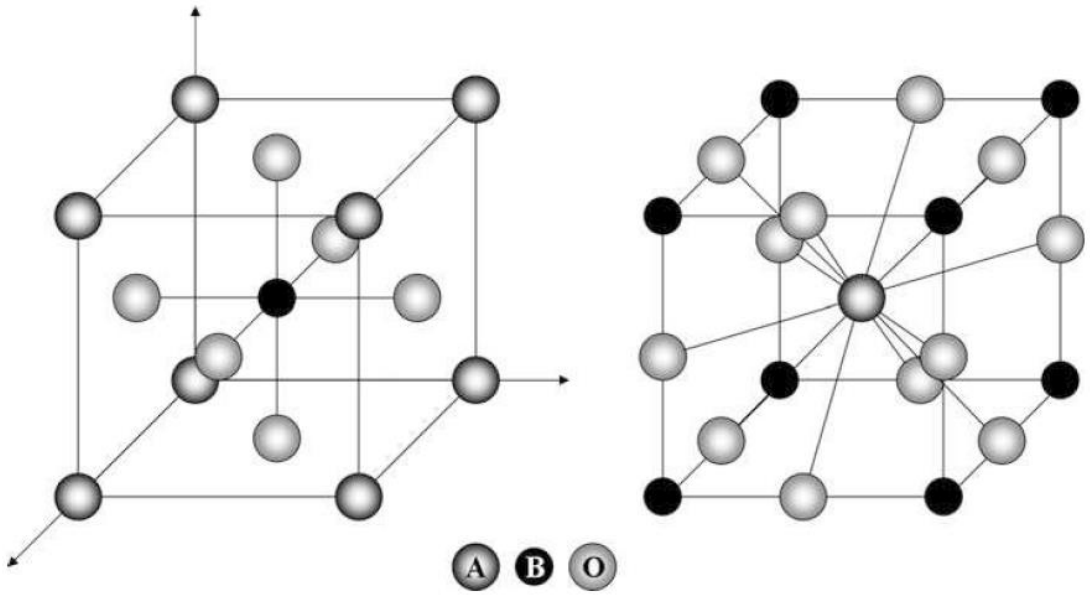

Figure 6: Ideal perovskite structure with B-site cation in the center (left) and A-site cation centered (right).[70]

The A-site is the bigger ion and, in this case, occupied by Nd, that is coordinated by 12 oxygen ions. The smaller B ions, here Fe, are coordinated by 6 oxygen ions and form corner sharing octahedra.[70–74] However, stoichiometric and undoped $NdFeO_3$ has very few electronic and ionic point defects and therefore a rather high resistance that is not beneficial for the application as electrode material, because high ionic and electronic conductivity are desired. This problem can be solved by doping. Doping with Ca^{2+} on the A-site has reportedly shown a huge increase in the electrical conductivity. Due to the lower oxidation state of Ca^{2+} compared to Nd^{3+} holes and oxygen vacancies are introduced to balance the charge difference, as shown in the following equation.

$$2Fe_{Fe}^{x} + 2Nd_{Nd}^{x}(+2Ca - 2Nd) \rightarrow 2Fe_{Fe}^{\cdot} + 2Ca_{Nd}' \qquad (13)$$

According to Wang et. al.[71] the holes (or Fe^{4+} ions, denoted as $Fe_{Fe}^{\cdot}$) that are introduced through doping with Ca^{2+} can move in not fully populated bands just above the Fermi level along the Fe-O-Fe network, thus leading to a high hole mobility and electronic conductivity with features consistent with LSF, which also exhibits high electronic conductivity. Furthermore, the introduction of Ca^{2+} generates oxygen vacancies, as seen in equation 13. Because the oxygen ion diffusion occurs via a vacancy hopping mechanism, the ionic conductivity increases with the number of oxygen vacancies. Hence, doping of $NdFeO_3$ with Ca^{2+} can greatly increase the electronic and ionic conductivity, leading to MIEC properties.[71,75,76]

The defect equilibrium of the charge compensation with either oxygen vacancies or holes due to doping with Ca^{2+} ions on the Nd^{3+} sites can be described with the following equation.[76]

$$\frac{1}{2}O_2 + V_O^{\cdot\cdot} + 2Fe_{Fe}^{x} \rightleftharpoons O_O^{x} + 2Fe_{Fe}^{\cdot} \qquad (14)$$

Because of the charge compensation with oxygen vacancies and Fe^{4+} ions and the hole conduction mechanism along the Fe-O-Fe network it is assumed that $Nd_{0.6}Ca_{0.4}FeO_{3-\delta}$ (NCF) and $Nd_{0.6}Ca_{0.4}Fe_{0.9}Co_{0.1}O_{3-\delta}$ (NCFC) behave qualitatively similar to LSF, which shows the same defect equilibrium and conduction mechanism. Therefore, and since significantly more research has been done on the defect model of LSF compared to NCF the following considerations on defect chemistry focus mainly on literature about LSF. In addition to the defect equilibrium of oxygen vacancies and Fe^{4+} there is also the disproportionation of iron:

$$2Fe_{Fe}^{x} \rightleftharpoons Fe_{Fe}' + Fe_{Fe}^{\cdot} \qquad (15)$$

Moreover, charge neutrality and the B-site balance for LSF result in the following equations.

$$[Fe'_{Fe}] + [Sr'_{La}] = [V_O^{\cdot\cdot}] + [Fe^{\cdot}_{Fe}] \quad (16)$$

$$[Fe'_{Fe}] + [Fe^{x}_{Fe}] + [Fe^{\cdot}_{Fe}] = 1 \quad (17)$$

To show the concentration of the occurring defects the number of the different point defects can be plotted in a Brouwer diagram. Figure 7 shows the Brouwer diagram for $La_{0.6}Sr_{0.4}FeO_{3-\delta}$ at 600°C. In this diagram the number of holes, electrons, oxygen vacancies and O^{2-} and Fe^{3+} on their ideal lattice sites per unit cell are plotted over the oxygen partial pressure. The number of lattice oxygen does not change significantly over the whole displayed pO_2 range. However, for Fe^{3+} there is a notable decrease at higher oxygen partial pressures leading to Fe^{3+} values of similar magnitude to the number of holes, which correspond to Fe^{4+}. The amount of oxygen vacancies stays pretty much constant in reducing conditions and then decreases at higher pO_2, due to the driving force for O_2 to reintegrate into the lattice and compensate vacancies in oxidizing conditions. Defect concentrations of electrons and holes behave conversely, with electrons decreasing and holes increasing with oxygen partial pressure until they reach a constant concentration at higher pO_2. Furthermore, the slope markers shown in the diagram display the power law exponents for defect concentrations depending on the oxygen partial pressure in a certain pO_2 region.[77,78]

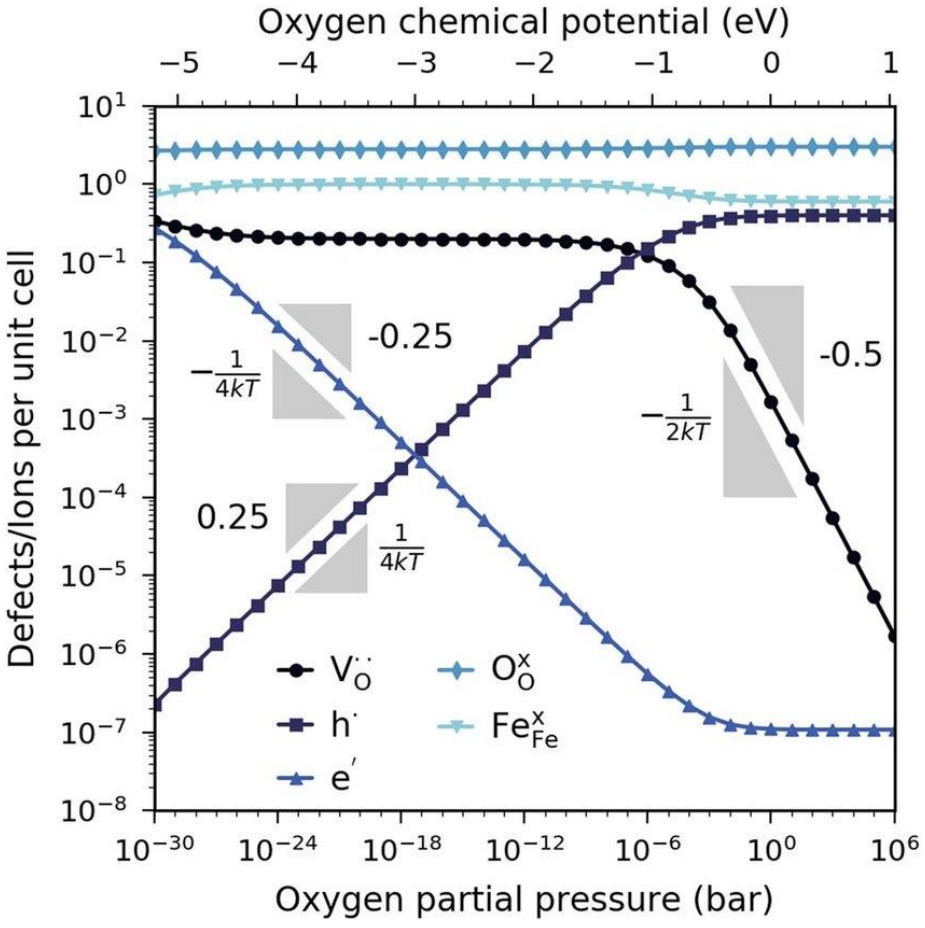

Figure 7: Brouwer diagram for LSF at 600°C. Reprinted from Ref.[78]

At very low oxygen partial pressures, depending on the temperature, LSF starts to decompose and exsolved metallic iron particles form on the surface. By the introduction of an additional B-site dopant the properties of the material can be further optimized and fine-tuned. For LSF iron can be partially substituted by cobalt, which leads to a reduced area specific resistance (ASR), beneficial for SOFC operation. Moreover, the exsolution of catalytically active Co particles can be observed at less reducing conditions than the Fe exsolutions, which is attributed to the lower stability of $LaCoO_{3-\delta}$ compared to $LaFeO_{3-\delta}$. The formation of these exsolutions can be described be the following mechanism:

$$2M_B^x + O_O^x \rightleftharpoons 2M_B' + V_O^{\cdot\cdot} + \frac{1}{2}O_2 \qquad (18)$$

$$M_B' + O_O^x \rightleftharpoons MO + V_B''' + V_O^{\cdot\cdot} \qquad (19)$$

$$MO \rightleftharpoons M + \frac{1}{2}O_2 \qquad (20)$$

M_B^x is the transition metal cation on the B-site and the charge of the metal on its ideal lattice place is in this example assumed with 3+ as for Fe^{3+}. The exsolution of metal particles happens, because at certain reducing conditions the oxygen vacancies created to compensate the reduced cations destabilize the perovskite structure and as a consequence, the creation of oxygen vacancies is accompanied by the formation of cation vacancies and additional phases occur.[77,79,80]

NCF and NCFC have also been reported to exsolve Fe and Co particles, with Co exsolutions forming in NCFC at lower temperatures than Fe exsolutions in NCF, as expected due to the easier reducibility of cobalt. The host perovskite stays intact after exsolution.[81]

2.5. Chemical capacitance

The chemical capacitance C_{chem} describes the chemical storage capacitance of a material and depends on the charge carrier concentrations. Therefore, the chemical capacitance obtained from EIS measurements can be used to gain insight into the defect chemistry. It depicts the ability of an MIEC oxide to change its stoichiometry in response to a variation in oxygen chemical potential. In contrast to an electrostatic capacitance that is indirectly proportional to the sample thickness, the chemical capacitance is directly proportional to the thickness, more specifically to the sample volume. Consequently, it can be several magnitudes bigger than the electrostatic capacitance of a sample. For dilute defects and one relevant electronic defect the chemical capacitance is given as follows:

$$C_{chem} = \frac{e^2}{k_B T} n_{uc} \left(\frac{1}{4c_V} + \frac{1}{c_{eon}} \right)^{-1} \quad (21)$$

T denotes the temperature, k_B the Boltzmann constant and e the elementary charge. n_{uc} is the concentration of unit cells and c_V and c_{eon} are the defect concentrations of vacancies and electronic defects in defects per unit cell.[60,82,83]

3. Experimental part

3.1. Sample preparation

For this thesis porous electrodes on GDC-basis and thin-film (Nd,Ca)(Fe,Co)O_3 electrodes on either recycled polycrystalline YSZ electrolytes or YSZ single crystal electrolytes were prepared. Furthermore, samples with wing geometry for three-point impedance measurements were manufactured.

3.1.1. Porous GDC based electrodes

To prepare the porous GDC based electrodes either on side polished 5 mm x 5 mm x 0.5 mm single crystalline YSZ electrolytes with 100 orientation or recycled 11 mm x 11 mm x 0.15 mm polycrystalline YSZ electrolytes were used. To obtain the recycled electrolytes the electrodes of old samples were grinded off with fine abrasive paper. Then the samples were purged off eventual metal residues in concentrated HNO_3 (Sigma Aldrich) before further cleaning with p.a. ethanol in an ultrasonic bath. The single crystal electrolytes were directly used after thoroughly rinsing with p.a. ethanol and drying with N_2.

For the electrode preparation at first a GDC paste was prepared by mixing GDC powder (GDC10, Treibacher) with a fuel cell paste (Ink vehicle, Fuelcellmaterials) consisting of a binder and an organic solvent in a 1:1 weight ratio. Afterwards the viscosity of the paste was adjusted by adding around 10 weight percent of terpineol (Sigma Aldrich). The mixture was then homogenized in a ball mill (Fritsch) with zirconia beads for 15 minutes. A Pt-GDC paste was manufactured by mixing the GDC paste with a commercially available Pt paste (Tanaka). To prepare the symmetric sample cells either the GDC paste or the Pt-GDC paste were brushed onto the electrolyte. Then the samples were dried at around 100°C for several minutes. For most samples, an additional layer of Pt paste was applied by brushing, serving as current collector, and they were dried again at 100°C. All samples except one with a Pt-GDC electrode and Pt current collector were sintered at 1150°C for 3 hours with a heating and cooling rate of 5°C per minute in a tube furnace with $MoSi_2$ heater elements (Carbolite). One sample with Pt-GDC electrode and Pt current collector was sintered at 1050°C for 3 hours with a heating and cooling rate of 5°C per minute to investigate possible performance differences due to the lower sintering temperature. Furthermore, three-layer porous electrodes were manufactured. For these electrodes at first a layer of GDC paste was deposited on the electrolyte by spincoating at 6000 rpm for 1 minute. The samples were dried at 100°C. Then a layer of Pt-GDC paste and last a layer of Pt paste were added by brushing, with a drying step at 100°C between each layer. The sintering conditions were the same as before with 1150°C for 3 hours and a heating and cooling rate of 5°C per minute. These three-layer GDC electrodes were also used as counter electrodes on the rough side of

10 mm x 10 mm x 0.5 mm one side polished single crystal YSZ electrolytes with 100 orientation for the investigation of thin-film electrodes. Due to optimization efforts one symmetric sample with a three-layer GDC electrode was prepared with an additional thin GDC layer deposited by pulsed laser deposition between electrolyte and spincoated GDC layer.

3.1.2. Thin-film electrodes

To manufacture the thin-film electrodes at first a current collector was deposited. The first attempt was to deposit the current collectors in the form of either a grid structure or finger structures, as shown in Figure 8, using lift-off lithography. For the lift-off lithography a layer of photoresist (Micro Resist Technology) was spincoated on the polished side of 10 mm x 10 mm x 0.5 mm YSZ single crystal electrolytes with 100 orientation and already prepared three-layer GDC counter electrode, and on the polished side of 10 mm x 10 mm x 0.5 mm MgO substrates with 100 orientation and without counter electrodes. The spincoating parameters were 70 rps for 25 s followed by 150 rps for 3 s to keep the thicker photoresist coverage on the edges as small as possible. The samples were dried on a heating plate at 100°C for 2 min. Then a positive mask of the desired structure was aligned above the photoresist on the sample using an optical microscope and the sample was exposed to a UV-lamp with 400W for 60 s to polymerize the uncovered areas of the photoresist. Afterwards the sample was developed in a developer from Micro Resist Technology for 60 s and thoroughly rinsed with deionized water. Due to adhesion issues of the photoresist on the substrates the surface of some substrates was roughened by ion beam etching for a few minutes to eventually fix these problems. However, the lithography structures still showed a huge number of defects after developing and the solution to overcome this problem turned out to be an increase in UV exposure time from 60 s to 120 s. The next step was to sputter the current collector using Ar plasma. First a 2 nm thick layer of Ti for a better interface was sputtered with 100 mA and an Ar pressure of $7.3*10^{-3}$ mbar, followed by a 100 nm thick layer of Pt with a current of 100 mA and an Ar pressure of $2*10^{-2}$ mbar. At last the photoresist was dissolved by keeping the sample in p.a. ethanol for 30 minutes and then gently rinsing it with p.a. ethanol to yield the desired current collector structure.

However, the current collector structures established by lift-off lithography still showed many defects and were not really viable, especially for the finger structures where most of them showed short circuits. Therefore, a second approach to manufacture the current collectors by ion beam etching was made. In this attempt first a 2 nm layer of Ti followed by a 100 nm layer of Pt were sputtered on the polished side of the thoroughly with ethanol cleaned substrates using the same sputter parameters as before. Then the photoresist was spincoated onto the Ti-Pt layer with 70 rps for 25 s followed by 150 rps for 3 s and dried at

100°C for 2 min. For this approach, a negative mask was aligned to the sample the photoresist exposed to UV light for 120 s. The sample was developed and cleaned with deionized water. Subsequently, the noncovered parts of the Ti-Pt layer were removed by ion beam etching with Ar for approximately 45 min. Last the remaining parts of the photoresist were removed by putting the sample into p.a. ethanol for 30 min and then rinsing and gently cleaning it with an ethanol-soaked cloth. The resulting current collectors showed way less defects than with lift-off lithography, as displayed in Figure 8.

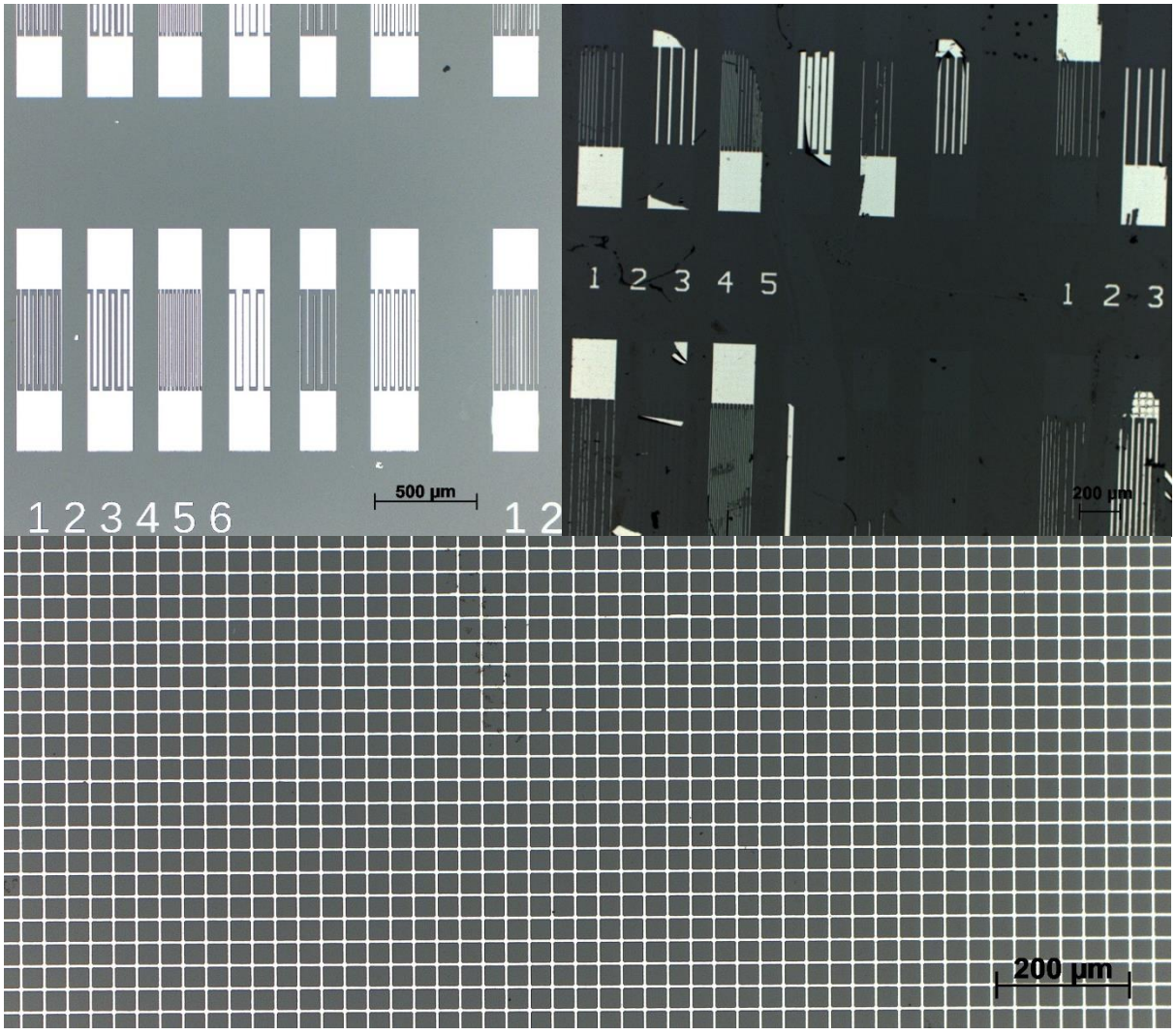

Figure 8: Current collector finger structure prepared via ion beam etching (top left), via lift-off lithographie (top right) and grid structure prepared via ion beam etching (bottom).

In order to make the contact pads of the finger electrodes accessible after the deposition of the thin-films they were covered with a ZrO_2 paste that doesn't sinter at the deposition temperature using a very fine brush and optical magnification. Once the current collectors had been structured a thin-film of either $Nd_{0.6}Ca_{0.4}FeO_{3-\delta}$ (NCF) or $Nd_{0.6}Ca_{0.4}Fe_{0.9}Co_{0.1}O_{3-\delta}$ (NCFC) was deposited on top of it via pulsed laser deposition (PLD) with 9000 pulses and a frequency of 10 Hz. The working distance was 6 cm, the laser energy 400 mJ, the oxygen

pressure 0.04 mbar and the temperature 600°C. The targets have been previously synthesized using the Pechini method[84] by dissolving the according amounts of the precursors Nd_2O_3, $CaCO_3$, Fe and Co to yield the desired composition in HNO_3. Citric acid was added in a 1:1.1 ratio to form cation complexes, a gel was formed after the evaporation of H_2O and heated until self-ignition and the resulting powder was calcinated 3 hours at 900°C, grounded, isostatically pressed into the target form and sintered at 1200°C for 12 hours. The targets were grinded and thoroughly cleaned with p.a. ethanol before fixing them in the rotating target holder to ensure a flat surface. Directly before each deposition the laser was fired onto the target with a closed shutter over the sample for 1200 pulses with 5 Hz to get rid of eventual impurities on the target surface. After the samples had cooled down to room temperature the ZrO_2 paste was removed from the finger electrode samples by gently cleaning them with ethanol-soaked cloths. The finger electrode samples were broken into two approximately 10 mm x 5 mm parts and the ones with a grid current collector into four approximately 5 mm x 5 mm parts using a diamond scratcher and mechanical force to increase to number of measurable samples per sample manufacturing cycle and thus save time.

Furthermore, an approach to recycle already measured samples by etching off the thin-film and ideally not degrading the current collectors and counter electrodes was made, so a new sample could be prepared by only one recycling step and the deposition of a new thin-film. A first try of treating the sample in concentrated HNO_3 wasn't successful because the thin-film didn't dissolve in a reasonable amount of time. However, by putting the old, already measured samples in concentrated HCl the thin-films could be etched off in about 40 minutes without major visible damage to the current collectors and counter electrodes under the optical microscope. Hence, new thin-films could be deposited onto these recycled samples, after a rinsing step first with deionized water and then with ethanol to get rid of eventual acid residues.

3.1.3. Wing samples

To manufacture the wing samples for three-point impedance measurements 5 mm x 5mm x 1 mm two-side polished single crystal YSZ electrolytes with 100 orientation were cut into the shape visible in Figure 9 with a CNC milling machine (EAS(Y) 440 KG PRO) to provide a place for a third electrode, functioning as reference electrode with ideally no current flow during a measurement.

A three-layer GDC counter electrode consisting of a spincoated GDC layer, a brushed Pt-GDC layer and a brushed Pt layer as described before was prepared on one side of the sample. Moreover, such a three-layer electrode was also brushed onto the wing using a very fine brush and optical magnification. On the wing the normally spincoated GDC layer was

brushed because of the small surface area. To make sure that there is no electrical contact between the wing electrode and the other electrodes the areas separating them were purged of eventual electrode paste residues by scratching with a needle. After the sintering step at 1150°C for 3 h with a ramping rate of 5°C per minute, a thin-film Pt mesh current collector was prepared as described above, and the NCFC thin-film electrode was deposited via PLD on top of the current collector at the polished side of the sample with the same deposition parameters as described in 3.1.2.

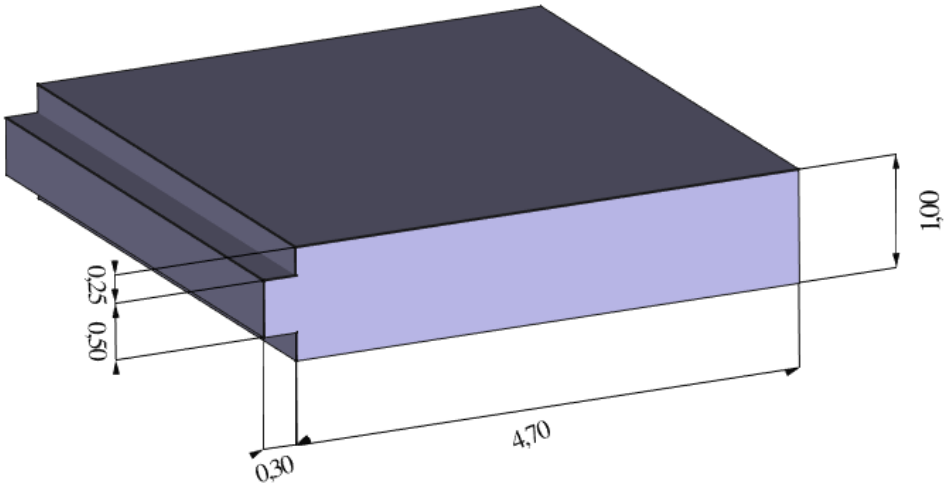

Figure 9: Geometry of the wing samples, all measurements are in mm.

3.2. Evaluation of electrode thickness

The thickness of the porous GDC layers was approximated by a simple scratch test. At first a layer of GDC paste was either brushed or spincoated on a YSZ substrate and then dried at 100°C. Afterwards, several scratches were made with a steel needle and enough pressure to penetrate the GDC layer down to the YSZ substrate on different positions. To roughly measure the thickness first the bottom of the scratch was focused under an optical microscope and the level on the depth axis was noted. Next the areas surrounding the scratch were focused and the difference on the depth axis showed a good approximation of the layer thickness for comparing brushed and spincoated layers. The thickness of the NCF and NCFC thin-films was evaluated by using a profiler (DektakXT, Bruker) on several positions of samples with edges from the thin-film down to the YSZ substrate.

3.3. Impedance measurements

The impedance measurements were mainly carried out in four different measuring setups, a four-sample setup, a micro setup, a wing sample setup, and a micro/macro setup, which are explained in detail in the following part.

3.3.1. Four-sample setup

The four-sample measuring setup was mainly used for impedance measurements of the different GDC based samples. The major advantage of this setup was, as the name suggests, that it was possible to measure four samples at the same time without the need to cool down and change the sample in between. This was achieved by applying a multiplexer and a sample holder that fits four samples, which are electrically separated from each other, at once. A picture of the sample holder is shown in Figure 10.

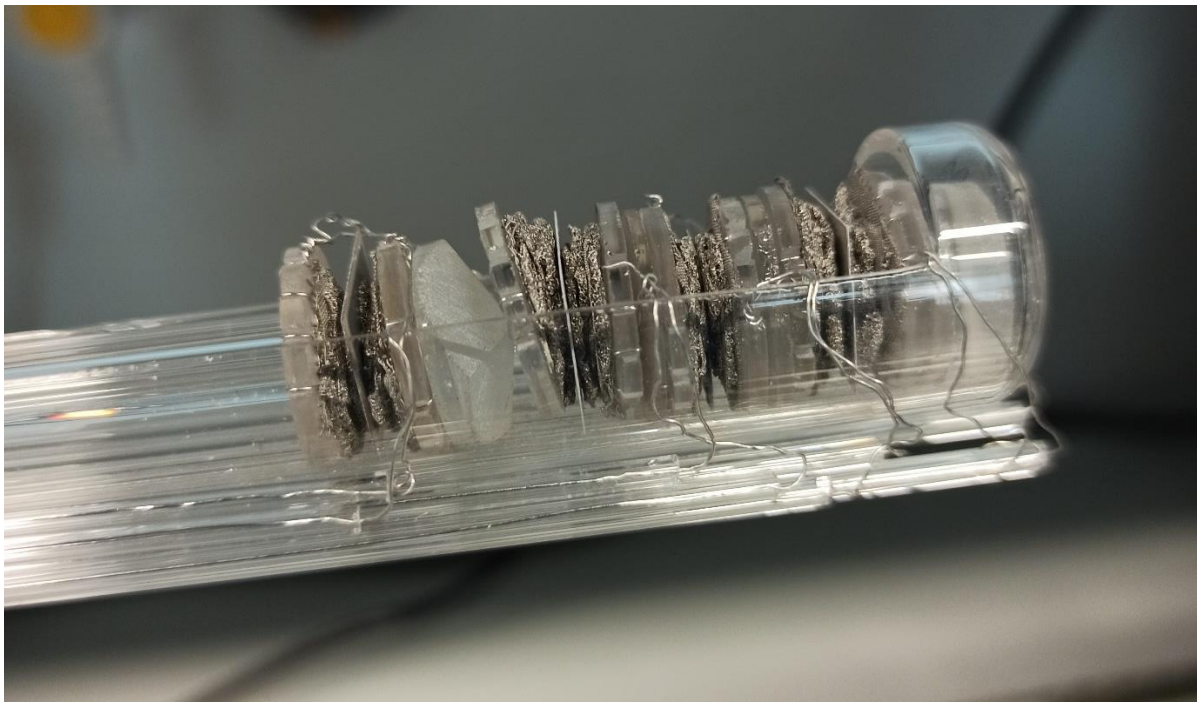

Figure 10: Sample holder of the four-sample setup.

The whole test rod was made of quartz and small quartz tubes were used to guide platinum wires to the foams contacting the samples. The ends of the tubes carrying the platinum wires were displaced to ensure that the wires cannot form a short circuit easily. The contacting foams were made from Ni and their purpose was to make sure the sample is contacted well while still not hindering gas diffusion significantly. Although the Ni foams were rather soft with a high porosity and adapted to the sample surface very well, a downside was that it was only possible to measure in reducing atmospheres, because these foams can oxidize in oxidizing atmospheres and consequently degrade very fast. Between each sample there was a quartz placer. To hold the contacts and samples together during measurements a slight pressure was applied from one side through a quartz rod connected to a spring. To allow for a controlled atmosphere during measurements, the sample holder was covered and sealed with a quartz tube that was closed tightly with screws at the end of the test rod opposite to the samples. In order to avoid damage of the quartz tube due to mechanical stress and

ensure tightness an O-ring seal between the tube and the back end of the test rod was applied. The closed measuring setup is displayed in Figure 11.

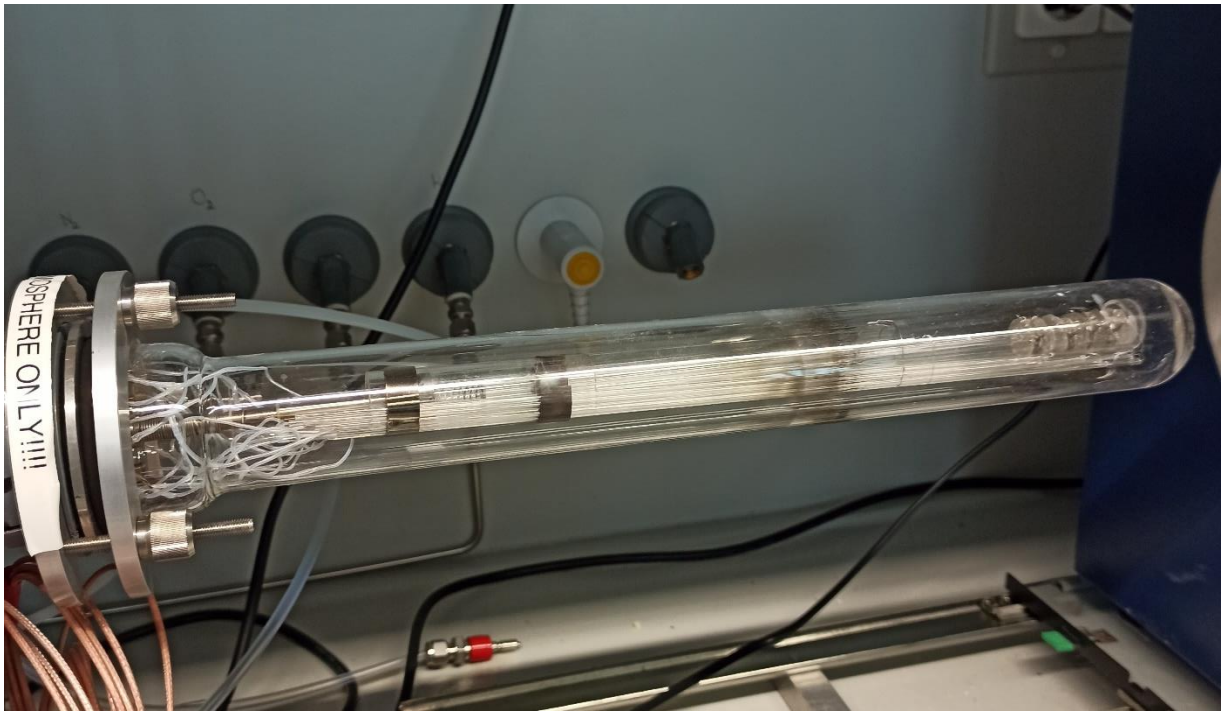

Figure 11: Closed test rod.

Because most measurements in this setup were conducted with the same flow rate and to know the exact value was not crucial for this study it was controlled via a needle valve prior to the gas inlet. The gases needed to generate the desired atmospheres were supplied to the setup via flexible PTFE tubes and all connections were made using Swagelok connectors. Before entering the test rod, the gases were led through a humidifier as pictured in Figure 12. It consisted of three steel cylinders connected via tubes and forced the gases to pass through the water in the middle cylinder. The other two cylinders acted as a precaution to avoid water flow back to the gas supply or to the test rod in case of pressure differences. For most measurements in this setup a lambda sensor and a pressure sensor were mounted after the gas outlet of the test rod to monitor the atmosphere and pressure. However, due to a missing temperature sensor for the lambda sensor and the fact that the temperature can change with different gas flows the obtained values were mainly used to qualitatively check if the atmosphere is oxidizing or reducing and thus make sure to avoid damage of the Ni foams because of heating in oxidizing atmospheres. The outlet tube was either going to the fume hood or connected to a vacuum pump in case low pressure experiments were carried out. Furthermore, for low pressure experiments with pure hydrogen the outlet gas was diluted with ARCAL (2.5% H_2 in Ar) before flowing into the lab air to prevent explosive hydrogen oxygen mixtures from forming. For heating of the test rod, a tube furnace (Carbolite) was applied with the samples positioned approximately in the middle of the furnace. The end of

the test rod opposite to the samples was cooled via a fan to protect the polymer parts from heat damage. To avoid artifact features in the impedance spectra the test rod was protected by a shielding braid, which was grounded to prevent dangerous induction currents from forming.

Figure 12: Humidifier for generating wet gas atmospheres.

The impedance was measured with an Alpha-A High Performance Frequency Analyzer coupled with an Electrochemical Test Station POT/GAL from Novocontrol and the contacted samples were connected via BNC cables and a multiplexer, that allowed to switch between the four samples. The measurements were performed in four-point mode and which electrode was connected to the WE (working electrode) and CE (counter electrode) terminal did not matter since all the samples in this testing setup were symmetric and measured without additional bias. Typically, impedance spectra were recorded in a frequency range from 0.1 Hz to 100000 Hz and with an AC amplitude of 20 mV with small adjustments corresponding to the type of sample measured. To investigate the behavior of the samples either temperature or atmosphere were varied. Multiplexer, impedance analyzer, furnace, and eventually mass flow controllers were controlled via the software Javalab.

Moreover, experiments in CO atmosphere were conducted in this setup. The necessary CO was produced in a prototype furnace through electrolysis of CO_2 using a YSZ tube with electrodes made of GDC and a Pt current collector. The electrode area was approximately

30 cm^2. That way only small amounts of the toxic CO could possibly be released into the air in case of error or fracture of the apparatus. The setup for CO measurements is shown in Figure 13. The temperature of the CO furnace was kept at around 770°C to avoid the formation of carbon due to the exothermic Boudouard reaction shown in (22).

$$2CO \rightleftharpoons CO_2 + C \qquad (22)$$

The amount of CO generated was controlled via the current of the power generator (Voltcraft DPS-4005PFC) for the electrolysis. To control the flow of the gas, a mass flow controller (Alicat scientific) was incorporated before the gas inlet of the test rod.

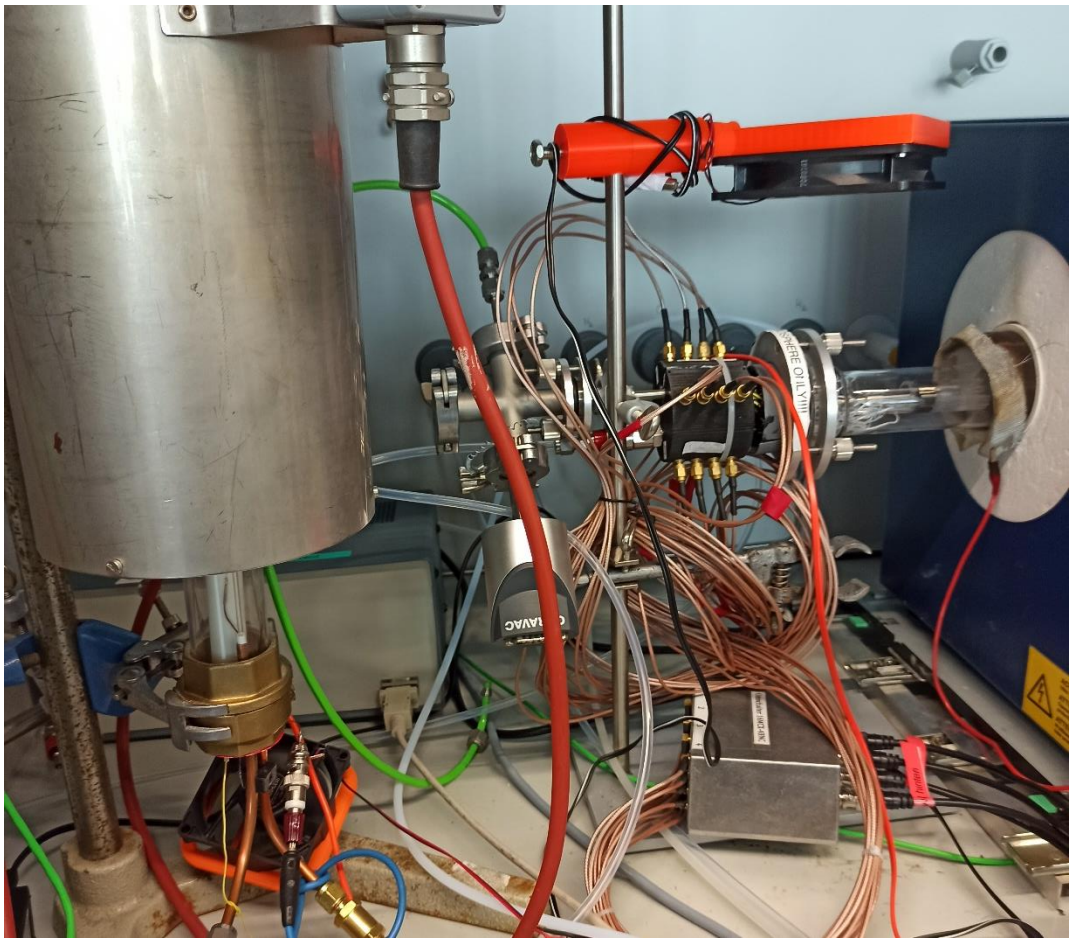

Figure 13: Measurement setup for CO atmosphere experiments with the CO electrolysis furnace on the left side and the braid shielded test rod in the tube furnace on the right side.

The impedance spectra were recorded with an N4L PSM1735 impedance analyzer controlled via Javalab at different CO concentrations.

3.3.2. Micro setup

The micro setup was used for in-plane measurements on NCF and NCFC thin-film samples with finger structured microelectrodes. It consisted of a pot-shaped measuring chamber with a bottom heater that was cooled with a water-cooling system during operation. The electrode

pads could be contacted with Pt needles that were controlled via PC software. These measurements were conducted in humidified ARCAL (2.5% H_2 in Ar) at a constant temperature of approximately 600°C. Due to the long durations needed to reach a stable system and temperature fluctuations because of contacting with the relatively colder Pt needles the measurements in this setup were mainly performed to investigate the electrode behavior of different geometries of the interdigitating electrodes qualitatively. Impedance spectra were recorded with an Alpha-A High Performance Frequency Analyzer coupled with an Electrochemical Test Station POT/GAL from Novocontrol in four-point mode to compensate the cable resistances. An image of the micro setup can be seen in Figure 14.

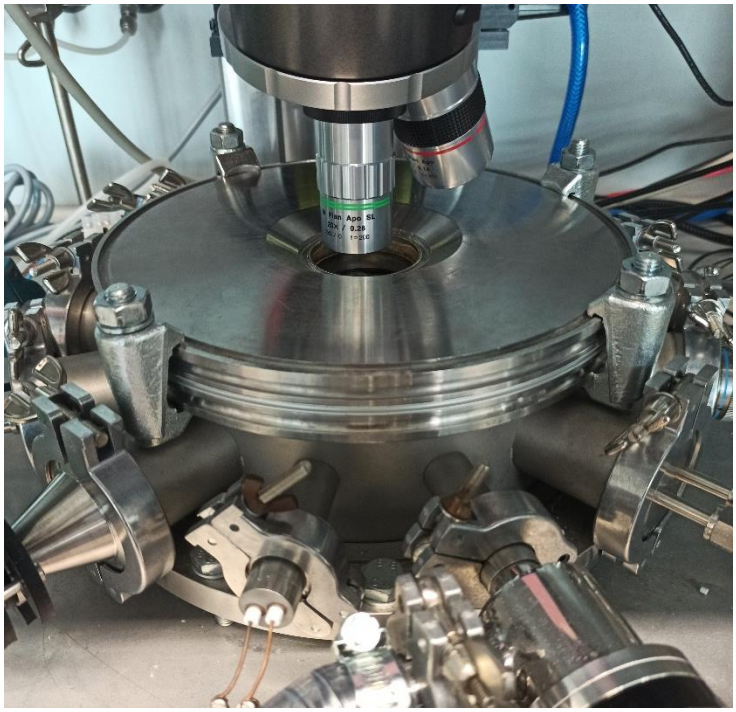

Figure 14: Micro setup.

The measuring chamber could also be evacuated, and it was possible to observe the sample during the measurement via an optical microscope, which was also used to monitor the Pt needles during contacting.

3.3.3. Micro/macro setup

The micro/macro setup was used for measuring in-plane and electrochemical impedance of NCF and NCFC samples with interdigitated microelectrodes. Furthermore, electrochemical measurements of macro thin-film samples with grid current collectors could be performed. The sample holder was made of alumina with a Pt sheet at the bottom for contacting the counter electrode and four Pt needles for contacting the thin-film or the finger electrode contact pads, according to the performed measurement type. For better contacting of the counter electrode a Pt mesh could be applied between the sample and the Pt bottom

contact. Because bringing the Pt needles into place by hand is very time-consuming and not accurate a special device for contacting was built, as displayed in Figure 15.

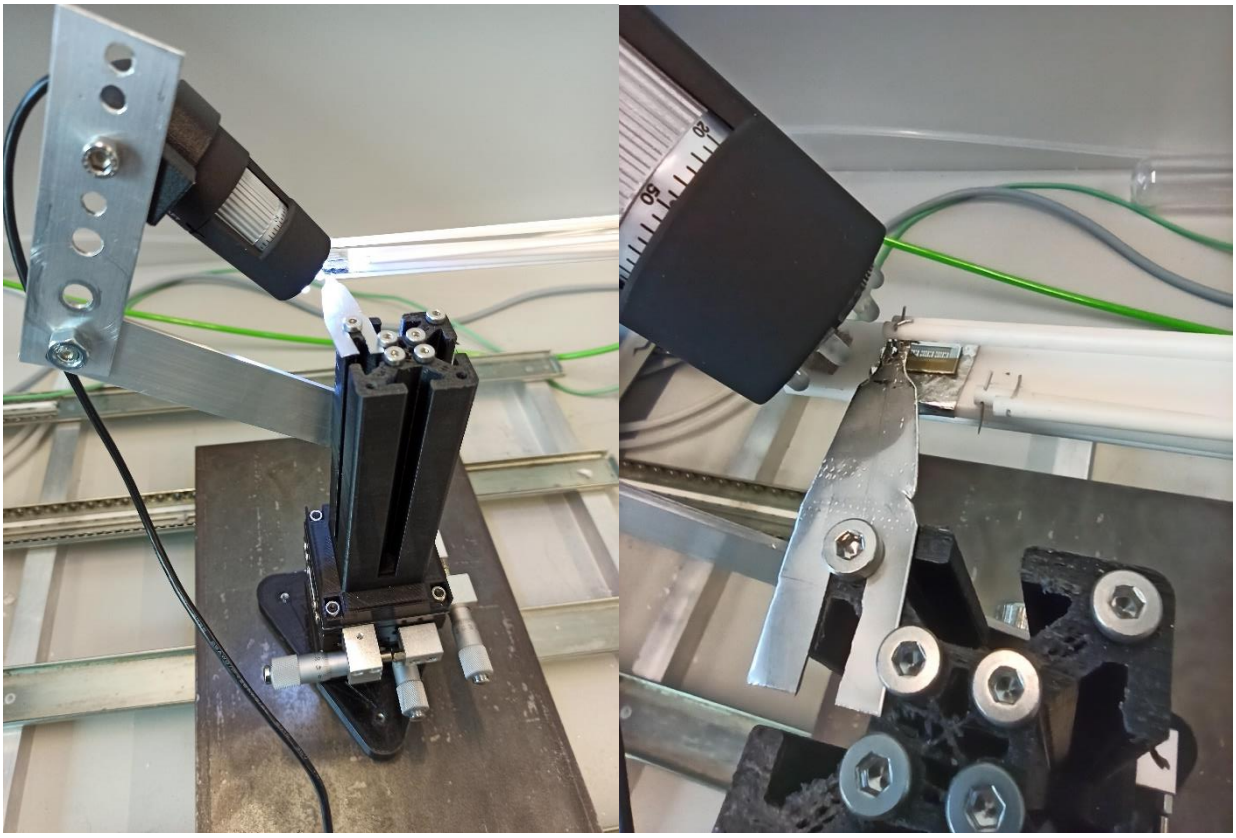

Figure 15: Device for contacting microelectrode contact pads.

The main part was a 3D printed profile that could be moved along the x, y and z axis very precisely and allowed to mount additional parts using T-sections. For more stability, the device had magnets at the bottom and was placed on a rather heavy metal plate during the contacting procedure. Furthermore, a USB camera to monitor the tip of the Pt needles while contacting was mounted on the device via moveable aluminum parts. In order to lift the needles a metal fork was used and to make sure they stay in place they were pushed down with slight pressure via elastic force. That allowed the microelectrodes to stay contacted even during vibrations, which could occur due to near doors or drawers closing.

For the electrochemical measurements of macro samples with grid current collectors the samples were placed on the Pt mesh with the counter electrode down and the thin-film on top contacted with four short-circuited Pt needles. To measure impedance of the samples with interdigitating current collectors they were placed on the Pt sheet with the thin-film side on top and the contact pads of a microelectrode were contacted using two Pt needles and the previously explained contacting device. Due to the usage of a trigger box with the wiring shown in Figure 16 it was possible to switch between in plane measurements and electrochemical measurements without changed any cables or the contacting of the sample.

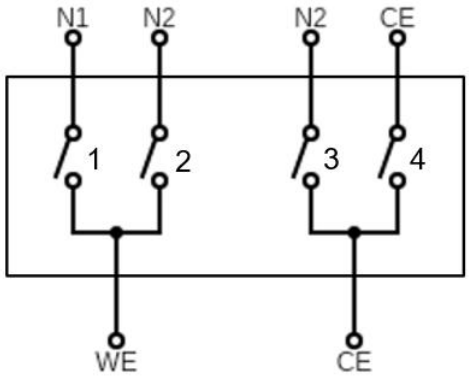

Figure 16: Wiring of the trigger box for switching between in plane and electrochemical measurements.

On the bottom side there are the two contacts for the WE and CE terminals of the impedance analyzer. N1 and N2 denote the needles, and CE on the top side is the Pt sheet contact for the counter electrode. To measure in plane impedance the switches 1 and 3 were closed, while for electrochemical measurements 1, 2 and 4 had to be closed with the two needles acting as the working electrode contact and the Pt sheet as the counter electrode contact. Figure 17 shows the sampler holder with a contacted microelectrode sample and a contacted macroelectrode sample.

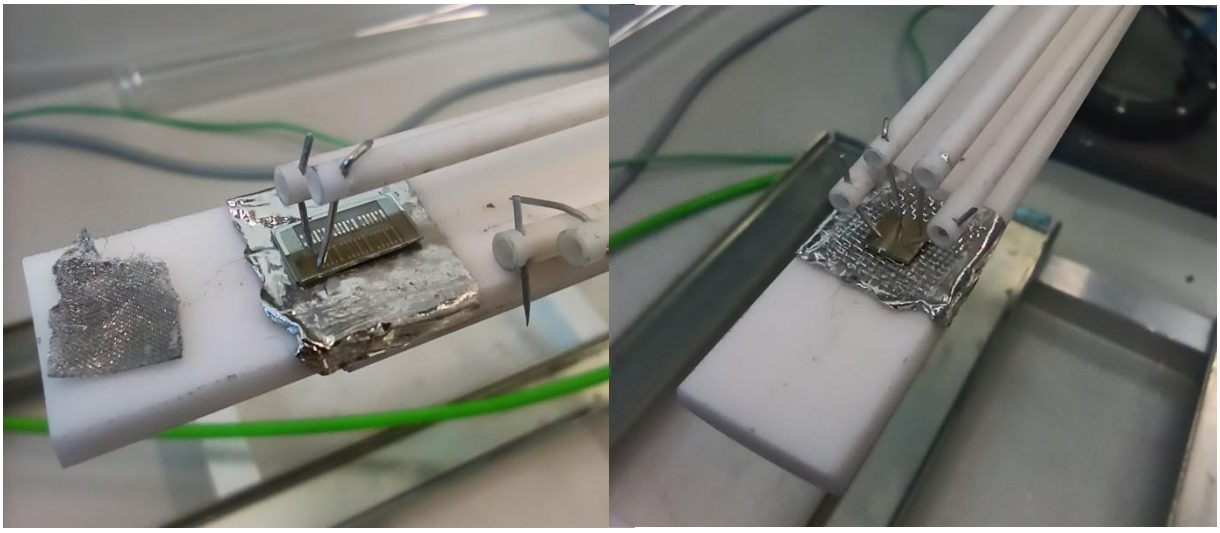

Figure 17: Contacted microelectrode sample (left) and contacted macroelectrode sample (right).

During the measurements, the sample holder was sealed with a quartz cylinder and for heating a tube furnace (Carbolite) was used.

Because in this setup the behavior of the electrodes in different gas atmospheres was studied, four mass flow controllers (MFCs) were connected via metal tubes and Swagelok connectors in a way that allowed mixing and adjusting the flow of ARCAL (2.5% H_2 in Ar), O_2, N_2 and through the humidifier. The mass flow controllers have not been used to set the flow of the mentioned gases before and consequently, had to be calibrated before usage. To

calibrate the MFCs a steel cylinder that had two openings and could be evacuated via one of them was used. It was filled with a few fiber tissues that could take up heat energy and thus help to avoid possible adiabatic temperature changes due to pressure changes. The second inlet was connected to the MFC that should be tested. For calibration, the cylinder was evacuated to a pressure of around 500 mbar, the MFC was set to a certain flow of the desired gas and the time needed until the pressure had risen to a certain level was noted. The gas flow in sccm (standard cubic centimeter per minute) was calculated according to equation 23.

$$Flow\ rate\ [sccm] = \frac{V * \Delta p * 60}{1000 * t} * \frac{273K}{273K + T} \tag{23}$$

V denotes the volume of the steel cylinder, which was measured to be 600 cm^3, Δp the pressure difference from the start of the test until the end in mbar, t the time in s and T the temperature in °C. This test was performed for every of the four MFCs with the corresponding gases at different flow rates. Hence, it was possible to fit the results with a linear regression and calculate the set flows needed for a certain flow rate.

Due to this MFC setup it was possible to test the electrodes in a wide range of oxygen partial pressure. The impedance spectra were recorded in the micro/macro setup via an Alpha-A High Performance Frequency Analyzer coupled with an Electrochemical Test Station POT/GAL from Novocontrol in two-point mode and in this setup mainly the impact of different atmospheres on the thin-film electrodes, degradation in reducing atmospheres and the electrode behavior with an additional applied bias were investigated.

3.3.4. Wing setup

The wing setup was designed for measuring the wing samples described in 3.1.3, but was primarily used for recording impedance spectra of GDC based electrodes and thin-film macro electrodes at different temperatures, atmospheres and with additionally applied bias. Due to a rather strong degradation of the thin-film samples in this setup, the wing samples were not measured there. The sample holder, as shown in Figure 18, was made of alumina.

For contacting of the WE and CE, several layers of Pt mesh were used, which were pressed against the electrodes by elastic force during the measurements. Furthermore, a Pt contact on an alumina rod could be used to contact the reference electrodes of a wing sample. However, for measuring samples without a reference electrode it was connected to the Pt foam that was only contacted by one Pt wire, to form a short circuit and allow four-point impedance measurements. To seal the test rod a quartz cylinder was applied. The mass flow controllers, tube furnace and Impedance analyzer were the same as used in the macro/micro setup, explained in detail in 3.3.3.

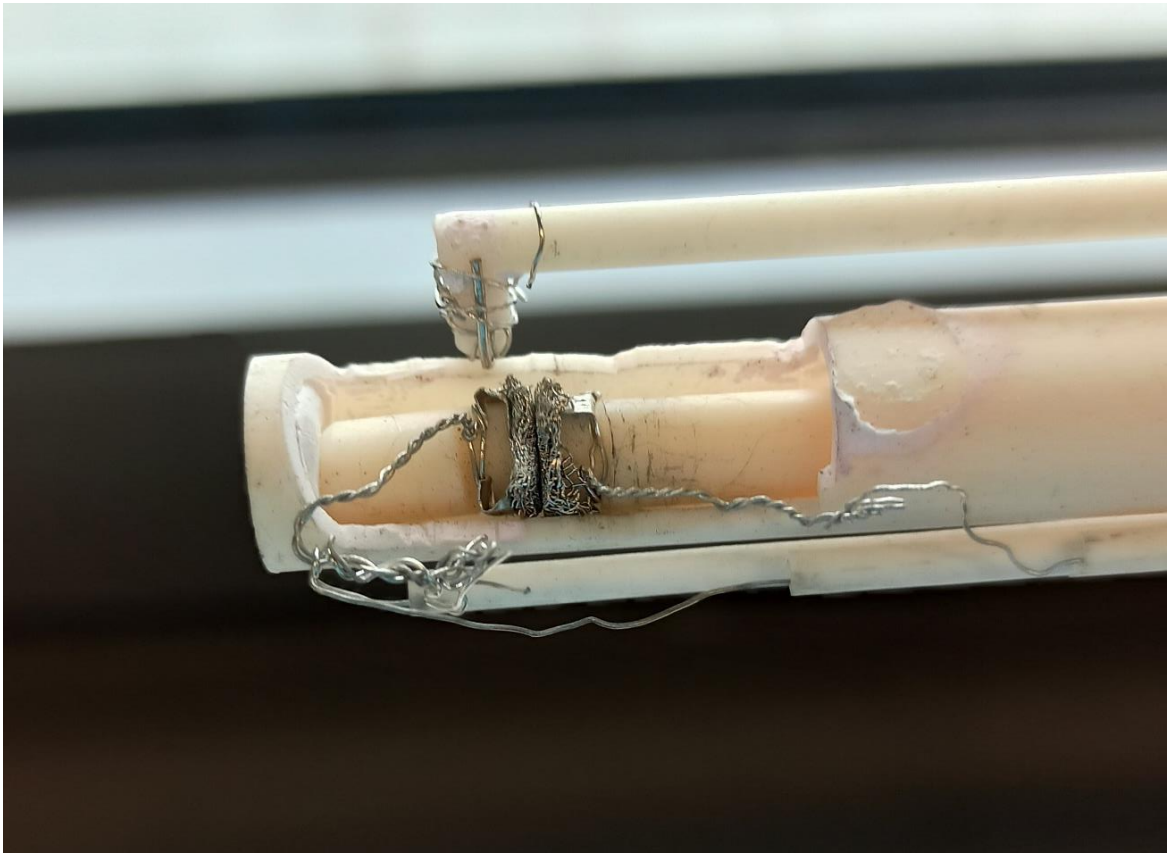

Figure 18: Sample holder of the wing sample measuring setup.

3.3.5. XPS measurements

XPS measurements were performed on thin-film samples after EIS measurements to investigate if an eventual deposition or segregation of impurities on the surface, that is to blame for the degradation of the samples, takes place. Furthermore, near ambient pressure XPS (NAP-XPS) measurements were conducted in situ on the prepared wing samples while measuring impedance, to monitor surface changes during experimental conditions like an additional applied bias. In contrast to normal XPS, which only works in high vacuum conditions, NAP-XPS allows to investigate the composition and electronic state of the surface elements in certain gas atmospheres that resemble real operation conditions more properly. To contact the wing samples and perform three-point impedance measurements the sample holder displayed in Figure 19 was used. The sample was positioned on an alumina plate, which got heated by and infrared laser from the back side, and the counter electrode contacted by a bottom contact. The working electrode (thin-film electrode) was contacted in two corners and these contacts also helped to lock the sample in place via elastic force. The reference wing electrode was contacted via a bow-shaped contact. The NAP-XPS measurements were conducted in an NAP-XPS device from SPECS equipped with a hemispherical energy analyzer.

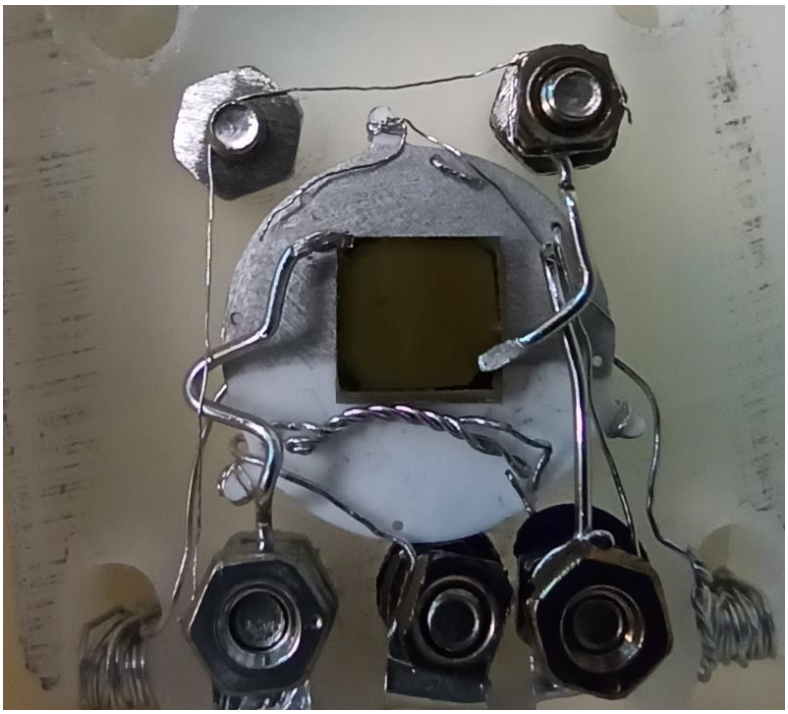

Figure 19: Sample holder for in situ NAP-XPS measurements of wing samples.

4. Electrochemical properties of GDC based electrodes

The main goal of this thesis is to get insight into the exsolution behavior and electrochemical properties of $Nd_{0.6}Ca_{0.4}FeO_{3-\delta}$ (NCF) and $Nd_{0.6}Ca_{0.4}Fe_{0.9}Co_{0.1}O_{3-\delta}$ (NCFC). For this, however, we first have to understand and characterize the electrochemical properties of the used GDC based counter electrodes that are required for electrochemical characterization of the NCF and NCFC materials.

Interestingly, the GDC based electrodes exhibited excellent polarization resistance, which renders these electrodes also promising for SOFC and SOEC application. Therefore, the characterization of these electrodes was extended in order to better understand the underlying reaction mechanisms.

4.1. EIS measurements for comparison of GDC based electrodes

The first measurements were conducted in the four-sample setup with four differently prepared samples. The electrolyte was recycled polycrystalline YSZ (11 mm x 11 mm x 0.15 mm) obtained by grinding off electrodes from model cells with symmetrical Ni-GDC anodes and cleaning them thoroughly. The samples were prepared symmetrically by brushing the same electrode pastes on both sides and then drying and sintering. The electrode materials used for each sample and the sintering conditions are listed in Table 1. Throughout this work, the nomenclature for cermet layers is PtGDC, whereas the names for different electrode layers are separated by a vertical line, e.g. PtGDC|Pt.

Table 1: Electrode composition and preparation conditions.

Name	Electrode material	Current collector	Sintering temperature
GDC|Pt	GDC (brushed)	Pt (brushed)	1150°C
PtGDC	PtGDC (brushed)	none	1150°C
PtGDC|Pt	PtGDC (brushed)	Pt (brushed)	1150°C
PtGDC|Pt	PtGDC (brushed)	Pt (brushed)	1050°C

The impedance spectra were recorded in four-point mode with an AC amplitude of 20 mV in a frequency range from 0.1 to 900000 Hz, ten measuring points per decade and temperature cycles from 500 to 800°C in 50°C steps. The first measurements with these samples were performed in humidified ARCAL with an H_2 to H_2O ratio of approximately 1:1. Afterwards, measurements at a low pressure of around 60 mbar (28 mbar H_2O, depending on ambient temperature, rest H_2) with humidified pure hydrogen were carried out. Due to the low pressure the ratio of H_2 and H_2O stayed the same with around 1:1. The flow was adjusted via

a needle valve to approximately 100 sccm for both measuring atmospheres. The values for ASR and capacitance were obtained by fitting each feature with a parallel R||CPE circuit and in case that was not possible due to high noise or features deviating a lot from the expected semicircle shape the ASR was estimated by subtracting the high frequency intercept on the x-axis from the low frequency intercept.

4.1.1. Temperature cycles of GDC|Pt

Figure 20 shows the Nyquist plots of the symmetric GDC|Pt sample measured in humidified ARCAL.

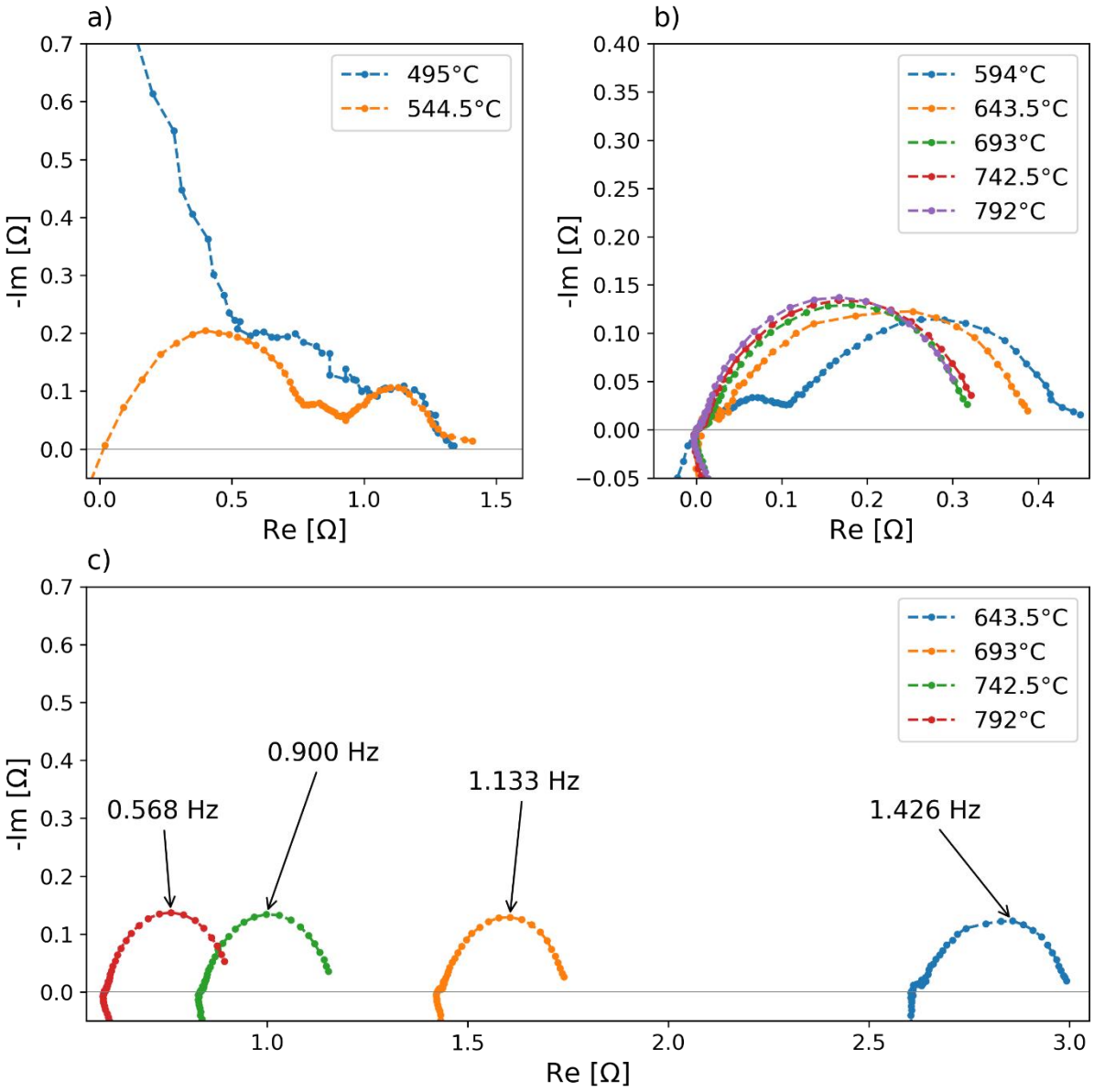

Figure 20: Nyquist plots of a symmetric sample with a polycrystalline YSZ electrolyte and GDC|Pt electrodes measured at different temperatures in humidified ARCAL (hydrogen to water ratio of about 1:1) with subtracted high frequency x-axis intercept (a), (b) and unedited (c).

Figure 20 a) and b) show the impedance spectra with subtracted high frequency x-intercept to make a comparison of different temperatures easier and c) additionally displays the different intercept on the x-axis for the higher measured temperatures and the peak frequencies of the dominant semicircle feature. Although several up and down temperature cycles were measured, only the first cycle is shown here, because most of the other cycles did not yield reliable results, with the spectra often consisting only of noise. The reason for that was probably a defective connection.

The impedance spectra in Figure 20 a) for the lower measured temperatures consist of more than one feature. For the lowest temperature of 495°C only one clearly semicircle like feature at high frequencies is visible and the whole spectra is rather noisy with capacitive behavior at low frequencies. The spectrum for 544.5°C shows three features at different frequencies with the high frequency feature being attributable to an electrolyte effect because of the high peak frequency of around 70000 Hz and consequently lower capacitance characteristic for electrolyte features. The lower frequency semicircle probably displays an electrode effect because of the lower peak frequency and therefore high capacitance. Figure 20 b) shows the normalized spectra for the higher temperatures and they consist of one big semicircle at low frequencies and a comparably small feature at slightly higher frequencies near the high frequency intercept on the x-axis. Contrary to the expectation that the surface reaction feature should become smaller at higher temperatures due to faster kinetics, the low frequency semicircles are equal in size to a certain extent, which suggests that this feature does not represent the electrode reaction. Furthermore, the smaller slightly overlapping feature at higher frequencies decreases in size with increasing temperature and is hardly visible anymore at a temperature of 792°C. The spectra in Figure 20 c) are the same displayed in b) but with the original intercept on the x-axis. Moreover, the peak frequency of the semicircles is displayed, and it decreases slightly with increasing temperature. The offset resistance represents the electrolyte resistance and decreases at higher temperatures due to better ionic conductivity.

In Figure 21 a) and b) the Nyquist plots, with subtracted high frequency intercept, of the symmetric GDC|Pt samples measured at temperatures from around 500 to 800°C in humidified H_2 at approximately 60 mbar are shown. At the temperatures 495°C and 544.5°C several overlapping features with the high frequency ones probably describing the electrolyte, but no clear separation of the features was possible and thus no reliable interpretation can be made. The impedance spectra from 594 to 792°C consist of a semicircle that decreases in size with increasing temperature, as expected from an electrode feature describing the surface reaction. However, the spectra at the higher temperature end could also consist of two semicircles, which could not be clearly determined due to the high

noise amplitude, which is a consequence of the very small electrode arc. Furthermore, the peak frequencies of the semicircles are significantly higher compared to the measurements in humidified ARCAL atmosphere with the same H_2 to H_2O ratio. Figure 21 c) displays the ASR of the features attributable to electrode effects from the measurements in humidified ARCAL and humidified H_2 plotted over 1000/T. The data points were fitted, and the activation energy E_A could be calculated via the following equation.

$$E_A\,[eV] = \frac{k * 1000 * k_B}{e} \tag{24}$$

The factor 1000 was needed due to the x-axis being chosen as 1000/T, k denotes the slope of a linear fit of the natural logarithm of the ASR over 1000/T, k_B is the Boltzmann constant and e the elementary charge.

The ASR and chemical capacitance are in this work always shown for one electrode, so in case of symmetric samples the area normalized results had to be additionally either divided (for the ASR) or multiplied (for the chemical capacitance) with the factor 2.

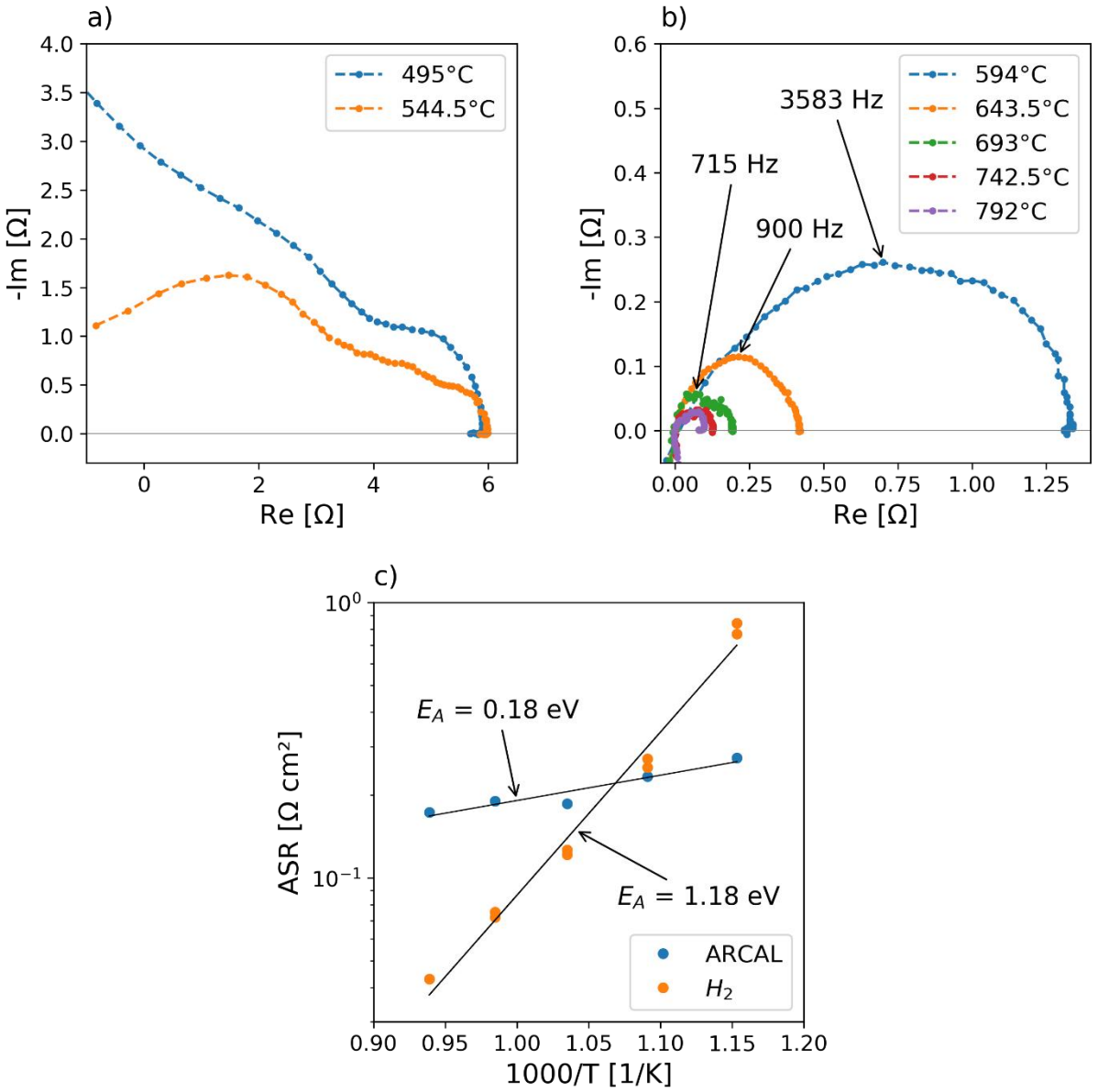

Figure 21: Nyquist plots of a symmetric sample with a polycrystalline YSZ electrolyte and GDC|Pt electrodes measured at different temperatures in humidified H_2 (hydrogen to water ratio of about 1:1) at 60 mbar (a), (b) and ASR plotted over 1000/T of the measurements in H_2 and ARCAL(c).

It can be noticed that the ASR of the spectra recorded in humidified H_2 atmosphere decreases exponentially with increasing temperature while the ASR of the measurements in humidified ARCAL does not really change substantially over the whole temperature range. That leads to a huge difference in the activation energy and thus provides further evidence that the semicircle features of the spectra recorded in different atmospheres describe different processes. As a result of the described findings the low frequency semicircle feature of the measurements in humidified ARCAL could be identified as gas diffusion feature, matching well with the very low peak frequencies and the fact that its resistance does not change noteworthily over the whole temperature range. Furthermore, this low frequency feature disappears in humidified H_2, although the H_2 to H_2O ratio stays the same, which

points further towards a gas diffusion limitation in ARCAL, due to more gas molecules being available for collisions in humidified ARCAL than in humidified H_2 at low pressure, thus lowering the diffusion coefficient.

4.1.2. Temperature cycles of PtGDC

In Figure 22 the impedance spectra of the PtGDC sample without Pt current collector measured from around 500 to 800°C in humidified ARCAL, a) and b), and in humidified H_2 at a low pressure of approximately 60 mbar, c) and d), are displayed. The ratio of H_2 to water was in both cases close to 1:1 and consequently similar results were expected. Due to easier comparability of the results the high frequency x-axis intercept was subtracted.

The spectrum recorded in ARCAL at 495°C shows two semicircle features, one at higher frequencies, that probably describes an interface or electrolyte process, because of the high peak frequency, and one at lower frequencies, that can be attributed to the electrode. With increasing temperature, the high frequency feature disappears, and an additional overlapping semicircle feature gets more and more visible, due to a minor shift of the peak frequency of the electrode feature to higher frequencies. Moreover, in the spectrum measured in humidified ARCAL at 742.5°C a jump along the x-axis, that was very likely caused by a change of contacting during the measurement can be seen. The size of the semicircle features ascribed to the electrode decreases with increasing temperature, as expected due to faster kinetics of the electrode material. They could be fitted relatively well with an equivalent circuit of an offset resistance and a parallel circuit of a resistance and a CPE for each semicircle feature. However, due to the overlapping nature of the features, only moderately accurate separation of the features is expected. The spectra in Figure 22 c) and d), measured in humidified H_2 at low pressure, look very similar in shape to the ones measured in ARCAL without the low frequency feature appearing at higher temperatures. Hence, they were easy to fit with an offset resistance and an R, CPE parallel circuit in series. Since the low frequency feature only appears in the spectra recorded in ARCAL, it can most likely be attributed to a gas diffusion process. The peak frequencies are slightly lower than the ones measured in ARCAL, but in the same order of magnitude and the resistance decreases with increasing temperature.

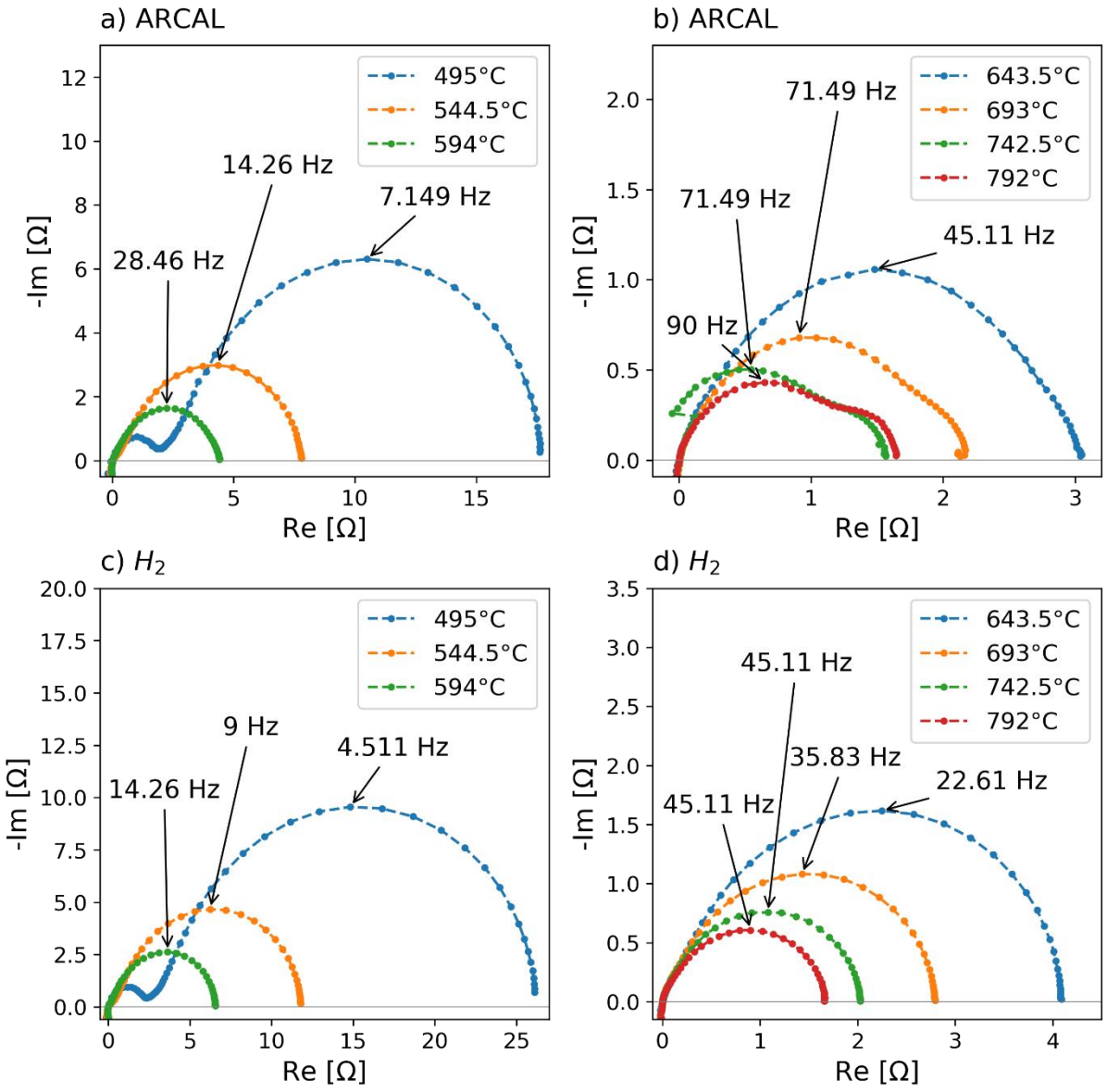

Figure 22: Nyquist plots with subtracted high frequency intercept of a sample with PtGDC electrodes measured at different temperatures in either humidified ARCAL (a), (b) or in humidified hydrogen at 60 mbar (c), (d) with a hydrogen to water ratio of 1:1.

Figure 23 a) shows the ASR of the PtGDC sample measured in humidified ARCAL and H_2 plotted over 1000/T and b) the capacitance, which was obtained from the fits according to equation (9) and normalized to the electrode area, over the temperature.

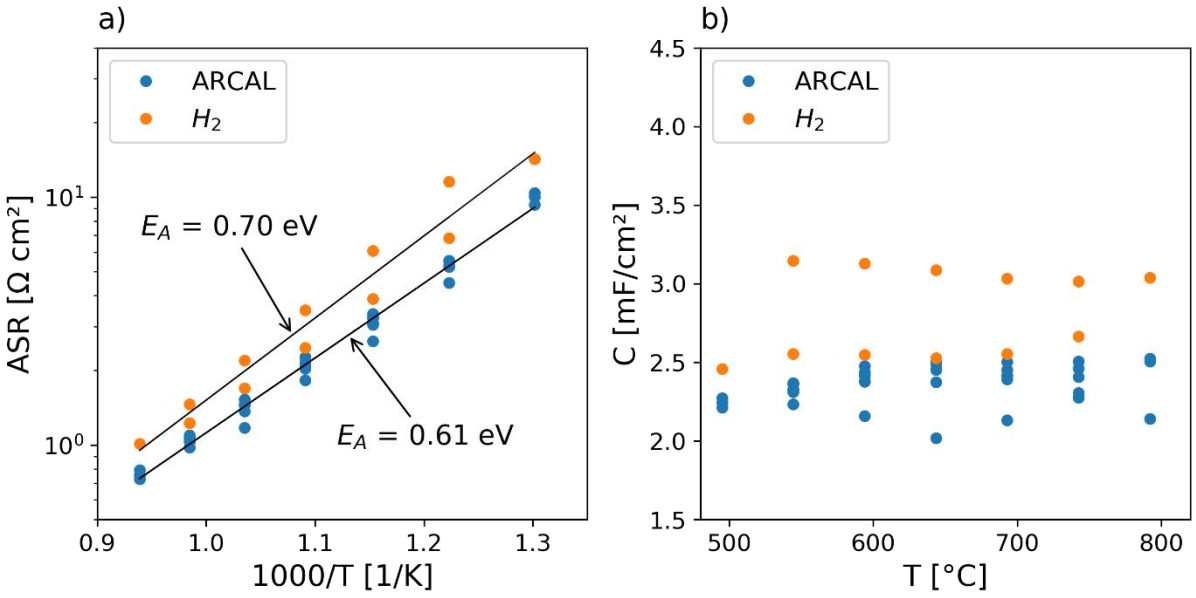

Figure 23: ASR of the sample with PtGDC electrodes plotted over 1000/T (a) and C of this sample plotted over T (b), measured in either humidified ARCAL or hydrogen atmosphere.

The activation energy of the electrode process is similar for the measurements in ARCAL and H_2 and the ASR does not change significantly between the two measuring atmospheres either. However, the ASR from the measurements in H_2 is slightly higher than for the ones in ARCAL, most likely because of a degradation of the sample. In comparison to the GDC|Pt the electrode performance is by far worse, with an ASR more than a factor 10 higher. That can be partially explained by the missing Pt current collector hindering current distribution. Moreover, the activation energy differs from that of GDC|Pt, and hence could be indicating a different limiting process. The capacitance obtained from fitting the main semicircle feature attributed to the electrode process does not change a lot with the temperature and atmosphere and no clear trend can be observed.

4.1.3. Temperature cycles of PtGDC|Pt

The Nyquist plots from the PtGDC|Pt sample sintered at 1050°C in either humidified ARCAL or humidified H_2 are shown in Figure 24 a) and b), and the ones for the sample sintered at 1150°C in Figure 24 c) and d). The spectra were subtracted to yield the same intercept on the x-axis. The ratio of hydrogen to water was for both atmospheres approximately 1:1, because the measurements in pure hydrogen were performed at a low pressure of around 60 mbar. Although more than one temperature cycle was measured, only the first one is shown in each plot. Due to the comparably big size of the spectra recorded at around 500°C and the fact that they look similar to the ones at the following temperature steps with an additional feature at high frequency, as could be also noticed for the spectra of the PtGDC sample at 500°C (Figure 22 a), they are not explicitly displayed. The spectra of the PtGDC|Pt sample

sintered at 1050 °C and measured in humidified ARCAL atmosphere consist of a dominant semicircle feature that can be attributed to the electrode and a shoulder at low frequencies. The resistance of the electrode feature decreases with increasing temperatures, the size of the low frequency shoulder, however, stays the same, which leads to it being more noticeable at high temperatures. The peak frequency of the electrode feature increases with increasing temperature.

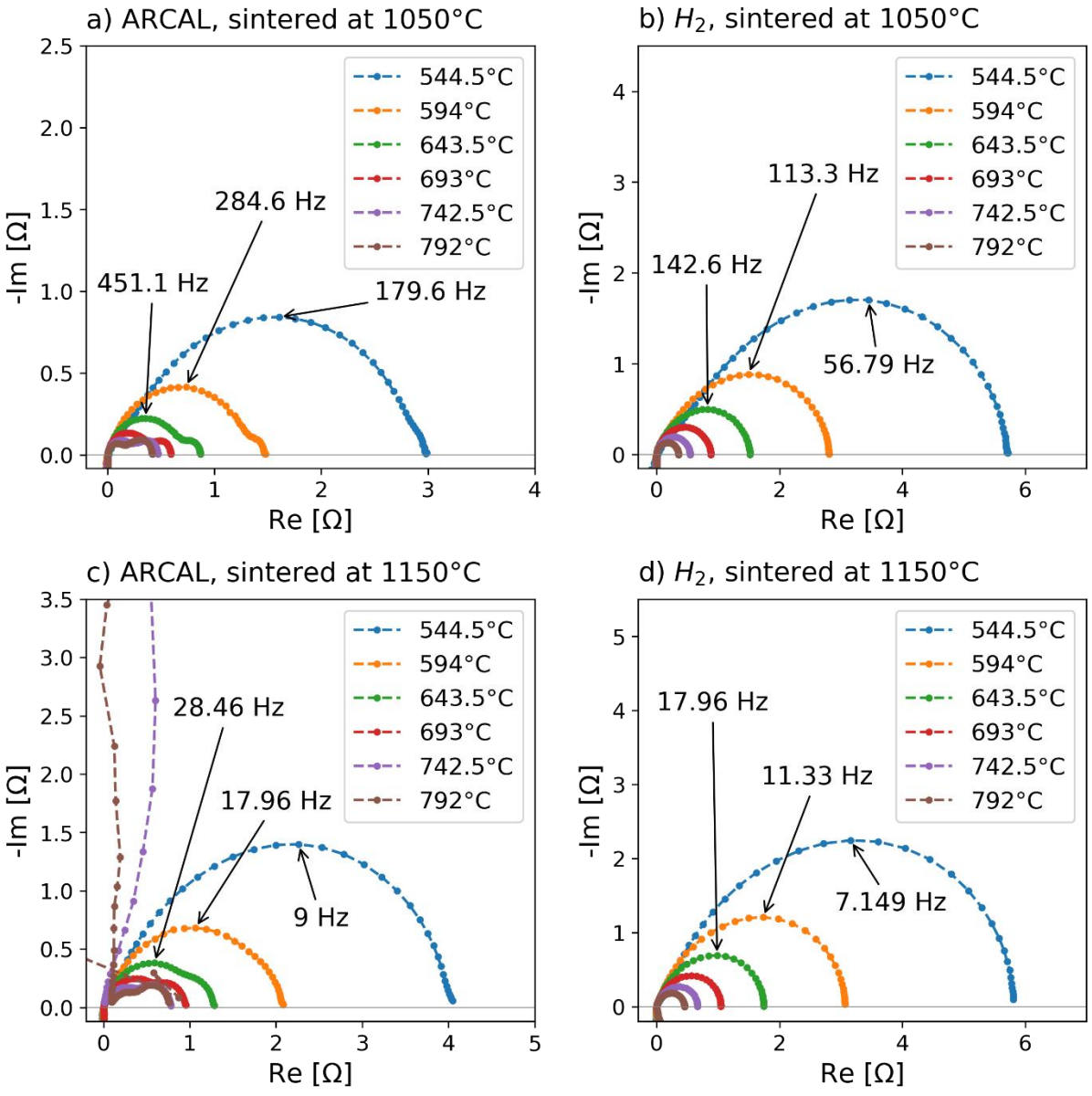

Figure 24: Nyquist plots with subtracted x-intercept of the PtGDC|Pt samples measured at different temperatures in either humidified ARCAL or in humidified hydrogen at low pressure with a hydrogen to water ratio of 1:1.

In contrast to these spectra the ones of the same sample recorded in humidified H_2 atmosphere (Figure 24 b) do not show the low frequency shoulder, leading to the same conclusion as for the GDC|Pt and PtGDC samples that the low frequency feature in ARCAL is attributable to a gas diffusion process. The measurements made on the PtGDC|Pt sample

sintered at 1150°C yielded spectra that look very similar to the ones of the sample sintered at 1050°C. The low frequency shoulder in ARCAL atmosphere seems to be a bit bigger, but the overall size of the semicircles is comparable. In H_2 atmosphere no major difference concerning the shape or size can be noted. As expected, the size of the electrode features decreases with increasing temperature in both atmospheres. The only essential difference, compared to the sample sintered at 1050°C, is the lower peak frequency of the electrode feature, with the peak frequency also slightly increasing with rising temperature.

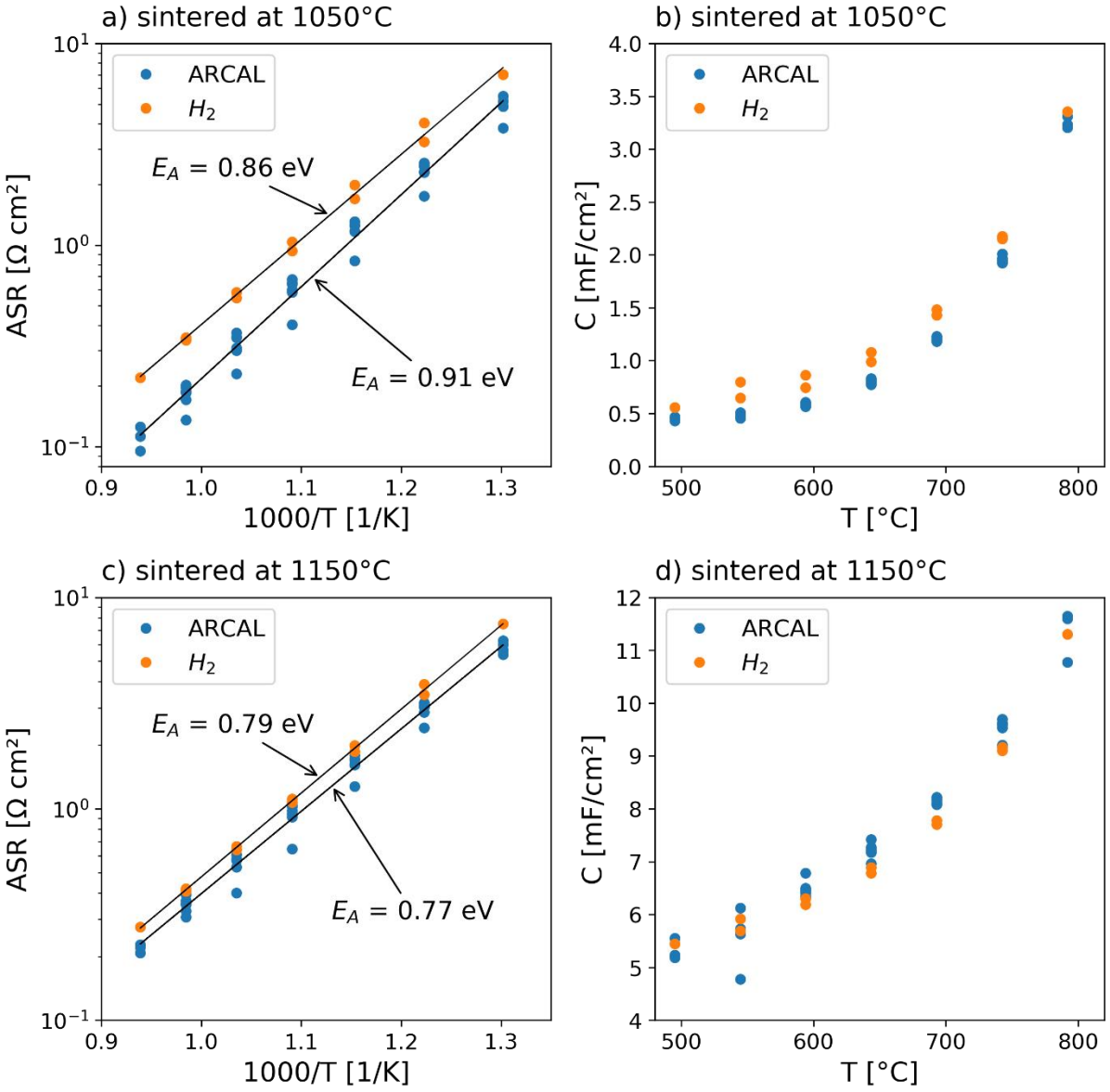

Figure 25: ASR over 1000/T and capacitance over T for the PtGDC|Pt sample sintered at 1050°C (a, b) and for the sample sintered at 1150°C (c, d).

In Figure 25 a) and b) the ASR of one electrode over 1000/T and the capacitance over T of the PtGDC|Pt sample sintered at 1050°C are plotted. Figure 25 c) and d) show the ASR over 1000/T and the capacitance over T for the sample sintered at 1150°C. The ASR and

capacitance were obtained by fitting the electrode feature with an R, CPE parallel circuit and normalizing to the respective electrode area. That yielded very good results with low error for the spectra measured in H_2. However, for the spectra recorded in ARCAL the results are not that precise, due to the overlapping and especially for higher temperatures hard to separate low frequency shoulder attributed to gas diffusion. The results show that there is no significant difference in ASR of the samples sintered at different temperatures and in either humidified ARCAL or H_2 atmosphere with the same hydrogen to water ratio. The measurements in H_2 show a tendentially higher ASR, which is most probably caused by a slight degradation of the samples during the measuring time. That degradation can also be observed without a change in atmosphere, for example in Figure 25 a) and c) for the measurements in ARCAL, where the measuring points at lower ASR depict the first temperature cycle and the points at higher ASR the later temperature cycles for each temperature respectively.

The activation energy does not differ substantially between the measurements of the different samples and in different atmospheres and was obtained from the slope of a linear fit through the data points with natural logarithmic y-axis. The capacitance of each sample does not change significantly by changing the atmosphere from ARCAL to H_2 and there is a general trend of exponential nature for higher capacitance values at higher temperatures. The capacitance of the PtGDC|Pt sample sintered at 1150°C is higher than the one for the sample sintered at 1050°C, which is reflected in the lower peak frequency with similar ASR of the sample sintered at 1150°C. In conclusion, the reduced sintering temperature of 1050°C did not provide any major advantages and the delamination behavior did not change either. The major difference was a lower capacitance. As the measured capacitance scales with the amount of electrochemically active GDC in the electrode, it is likely that the higher sintering temperature increases the thickness of the electrochemically active layer due to better effective ion conductivity. Therefore, all samples prepared for the following measurements were sintered with the previously used standard sintering temperature of 1150°C.

Out of the three electrode materials, GDC|Pt shows the best performance with an extraordinarily low ASR of around 0.015 Ωcm^2 at 800°C. However, the exact values could not be obtained from the first measurements of this electrode material due to a very high noise to signal ratio, especially for high temperatures. Hence, it was also not possible to analyze the capacitance of GDC|Pt. PtGDC|Pt displays the second-best performance, though already a significantly higher ASR than GDC|Pt, and PtGDC the worst performance. That can be explained by the lack of a current collector for PtGDC. The comparatively low performance of the Pt-GDC cermet electrodes also proofs that the GDC phase and not the Pt current collector is responsible for the high activity of the GDC|Pt electrodes. The delamination of the

current collector on the other hand was the worst for the GDC|Pt sample and can be explained by a different thermal expansion behavior of GDC and Pt. Consequently, the focus of the following measurements was majorly on the electrochemical behavior of GDC|Pt electrodes.

4.2. Temperature and p(O_2) dependence of GDC|Pt and PtGDC|Pt

The next measurements were performed on samples with recycled polycrystalline YSZ electrolytes (11 mm x 11 mm x 0.15 mm), where the old electrodes had been grinded off, in the four-sample setup. For two of the samples PtGDC electrodes and a Pt current collector, and for the other two samples a GDC electrode and a Pt current collector were brushed on each side and they were sintered for 3 h at 1150°C. The impedance spectra were recorded in a frequency range from 0.1 to 900000 Hz in four-point mode and this time with an amplitude of 100 mV instead of 20 mV, to reduce the noise for the measurements of the GDC|Pt electrodes with very low ASR. Temperature cycles from 500°C to 800°C with 50°C steps were conducted in humidified ARCAL and in humidified H_2 at a total pressure of around 60 mbar to yield for both atmospheres a hydrogen to water ratio of approximately 1:1. The flow was set to 100 sccm via a needle valve. Moreover, measurements at a fixed temperature of 600°C were carried out to investigate the impact of the oxygen partial pressure on the electrode behavior. These measurements were performed in humidified pure hydrogen and humidified ARCAL, depending on the atmosphere that should be set. The oxygen partial pressure was indirectly changed by varying the total pressure in the test rod and therefore also the hydrogen to water ratio. Consequently, the oxygen partial pressure changed due to the equilibrium of hydrogen, water, and oxygen.

4.2.1. Temperature and p(O_2) dependence of PtGDC|Pt

The ASR of the two samples measured in humidified H_2 and of the previously measured sample in humidified ARCAL and humidified H_2 plotted over 1000/T is displayed in Figure 26. Moreover, the activation energies are shown. The corresponding impedance spectra are not explicitly depicted due to the major similarities with the spectra in Figure 24. The ASR values, peak frequencies and activation energies of the two samples and also the PtGDC|Pt sample analyzed in 4.1.3 are very consistent, which shows that the preparation and measurement of the manufactured PtGDC|Pt electrodes is reproduceable.

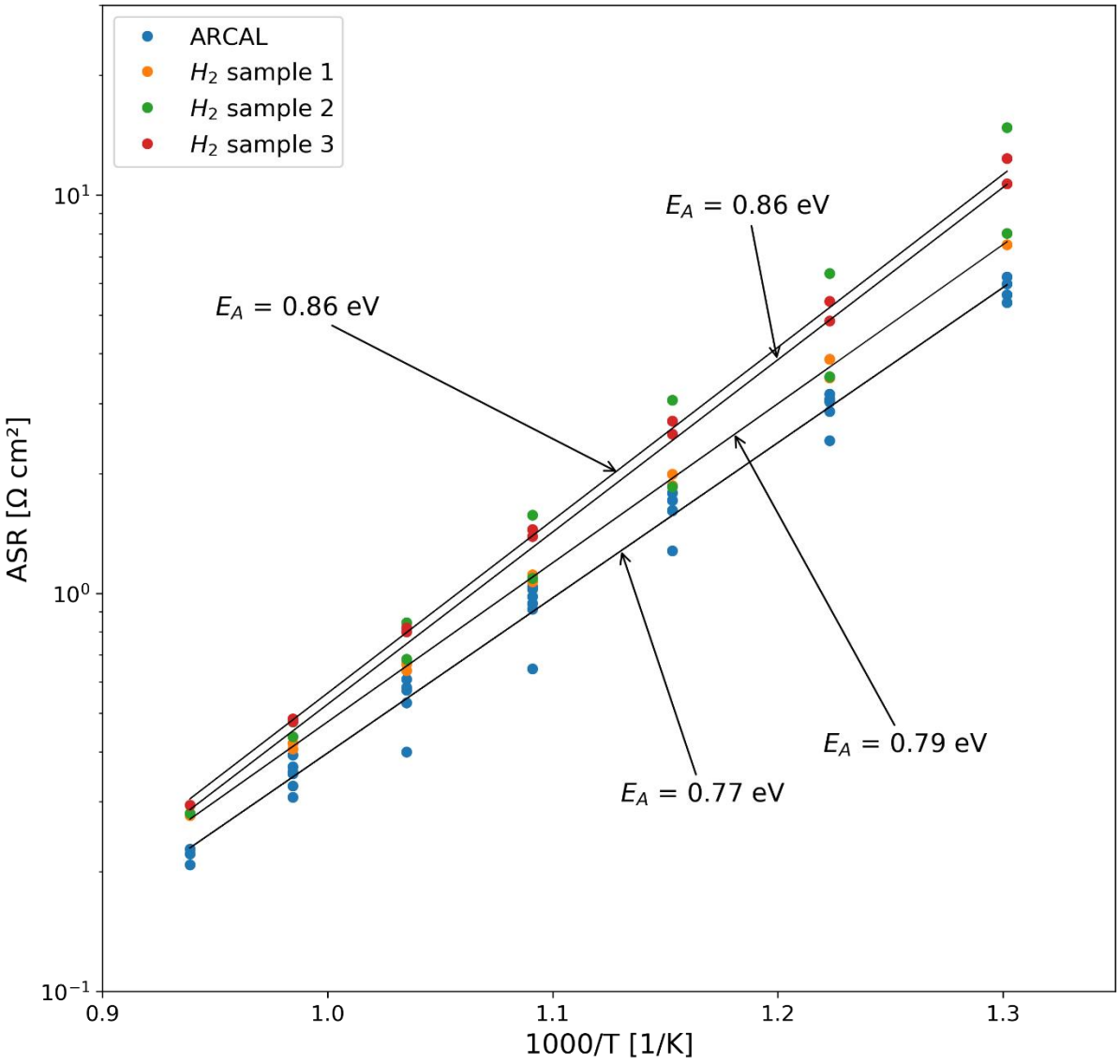

Figure 26: ASR of the three PtGDC|Pt samples measured at different temperatures in humidified ARCAL and humidified hydrogen at 60 mbar plotted over 1000/T.

Figure 27 a) and b) show the impedance spectra of the two PtGDC|Pt samples measured at 594°C and different hydrogen partial pressures.

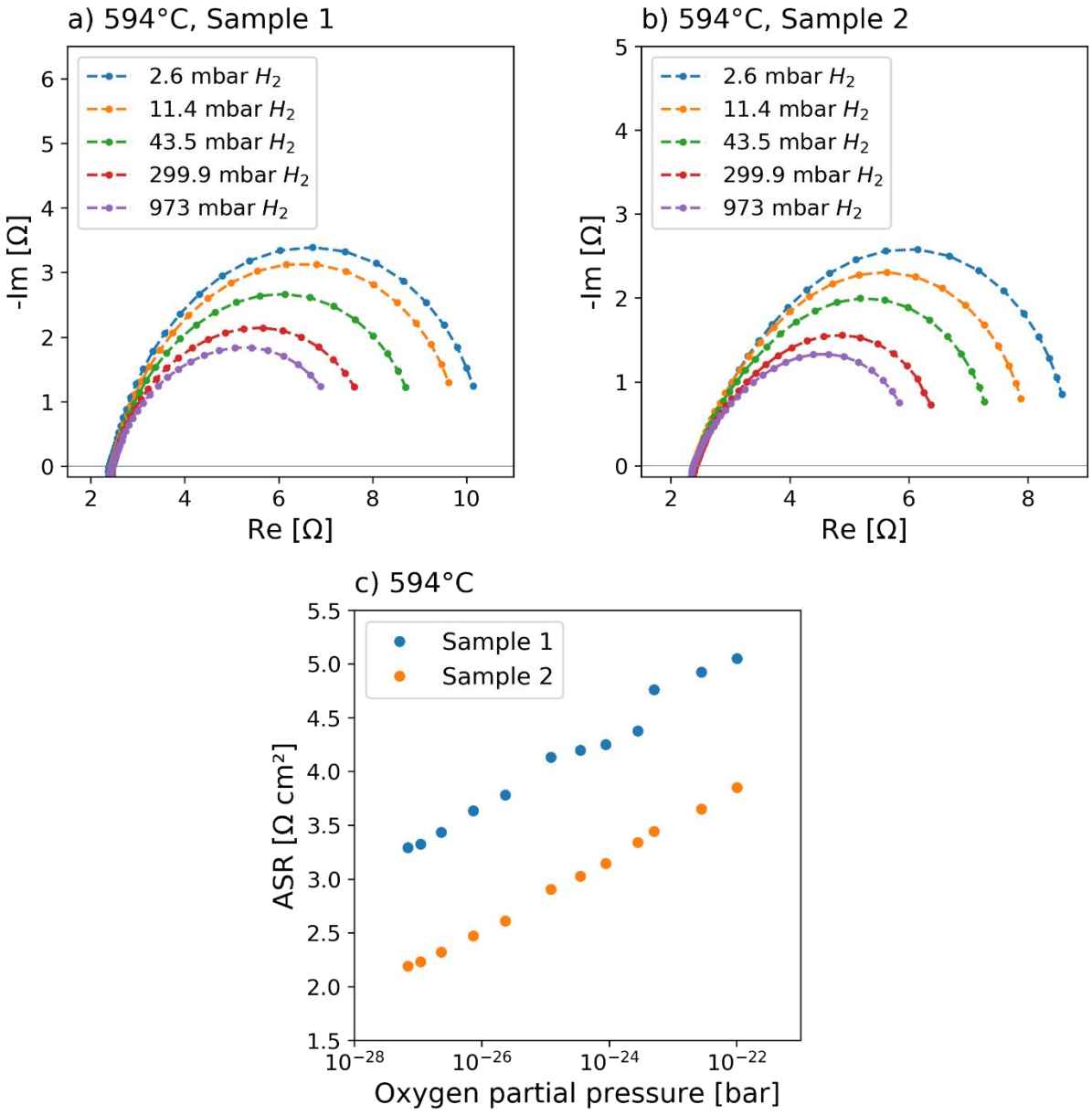

Figure 27: Nyquist plots of the two PtGDC|Pt samples measured at 594°C at different hydrogen partial pressure (a, b) and ASR of the 2 samples plotted over the oxygen partial pressure (c).

Because of the humidifier the partial water pressure in the measuring atmosphere was fixed at around 28 mbar, depending on ambient temperature, and the hydrogen partial pressure in the test rod was adjusted manually via a needle valve. Because changing the atmospheres required permanent presence at the measuring setup, the bottom limit of the frequency range was adjusted to 0.5 Hz to speed up the measurements. The spectra show one semicircle feature describing the electrode process. The plots for both samples display resistances in the same order of magnitude with the resistance decreasing with increasing hydrogen partial pressure. That can be explained by either the fact that at more reducing conditions more hydrogen molecules that can potentially react are present and consequently the chance for the electrode reaction to happen is increased, or because the reactions happen at point

defects, which are more frequent in reducing conditions due to the increased number of oxygen vacancies and Ce^{3+}-ions. Furthermore, it can be noticed that the intercept on the x-axis does not change by varying the hydrogen and consequently the oxygen partial pressure. This intercept depicts the electrolyte resistance, which does not vary notably with the oxygen partial pressure, in contrast to the porous electrodes, due to the defect concentration depending majorly on the amount of dopant and thus being by approximation constant. In Figure 27 c) the ASR of the PtGDC|Pt samples is plotted over the oxygen partial pressure. The oxygen partial pressure was calculated by utilizing the known hydrogen and water partial pressures in the following equation.

$$p(O_2) = \frac{K * p(H_2O)^2}{p(H_2)^2} \qquad (25)$$

K depicts the equilibrium constant of the reaction $2H_2O \rightleftharpoons 2H_2 + O_2$, obtained from NIST data.[85–87] It can be further noticed that the ASR increases in a logarithmic manner, going to less reducing conditions, and that the trend is very similar for both samples with only a slight difference in the offset on the y-axis.

4.2.2. Temperature and p(O_2) dependence of GDC|Pt

In Figure 28 a) and b) the impedance spectra of the two symmetric samples with GDC|Pt electrodes measured at different temperatures in either humidified ARCAL or hydrogen atmosphere with a hydrogen to water ratio of about 1:1 are depicted. The spectra of both samples recorded in ARCAL at roughly 600°C consist of a bigger low frequency semicircle and a smaller high frequency feature. At higher temperatures only the low frequency semicircle remains. Moreover, the size of the low frequency feature does not change significantly with the temperature and has a rather low peak frequency, indicating a gas diffusion process, which is reasonable due to the ARCAL atmosphere. Therefore, the electrode feature was identified as the small feature at higher frequencies, only visible at the lower measured temperatures due to its size and overlap with the gas diffusion feature. The shape and size of the features is very similar to the previously recorded spectra of another GDC|Pt sample measured at the same conditions (Figure 20 b), only with lower AC amplitude, which shows good reproducibility of the measurements in ARCAL atmosphere. The spectra recorded in H_2 at a pressure of around 60 mbar consist majorly of one semicircle feature that is substantially smaller than the gas diffusion feature in ARCAL and has a higher peak frequency, with the spectra at some temperatures indicating two overlapping features. Furthermore, it can be noticed that the size of this feature, attributed to the polarization of the electrode, decreases with increasing temperature. The higher AC amplitude compared to previous measurements of the same electrode material in the same conditions seemed to solve the issue of high noise due to the low polarization resistance very well.

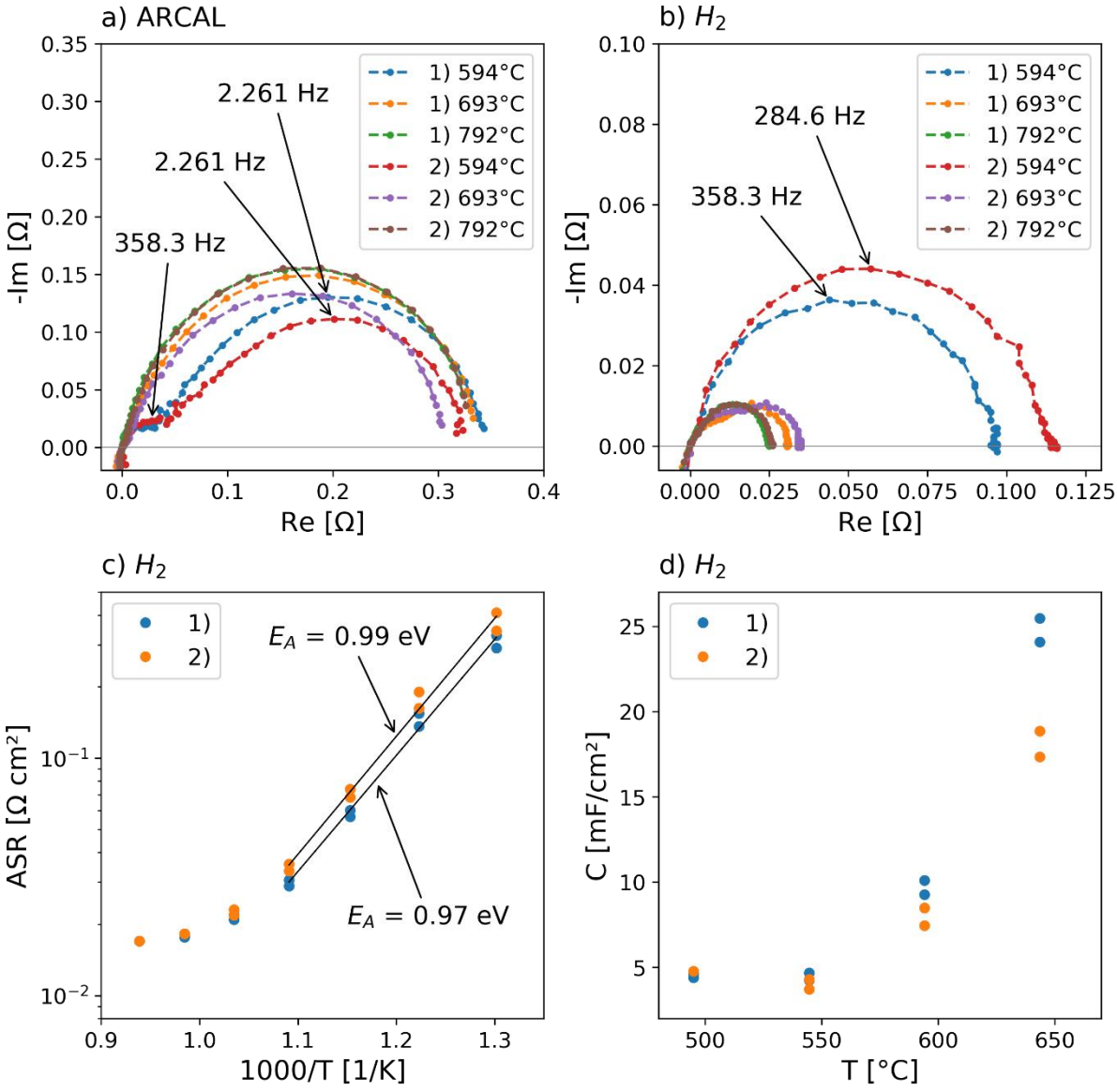

Figure 28: Nyquist plots with subtracted x-axis intercept of two samples with GDC|Pt electrodes measured at different temperatures in humidified ARCAL (a) and humidified hydrogen at low pressure (b), ASR over 1000/T (c) and C over T (d) for those 2 samples measured in humidified hydrogen.

Figure 28 c) shows the ASR of the two GDC|Pt samples over 1000/T. Both samples exhibit extraordinarily low ASR values with approximately 0.07 Ωcm^2 at 600°C. The decrease of the ASR at higher temperatures is linear with a logarithmic y-axis at the lower measured temperatures and in this temperature range the activation energies were calculated from a linear fit of the data points with the natural logarithm of the ASR on the y-axis and 1000/T on the x-axis. At the higher temperatures, the curve flattens and another factor that limits the ASR occurs, which might be again a gas diffusion process. The chemical capacitance over the temperature, as seen in Figure 28 d), was obtained in the same way as the ASR via a fit of the impedance spectra with an R, CPE parallel circuit for every semicircle feature and an offset resistance in series. However, due to the overlapping second feature, that can be

mainly seen in the spectra measured at higher temperatures, a good fit was not possible for the whole temperature range. It can still be noticed though, that the capacitance increases with increasing temperatures. Moreover, the active film thickness was approximated by dividing the capacitance obtained through fitting by the specific chemical capacitance of dense GDC obtained from thermogravimetric measurements in literature[30] at different temperatures. According to that measurements at 600°C in 35+25 mbar H_2+H_2O, the theoretical chemical capacitance of a GDC electrode with 50% porosity phase is ~80 F/cm^3, and the measured porous electrodes have a chemical capacitance of 8 mF/cm^2. This calculation yields an electrochemically active thickness of only 1 µm. Given the uncertainties from the fitting process, the active film thickness is most likely between 1 and 2 µm. A scratch test and cross-sectional SEM imaging, performed as explained in 3.2, roughly approximating the film thickness as 13-15 µm. Consequently, thinner GDC electrodes should still get the same excellent values for the polarization resistance. A thinner GDC layer is expected to have large advantages in terms of electron conduction in across-plane direction.

The impedance spectra of the two samples with GDC|Pt electrodes recorded at 594°C in different hydrogen partial pressures are depicted in Figure 29 a) and b) and consist of either one or two semicircle features. In case of two features, the one at lower frequencies with the peak frequency of around 5.7 Hz can be attributed to gas diffusion. However, this gas diffusion feature differs in size at the different measured hydrogen partial pressures because the adjustment of these partial pressures also leads to a change in total pressure. The spectra of the two different samples measured at equal conditions look very similar to each other, showing good reproducibility of the measurements in the same measuring setup. An important observation is that the high frequency intercept on the x-axis depends on the hydrogen partial pressure, which in turn changes the oxygen partial pressure. Figure 29 c) shows the ASR of the high frequency feature plotted over the oxygen partial pressure and a trend to lower polarization resistances at less oxygen partial pressure and hence more reducing conditions can be observed. Due to the difficult separation of the two semicircle features, the ASR values have a rather large error margin though, which makes further interpretation of the trend not expedient. The lower ASR in more reducing atmospheres can be ascribed to the increased reaction rate due to more hydrogen molecules and defects available, as explained in 4.2.1. In Figure 29 d) the offset resistance is plotted as a function of oxygen partial pressure. It can be seen that the offset resistance increases with increasing oxygen partial pressure. Such an observation is uncommon because the offset normally shows the electrolyte resistance. This resistance should not change visibly in different oxygen partial pressures because the oxygen vacancy concentration in the electrolyte can be approximated as constant. In the spectra of the PtGDC|Pt samples measured at different hydrogen partial pressure (Figure 27 a, b) no such difference in offset resistance could be

noticed. We can therefore conclude that the offset resistance of the GDC|Pt samples is larger than the electrolyte resistance, and is also in part caused by the electrode, eventually due to an interface effect or the electronic conductivity of GDC. An impact of the electronic conductivity on the offset resistance would explain the decreasing offset at lower oxygen partial pressures, however, well-founded assumptions cannot be made solely based on these measurements. The logarithmic fit (which is linear in the plots, due to the logarithmic x-axis) is displayed for easier comparison with results from optimized electrodes shown later in this work and just serves as a measure for how much ASR_{Offset} per electrode changes with $p(O_2)$.

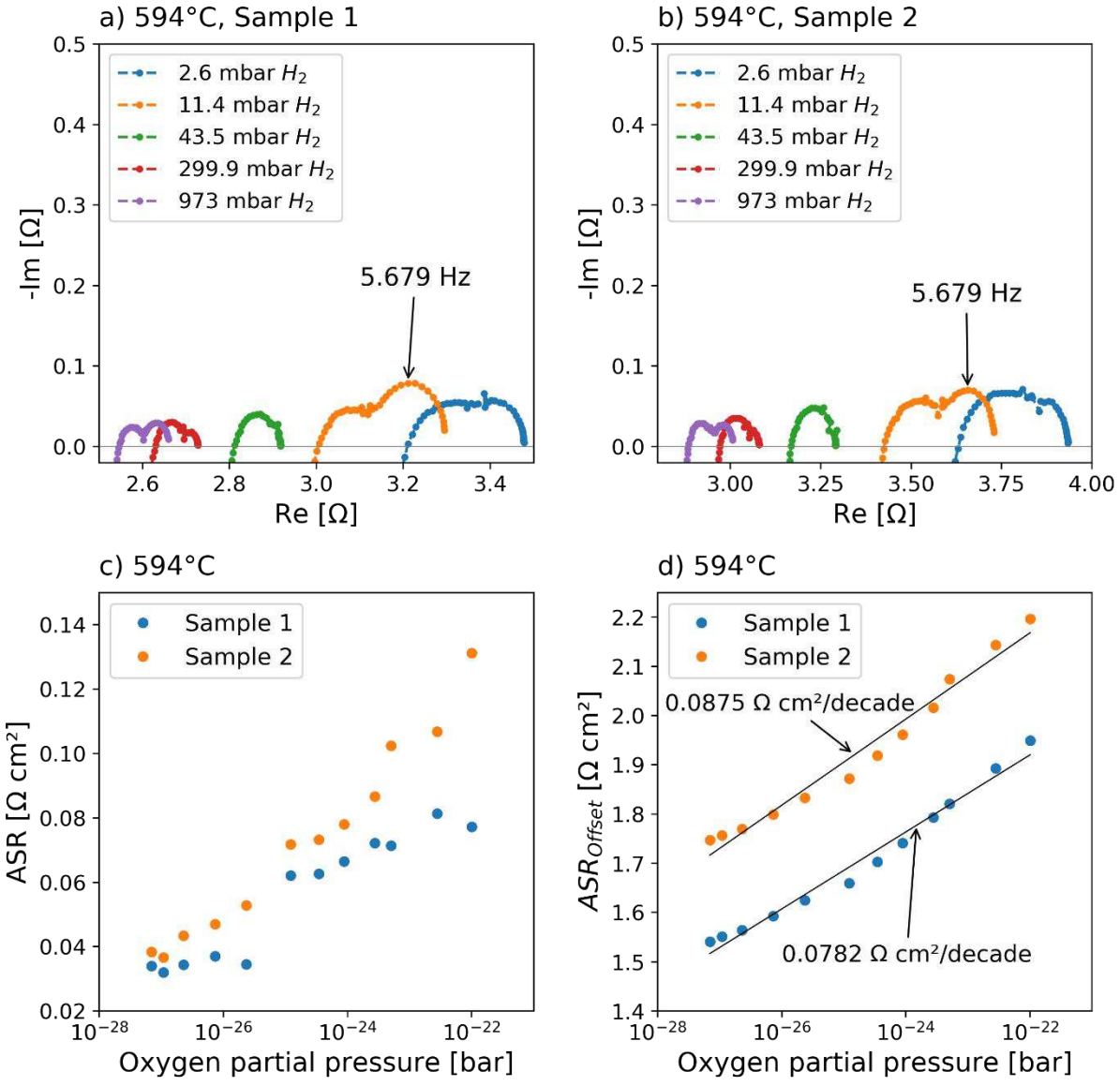

Figure 29: Impedance spectra recorded at 594°C at different hydrogen partial pressures for two samples with GDC|Pt electrodes (a, b), ASR of these samples over the oxygen partial pressure (c) and offset ASR over the oxygen partial pressure (d).

Figure 30 depicts the chemical capacitance, obtained through fitting of the semicircle feature attributed to the electrode polarization with an R, CPE parallel circuit, plotted over the oxygen

partial pressure of the two samples with GDC|Pt electrodes. As already mentioned for the ASR accessed by fitting, the capacitance values can only be approximated, due to difficult separation of the gas diffusion and electrode reaction features. As expected, the chemical capacitance shows a clear trend to higher capacitance at more reducing atmospheres, because more oxygen vacancies and Ce^{3+} ions form in more reducing conditions. Consequently, the chemical capacitance is expected to increase.[88]

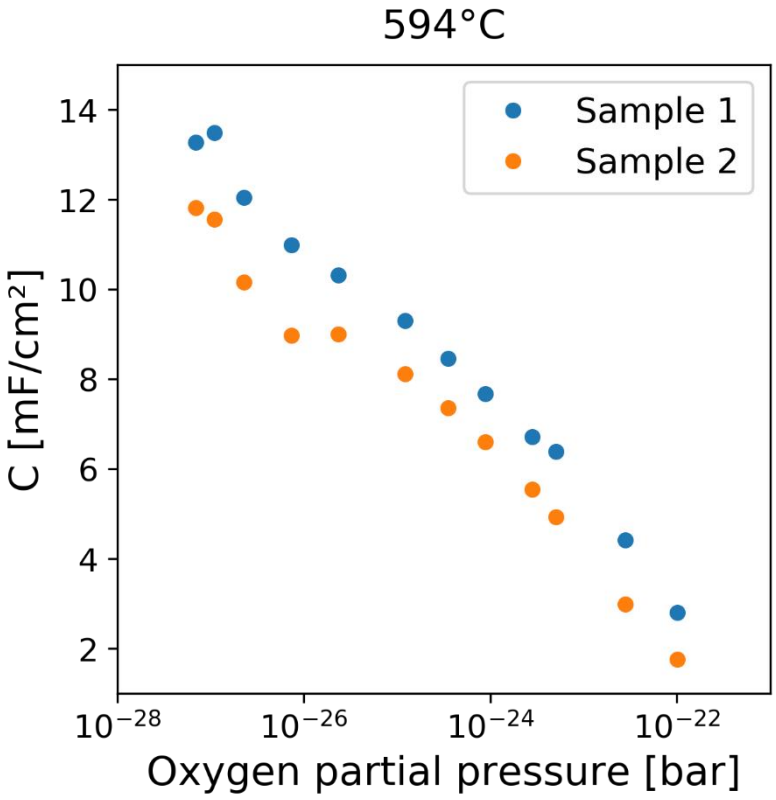

Figure 30: Chemical capacitance over oxygen partial pressure for the two GDC|Pt samples measured at 594°C.

4.3. EIS measurements of GDC|Pt electrodes in reducing and oxidizing atmospheres

In order to investigate the behavior of the GDC|Pt electrodes in oxidizing atmospheres, measurements in synthetic air (80% N_2 and 20% O_2) were carried out. The measurements were performed on a new sample consisting of a single crystalline YSZ electrolyte (5 mm x 5 mm x 0.5 mm) and electrodes made of a brushed GDC layer and a brushed Pt layer on both sides. The samples were sintered at 1150°C for 3 h. Because the four-sample setup did not allow measurements in oxidizing atmospheres due to possible oxidation of the Ni foams used for contacting, the measurements in oxidizing atmospheres were conducted in the wing setup. To avoid eventual errors because of a different behavior of the GDC|Pt electrodes in different measurement setups, the electrodes were measured in humidified ARCAL at ambient pressure and in humidified H_2 at around 60 mbar with the same H_2 to water ratio of

1:1 in the four-sample measuring setup previous to the measurements in humidified ARCAL and synthetic air in the wing setup. The impedance spectra were recorded in a frequency range from 0.1 to 900000 Hz with 10 data points per decade in the four-sample setup and 5 data points per decade in the wing setup. The AC amplitude was 100 mV for the measurements in ARCAL and H_2 atmosphere and 20 mV for the ones in synthetic air and the temperature was varied from 500°C to 800°C in 50°C steps. However, due to different furnaces being used in the two measuring setups their temperatures did not match at the same set temperature and hence it was read out using a thermocouple to get the actual temperature of the samples during the measurements. The flow was manually set to approximately 100 sccm in the four-sample setup via a needle valve and controlled via a mass-flow controller in the wing setup and set to 125 sccm for synthetic air and 140 sccm for humidified ARCAL.

Figure 31 depicts the impedance spectra, with subtracted x-intercept for easier comparison, of the measurements in ARCAL, H_2 and synthetic air atmosphere in the four-sample and the wing setup. The spectra in a) were measured in the four-sample setup and consist of a bigger low frequency semicircle feature, which can be attributed to the gas diffusion in ARCAL due to the low peak frequency and the fact that it does not notably change with the temperature, and a feature at higher frequencies, ascribed to the electrode reaction. The high frequency feature is best visible for the spectrum recorded at 594°C and becomes harder to separate from the gas diffusion feature at higher temperatures because of the overlap and decrease in size. Figure 31 b) shows the spectra recorded in the same measuring setup as a) but in humidified H_2 at low pressure. They consist majorly of one feature attributed to the electrode process, as the peak frequency indicates, which decreases in size with increasing temperature. At temperatures above 690°C, a second strongly overlapping impedance feature appears. This is likely attributed to a gas diffusion process even at low pressures, due to the extremely low polarization resistance of the GDC|Pt electrodes. In Figure 31 c) the impedance spectra measured in ARCAL atmosphere in the wing setup are displayed. They consist of a low frequency gas diffusion feature and higher frequency feature that decreases in size with increasing temperature for the electrode process. The spectrum measured at 592.5°C shows a third semicircle feature at even higher frequencies, however, the origin of that feature was not further investigated. Overall, they look very similar to the spectra recorded at the same conditions in the four-sample setup, indicating good reproducibility between the two measuring setups. Figure 31 d) depicts the impedance spectra of the measurements in the wing setup in synthetic air. They consist of one semicircle feature decreasing in size with increasing temperature and a slightly lower peak frequency than the electrode features of the measurements in reducing ARCAL or H_2 atmospheres.

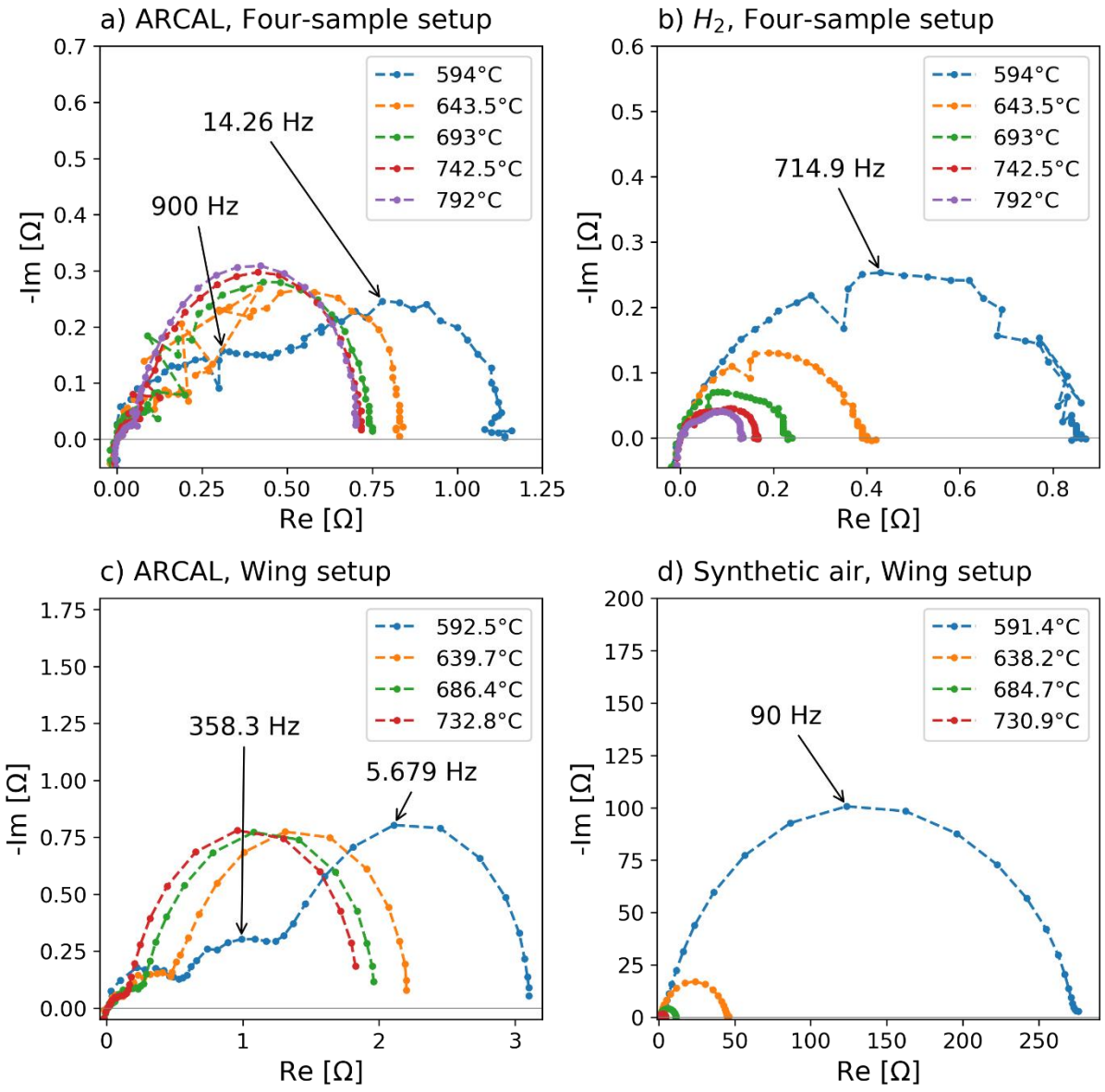

Figure 31: Normalized impedance spectra of a symmetric sample with GDC|Pt electrodes on a 5x5x0.5 mm sized electrolyte measured in humidified ARCAL and hydrogen in the four-sample setup (a, b) and in humidified ARCAL and synthetic air in the wing setup (c, d).

The ASR plotted over 1000/T and the capacitance over the temperature of the sample with GDC|Pt electrodes measured in reducing ARCAL or H_2 atmosphere and in either the four-sample or the wing setup are shown in Figure 32 a) and b). The ASR and capacitance of the electrode features were obtained by fitting the spectra with an equivalent circuit consisting of an offset resistance and one or two R, CPE parallel circuits for each semicircle feature in series. In case of two semicircles, the high frequency feature was attributed to the electrochemical electrode reaction. The ASR of the measurements in the wing setup in ARCAL atmosphere decreases with increasing temperature in an Arrhenius-type behavior. For the measurements of that GDC|Pt sample in the four-sample setup, however, such an Arrhenius-type behavior was only visible at the lower temperatures and the activation energy

was consequently only calculated for a fit in that area. At higher temperatures, the curve flattens, probably due to a limiting effect like gas diffusion and the difficult separation of gas diffusion and electrode process. The total values of the ASR seem to be about a factor 2 higher with 0.13 Ωcm^2 instead of 0.07 Ωcm^2 at approximately 600°C in the wing setup than in the four-sample setup, but part of that increase could be due to a slight degradation of the sample, as already described for previous measurements and also notable in this plots.

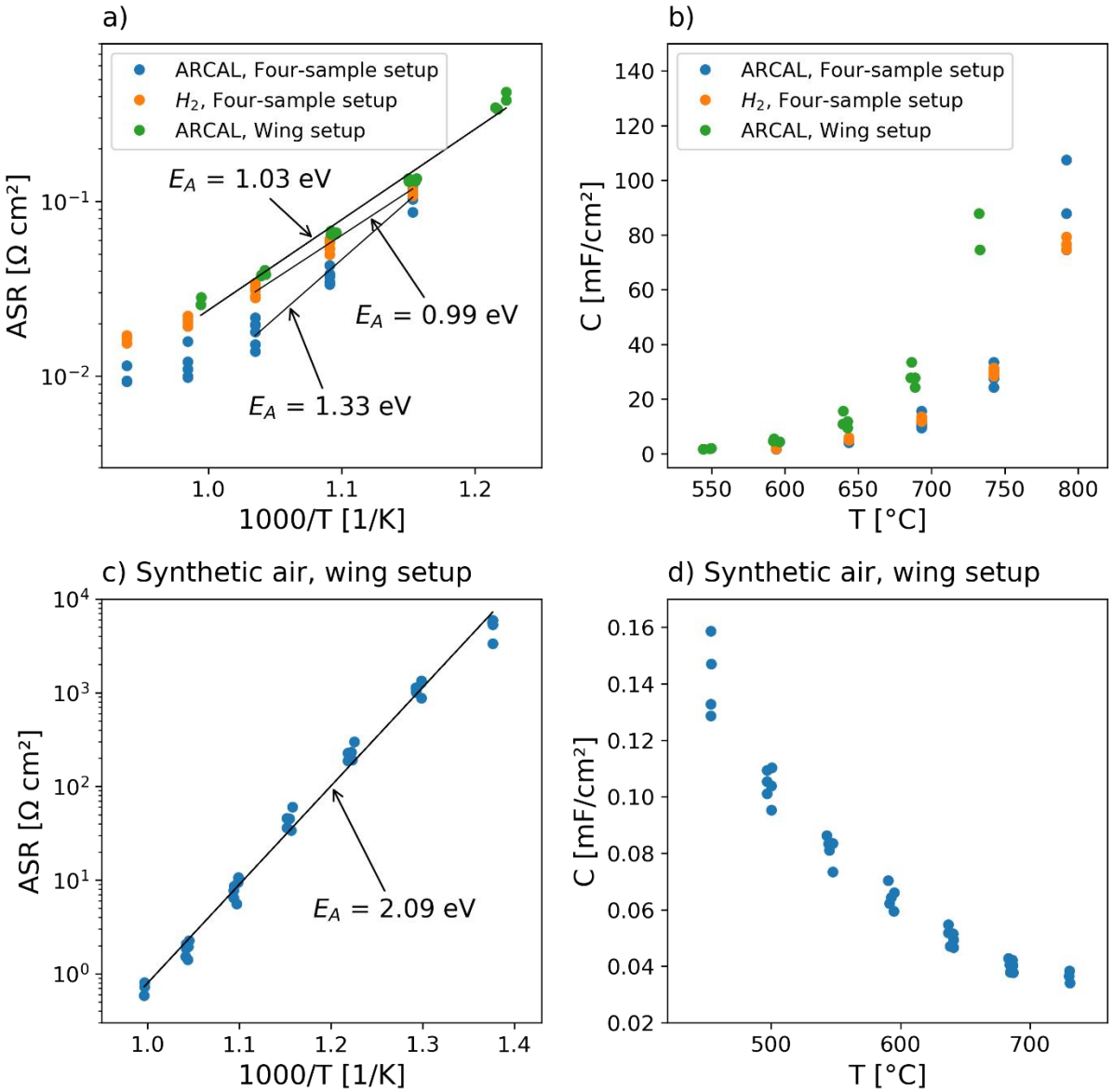

Figure 32: ASR over 1000/T of the sample with GDC|Pt electrodes in reducing atmospheres (a), capacitance over T in reducing atmospheres (b), ASR over 1000/T in oxidizing atmosphere (c) and capacitance over T in oxidizing atmosphere (d).

The activation energy of the measurements in the wing setup is equal to the ones obtained in the four-sample setup, with only the values from the measurement in the four-sample setup in ARCAL showing an abnormally high activation energy compared to the previous results

from measurements of the GDC|Pt electrodes. However, that difference can likely result from the fitting procedure, which only used three temperature values in the Arrhenius plot, and the difficult separation of the electrode feature in ARCAL due to the big gas diffusion feature. The chemical capacitance increases with the temperature and the absolute values fit rather well if the measurements at the same hydrogen to water ratio of 1:1 in different atmospheres and measuring setups are compared, with slightly higher values in the wing setup. The ASR values of the GDC|Pt electrodes in synthetic air are significantly higher than in reducing ARCAL or H_2 atmosphere, as displayed in Figure 32 c), with an ASR of 34 Ωcm^2 at around 600°C. Furthermore, the activation energy of the electrode process is way higher with 2.09 eV. Figure 32 d) shows the capacitance obtained from the measurements in synthetic air and the capacitance values are substantially smaller compared to reducing atmospheres, which can be explained by the defect chemistry of GDC, which has almost no intrinsic oxygen vacancies in oxidizing conditions. Also, there is a notable trend to a lower capacitance at higher temperatures, which is the opposite trend compared to the measurements in reducing atmospheres.

Additionally, it was possible to estimate the ionic conductivity of the GDC|Pt electrodes by analyzing the different intercepts on the x-axis of measurements in reducing and oxidizing atmospheres.

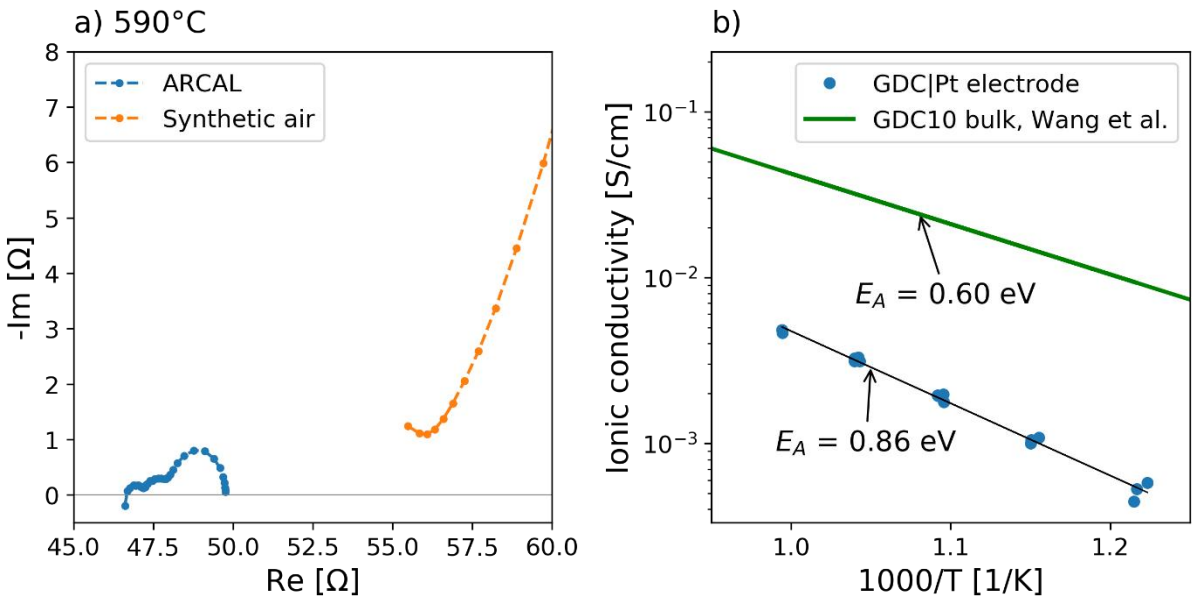

Figure 33: Offset resistance of the EIS measurements in ARCAL and synthetic air at 590°C (a) and ionic conductivity over 1000/T (b) of the GDC|Pt electrodes.

Figure 33 a) shows the offset resistance of the impedance spectra recorded in the wing setup at 590°C in either humidified ARCAL with a hydrogen to water ratio of 1:1 or synthetic air. The ionic resistance could be calculated from the difference of the high frequency

intercept on the x-axis due to the relation described by the following equation and certain approximations.

$$R_{HF} = R_{YSZ} + \frac{d_{GDC}}{\sigma_{total}} = R_{YSZ} + \frac{d_{GDC}}{\sigma_{ion} + \sigma_{eon} * p(O_2)^{-0.25}} \quad (26)$$

R_{HF} is the high frequency intercept on the x-axis, R_{YSZ} the electrolyte resistance, d_{GDC} the thickness of the GDC layer (15 µm), σ_{ion} the effective ionic conductivity of the GDC layer and σ_{eon} the effective electronic conductivity of the GDC layer in reducing atmospheres. The high frequency intercept of the spectra recorded in synthetic air does not include the electronic conductivity because GDC is only a MIEC in reducing conditions and the electronic conductivity in ARCAL is high enough for the offset resistance to be approximated as only the electrolyte resistance. Therefore, the ion conductivity of the GDC electrodes can be estimated by the following equation:

$$\sigma_{ion} = \frac{d_{GDC}}{R_{HF,ox} - R_{HF,red}} \quad (27)$$

In Figure 33 b) the ionic conductivity plotted over 1000/T can be observed and it is noticeable, that it increases with increasing temperature. The ionic conductivity is in a similar size range than that observed for Ni/GDC electrodes[30] but significantly smaller than the ionic conductivity of a dense GDC polycrystal[89] and exhibits a slightly higher activation energy.

4.4. Three-layer GDC|PtGDC|Pt electrodes

Although the polarization resistance of the GDC|Pt anodes is excellent in reducing conditions, they exhibit some weaknesses, such as weak adhesion of the Pt current collector, moderate kinetics, and a strong p(O2) dependence of the ohmic resistance. To further optimize these properties, electrodes consisting of three layers, GDC|PtGDC|Pt, were manufactured as shown in Figure 34 on recycled polycrystalline YSZ electrolytes (11 mm x 11 mm x 0.15 mm). The first layer after the electrolyte was a GDC layer applied by spincoating. The aim of that was to reduce the thickness of the GDC layer and thus reduce the part of the offset resistance, which is most likely not only caused by the electrolyte resistance but also by the electronic conductivity of GDC and therefore changes with the oxygen partial pressure. The thickness could be successfully reduced by spincoating to roughly 3 µm, compared to roughly 15 µm for the brushed GDC layers. These values were obtained by a scratch test as explained in 3.2 and SEM imaging (Figure 43 and Figure 44), and are still above the estimations of the electrochemically active film thickness, which means that the performance should not decrease due to the reduced thickness of the GDC layer. The second layer of these electrodes was a brushed PtGDC layer and the third one a brushed Pt layer. The main reason of the PtGDC in between the GDC and Pt layers was to

improve the interface and hence avoid strong delamination, that occurred often on the previous samples with a Pt layer brushed directly on the GDC layer and to improve the kinetics in oxidizing atmosphere, where the GDC-Pt-atmosphere TPB is decisive. The electrodes were sintered in one step at 1150°C for 3 h.

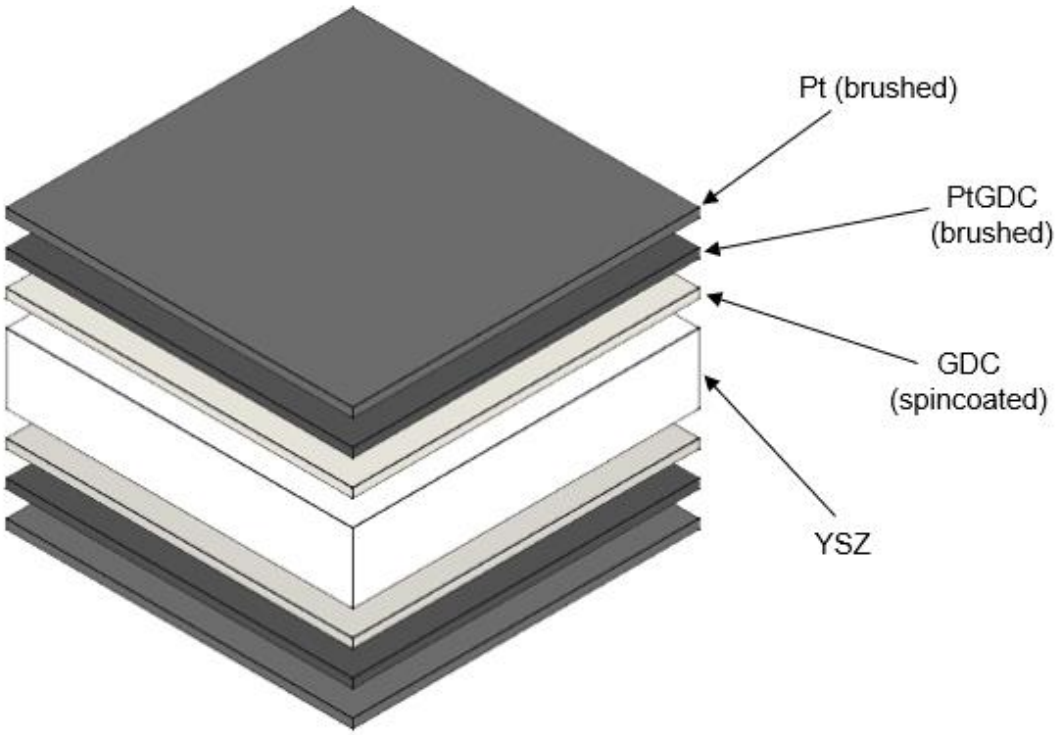

Figure 34: Structure of the three-layer electrodes.

The EIS measurements of these two three-layer electrode samples were performed in four-point mode in reducing conditions, oxidizing conditions and at different reducing oxygen partial pressures. The measurements in humidified H_2 at 60 mbar with a hydrogen to water ratio of 1:1 were carried out in the four-sample setup with an AC amplitude of 100 mV in a frequency range from 0.1 to 900000 Hz with 10 data points per decade. The temperature was varied from 500 to 800°C in 50°C steps and the flow rate set to approximately 100 sccm via a needle valve. For the measurements at different oxygen partial pressures, which were also conducted in the four-sample setup, the same settings were used, but instead of the temperature the hydrogen partial pressure was varied, the set temperature was kept constant at 600°C and it was only measured down to 0.5 Hz instead of 0.1 Hz. The impedance spectra of the three-layer electrodes in an oxidizing atmosphere were recorded in the wing setup in synthetic air at set temperatures from 500 to 800°C in 50°C steps. The AC amplitude was set to 20 mV and the frequency range from 0.1 to 900000 Hz with 5 points per decade.

4.4.1. Temperature cycles in reducing atmosphere

The impedance spectra, with subtracted high frequency intercept on the x-axis, of the two symmetric samples with three-layer electrodes measured in an reducing atmosphere are shown in Figure 35 a) and b). They consist of one semicircle feature that decreases in size with increasing temperature and is attributable to the electrode process. Because sample 2 broke into three parts during manufacturing of the electrode and only the biggest of the three parts was measured, the area of the sample is smaller than that of sample 1, which explains the bigger semicircle sizes of sample 2. The peak frequencies of the electrode features of the two three-layer samples and the ones of the previously described GDC|Pt electrode samples are in the same range. Compared to the GDC|Pt electrodes, even at higher temperatures no second overlapping feature at low frequencies could be observed.

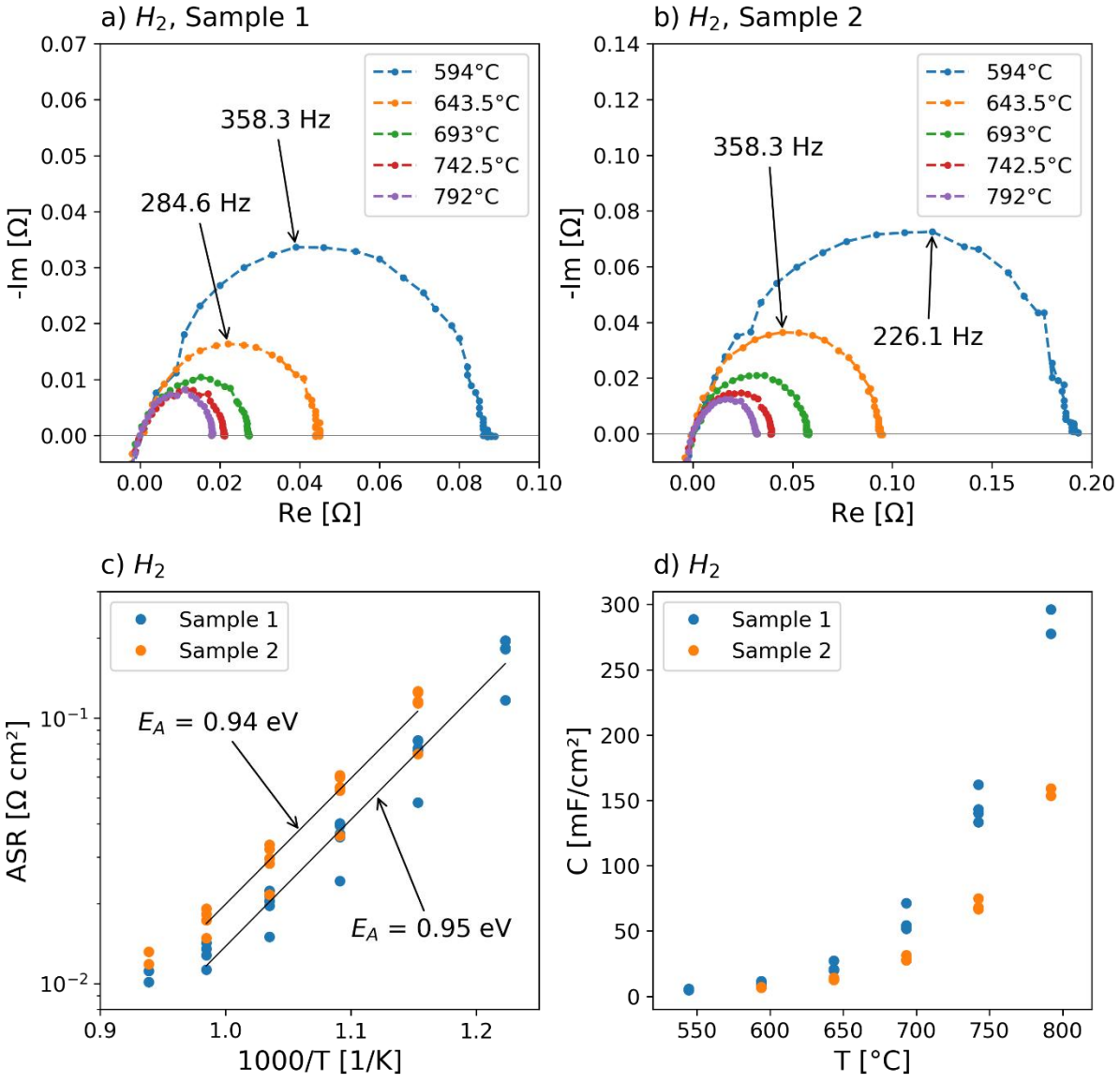

Figure 35: Nyquist plots with subtracted x-intercept of the two three-layer electrode samples measured in humidified hydrogen at 60 mbar (a, b), ASR over 1000/T (c) and the capacitance plotted over T (d).

Figure 35 c) depicts the ASR of the three-layer electrode samples plotted over 1000/T. The values were obtained by fitting the impedance spectra with an equivalent circuit consisting of an R, CPE parallel circuit describing the electrode semicircle feature and a resistor in series for the offset resistance. The ASR of sample 1 is 0.05 Ωcm^2 at around 600°C for the first temperature cycle. After the first temperature cycle a slight degradation of the electrodes can be noticed. Sample 2 shows a slightly higher ASR than sample 1 and both follow an Arrhenius type behavior with similar activation energies compared to the samples with GDC|Pt electrodes. The deviation from the Arrhenius type behavior noticeable by a change to a lower slope at high temperatures is not as distinct as for the GDC|Pt electrodes. Due to the outstanding ASR values of the three-layer electrodes in the same range as for the GDC|Pt electrodes it can be concluded that spincoating instead of brushing the GDC layer and the consequently reduced thickness do not impact the performance of the electrodes negatively and that the active film thickness is still smaller than the thickness of the GDC layer. In Figure 35 d) the chemical capacitance, calculated from the equivalent circuit fit, plotted over the temperature is displayed. The capacitance increases with increasing temperature and shows the same trend as for the GDC|Pt samples with a similar capacitance noticeable for sample 2 and approximately by a factor 2 higher capacitance values for sample 1.

4.4.2. Temperature cycles in oxidizing atmosphere

Figure 36 a) shows the impedance spectra of one of the three-layer electrode samples measured in an oxidizing atmosphere at different temperatures.

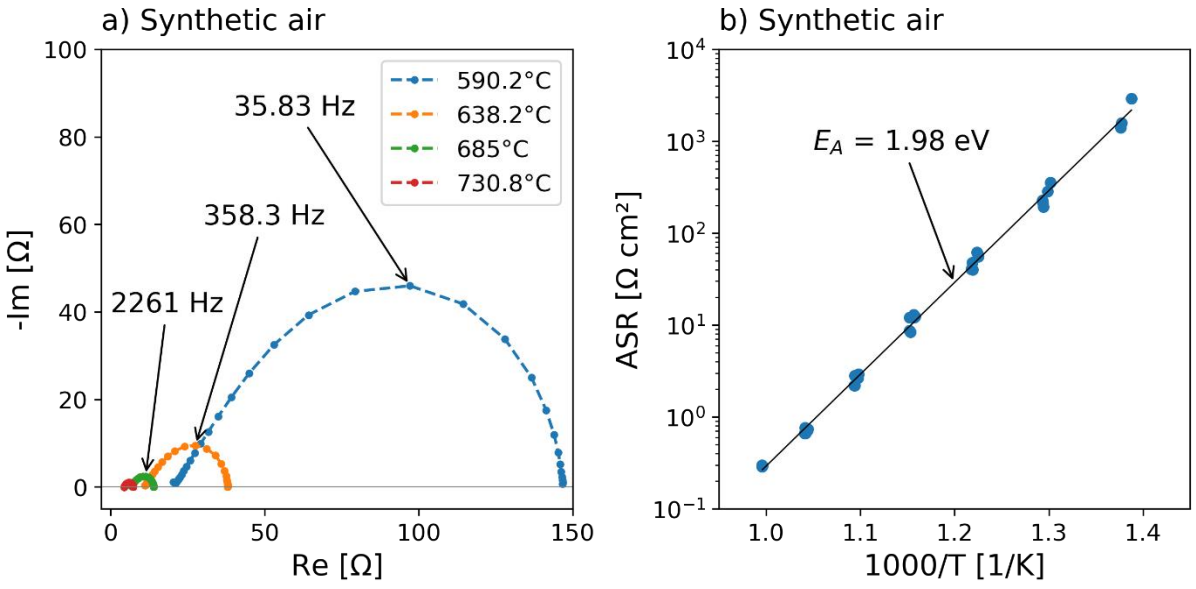

Figure 36: Impedance spectra of the samples with three-layer electrodes measured in synthetic air (a) and ASR plotted over 1000/T (b).

The spectra depict one semicircle feature attributable to the electrode. However, the features are not ideal semicircles and show a linear behavior with a slope of approximately 45° of the imaginary part over the real part of the impedance in the high frequency region of the semicircle. Therefore, as already used in literature for fitting porous electrodes[90], a Gerischer impedance type model was used to fit the semicircle features. The size of the features decreases with increasing temperature and the peak frequencies increase at higher temperatures significantly in contrast to the measurements of the three-layer electrodes in reducing atmospheres, where only slight changes of the peak frequency with the temperature could be observed. The ASR of the electrode reaction, obtained by fitting of the impedance spectra, plotted over 1000/T is depicted in Figure 36 b). It follows an Arrhenius type behavior with an activation energy of 1.98 eV, which is nearly the same value as for the GDC|Pt electrodes measured in the same atmosphere. The polarization resistance is slightly lower than for the GDC|Pt electrodes, probably due to a higher amount of GDC-Pt triple phase boundaries, but in the same order of magnitude.

4.4.3. Dependence on the oxygen partial pressure

In Figure 37 a) and b) the impedance spectra of the three-layer electrodes measured at different hydrogen partial pressures at a constant set temperature of 600°C are displayed.

The spectra measured show two overlapping features at most of the measured hydrogen partial pressures. Due to the small peak frequency the low frequency feature can be ascribed to the gas diffusion process. It differs in size at the different measured hydrogen partial pressures because the total pressure in the test rod changed during the variation of partial pressures. Furthermore, the offset resistance decreased with increasing temperature. The ASR of the electrode features over the oxygen partial pressure is displayed in Figure 37 c). It was obtained by fitting the electrode and gas diffusion features with an R, CPE parallel circuit each. Sample 2 shows a trend to a higher ASR at less reducing atmospheres. That trend could be also observed for the GDC|Pt electrodes, supported by the fact that less oxygen vacancies and hydrogen molecules are present at oxidizing conditions, which slows down the reaction rate of the electrode process. For sample 1 no clear trend can be observed. The reason for the high uncertainty of the ASR values is the difficult separation of electrode and gas diffusion feature, due to the gas diffusion feature varying in size at different total pressures and the rather similar peak frequencies of the two features. Figure 37 d) depicts the offset resistance of the two three-layer electrode samples and one sample with GDC|Pt electrodes for comparison plotted over the oxygen partial pressure. The offset resistance decreases with decreasing oxygen partial pressure, however, compared to the GDC|Pt electrodes the slope is substantially smaller for the three-layer electrodes. This supports the assumption that a part of the offset resistance can be ascribed to the electronic conductivity

of GDC, because according to that assumption a lower thickness of the GDC layer would lead to a decrease in the part of the offset resistance depending on the oxygen partial pressure, which could be exactly observed for the three-layer electrodes with a spincoated and thus thinner GDC layer than the GDC|Pt samples. The difference of the three-layer and GDC|Pt samples in the absolute values for the offset resistance is due to slight variations in the electrolyte thickness.

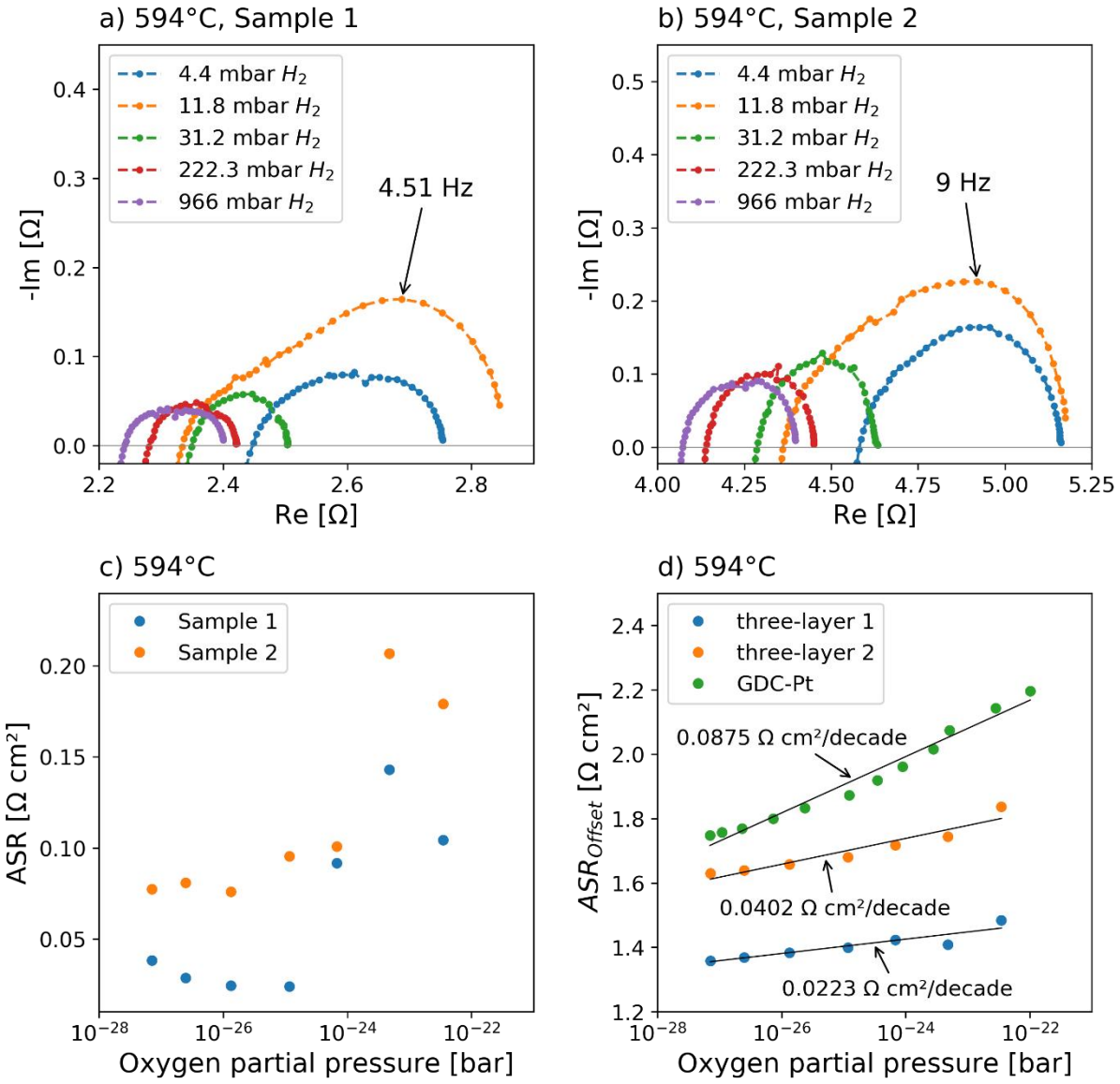

Figure 37: Nyquist plots of the samples with three-layer electrodes measured at different hydrogen partial pressure (a, b), ASR plotted over the oxygen partial pressure (c) and offset resistance over the oxygen partial pressure (d).

Overall, the three-layer structure with a spincoated GDC layer improved the performance compared to the GDC|Pt electrodes with a less oxygen partial pressure dependent offset resistance due to the thinner GDC layer and less delamination of the Pt current collector because of the PtGDC layer between GDC and current collector, while still maintaining the

excellent polarization resistance of <0.1 Ωcm^2 at 600°C, even surpassing Ni-GDC cermet anodes that are used in metal supported SOFCs with power density of 2 W/cm^2 at 650°C.[91] These exhibit an ASR of 0.2 - 0.3 Ωcm^2 at 600°C.[30] Consequently, these electrodes were used as counter electrodes for the NCF and NCFC thin-film samples.

4.5. Three-layer electrodes with an additional PLD deposited GDC layer

The activation energy of the electrode ASR in reducing conditions is remarkably similar to the YSZ-GDC interface ASR that was reported for Ni-GDC cermet anodes.[30] This observation suggests that a large part of the already excellent ASR of the GDC based anodes is actually caused by ion conduction through the GDC-YSZ interface.

To investigate a possible impact of the GDC-YSZ interface, impedance spectra of a symmetric sample consisting of a single crystalline YSZ electrolyte (10 mm x 10 mm x 0.5 mm) with a thin GDC layer deposited via PLD followed by the three-layer electrodes were recorded. The very thin and dense GDC layer deposited by PLD should eventually improve the interface between YSZ and the spincoated GDC layer. The measurements were carried out in the four-sample setup in humidified H_2 at 60 mbar total pressure, with a hydrogen to water ratio of 1:1. The temperature was varied from 500 to 800°C in 50°C steps and the frequency range from 0.1 to 900000 Hz with 10 data points per decade. The AC amplitude was set to 100 mV. The flow rate was approximately 100 sccm. Furthermore, spectra at different reducing oxygen partial pressures at a set temperature of 600°C were recorded with the same settings as for the temperature cycles except for the frequency range, which was 0.5 to 900000 Hz for these measurements.

Figure 38 a) displays the impedance spectra of the sample normalized to the same x-axis intercept, recorded in humidified H_2 at low pressure. The spectra consist of one semicircle feature, attributable to the electrode process with slightly lower peak frequencies than observed for the three-layer electrodes without the additional PLD deposited GDC layer. A shoulder or feature for gas diffusion cannot be identified in these spectra. The size of the semicircles decreases with increasing temperature. The ASR of the electrode feature, obtained by fitting the impedance spectra with an equivalent circuit consisting of an R, CPE parallel circuit and a resistor in series, over 1000/T is shown in Figure 38 b). It follows an Arrhenius type behavior over the whole temperature range measured with an activation energy of 0.63 eV. That is significantly lower than for the three-layer electrodes and the GDC|Pt electrodes, indicating a different limiting factor. The ASR is with 0.08 Ωcm^2 at 600°C set temperature in the size range as the polarization resistance of the three-layer and GDC|Pt electrodes. In Figure 38 c) the capacitance obtained from the equivalent circuit fit is plotted over the temperature. The capacitance increases with the temperature and has a

different temperature dependence compared to the three-layer electrode samples: it is higher at low temperatures and lower at high temperatures. However, that difference is not significant, because the deviation between the two three-layer samples has been already rather big.

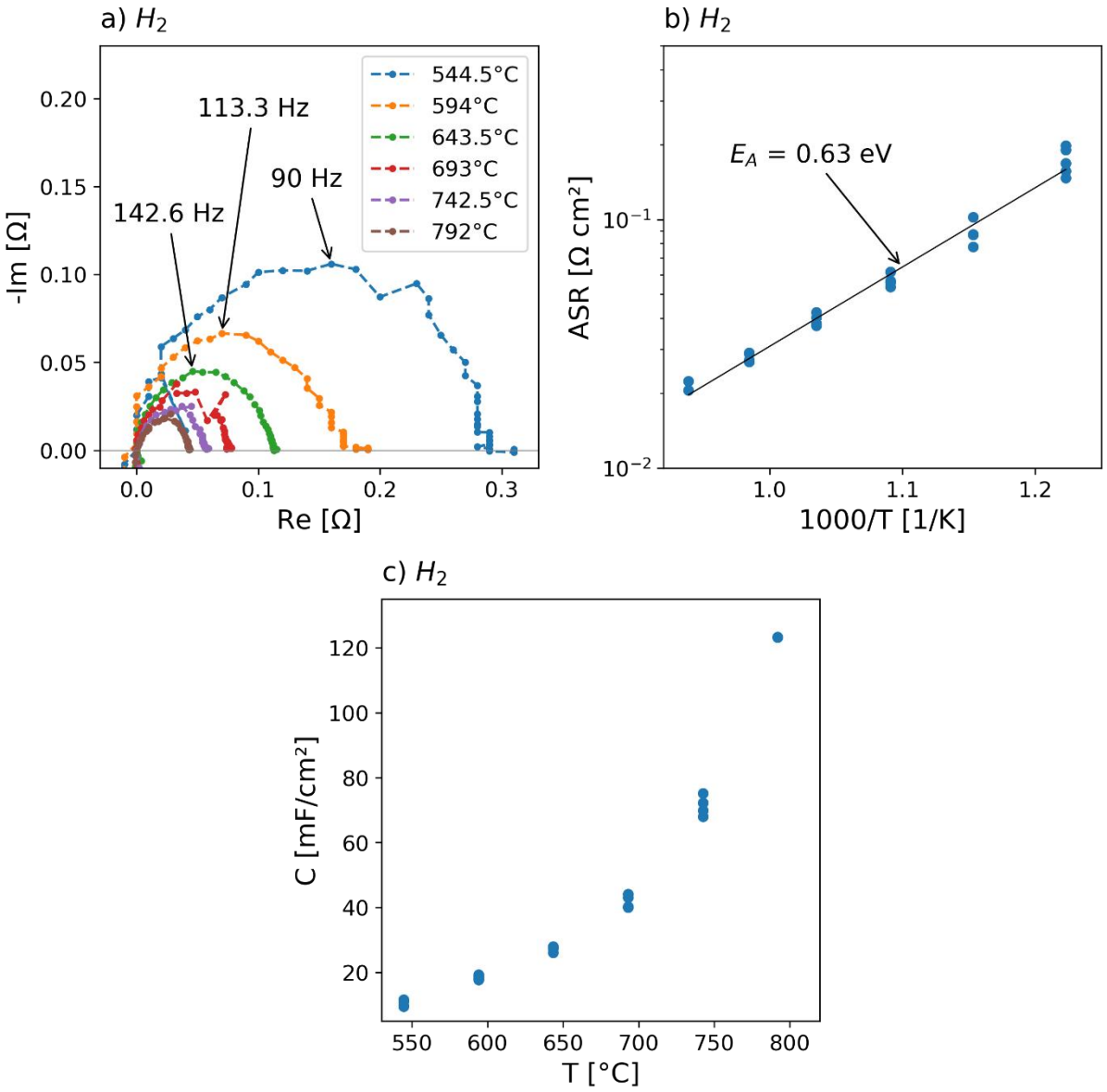

Figure 38: Impedance spectra with subtracted x-intercept of the sample with a PLD deposited GDC layer followed by three-layer electrodes measured in humidified hydrogen at 60 mbar (a), ASR of the electrodes over 1000/T (b) and the corresponding capacitance plotted over T (c).

Figure 39 a) depicts the impedance spectra of the sample with the PLD deposited GDC layer between YSZ and three-layer electrode at 600°C set temperature and different hydrogen partial pressures. They consist of one semicircle feature, that deviates from the ideal semicircle shape at low frequencies, probably due to and overlap with gas diffusion. However, a gas diffusion feature could not be clearly identified, because the electrode

features have a very low peak frequency and consequently would overlap with gas diffusion a lot. Another indication that gas diffusion overlaps is, that the size of the feature does not follow the trend to smaller sizes at higher hydrogen partial pressures, which could be observed for the electrode features of the three-layer and GDC|Pt electrodes.

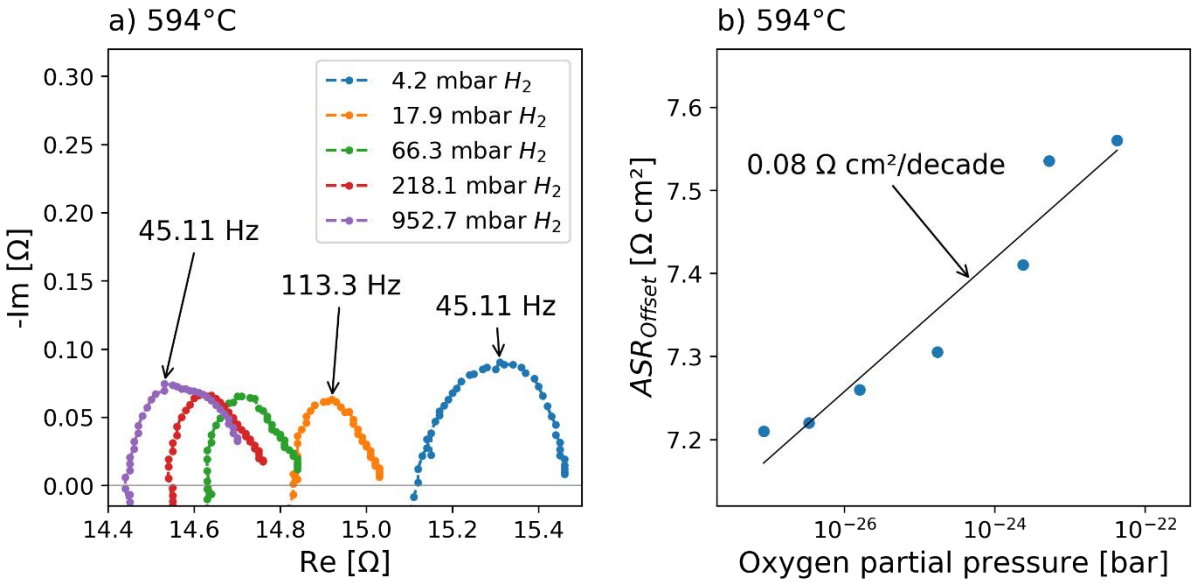

Figure 39: Nyquist plots of the sample with a PLD deposited GDC layer followed by three-layer electrodes measured at 600°C set temperature in different hydrogen partial pressures (a) and offset resistance plotted over the oxygen partial pressure (b).

The offset resistance shown in Figure 39 b) over the oxygen partial pressure decreases with decreasing oxygen partial pressure. That can be ascribed to the electronic conductivity of GDC, which gets better at more reducing conditions, being partially responsible for the offset resistance. In contrast to the three-layer electrodes the slope was nearly identical to that of the GDC|Pt electrodes and thus the additional GDC layer deposited via PLD seemed to reverse the improvement due to the use of three-layer electrodes, which was minimizing the contribution of the electronic conductivity of GDC to the offset resistance. In conclusion electrodes with the additional PLD deposited GDC layer did not show any substantial advantages with an overall worse performance than the three-layer electrodes.

4.6. Degradation of GDC based electrodes due to thin-film manufacturing

Because the GDC based three-layer electrodes were planned to be used as counter electrodes for the thin-film electrodes, it was analyzed if degradation occurs during the lithography steps that are required for preparation of the thin-film electrodes. To make sure that the GDC based electrodes do not interact with the developer used during the lithography process, one of the GDC|Pt samples, that has already been measured previously, was treated with the developer solution for an equal duration as the thin-film samples and

measured afterwards. Furthermore, to investigate if reusing the three-layer counter electrodes after etching away the thin-film of the thin-film samples is possible, an already measured three-layer electrode sample was treated with conc. HCl as long as it took to etch away the thin-film of a thin-film sample. The three-layer sample after the acid treatment and the GDC|Pt sample after the treatment with developer were both analyzed with EIS in 4-point mode in the four-sample setup. The impedance spectra were recorded in a frequency range from 0.1 to 900000 Hz with 10 points per decade in humidified H_2 atmosphere at around 60 mbar and a hydrogen to water ratio of 1:1. The flow was set to approximately 100 sccm and the temperature was varied from 500 to 800°C in 50°C steps.

4.6.1. Impedance analysis of the GDC|Pt sample after treatment with developer

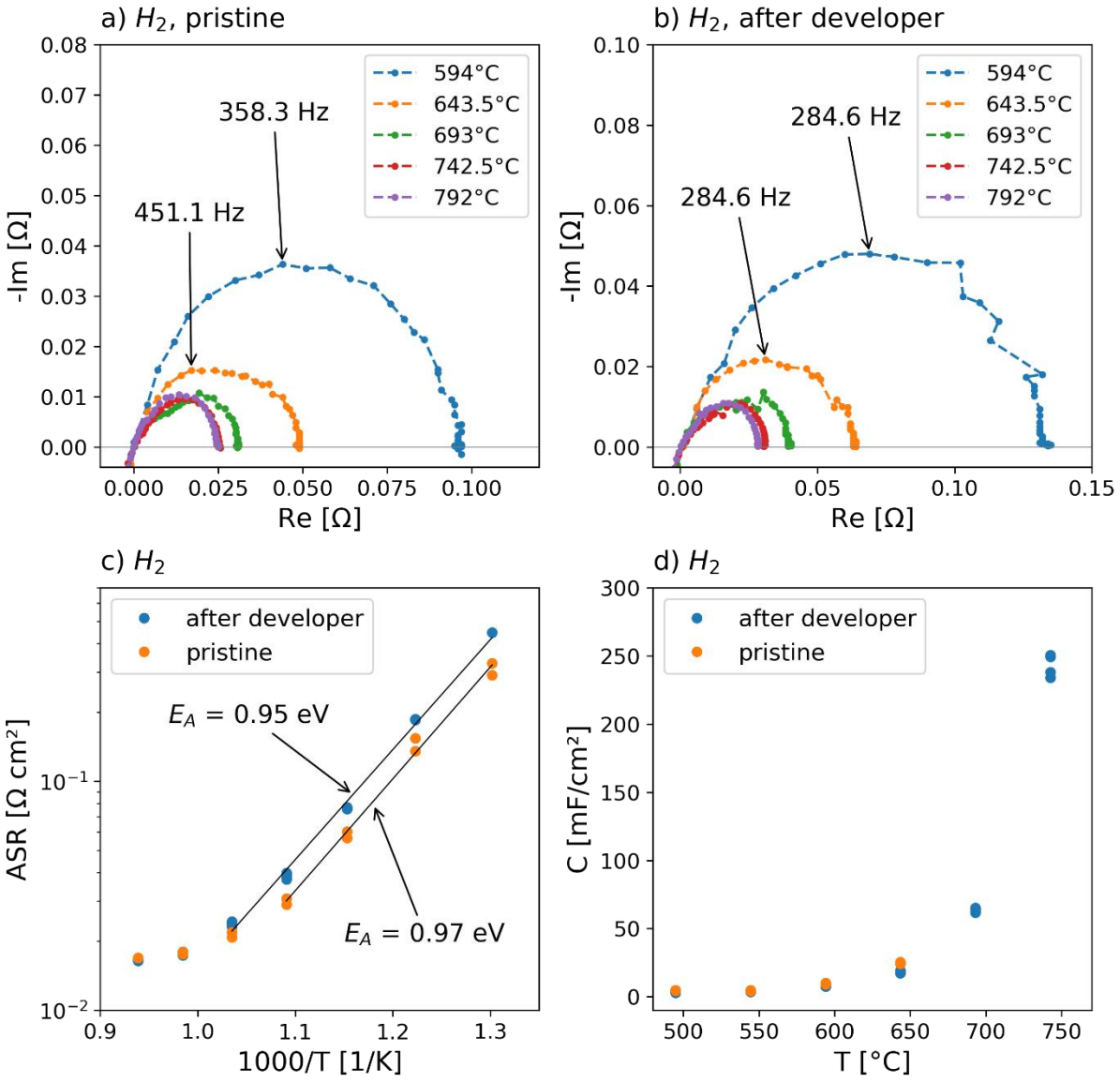

Figure 40: Impedance spectra with subtracted high frequency intercept of a GDC|Pt electrode sample recorded in humidified hydrogen at 60 mbar before and after the treatment with developer (a, b), ASR over 1000/T (c) and the capacitance over T for the treated and untreated sample (d).

Figure 40 a) shows the impedance spectra, with subtracted high frequency intercept, of the GDC|Pt sample before the treatment with developer and b) the spectra after treatment with developer. The impedance spectra before and after the treatment look very similar, with one semicircle feature attributable to the electrode process that decreases in size at rising temperatures. Some of the semicircle features deviate from the ideal shape and look flatter on the top, most likely due to an overlap with a gas diffusion process. The peak frequencies are within the same order of magnitude. In Figure 40 c) the ASR, obtained by fitting the electrode feature with an R, CPE parallel equivalent circuit, over 1000/T is displayed for the pristine sample and after the treatment with developer. The ASR after developer treatment is slightly higher than before. However, for high temperatures the gas diffusion limitation can still be observed. Both curves follow an Arrhenius-type behavior at the lower measured temperatures with similar activation energies. The capacitance plotted over T is depicted in Figure 40 d). The capacitance of the electrodes does not change significantly after the treatment with developer and the same trend to a higher capacitance as before the treatment can be seen. These results show that treating the GDC based counter electrodes with the developer, as necessary for manufacturing the thin-film electrodes, does not impact their performance negatively.

4.6.2. Impedance analysis of three-layer electrodes after acid treatment

Figure 41 a) and b) depict the impedance spectra, with subtracted high frequency x-axis intercept, of the three-layer sample measured in humidified hydrogen at low pressure before and after a treatment with HCl, used for recycling the counter electrodes of the thin-film samples. The spectra of the pristine sample show one semicircle feature that decreases in size with increasing temperatures. After the HCl treatment the spectra still consist of one feature that decreases in size with rising temperatures and is ascribable to the electrode process. However, the size of the features is substantially bigger than before the treatment and at higher frequencies the shape deviates from an ideal semicircle shape with a roughly linear relationship of imaginary and real part of the impedance. Moreover, the peak frequencies of the electrode features are significantly smaller after the acid treatment. The ASR, displayed in Figure 41 c) over 1000/T was obtained by fitting the semicircle feature of the electrode process with an R, CPE parallel circuit. For the sample after acid treatment also an approach to fit the spectra with a Gerischer impedance was made but did not yield very good results. The ASR before and after the HCl treatment decreases at higher temperatures and the ASR of the treated electrodes is significantly higher than for the pristine ones with 0.28 Ωcm^2 at 600°C. Consequently, the limitation because of gas diffusion at the higher measured temperatures can only be observed for the pristine sample. Furthermore, the activation energy of the electrode process differs substantially, indicating different limiting processes.

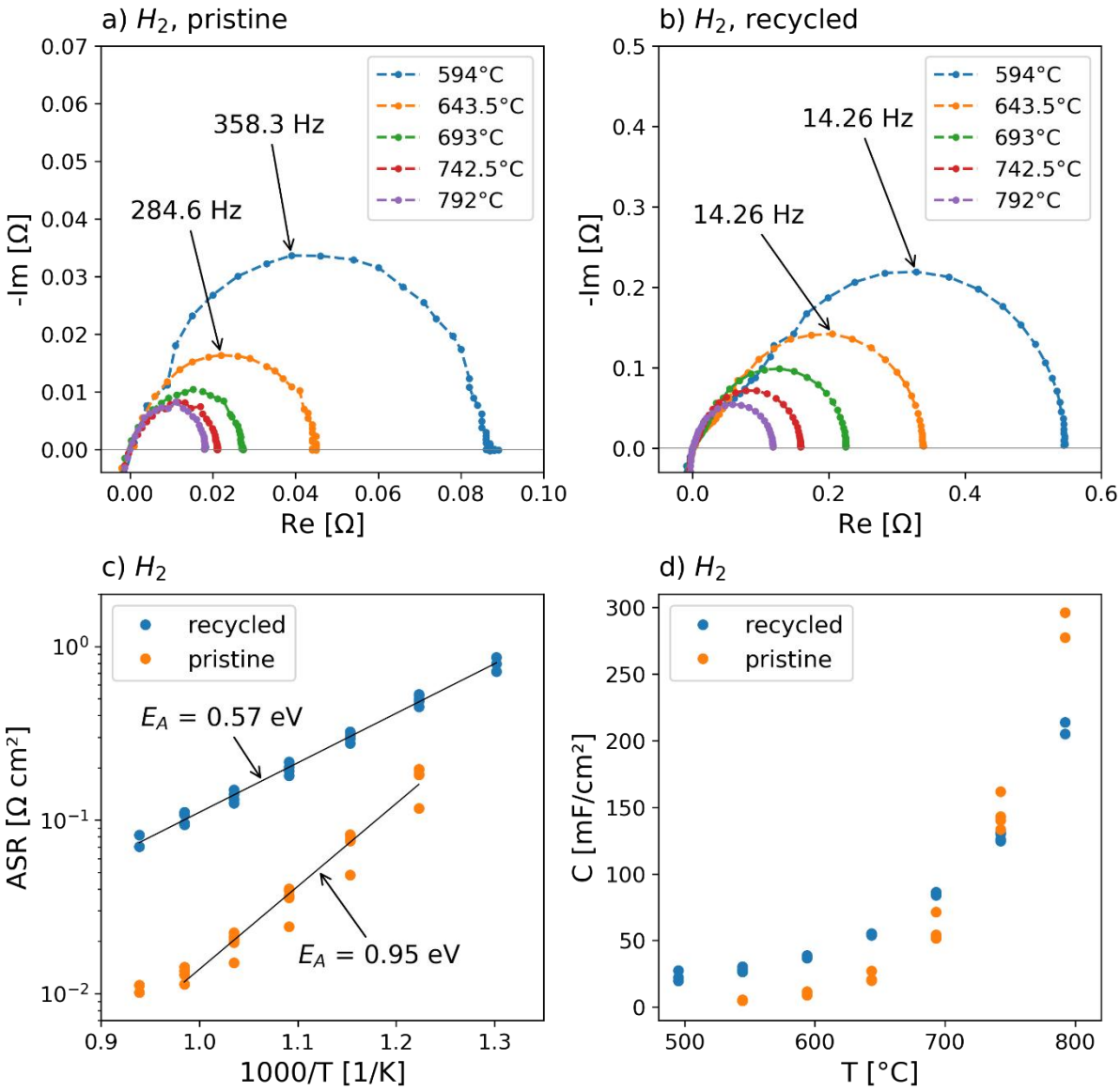

Figure 41: Nyquist plots with subtracted high frequency intercept of a three-layer electrode sample measured in humidified hydrogen at 60 mbar before and after treatment in HCl (a, b), ASR over 1000/T (c) and the capacitance over T (d).

Figure 41 d) shows the capacitance obtained from the fit of the electrode features before and after acid treatment. The trend to higher capacitance values at higher temperatures can be observed for the pristine electrodes and the ones after the recycling treatment. Especially at the lower temperatures, the capacitance is significantly larger, which indicates that the electrochemically active thickness increases. The higher ASR and capacitance lead to lower peak frequencies after HCl treatment. In conclusion the acid treatment of the three-layer electrodes degrades the electrodes noticeably, leading to significantly higher ASR values. The increased capacitance below 750°C indicates that the electrochemically active thickness is larger (maybe even as large as the electrode thickness) after the acid treatment, and the lower activation energy suggests a different limiting factor for the electrode process. An increase of the electrochemically active thickness is expected when the reaction rate of the

GDC surface decreases. However, recycling and reusing the three-layer counter electrodes once should be possible, because of the still relatively low ASR, compared to thin-film samples which typically exhibit >10 Ωcm^2 at 600°C.

4.7. EIS measurements of GDC based electrodes in CO atmosphere

In addition to H_2 + H_2O gas mixtures, EIS measurements of symmetric three-layer and GDC|Pt electrode samples with polycrystalline YSZ electrolytes were carried out in CO + CO_2 atmosphere in the four-sample setup. Temperature cycles were conducted at temperatures from 600°C to 750°C with an AC amplitude of 100 mV and in a frequency range from 0.1 to 900000 Hz. The flow was regulated with an MFC to 50 sccm and the current for the electrolysis of CO_2 in the CO_2-furnace was set to 0.5 A, yielding a measuring atmosphere that contained approximately 7% CO. Furthermore, measurements at 615°C with electrolysis currents of 0.25 A and 0.1 A, resulting in atmospheres with less CO, were performed. Because no lambda sensor was available at the time the measurements were conducted, the exact atmosphere could not be verified. All samples used for these experiments have already been measured previously in reducing hydrogen or ARCAL atmosphere.

Figure 42 a) shows the impedance spectra of the three-layer electrode sample after the recycling HCl treatment, a normal three-layer electrode sample and one with GDC|Pt electrodes. The spectra of all these sample consist of two semicircle features, one at low frequencies attributable to the electrode and a small shoulder at higher frequencies which seems to be constant in size for all samples. The peak frequencies are smaller compared to the measurements of the same samples in ARCAL and hydrogen atmosphere. The ASR of the electrode features is depicted in Figure 42 b) ,c) and d) and was obtained by fitting the spectra with one R, CPE parallel circuit for the three-layer sample after HCl treatment and by fitting with two R, CPE parallel elements in series for the three-layer and the GDC|Pt sample. As expected, the ASR of the three-layer electrode treated with HCl is higher than that of the untreated three-layer sample, indicating that HCl induced degradation affects H_2 and CO oxidation in a similar manner. However, contrary to the results obtained from the measurements in reducing hydrogen atmosphere, in CO atmosphere the GDC|Pt electrode sample shows an even lower ASR than the three-layer electrode. The decisive difference between those is that the GDC|Pt electrode was prepared by brushing, which yielded a much thicker GDC layer (SEM images in Figure 43 and Figure 44). The polarization resistance is much higher in CO-CO2 mixtures, which is most likely due to GDC being kinetically less active for the reaction of CO compared to the H_2 reaction. In such a case, the electrochemically active thickness is larger in CO + CO_2 atmospheres, and therefore the GDC|Pt sample with the thicker GDC layer shows better kinetics. In general, the ASR is

higher in CO than in hydrogen atmosphere. It follows an Arrhenius type behavior for all three samples with an activation energy of about 0.6 eV. Over the course of the temperature cycles, there is a jump to higher ASR values noticeable after some cycles and then again a rather reproducible behavior with approximately the same activation energy only at higher ASR values. Since this jump can be observed for all samples, it is probably a result of the change of some conditions in the setup. Possibly, the CO concentration, due to problems with the prototype CO_2 electrolysis setup. For the linear regression needed to calculate the activation energy only the first cycles were fitted. The activation energies of the GDC|Pt and the three-layer sample are similar but smaller than in hydrogen atmosphere. Interestingly, the activation energy of the HCl treated sample is higher than in hydrogen atmosphere. That indicates different limiting reaction steps in CO atmosphere.

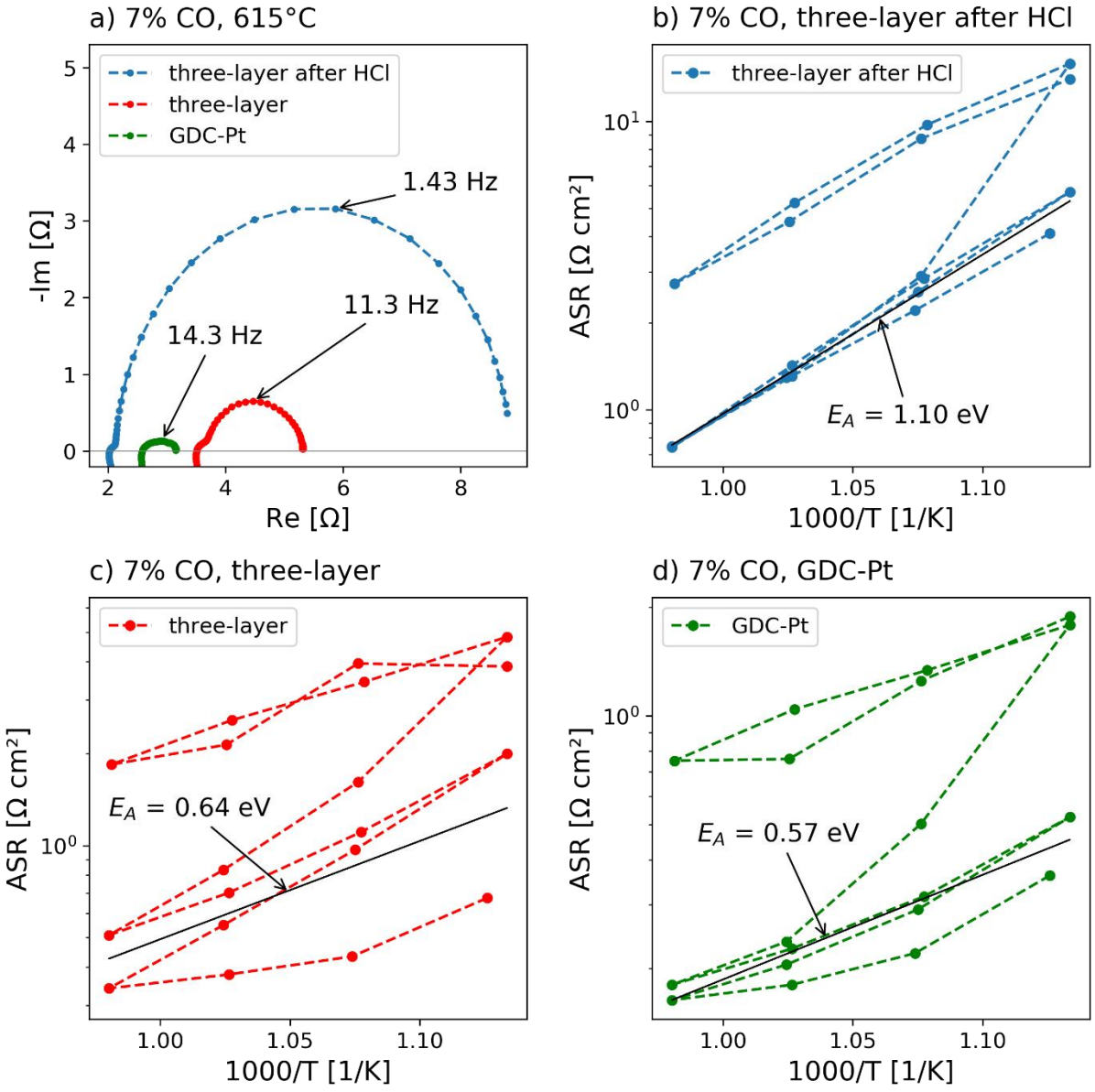

Figure 42: Impedance spectra (a) and the ASR plotted over 1000/T (b, c, d) of different GDC based electrodes.

The evaluation of the chemical capacitance from the fits of the spectra depicted a general trend to a higher chemical capacitance in atmospheres containing more CO for both three-layer samples, due to more oxygen vacancies in more reducing atmospheres. For the GDC|Pt sample no sound results concerning the chemical capacitance could be obtained, eventually due to the not easy to fit reliably, elongated semicircle shape of the impedance spectra.

4.8. SEM images of GDC based electrodes

The microstructure of the GDC|Pt and three-layer GDC electrodes, film thickness and particle sizes were investigated with SEM.

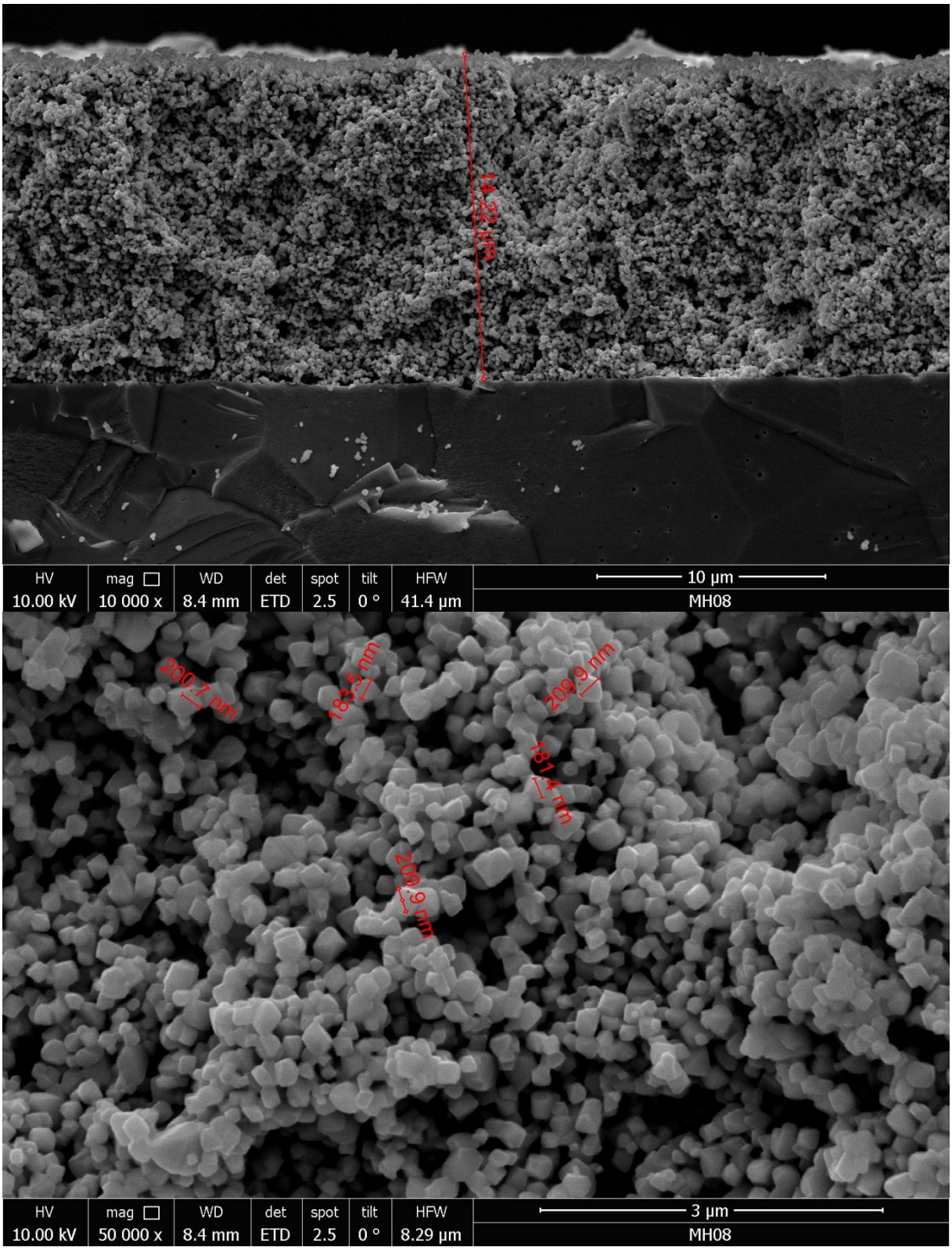

Figure 43: SEM images of a GDC|Pt electrode.

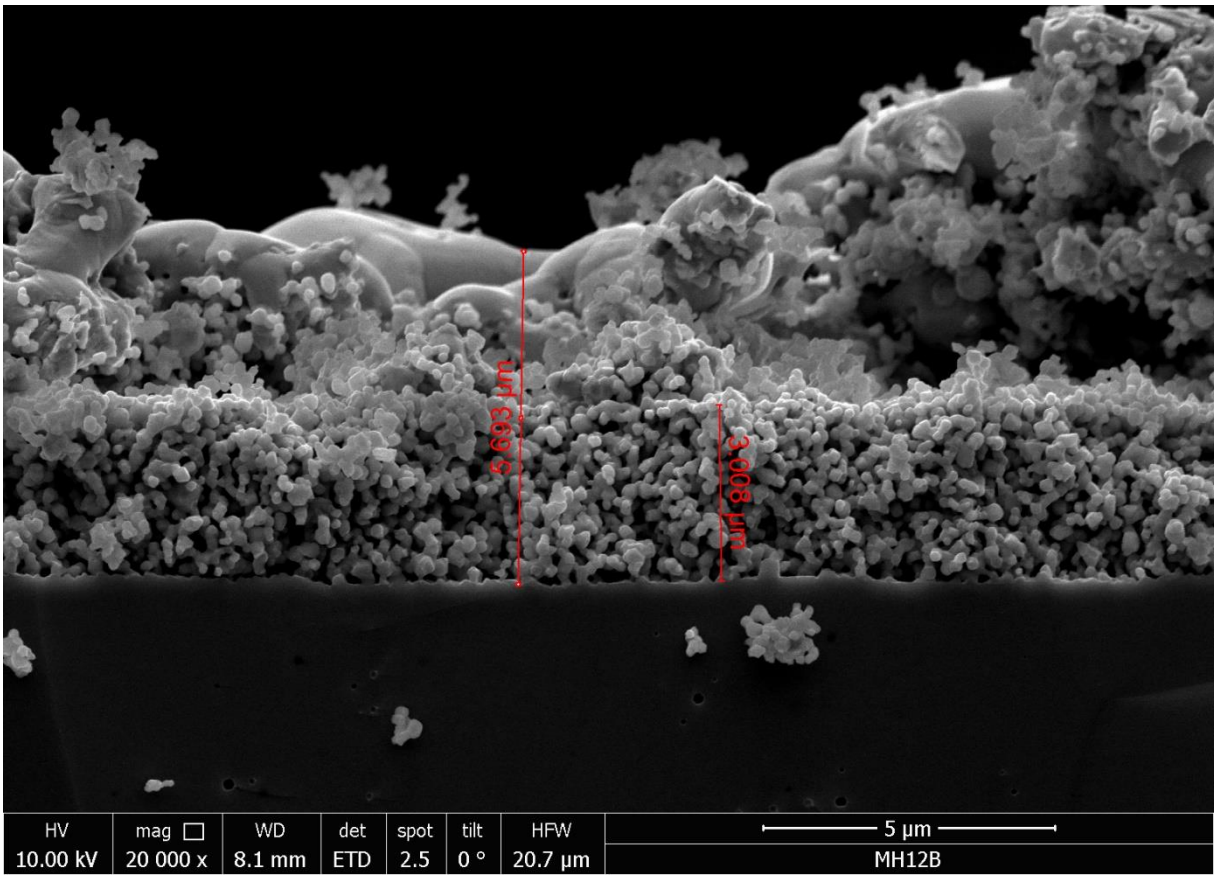

Figure 44: SEM image of a three-layer GDC electrode.

Figure 43 depicts SEM images of the profile of a GDC|Pt electrode and Figure 44 of a three-layer electrode. It can be observed, that the GDC layer, which was brushed for the GDC|Pt electrode and spincoated for the three-layer electrode, consists of a network of particles approximately 200 nm in diameter. The particles are rather homogeneous, and the network offers high porosity, resulting in good gas diffusion properties and a large GDC surface area for the electrode reaction, which is most likely a key factor responsible for the excellent kinetic performance of the GDC based electrodes. The thickness of the GDC layer of the brushed GDC|Pt electrode measured around 14 µm, whereas the spincoated GDC layer of the three-layer electrode was only 3 µm. These results fit surprisingly well with the values obtained from estimation with the scratch test, where the thickness was simply estimated by focusing the bottom and the top of a scratch in the GDC layer with an optical microscope and noting the difference in the depth axis. Moreover, it can be noticed, that the surface of the three-layer electrode looks way less homogenous with rather big differences in height and aggregates of GDC particles between a continuous layer of Pt, compared to the GDC|Pt electrode. That difference can be attributed to the PtGDC layer, in between the Pt current collector and the electrochemically active GDC layer, of the three-layer electrode. While this interlayer has little catalytic activity in reducing conditions, it ensures good mechanical (and therefore electrical) contact between the Pt and GDC layers.

4.9. Summary of the impedance characterization of porous GDC based anodes

In light of all the previously described findings it can be concluded that single phase GDC anodes exhibit a much lower polarization resistance than Ni-GDC or Pt-GDC cermets in H_2 with an ASR of 0.08 Ωcm^2 at 600°C and < 0.02 Ωcm^2 at 800°C. Noteworthy, these values were found even at very low H_2 and H_2O partial pressures (35 + 25 mbar). Moreover, the electrode arc size and capacitance are independent of the GDC layer thickness (3 vs. 14 µm), probably due to a very small electrochemically active thickness, which is in line with estimations that use the chemical capacitance. The Arrhenius plots flatten above 700°C, even in diffusion optimized measurement conditions, most likely due to gas phase diffusion contributions that are only observed because of the excellent kinetics.

A modification of the interface with a PLD deposited GDC interlayer lowers the activation energy to the value that was found for Ni-GDC cermet or HCl treated GDC anodes, whereas the activation energy of the "standard" GDC anodes is very similar to the value found for ion transfer through the YSZ-GDC interface in Ni-GDC cermets.[30] Therefore, it is likely that either ion conduction through the GDC layer and the surface reaction on GDC (for electrodes with low activation energies) or ion conduction through the interface (for electrodes with higher activation energy) are the rate limiting factors. Measurements in $CO+CO_2$ atmosphere showed significantly slower kinetics than in H_2+H_2O and consequently a larger active film thickness of the GDC layer. Due to this larger active film thickness, the brushed GDC layers with ~14 µm thickness exhibited lower polarization resistance than the ~3 µm thick spin-coated layers.

In conclusion, the obtained electrodes are excellent for the use as counter electrodes in thin-film model cells but show as well interesting properties for application in SOFC or SOEC systems.

5. Electrochemical properties and exsolution behavior of NCF and NCFC thin-film electrodes

Thanks to the excellent kinetics of the three-layer GDC counter electrodes, the impedance and overpotential of cells with NCF and NCFC thin-film electrodes is dominated by the properties of the thin-film. Therefore, experiments at well-defined NCF/NCFC half-cell overpotentials are possible in a two-electrode configuration.

Due to the complexity of exsolution phenomena and their electrochemical implications, several testing protocols, including variation of the H_2:H_2O mixing ratio, applied bias and current collector geometry were performed in order to explore the conditions in which electrochemical measurements deliver a fingerprint for exsolution processes.

5.1. EIS of NCFC thin-film electrodes at different temperatures

The first measurements with thin-film samples were carried out on a sample consisting of a one-side polished single crystalline YSZ electrolyte (10 mm x 10 mm x 0.5 mm) with a three-layer GDC based electrode on the rough side and a current collector made of a 2 nm layer Ti for better adhesion and a 100 nm Pt layer, followed by a PLD deposited NCFC layer on the polished side. A general scheme of the thin-film samples is shown in Figure 45.

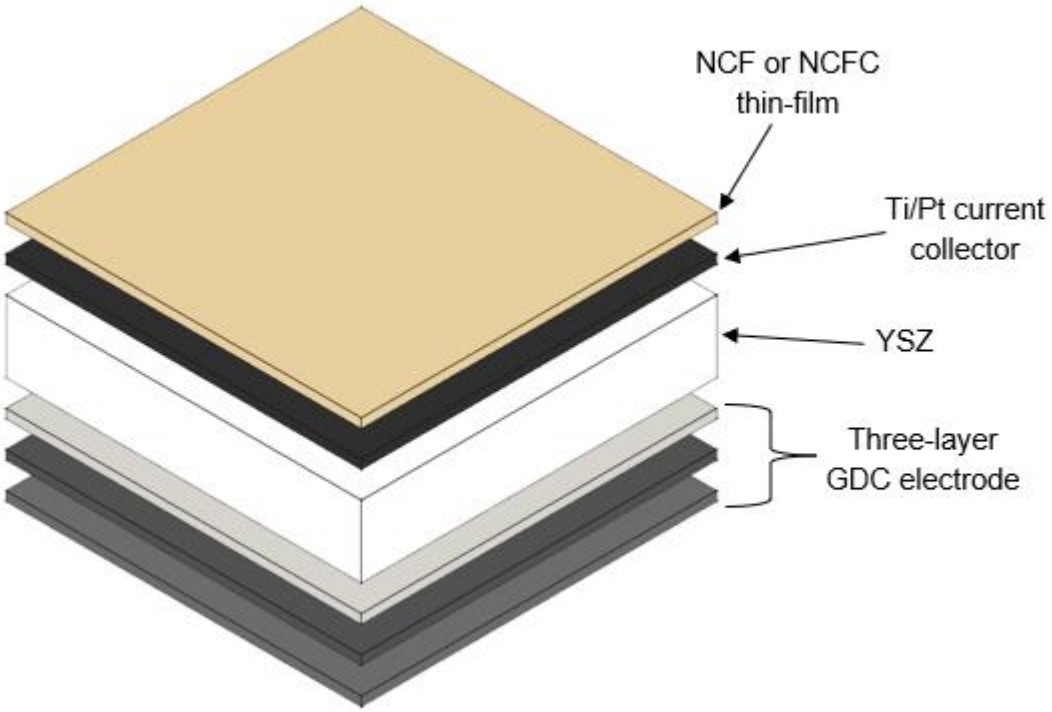

Figure 45: General structure of the thin-film samples.

The current collector was structured via lift-off lithography in a grid structure. Due to the problem of bad adhesion of the current collector, as described in 3.1.2, the grid had rather

many defects, which should not be a huge problem for the grid current collectors though, because its only purpose is to distribute the current evenly. The sample was broken into four parts before measuring, to allow more measurements being performed without the need to manufacture a new sample. The EIS measurements were conducted in the wing setup in four-point mode and a frequency range from 0.1 to 900000 Hz with 5 data points per decade. The AC amplitude was 20 mV and the set temperature was varied from 500 to 800°C in 50°C steps. The spectra were recorded in two different atmospheres with a flow rate of approximately 100 sccm, in humidified ARCAL with a hydrogen to water ratio of about 1:1 and in synthetic air. The resulting impedance spectra of the measurements in humidified ARCAL are displayed in Figure 46 a) and b).

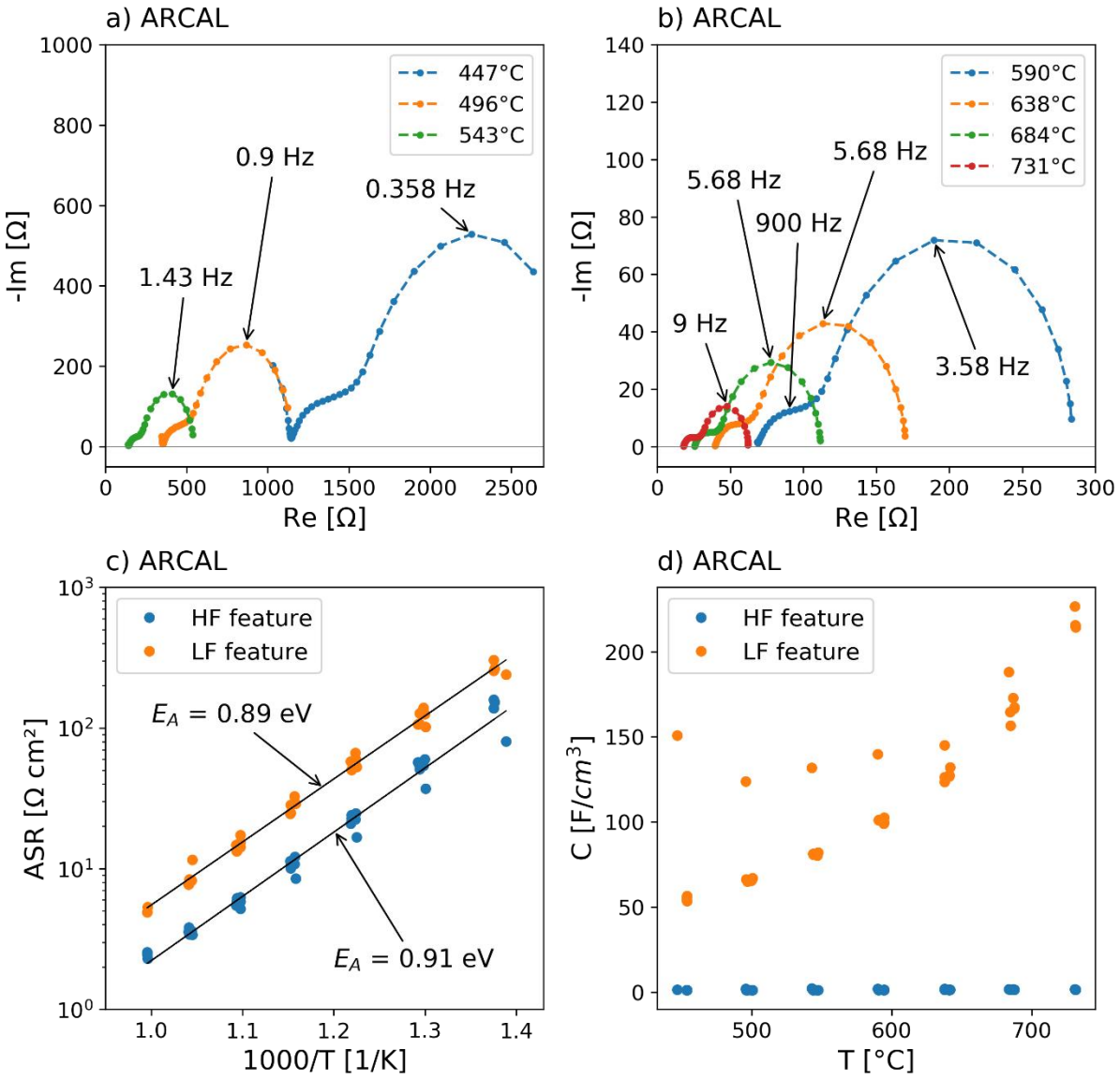

Figure 46: Nyquist plots of the sample with an NCFC working electrode measured in humidified ARCAL at different temperatures (a, b), ASR of the semicircle features over 1000/T (c) and capacitance over T (d).

In contrast to the expectation that only one feature attributable to the electrode process should be visible, the spectra consist of one semicircle feature with a very low peak frequency and one semicircle feature partly overlapping with a higher peak frequency. Both, the low frequency (LF) and the high frequency (HF) feature decrease in size with increasing temperature. Figure 46 c) shows the ASR, obtained by fitting the semicircle features with an R, CPE parallel equivalent circuit each, of the LF and HF feature plotted over 1000/T. It can be noticed that the ASR of both features can be described by the Arrhenius equation due to the linear relation of the logarithm of the ASR and 1000/T with decreasing ASR at rising temperatures. The activation energies of both features are similar at around 0.9 eV. However, the low frequency feature has a significantly higher ASR with 29.0 Ωcm^2 compared to the high frequency feature with 8.5 Ωcm^2 at a temperature of approximately 600°C. In Figure 46 d) the capacitance of the features over the temperature is depicted. The capacitance of the low frequency feature generally increases with increasing temperature and is in the range of several mF/cm^2. The high frequency feature has a capacitance of around 20 $\mu F/cm^2$ and shows a tendency to higher capacitance values at higher temperatures with a less clear trend than the low frequency feature capacitance though. In light of these findings the low frequency feature could be associated with the electrode reaction, due to the high capacitance values characteristic for a chemical capacitance. Therefore, in the plot in Figure 46 d), this capacitance was normalized to the volume of the 130 nm thick electrodes, which was measured by profilometry. The origin of the overlapping high frequency feature could not be clearly identified, albeit the low capacitance in a typical range of double layer capacitances and the problems with the adhesion of the current collector that occurred during lift-off lithography hint to a possible interface contribution resulting in this HF feature. The Nyquist plots of the NCFC thin-film sample measured in synthetic air are shown in Figure 47 a) and b). As for the measurements in ARCAL atmosphere, two semicircle features can be observed, one at low frequency probably attributable to the electrode reaction and one at higher frequencies. The peak frequencies of the features are slightly lower than the ones of the spectra recorded in humidified ARCAL. Moreover, the size of the low frequency and high frequency feature decreases with increasing temperature.

Figure 47 c) depicts the ASR of both semicircle features plotted over 1000/T. The ASR was obtained by fitting the spectra with an R, CPE parallel circuit for each of the two features and a resistor in series to account for the electrolyte resistance. The values at the lowest measured temperature of the LF feature were not used for calculating the activation energy because of an unreliable fit due to only a part of the feature being visible in the measured frequency range. Furthermore, the data from the first rising temperature cycle, noticeable as the datapoints with substantially lower ASR compared to the other points at equal

temperatures, were excluded from the fit to obtain the activation energy. Other than that, the ASR of both features follows a behavior according to the Arrhenius equation with an activation energy of 1.89 eV for the LF feature and 1.04 eV for the HF feature.

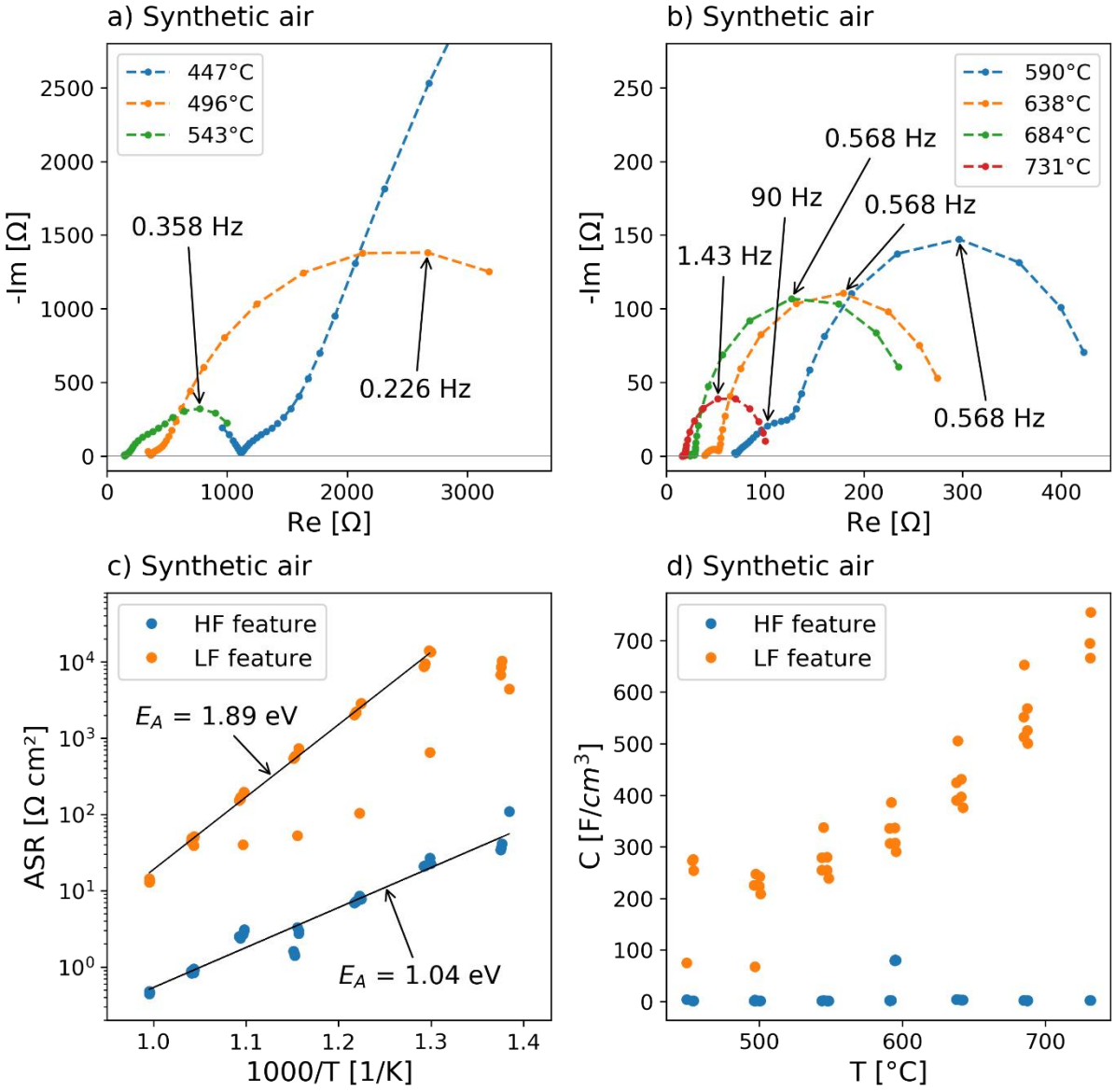

Figure 47: Nyquist plots of the sample with an NCFC working electrode measured in synthetic air at different temperatures (a, b), ASR of the semicircle features over 1000/T (c) and capacitance over T (d).

The capacitance, as displayed in Figure 47 d), of the LF feature shows a trend to an increasing capacitance at higher temperatures and has a significantly higher capacitance than the HF feature. The capacitance of both features is in the same size range as for the measurements in ARCAL atmosphere and due to the very low capacitance values of the high frequency feature, the low frequency feature could be ascribed to the electrode reaction.

5.2. EIS of NCFC and NFC electrodes with applied bias up to ±300 mV

The NCFC sample used for the impedance measurements with applied bias was a fracture part of the sample described in 5.1 with single crystalline YSZ electrolyte, three-layer counter electrode, Ti/Pt grid current collector manufactured via lift-off lithography and NCFC thin-film electrode. The NCF sample was made of a single crystalline YSZ electrolyte (10 mm x 10 mm x 0.5 mm), a three-layer counter electrode, a 2 nm Ti and 100 nm Pt grid current collector structured via lithography and ion-beam etching, and an NCF thin-film deposited by PLD. This sample was broken into four parts of approximately 5 mm x 5 mm x 0.5 mm with a diamond scratcher and mechanical force. A third sample was prepared equally to the first NCFC sample but with a current collector structured with lithography and ion-beam etching instead of lift-off lithography. The measurement conditions were equal for all three samples. The impedance spectra were recorded in the wing setup in humidified ARCAL atmosphere with a hydrogen to water ratio of 1:1 at a temperature of 600°C and a flow of approximately 100 sccm, which corresponds to a $p(O_2)$ of $1.35*10^{-24}$ bar, according to NIST data[85–87]. The frequency for the measurements ranged from 0.1 to 900000 Hz with ten points per decade and an AC amplitude of 20 mV. The exact cycles with an additional applied bias are described in Table 2 and the progression is displayed in Figure 48.

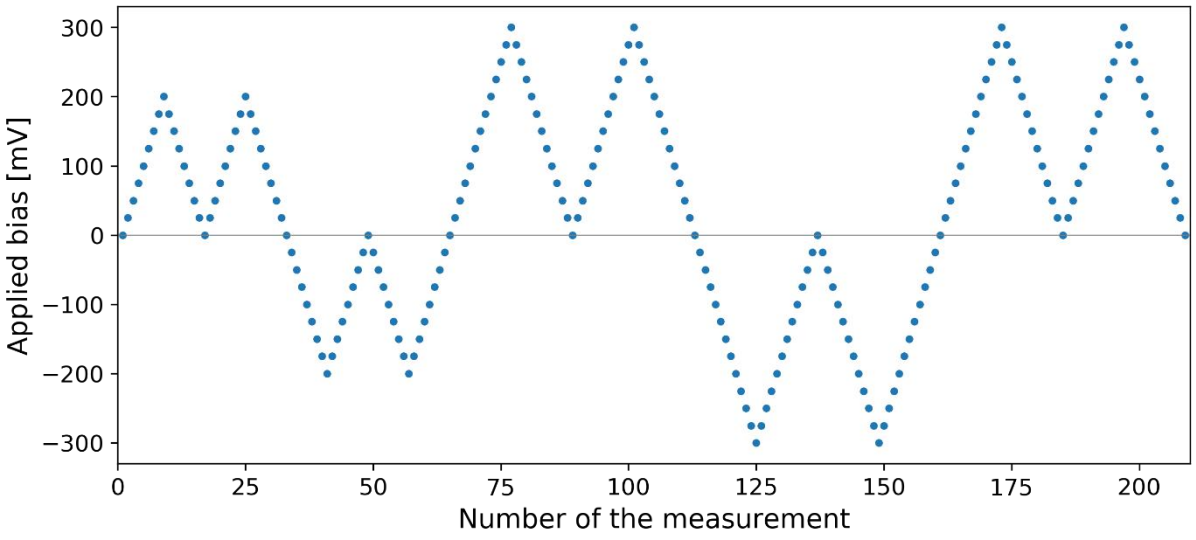

Figure 48: Sweeping cycles with applied bias.

Table 2: Bias cycles of the samples with NCFC and NCF electrodes.

Cycle	Step size	Bias cycle range
1	25 mV	0 mV to 200 mV to 0 mV
2	25 mV	0 mV to 200 mV to 0 mV

3	25 mV	0 mV to -200 mV to 0 mV
4	25 mV	0 mV to -200 mV to 0 mV
5	25 mV	0 mV to 300 mV to 0 mV
6	25 mV	0 mV to 300 mV to 0 mV
7	25 mV	0 mV to -300 mV to 0 mV
8	25 mV	0 mV to -300 mV to 0 mV
9	25 mV	0 mV to 300 mV to 0 mV
10	25 mV	0 mV to 300 mV to 0 mV

5.2.1. NCFC electrode sample with lift-off lithography current collector

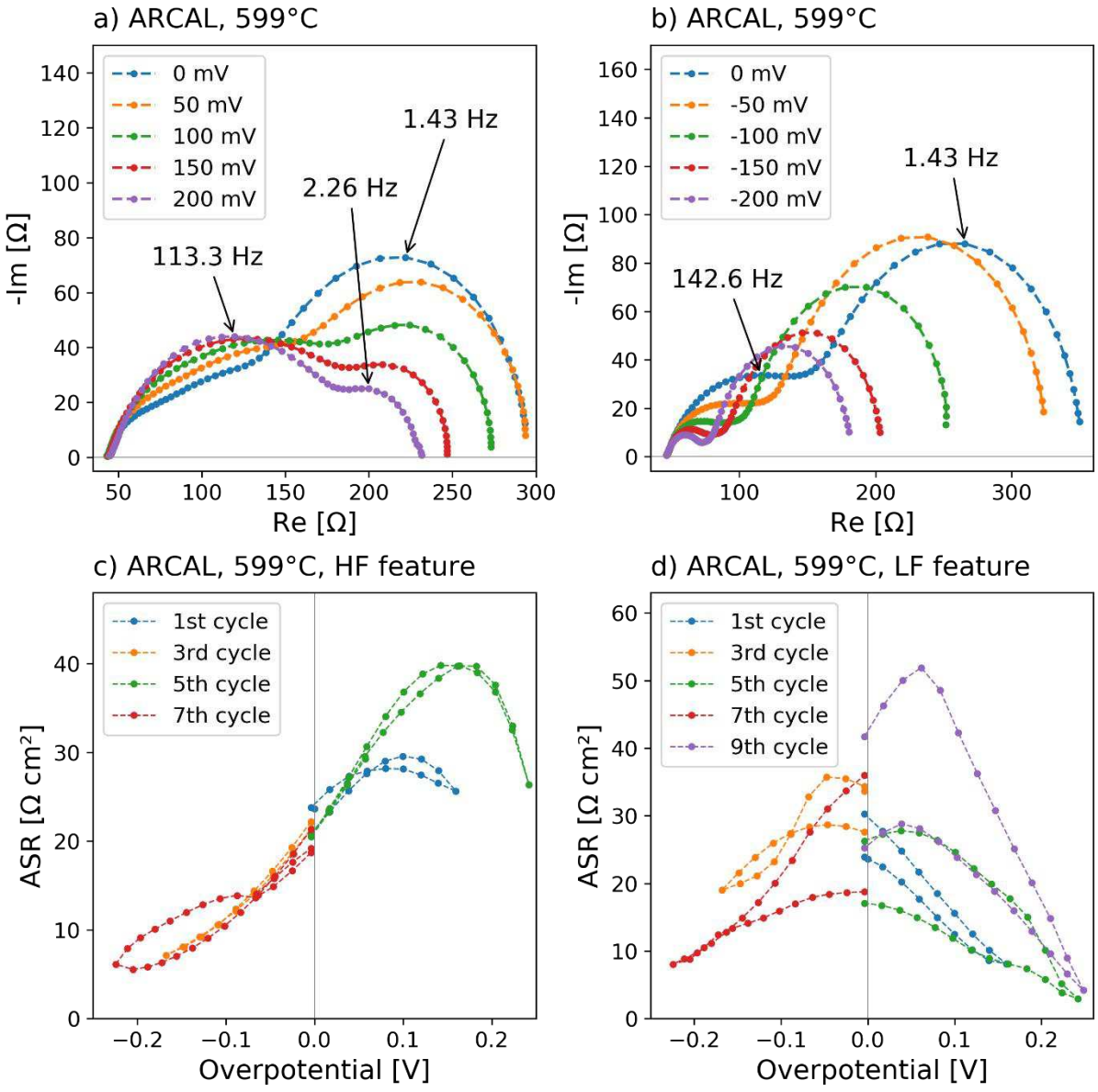

Figure 49: Nyquist plots of the sample with an NCFC electrode measured at 599°C with a different applied bias (a, b) and ASR over the overpotential of the HF feature (c) and the LF feature (d).

The impedance spectra recorded at around 600°C with different applied bias are shown in Figure 49 a) and b) and consist of two features, same as the spectra measured at different temperatures described in 5.1. The low frequency feature has already previously been identified as the electrode feature and decreases in size with increasing cathodic and increasing anodic bias. The high frequency feature of the spectra measured with negative bias decreases in size with more negative bias, the HF feature of the spectra recorded with positive applied bias does not change significantly in size but in shape, with a flatter shape at a low applied bias and a more semicircle like shape at a higher applied bias.

Figure 49 c) and d) display the ASR of the HF and LF feature plotted over the overpotential. It was obtained by fitting the spectra with an equivalent circuit consisting of two R, CPE parallel circuits and a resistor in series. The thin-film electrode overpotential was calculated by subtracting the ohmic electrolyte losses (I_{DC}*R_{YSZ}) from the applied bias. Kinetic losses of the counter electrode are negligible, due to the excellent kinetics. The ASR of the HF feature shows a tendency to higher values at more positive bias, however, at the higher measured applied bias values, the ASR decreases again. Moreover, the HF feature ASR of the cycles with down to -300 mV applied bias show a hysteresis, while the cycles with down to -200 mV bias yielded reproducible results when going down to -200 mV and up to 0 mV after. The ASR of the LF feature depicts variations over a rather big ASR range at the same measuring conditions, which makes interpretation hard. However, a trend to a lower ASR by applying cathodic or anodic bias can be observed.

In Figure 50 a) the capacitance of the HF feature, scaled to the volume, over the oxygen partial pressure is depicted. The thickness of the thin-film, needed to scale to the volume, was measured via a profiler and resulted in 130 nm on average. The effective oxygen partial pressure corresponding to the overpotential was calculated from the set hydrogen and water partial pressures of the gas atmosphere and the overpotential via the equilibrium shown in equation (25) and the Nernst equation, as follows.

$$E = E_0 + \frac{RT}{zF} \ln\left(\frac{a_{Ox}}{a_{Red}}\right) \qquad (28)$$

E denotes the electrode potential, E_0 the standard electrode potential, R the gas constant, T the temperature, z the number of electrons exchanged, F the Faraday constant and a_{Ox} and a_{Red} the activities of the redox pair involved. Due to the gaseous state of the reactants the activities could be simplified to the corresponding partial pressures. The capacitance of the HF feature increases with rising oxygen partial pressure. The different trend of the first cycle can be most likely ascribed to the rather poor fit due to the flattened semicircle shape of the features. The capacitance of the LF feature is substantially higher than that of the HF feature and shows a tendency to higher capacitance values at both more reducing and more oxidizing conditions coming from the starting point without applied bias. The increase at more reducing conditions can be explained by the higher number of oxygen vacancies in that conditions. For the increase in more oxidizing conditions no straightforward explanation can be given from the available data. Moreover, it can be noticed that the third cycle, which goes down to -200 mV applied bias, behaves reproducible, while the seventh cycle, going down to -300 mV, shows a hysteresis.

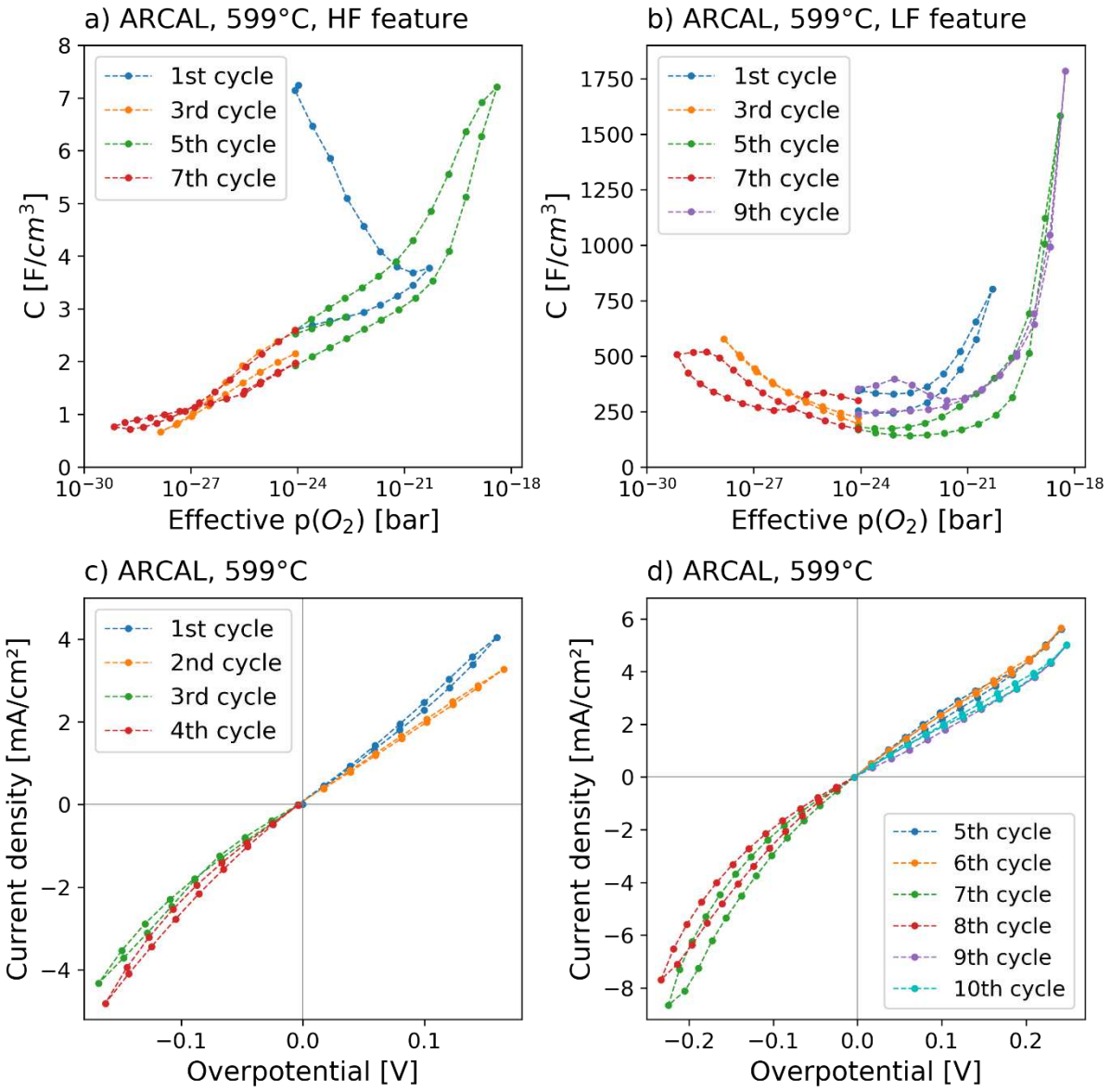

Figure 50: Capacitance of the NCFC electrode sample HF feature (a) and LF feature (b) plotted over the oxygen partial pressure and the current density over the overpotential (c, d).

The current density of the NCFC electrode plotted over the overpotential of the bias cycles with up to ±200 mV applied bias is displayed in Figure 50 c) and the current density of the cycles up to ±300 mV in d). The cycles in c) show rather reproducible results for the same conditions, indicating that no irreversible changes happen to the sample with a bias of ±200 mV applied. For the cycles with ±300 mV bias no significant deviation from reversible behavior can be observed either, and a jump in the anodic overpotential region, hinting to a possible exsolution of Fe or Co is also not visible. The current density at the same conditions seems to decrease with time, yielding lower current densities for later cycles, probably due to a slight degradation of the thin-film electrode.

5.2.2. NCF sample with current collector structured by ion-beam etching

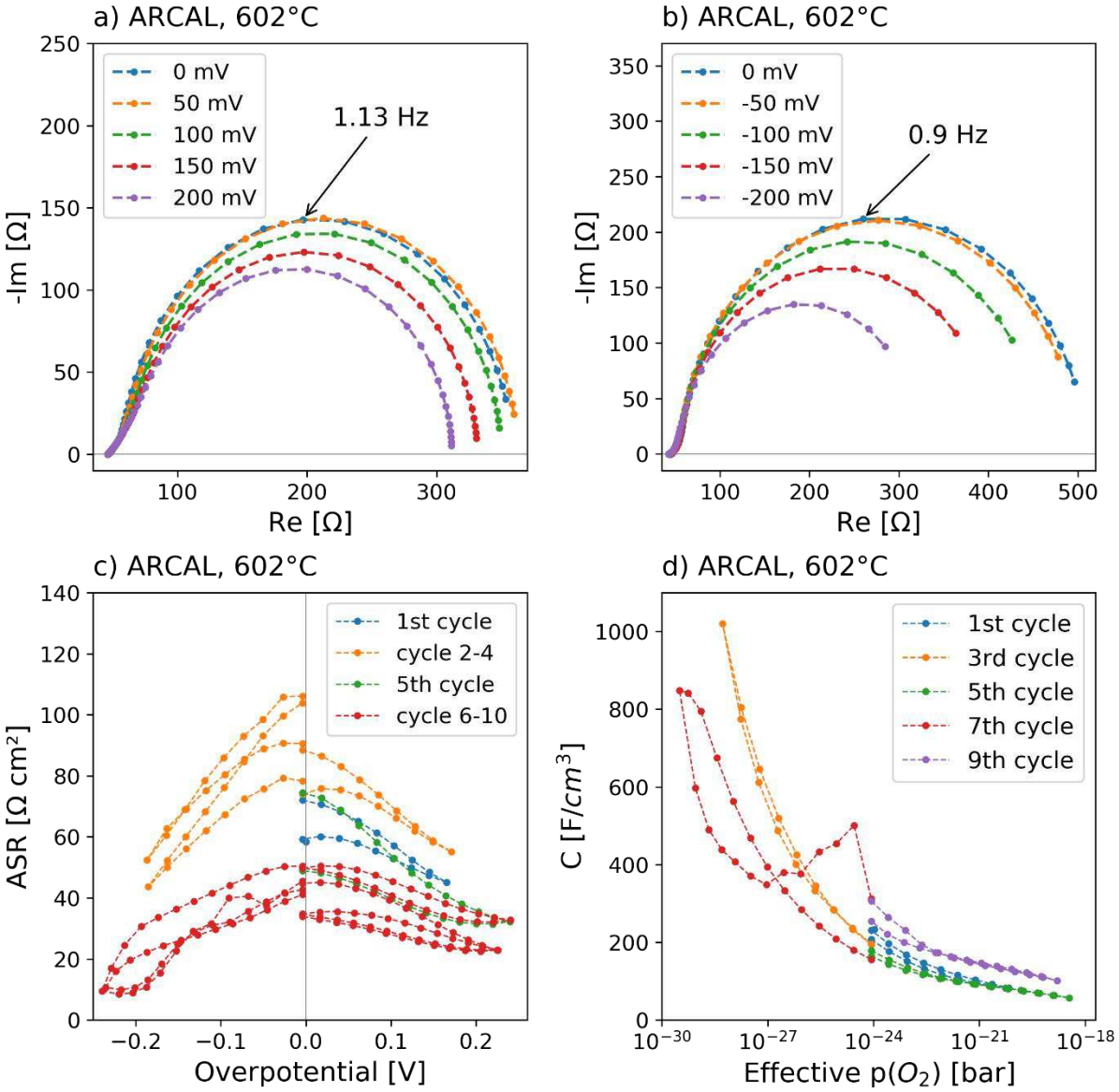

Figure 51: Nyquist plots of the sample with an NCF working-electrode measured at 602°C and positive (a) or negative applied bias (b), ASR plotted over the overpotential (c) and the capacitance over the oxygen partial pressure (d).

Figure 51 a) and b) depict the Nyquist plots of the NCF electrode samples with different applied bias. The spectra consist of one semicircle shaped feature attributable to the electrode that decreases in size going from no applied bias to either positive or negative applied bias. The ASR of the NCF electrode, visible in Figure 51 c), was obtained by fitting the electrode feature with an R, CPE parallel equivalent circuit and tends to decrease with negative and positive overpotential. Comparing the first cycle to the following cycles with up to ±200 mV applied bias, the ASR increases at the same conditions, probably due to degradation. The following cycles with up to ±300 mV though show a lower ASR, indicating a possible reactivation that counteracts the degradation due to the high applied bias. Overall,

the ASR of the NCF electrode depicts a similar tendency as the NCFC electrode with lift-off current collectors, except for slightly higher ASR values. Figure 51 d) displays the capacitance of the NCF electrode and in contrast to the NCFC electrode described in 5.2.1 it shows the expected trend to a higher capacitance at lower oxygen partial pressures due to the increased number of oxygen vacancies and Fe^{2+} ions in more reducing conditions. Furthermore, it is noticeable that the capacitance of the cycles up to ±200 mV behaves reversible with the same capacitance values when increasing and decreasing the applied bias, while the cycles to -300 mV, like cycle 7 in Figure 51 d), show a hysteresis. As the chemical capacitance is a bulk property, this indicates that not only the surface catalytic properties, but also the bulk defect chemistry is altered due to the high applied bias.

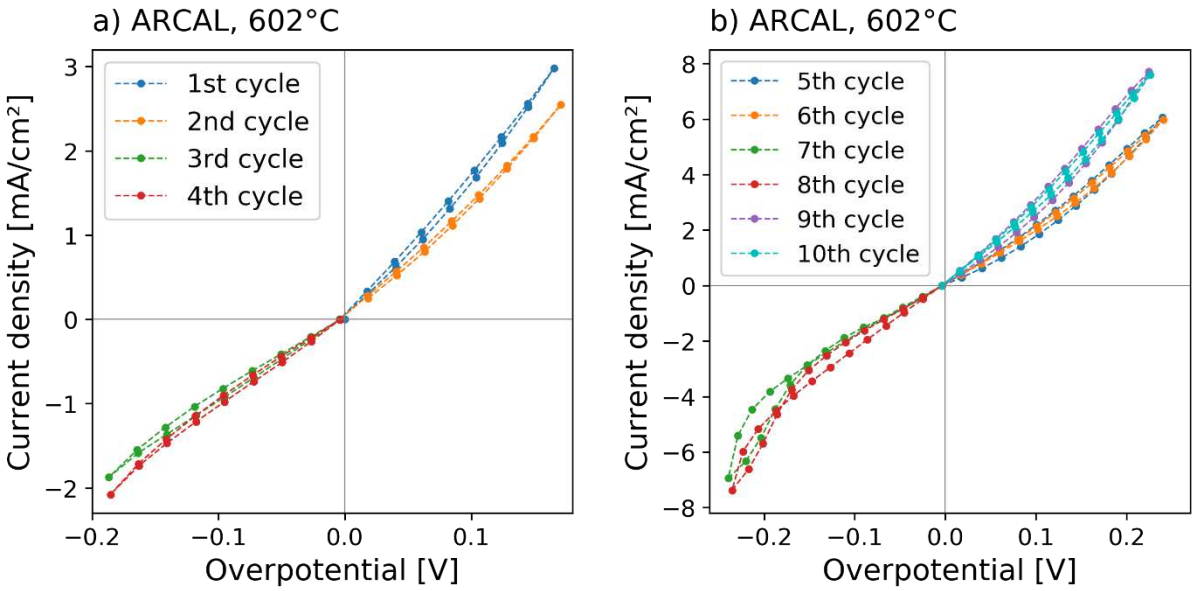

Figure 52: Current density of the NCF electrode plotted over the overpotential.

Figure 52 a) depicts the current density of the NCF electrode over the overpotential with up to ±200 mV applied bias and b) with up to ±300 mV. The cycles shown in a) behave rather reversible with a slight decrease in current density at later cycles with positive bias, most likely due to degradation of the sample. For the cycles in b) it can be noticed that the first two positive cycles behave very similar. The following cathodic ones show a hysteresis, as could also be observed for the capacitance of these cycles, and the last two anodic cycles behave again similar, but with a steeper slope than the cycles measured prior to the cathodic polarization. That hints towards a possible activation process happening in the cathodic regime, where the hysteresis is noticeable, which increases the performance of the electrode. An explanation for this behavior would be the formation of Fe exsolutions on the surface, a characteristic jump in the anodic part due to oxidation of these exsolutions cannot be observed though.

5.2.3. NCFC sample with current collector structured by ion-beam etching

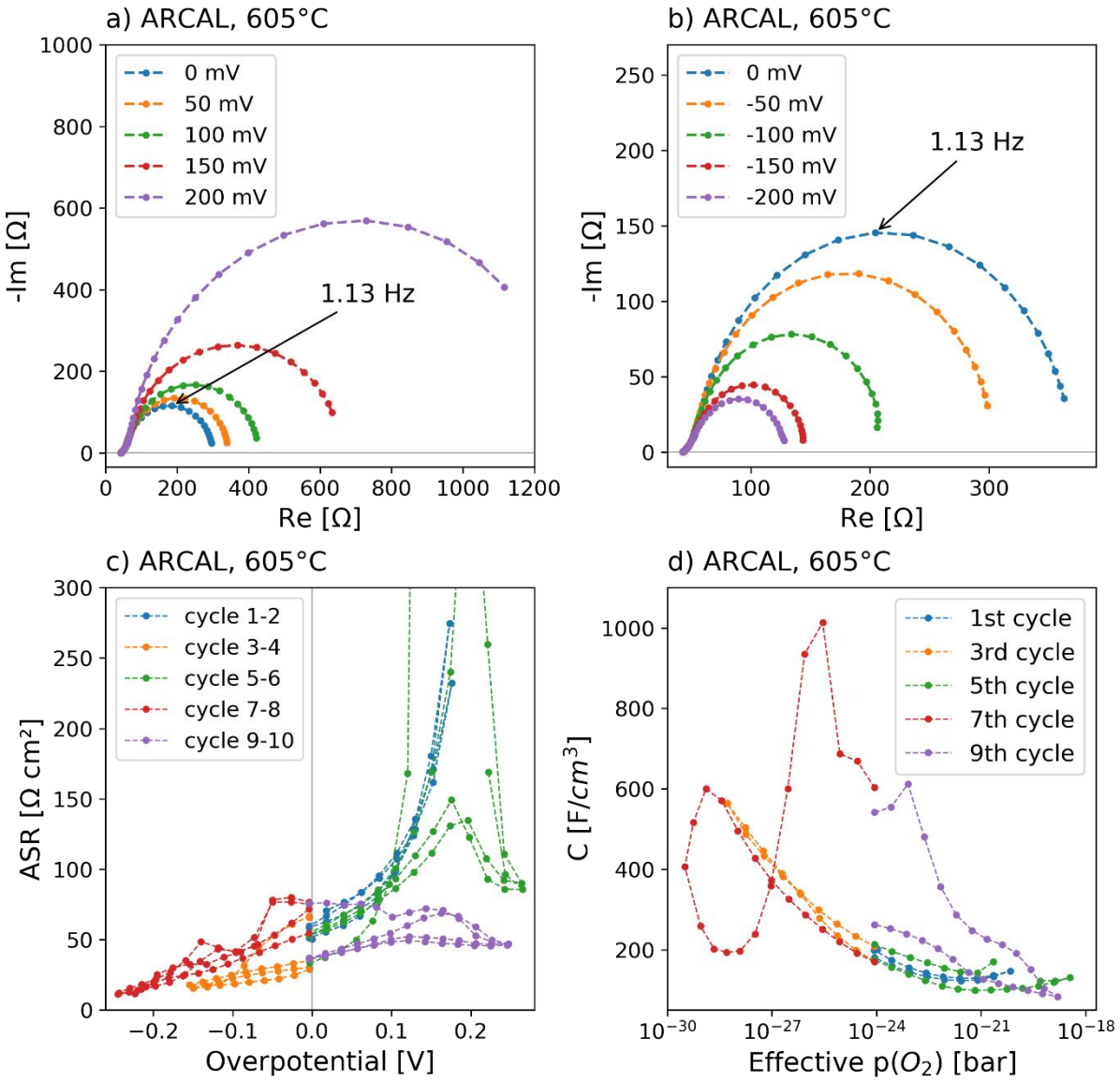

Figure 53: Impedance spectra of the NCFC electrode samples measured at 605°C with different applied bias (a, b), ASR of the bias cycles plotted over the overpotential (c) and the capacitance plotted over the oxygen partial pressure (d).

Because the first NCFC sample, displayed in 5.2.1, showed rather unexpected results like impedance spectra with two semicircle features instead of one, and the fact that manufacturing the grid current collector via lift-off lithography resulted in mediocre adhesion and many defects, which may be responsible for the second semicircle feature, another NCFC electrode sample with a grid current collector structured via lithography and ion-beam etching was measured.

Figure 53 a) and b) depict the Nyquist plots of the NCFC electrode sample with lithography and ion-beam etching structured current collector with different applied bias. In contrast to the NCFC sample with lift-off lithography current collector only one semicircle feature with

rather high capacitance is visible, so it can be ascribed to the electrode reaction. The peak frequency of this feature is similar to that measured on the lift-off NCFC electrode sample and the NCF sample. Furthermore, the size of the features decreases going from positive to negative applied bias. Contrary to the trend for the NCFC and NCF samples observed in 5.2.1 and 5.2.2, the ASR, as shown in Figure 53 c), does not decrease going from open circuit to negative and positive applied bias, but has a tendency to increase with more oxidizing bias and decrease with more reducing bias. It was obtained by fitting the electrode feature with an R, CPE parallel equivalent circuit. The cycles 1 to 4 with applied bias up to ±200 mV yielded reproducible results, with a slight shift to a lower ASR going from positive to negative applied bias. The ASR of the cycles 5 and 6 with positive applied bias up to +300 mV display a peak at around 0.18 V overpotential, the ASR of the next cycles with negative bias show results following the overall tendency to smaller ASR at more reducing bias and the last cycles with positive polarization depicted a rather constant ASR. In Figure 53 d) the behavior of the capacitance over the oxygen partial pressure can be observed. For the cycles with up to ±200 mV applied bias the same trend as for the NCF electrode with increasing chemical capacitance in more reducing conditions, due to a larger number of oxygen vacancies, can be observed. Starting with the first cycles with up to ±300 mV bias, an unexpected behavior of the capacitance, especially in the cathodic region, with a hysteresis can be recognized. The reason for this irregular behavior could be a structural change of the NCFC electrode like the exsolution of Fe or Co particles. Although this interpretation is rather speculative from the electrochemical measurements alone, it is in line with SEM images as well as ambient pressure XPS measurements that indicate the presence of metallic exsolutions as well and will be shown in the later chapters of this thesis.

The current density over the overpotential in Figure 54 a) behaves very reproducible, with significantly higher current densities with negative than with positive applied bias. . When the applied voltage is increased to ±300 mV, shown in Figure 54 b) it can be observed that the 5th cycle at first follows a steep curve and then at an overpotential of around 0.15 V a jump to a lower current density happens. At ~200 mV overpotential the current density rises again with the anodic overpotential, but at a lower slope than before the jump and similar to the slope of the first and second cycle. The next cycle follows the curve with the lower slope. The cathodic cycles afterwards show a hysteresis and the current density of the last two anodic cycles behaves like before the jump visible in the 5th cycle over the whole overpotential range. Figure 54 c) depicts the 5th cycle including the characteristic jump in higher resolution and d) displays the impedance spectra recorded during the jump. The drop in the current-voltage curve also means that the differential resistance, which is measured by EIS, should be negative. Indeed, the impedance spectra show an unusual negative real part at low frequencies, which can happen at non-stationary conditions. These findings can be most

likely explained by the exsolution of catalytically active Fe or Co particles onto the surface. The absence of hysteresis during the ± 200 mV cycles may be either due to the absence of exsolution particles the surface, or they remain in the metallic state. With the reducing bias they exsolve, leading to a higher absolute current density with negative applied bias. The shift from the higher slope curve to the lower slope curve through the jump at the next positive bias cycle can be explained as a jump from high to low activity of the electrode due to an oxidation of the exsolved particles. The oxygen partial pressure associated with Co oxidation is ~$2*10^{-21}$ bar, corresponding to 140 mV overpotential in the used H_2 + H_2O atmosphere, so the oxidation of Co particles likely appears in the corresponding conditions. The electrode stays in its low activity state for cycle 6, because no conditions reducing enough to go to high activity state were encountered during this cycle. The following cycles with cathodic bias reduce the oxidized exsolution particles again, which leads again to the current density following the high activity curve for the next two cycles with anodic bias. However, for these last two cycles no jump to the low activity state could be observed, probably due to kinetic limitations. Comparing the current density with that of the NCFC electrode described in 5.2.1, the results suggest that the NCFC electrode of the sample shown there was in its active state for the whole bias measurements conducted. A meaningful interpretation on why the jump and the following low activity state can be only observed once out of all the anodic bias cycles measured with NCFC electrode samples cannot be given from the available findings.

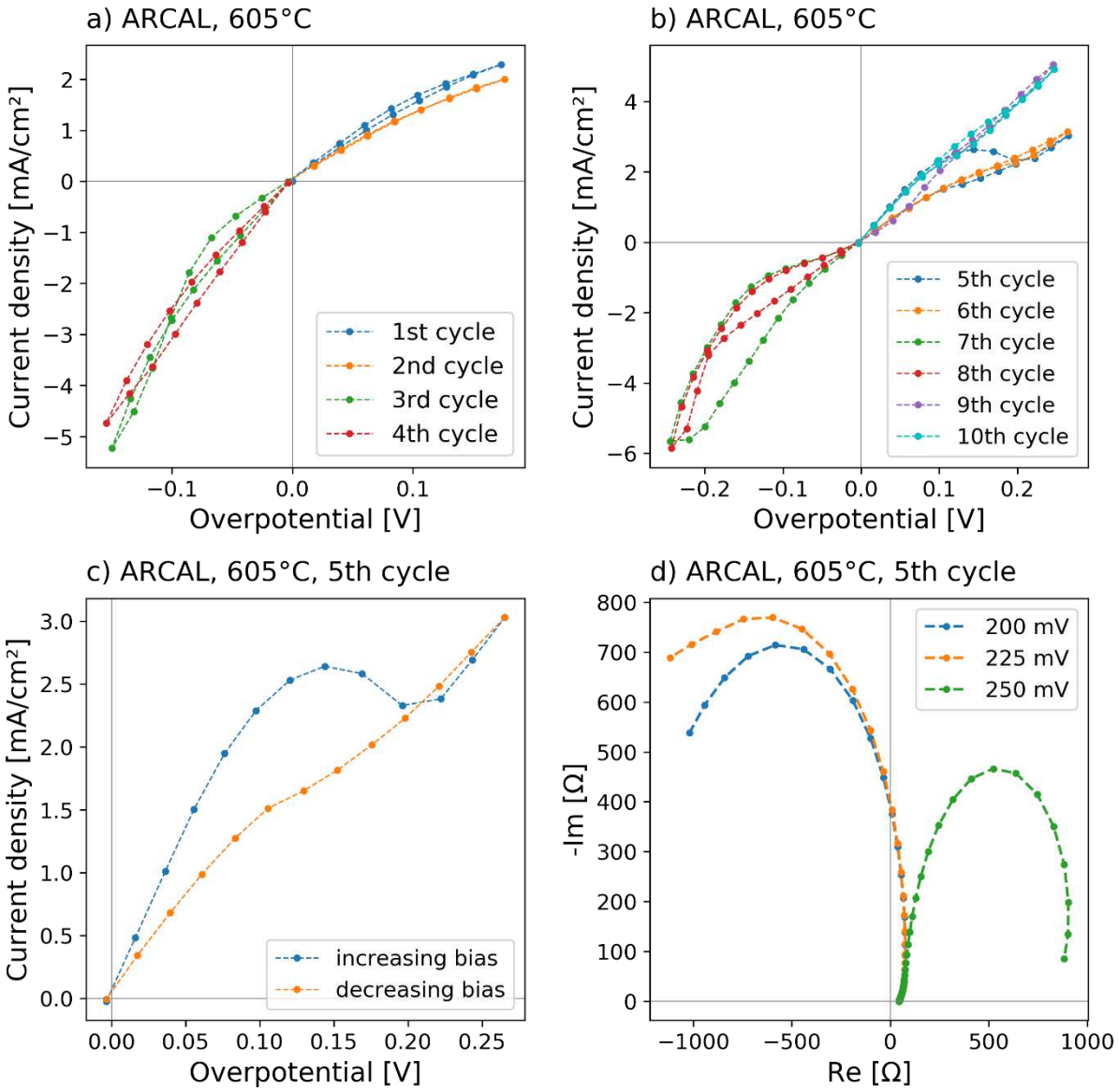

Figure 54: Current density of all measured cycles of the NCFC electrode sample over the overpotential (a, b), current density of the cycle indicating exsolutions over the overpotential (c) and impedance spectra of this cycle near the characteristic jump (d).

5.3. EIS of NFC electrodes in different reducing atmospheres

To investigate the behavior of the NFC thin-film electrodes at different oxygen partial pressures, EIS measurements were conducted on a pristine sample in different reducing atmospheres. The sample was one of the fracture parts of the same sample used in 5.2.2 and consisted of a single crystalline YSZ electrode with a GDC based three-layer counter electrode, a Ti/Pt grid current collector structured via lithography and ion-beam etching and a NCF thin-film working-electrode deposited via PLD. The measurements were carried out in the wing setup. The temperature was set to 600°C, the AC amplitude to 20 mV and data points were recorded from 0.1 to 900000 Hz with ten points per decade. To change the measuring atmosphere the MFC setup was applied. The variation in oxygen partial pressure

was achieved by either keeping the ARCAL and thus the hydrogen partial pressure constant and changing the water pressure, for the more reducing atmospheres, or by keeping the water partial pressure in the test tube constant and changing the hydrogen partial pressure, for the less reducing atmospheres. Impedance spectra were recorded in four cycles, first going from less reducing to more reducing atmospheres, next going from there to less reducing atmospheres and then repeating that procedure for the last two cycles.

Impedance spectra of the sample at different hydrogen to water ratios are shown in Figure 55 a). They consist of one semicircle feature, which was easy to fit with an R, CPE parallel circuit to obtain the ASR and the chemical capacitance of the electrode. The peak frequencies are in the same magnitude as observed for the bias measurements of another fracture part of the same sample in 5.2.2 and the shape of the electrode feature does not change over the whole measured oxygen partial pressure range. In Figure 55 b) the ASR of the electrode feature is plotted over the oxygen partial pressure. It can be observed that the ASR slightly decreases from the first to the second data point in cycle 1 and then increases for the rest of the cycle. In cycle 2 it decreases minimally at first and then suddenly increases at a high rate going to less reducing atmospheres. The ASR of cycle 3 and 4 behaves similar, but with a substantially higher absolute value. The increase at more reducing conditions was unexpected, because in previous measurements the opposite trend could be observed, which can be explained by a faster electrode reaction due to a higher number of hydrogen molecules that can react and more defects that act as reaction sites. That unexpected trend and the fact that the ASR at the same conditions increases a lot from cycle to cycle can be linked to a high degradation of the electrode. Furthermore, not only the resulting oxygen partial pressure, but also the water and hydrogen partial pressures seem to impact the behavior of the NFC electrode, because at the point where the oxygen partial pressure adjustment was changed from keeping the water pressure constant to keeping the hydrogen pressure constant a significant change in the behavior of the ASR can be observed. Figure 55 c) depicts the chemical capacitance of the electrode over the oxygen partial pressure, which increases with decreasing oxygen partial pressures, as expected due to the higher number of oxygen vacancies present in more reducing atmospheres. There is also a slight degradation with time noticeable, however, by far less than for the ASR.

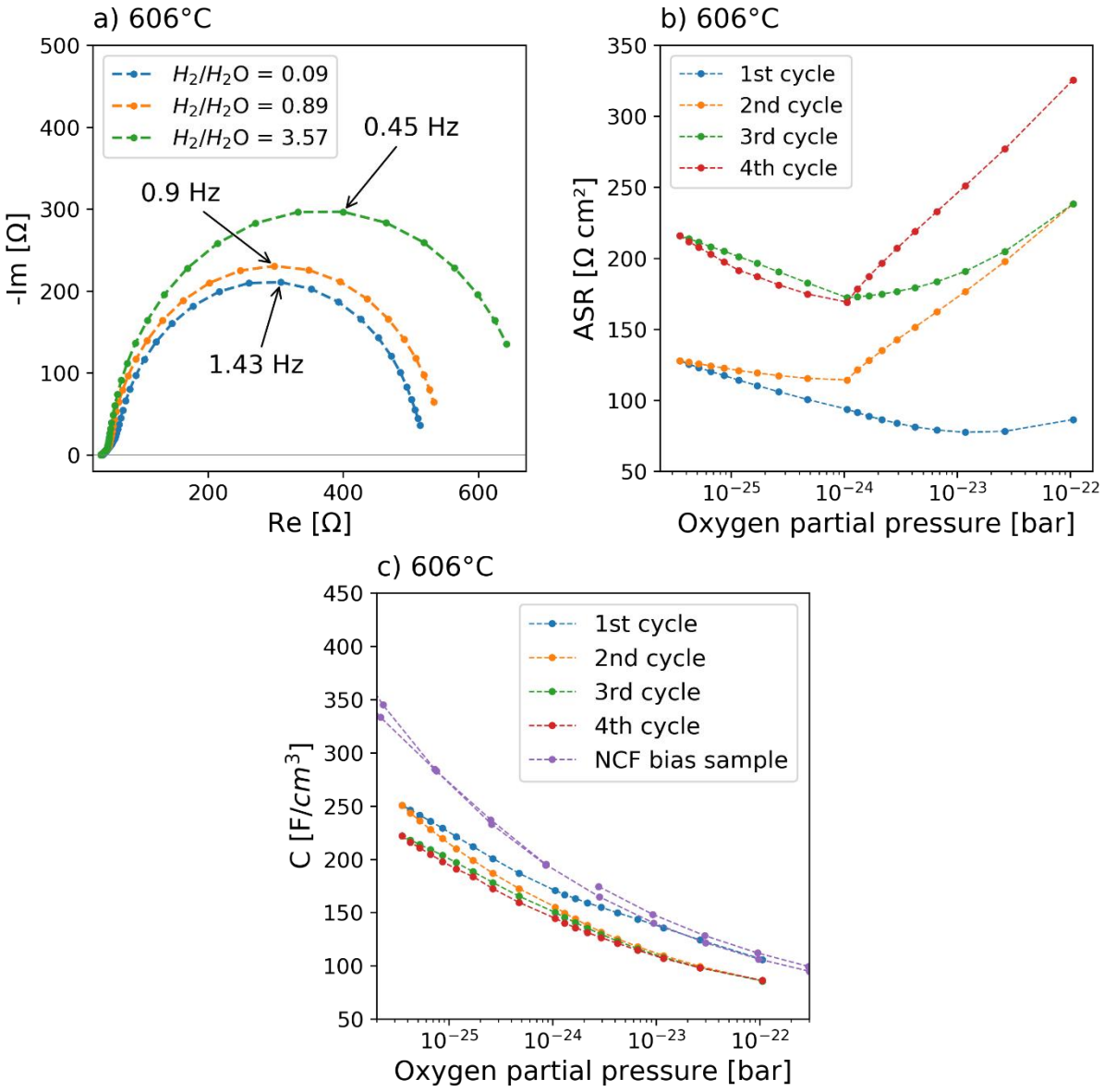

Figure 55: Nyquist plots of a sample with NCF electrode measured at 606°C in different reducing atmospheres (a), ASR of the electrode over the oxygen partial pressure (b) and the capacitance over the oxygen partial pressure (c).

Moreover, the capacitance values fit quite well with the ones of the NCF sample measured with applied bias, indicating that it does not matter for the chemical capacitance if the polarization of the electrode is achieved by a change in atmosphere or by an applied bias, which was already previously described for LSF thin-films by Schmid et al[83]. The absolute values for the chemical capacitance of NCF and NCFC seem to be slightly smaller, though in the same order of magnitude, compared to that of LSF.

Because of the high degradation encountered and thus subpar interpretability of these results, no measurements with NCFC electrodes at different oxygen partial pressures, which were achieved by a change in atmosphere were conducted in the wing setup.

5.4. Degradation and bias measurements of NCF and NCFC electrodes

To investigate if the origin of the high degradation is the electrode material or eventual impurities in the measurement setup, degradation measurements followed by bias cycles were carried out in two different measuring setups, the wing setup and the micro/macro setup.

5.4.1. Degradation and bias measurements in the wing setup

At first impedance spectra of the samples (approximately 5 mm x 5 mm x 0.5 mm), consisting of a single crystalline YSZ electrolyte, a three-layer counter electrode, a Ti/Pt grid current collector structured by lithography and ion-beam etching and either an NCFC or NCF electrode deposited via PLD were recorded in intervals of a few minutes for several hours to analyze the degradation behavior at stationary conditions. The temperature was kept at around 600°C and the atmosphere was humidified ARCAL with a hydrogen to water ratio of 1:1. The AC amplitude was set to 20 mV and the frequency ranged from 0.1 to 900000 Hz with ten data points per decade. For the bias measurements, a modified test protocol was used, in which each bias set point was applied for only 30 seconds, and only the DC component of the (incomplete) impedance spectra was evaluated. The protocol, abbreviated as “ExPo” cycles, is as follows: The measurements with applied bias were performed next with the same settings and in the same atmosphere, but at a temperature of approximately 625°C. Instead of the sweeping bias cycles from previous measurements, this time the applied bias was first increased from 0 mV to 400 mV and reduced again to 0 mV. Afterwards, it was reduced to -25 mV and then increased to 0 mV. Next another full anodic cycle, up to 400 mV and down to 0 mV, was measured and then a cathodic cycle, down to -50 mV and up to 0 mV. The cycles were continued in this pattern with a decreasing negative bias each cycle until -400 mV were reached and full anodic bias every cycle. The datapoints were measured in 25 mV steps. The aim of this cycle structure was to determine the negative bias needed to form exsolution particles, by identifying the first anodic cycle where a characteristic jump, indicating oxidation of the exsolved particles, occurs. For the sample with an NCFC electrode another open circuit degradation cycle was measured after the bias cycles to investigate the impact of the bias cycles on the ASR.

Figure 56 a) and b) show the impedance spectra of the degradation measurements for NCF and NCFC electrodes. They consist of one dominant feature, clearly attributable to the electrode due to very similar size and peak frequencies as observed for the previous measurements conducted on the NCF and NCFC electrodes. Moreover, a degradation is noticeable for both NCF and NCFC electrodes because the size of the semicircle features increases with time. The ASR of the electrodes, as depicted in Figure 56 c) and d) and obtained by fitting the semicircle features with an R, CPE equivalent parallel circuit,

increases significantly with time. For the NCF electrode the degradation is highest at the start and the curve then flattens steadily. The ASR of the NCFC electrode in comparison shows a similar trend with a less steady behavior, degrading at a constant high rate at first and then switching to a constant lower rate. Overall, for both electrode materials a degradation of a factor 3 or more can be observed, which also explains the very high degradation of the NCF electrodes measured in different reducing atmospheres previously. However, the degradation cycle of the NCFC electrode after the bias measurements shows an at first decreasing and then pretty much constant ASR of around 30 Ωcm^2 and thus at a similar level as observed at the start of the first degradation cycle and significantly lower than at the start of the bias measurements.

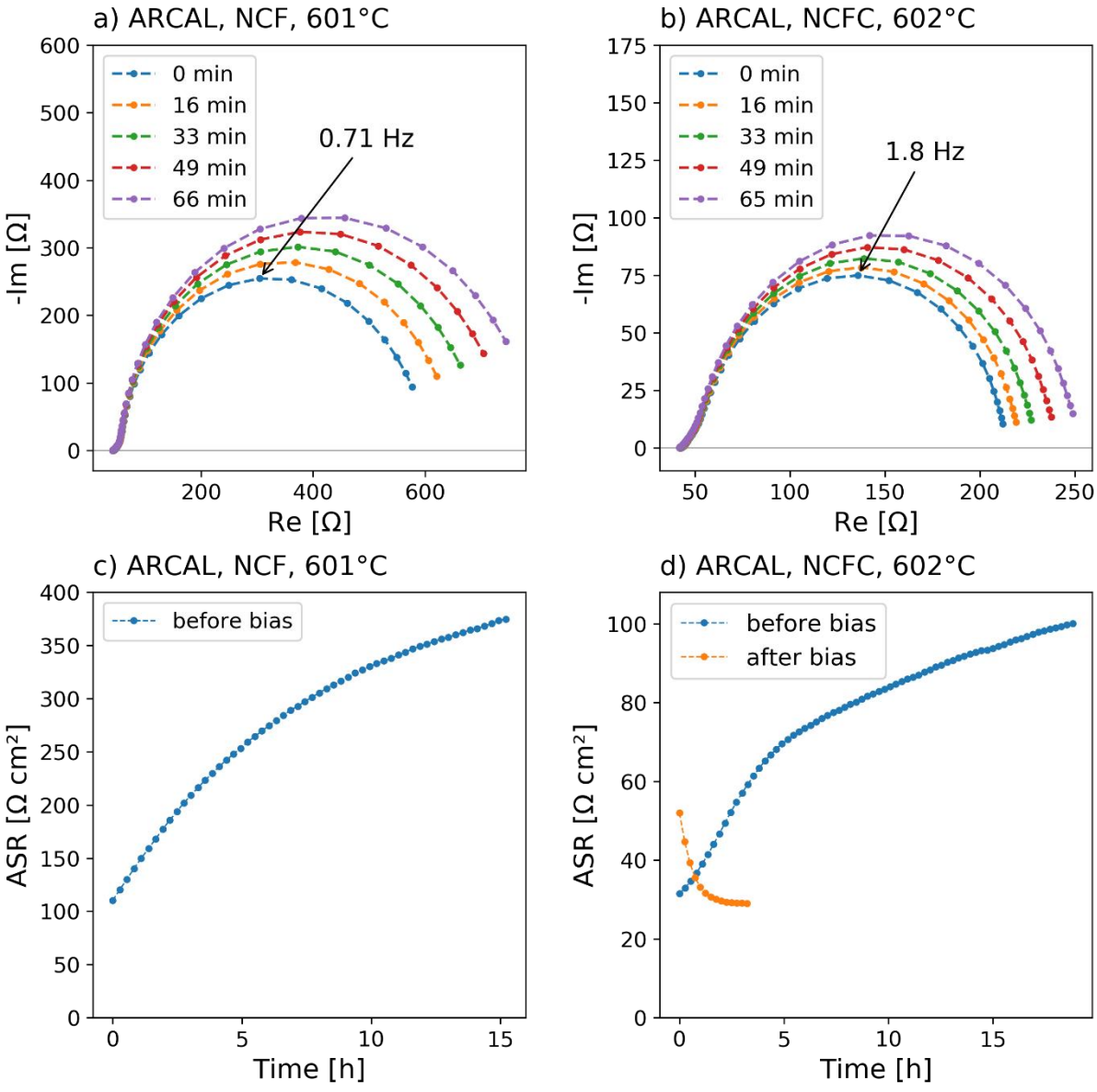

Figure 56: Nyquist plots of the degradation measurements with NCF (a) and NCFC (b) electrodes, ASR of the electrode features of the NCF (c) and NCFC (d) electrodes plotted over the time.

For the NCF electrode no degradation cycle after the bias cycles was measured, but for the last few bias steps full impedance spectra were recorded and the ASR at open circuit was 36 Ωcm^2. That substantial decrease in ASR after the bias measurements of the NCF and the NCFC electrodes indicates some form of reactivation of the electrodes, most likely due to the exsolution of catalytically active metal particles during the bias cycles. Furthermore, the ASR seems to be rather constant after an initial drop following the bias measurements, which could mean that the surface with the exsolved particles is less prone to degradation.

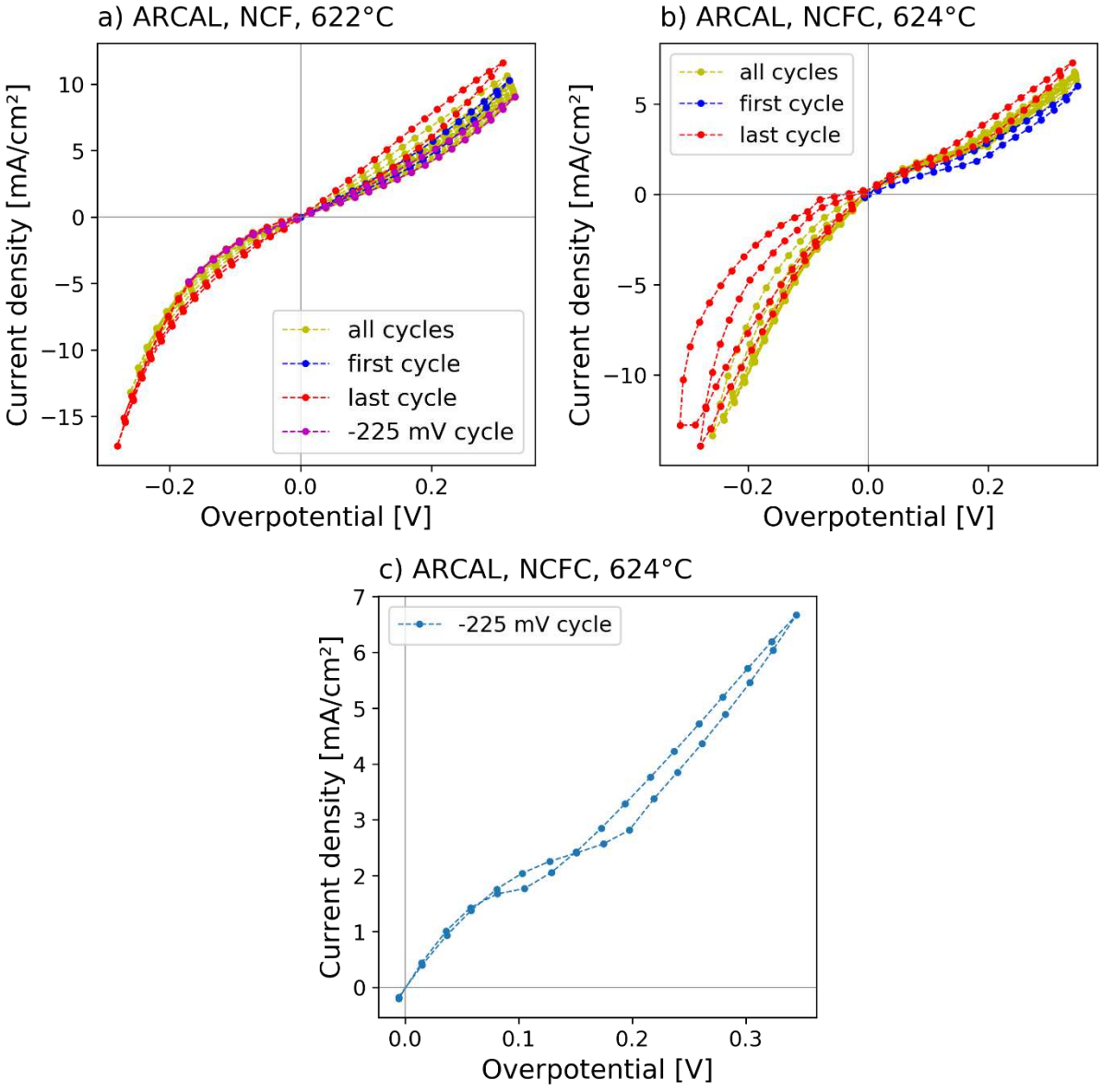

Figure 57: Current density over the overpotential of the NCF (a) and NCFC (b, c) electrode samples measured in humidified ARCAL.

Figure 57 a) depicts the bias cycles of the NCF electrode sample. They seem to be rather reversible with only minor changes in current density from cycle to cycle. A jump indicating the oxidation of exsolved particles cannot be observed. The anodic cycles at first slightly

decrease in current density from cycle to cycle, before hitting a minimum at the -225 mV cycle. Afterwards, it increases reaching the maximum at the last cycle. That behavior indicates that the electrode degrades at first until a process reactivating the electrode occurs after the cathodic cycle down to -225 mV. That could be the exsolution of Fe particles or another structural change of the surface. The further increase of the current density up to the last cycle supports the assumption of exsolutions, due to more exsolved particles resulting in better electrode performance. The current density of the NCFC electrode sample, displayed in Figure 57 b) and c), shows an increasing trend in the anodic region from cycle to cycle right from the start. Based on the assumption of exsolutions causing the increase, that would mean that the humidified ARCAL atmosphere is already reducing enough to exsolve particles or to change the structure of the surface favorably. For the cathodic cycles with higher absolute overpotential a strong hysteresis can be noticed. A clear jump indicating exsolved particles cannot be observed, however, nearly all the anodic cycles follow the trend depicted in Figure 57 c) with a slight kink followed by a small overpotential range with less current density slope at approximately the same overpotential where the jump of the NCFC sample described in 5.2.3 occurred.

5.4.2. Degradation and bias measurements in the micro/macro setup

For the degradation and bias measurements in the micro/macro setup samples consisting of a single crystalline YSZ electrolyte, a three-layer counter electrode, a Ti/Pt grid current collector structured by lithography and ion-beam etching and a PLD deposited NCF or NCFC thin-film electrode were used. The measurements were performed in humidified ARCAL atmosphere with a hydrogen to water ratio of 1:1 and an AC amplitude of 10 mV at around 625°C.

Table 3: Bias cycles of the NCF and NCFC electrode samples measured in the micro/macro setup.

Cycle	Step size	Bias cycle range
1	25 mV	0 mV to 200 mV to 0 mV
2	25 mV	0 mV to -200 mV to 0 mV
3	25 mV	0 mV to 200 mV to 0 mV
4	25 mV	0 mV to -200 mV to 0 mV
5	25 mV	0 mV to 300 mV to 0 mV
6	25 mV	0 mV to -300 mV to 0 mV
7	25 mV	0 mV to 300 mV to 0 mV

8	25 mV	0 mV to -300 mV to 0 mV
9	25 mV	0 mV to 300 mV to 0 mV
10	25 mV	0 mV to -300 mV to 0 mV

The frequency ranged from 0.1 to 900000 Hz with five data points per decade. For the degradation measurements before and after the bias cycles impedance spectra were recorded in intervals of a few minutes over several hours and the bias cycles are displayed in Table 3. For the bias cycles only a very narrow frequency range was measured and hence no full impedance spectra were recorded.

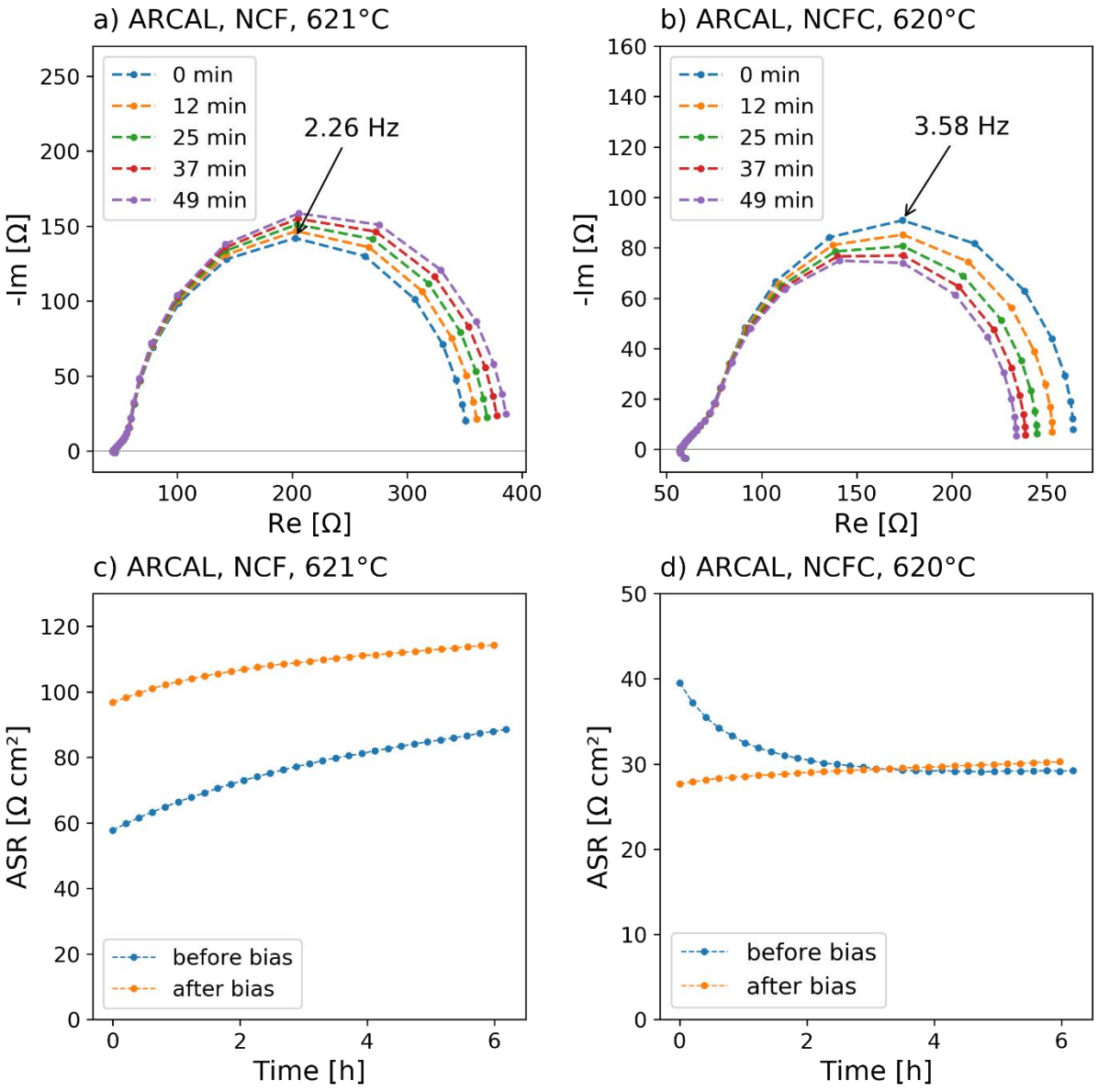

Figure 58: Nyquist plots of the degradation measurements conducted on the NCF (a) and NCFC (b) electrode samples and ASR of the electrode features over the degradation time (c, d).

Figure 58 a) and b) depict the impedance spectra of the NCF and NCFC electrode samples for the degradation measurements before applied bias cycles, which consist of one semicircle feature attributable to the electrode process. A degradation in form of a size increase of the feature is visible for the NCF electrode sample, for the NCFC sample the size of the features seems to decrease with time though. The ASR was obtained by fitting the electrode features with an equivalent circuit consisting of an R, CPE parallel circuit and a series resistor to account for the offset resistance and is displayed in Figure 58 c) and d). The degradation of the NCF sample before the bias cycles is substantially lower than it was in the wing setup, indicating that impurities originating from the wing setup caused the previously noticeable immense degradation. A reactivation of the electrode causing the ASR to drop again after the bias cycles cannot be observed for the NCF electrode. The ASR of the NCFC electrode drops right from the start to approximately 30 Ωcm^2 and stays there at a rather constant level until after the bias cycles with only minimal degradation being noticeable, which suggests that the reactivation process, probably caused by a surface structure change, already happened during heating up in the humidified ARCAL atmosphere. This drop to approximately 30 Ωcm^2 could also be noticed in the wing setup for the NCFC electrode. Overall, a drop of the ASR to a mostly constant level, while exposed to a reducing atmosphere and applied bias, could be observed for two out of three NCF and two out of three NCFC electrode samples. On all these samples bias measurements were conducted prior to degradation measurements.

Figure 59 a) shows the current density over the overpotential of the NCF sample. It behaves totally reversible over all measured bias cycles. A jump in the anodic region indicating exsolutions cannot be noticed and the absolute values of the current density are smaller than observed for the previous measurements of NCF electrode samples, which could be attributable to thin-film thickness and composition inhomogeneities. Also, the NCFC electrode sample, which is displayed in Figure 59 b) and c) and was measured only around 30 s for each bias data point, shows a reproducible behavior over all cycles and the full overpotential range. However, for these cycles the characteristic jump, which starts at an overpotential of around 0.1 V, is clearly noticeable. For the cycles with an applied bias up to ±200 mV a decrease in current density occurs beyond about 0.1 V overpotential. That decrease is fully reversible when decreasing the overpotential again, indicating that the oxidation process of the exsolution particles causing the jump was still ongoing. The cycles with up to ±300 mV applied bias depict a very clear jump in the anodic region, attributable to the oxidation of exsolved particles on the surface. This jump is not fully reversible when decreasing the applied bias again because the return to the original current density curve happens at a lower overpotential than the initial jump. That phenomenon can be explained by the oxidized exsolution particles being already thermodynamically unstable but still kinetically

hindered, eventually due to interactions of the particles with the host perovskite, which shifts the return to the original curve to a lower anodic overpotential, than thermodynamically needed. To reproduce the characteristic jump and gain further insight into the behavior of the ASR and chemical capacitance during the jump, a new fracture part of the same NCFC sample was measured at the exact same conditions, but instead of only measuring a few frequency points to obtain current and voltage for approximately 30 s, full impedance spectra were recorded with each applied bias. However, for these measurements the jump was not noticeable, indicating that either thin-film inhomogeneities or more likely time dependent effects play a huge role for the occurrence of the characteristic jump.

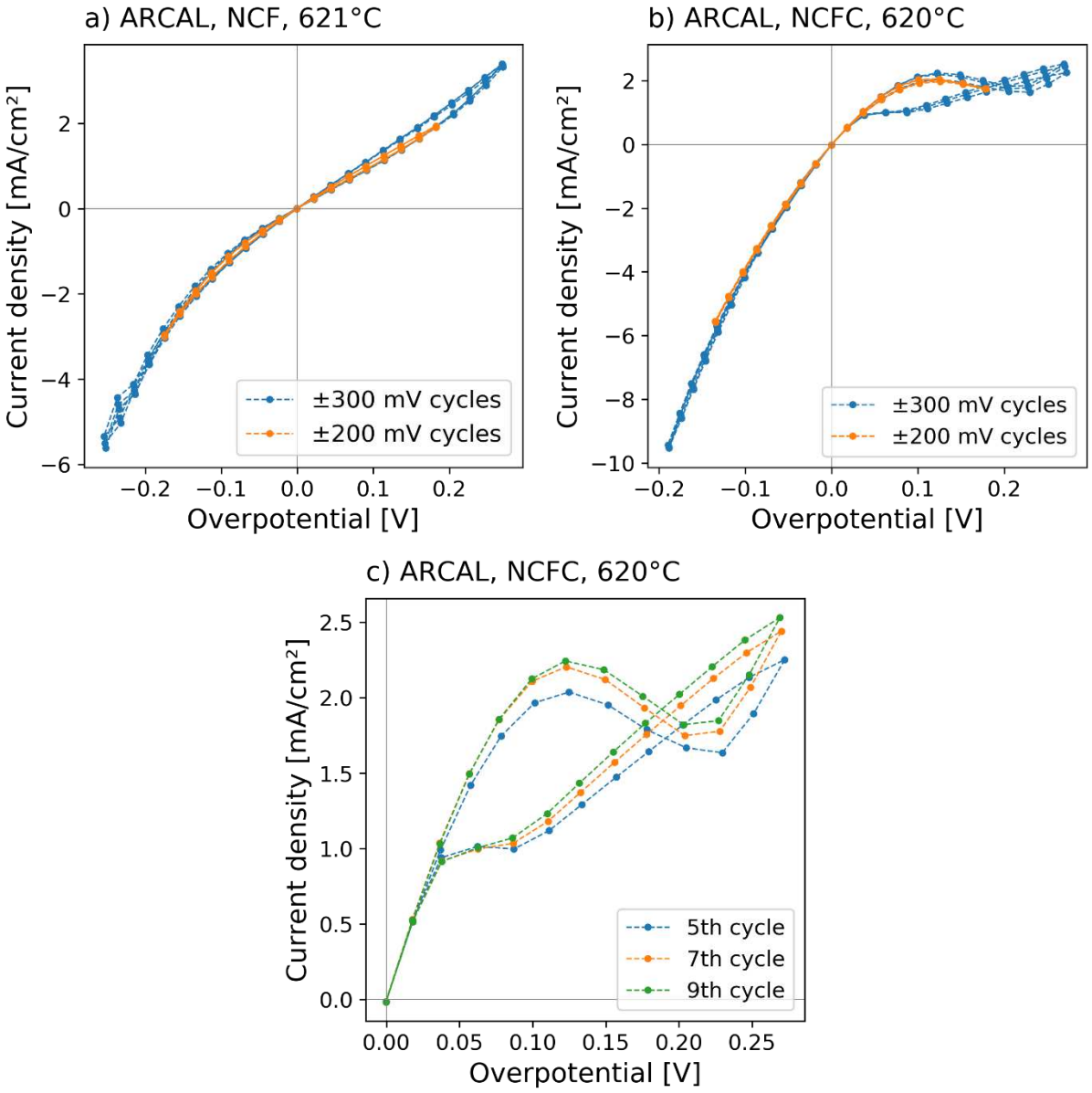

Figure 59: Current density plotted over the overpotential of the NCF sample (a) and the NCFC sample (b, c), measured in humidified ARCAL atmosphere.

5.5. Summary of the results from the bias measurements

A variety of testing protocols for NCF and NCFC electrodes in two different measurement setups was used to identify the electrochemical conditions in which exsolutions appear or become re-oxidized. Overall, the phenomenon is complex, and the sample characteristics depend not only on the testing conditions, but also bias history, measurement setup and measurement time per bias setpoint.

Regarding the comparison of both setups, we found much more severe degradation in the wing setup, compared to the micro/macro setup, which is most likely due to impurities coming from the used materials in the setup. Also, ion beam etching lithography was proven to be the better preparation technique of the current collectors. The most pronounced indication for reversible exsolution and oxidation of particles was found for fast voltage sweeping rates (30 seconds per setpoint) on NCFC films in the micro/macro setup. The tentative explanation for this is as follows:

Co-ions in NCFC are easier to reduce to metallic state, compared to Fe. Therefore, the Co-doping should enable metallic exsolutions in less reducing conditions, compared to NCF. In opposite to Fe, Co metal is thermodynamically stable in a 1:1 H_2 + H_2O atmosphere, so if exsolutions are present at the surface, they will be in the active metallic state at open circuit conditions. Only with application of anodic bias, Co becomes oxidized. The oxygen chemical potential at the Co/CoO equilibrium corresponds to an overpotential of +140 mV in the given atmospheric conditions – at this point, also the jump was observed.

The higher hysteresis for faster sweeping speeds is linked to the reaction kinetics of the surface modifications. Moreover, the fact that hysteresis is already observed on the first positive bias branch indicates that Co containing exsolutions are already present at OCV conditions and do not require application of cathodic bias. These findings are also in line with SEM imaging and XPS measurements that both show the presence of exsolutions already at OCV conditions.

5.6. In-plane EIS measurements of NCF and NCFC thin-films

After thorough characterization of the ASR in various atmospheres and bias conditions, measurements focusing on the electron and ion conductivity of these materials were performed. For this, in-plane EIS measurements were performed on samples consisting of a single crystalline MgO substrate, an interdigitating finger current collector made of Ti/Pt and structured by lithography and ion-beam etching, and a PLD deposited NCF or NCFC thin-film. At first in-plane measurements in the micro setup, due to the easy contacting of the contact pads with the Pt needles controlled via piezo motors, were carried out to qualitatively analyze if the EIS measurements of different finger geometries yield sound and reproducible

results. An imagine of the different finger geometries numbered from one to six is shown in Figure 60. Each sample accommodated every finger geometry three times with 0.5 mm distance and three times with 1 mm distance between the contact pads. The exact dimensions of the different finger structures are displayed in Table 4.

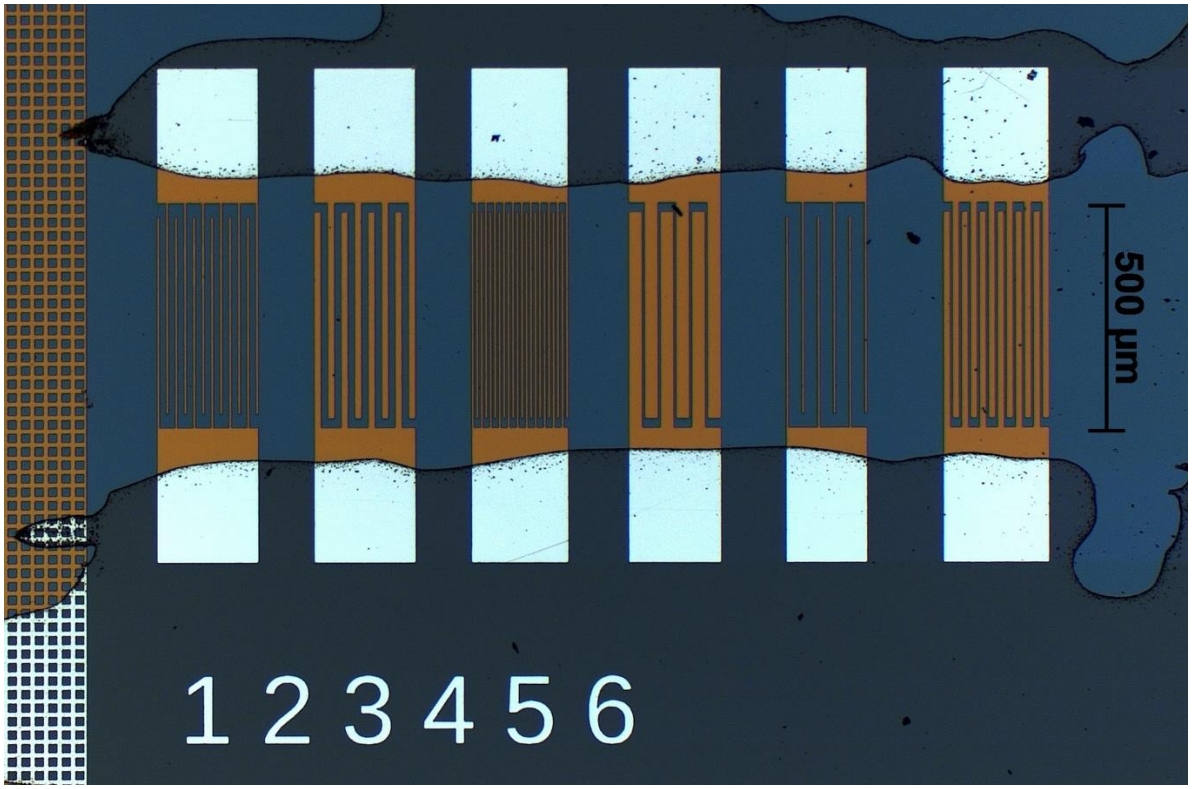

Figure 60: Different geometries of interdigitating finger structure electrodes.

Table 4: Exact dimensions of the different finger geometries with either 0.5 mm or 1 mm distance between the contacting pads.

Finger-system	Finger distance [µm]	Finger width [µm]	Finger length [µm]	Number of fingers	Meander length [µm]
1, 0.5 mm	15	5	470	12	5395
2, 0.5 mm	15	15	480	8	3585
3, 0.5 mm	5	5	480	22	10295
4, 0.5 mm	5	30	480	6	2605
5, 0.5 mm	30	5	470	6	2530
6, 0.5 mm	5	15	480	12	5515
1, 1 mm	15	5	970	12	10895

2, 1 mm	15	15	980	8	7085
3, 1 mm	5	5	980	22	20795
4, 1 mm	5	30	980	6	5105
5, 1 mm	30	5	970	6	5030
6, 1 mm	5	15	980	12	11015

After the measurements in the micro setup, pristine samples for in-plane measurements of NCF and NCFC thin-films were measured in the micro/macro setup at a wide range of reducing and oxidizing atmospheres to analyze the behavior of ionic and electronic conductivity of the thin-films at different oxygen partial pressures.

5.6.1. In-plane measurements in the micro setup

The EIS measurements on the NCF and NCFC electrode samples with MgO substrates in the micro setup were performed in humidified ARCAL with a hydrogen to water ratio of 1:1 at a temperature of approximately 600°C. The data points were recorded over a frequency range from 0.05 to 900000 Hz with ten points per decade and an AC amplitude of 10 mV. The measurements were carried out on microelectrodes with different finger structure geometries and dimensions. Representative impedance spectra of the NCF thin-film sample are shown in Figure 61 a) and b). The individual spectra are labeled with a number indicating the geometry followed by a letter, which simply indicates that for example 5A and 5B are different electrodes with the same geometry on the same sample. The number following an underline displays the order of the measurements, if more than one was performed on the same microelectrode. The length at the end indicates the distance between the two contact pads. In Figure 61 a) all shown spectra are results from measurements of the same finger electrode geometry. It is noticeable that there is a considerable difference in the offset resistance, even between 5A_3 and 5A_5, which were results from the same microelectrode with 5A_2 being measured approximately half an hour later than 5A_1. Moreover, the shape of the semicircle features differs and even shows loops, which could be caused by a displacement current to close-by metallic parts, as reported from Lee et.al.[92] These findings indicate that the temperature is most likely not stable during the measurements, due to the bottom heater and the fact that even contacting with the Pt needles resulted in a small temperature change of the sample. The impedance spectra of the finger geometry 1, displayed in Figure 61 b), consist of rather ideal semicircle features. Furthermore, the spectra of the microelectrode with 1 mm distance between the contact pads shows an offset resistance approximately half the size as the electrode with 0.5 mm distance, as expected because of the larger area of the film-thin cross-section. The NCFC thin-film shows a similar

offset as the NCF thin-film for the same finger geometry. However, as depicted in Figure 61 c), the semicircle feature is significantly smaller and deviates a lot from the ideal semicircle shape. Also, artifact features attributable to non-stationary conditions can be noticed.

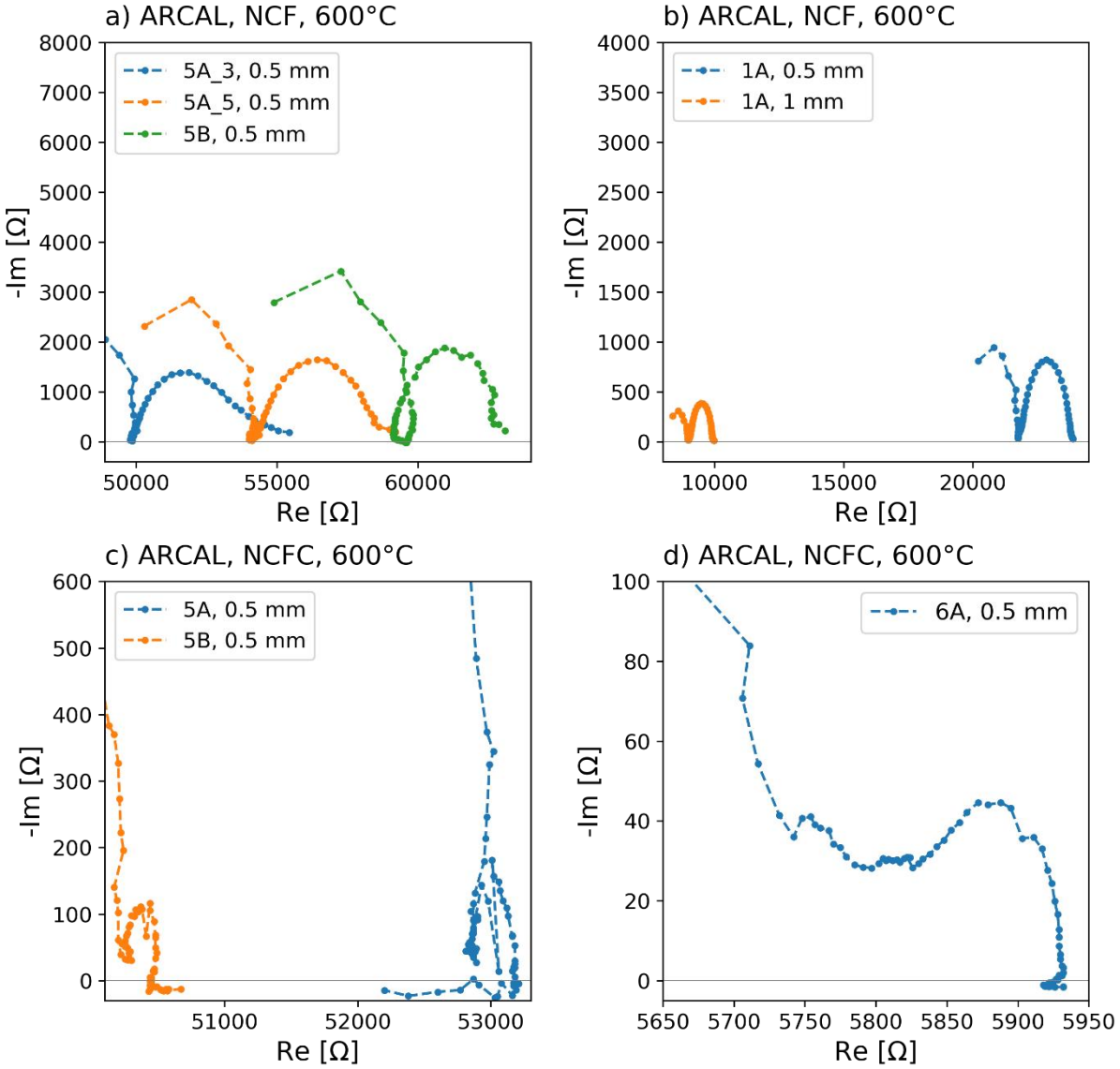

Figure 61: Representative impedance spectra of the in plane measurements of NCF (a, b) and NCFC (c, d) electrode samples at 600°C in humidified ARCAL.

To investigate electronic and ionic conductivity of the thin-films, the geometry normalized high frequency intercept resistance was estimated as $1/\sigma_{total}$, and the geometry normalized low frequency intercept as $1/\sigma_{eon}$. σ_{total} and σ_{eon} denote the total and electronic conductivity. Normalization was done with respect to finger distance (d) meander length (l) and film thickness (t) according to the following equation:

$$\rho = R * \frac{l * t}{d} \qquad (29)$$

The intercept resistances were obtained by fitting the semicircle features with an R, CPE parallel circuit for the NCF sample and by estimating it manually for the NCFC sample due to the strong deviation from the perfect semicircle shape. The results for the electronic and ionic conductivity of the NCF thin-film are displayed in Table 5 and the ones for the NCFC thin-film in Table 6.

Table 5: Conductivity of the NCF thin-film calculated from different finger electrode geometries.

Geometry	σ_{total} [mS/cm]	σ_{eon} [mS/cm]	σ_{ion} [mS/cm]
5A_1, 0.5 mm	15,92	14,64	1,27
5A_2, 0.5 mm	15,93	14,63	1,30
5A_3, 0.5 mm	20,95	19,59	1,35
5A_4, 0.5 mm	19,88	18,53	1,35
5A_5, 0.5 mm	19,25	17,90	1,35
5B, 0.5 mm	17,74	16,60	1,14
3A, 0.5 mm	17,84	16,88	0,96
2A, 0.5 mm	14,37	13,36	1,01
1A, 0.5 mm	17,46	16,23	1,23
1B, 0.5 mm	11,32	10,39	0,92
5A, 1 mm	12,55	11,24	1,31
1A, 1 mm	13,56	12,37	1,19
Mean value	**16,40**	**15,20**	**1,20**
Standard deviation	**3,00**	**2,93**	**0,16**

Table 6: Conductivity of the NCFC thin-film calculated from different finger electrode geometries.

Geometry	σ_{total} [mS/cm]	σ_{eon} [mS/cm]	σ_{ion} [mS/cm]
6A, 0.5 mm	11,96	11,74	0,22
5A, 0.5 mm	17,07	16,94	0,12
1A, 0.5 mm	16,95	16,73	0,22
1B, 0.5 mm	16,99	16,78	0,21

5B, 0.5 mm	17,95	17,85	0,09
2A, 0.5 mm	16,99	16,79	0,20
5C, 0.5 mm	9,09	9,04	0,05
6A, 1 mm	11,97	11,71	0,26
5A, 1 mm	16,57	16,45	0,12
3A, 1 mm	38,79	38,41	0,38
2A, 1 mm	15,46	15,22	0,23
1A, 1 mm	15,22	15,06	0,16
2B, 1 mm	15,45	15,24	0,21
1B, 1 mm	15,91	15,72	0,19
6B, 1 mm	12,55	12,02	0,53
2C, 1 mm	15,51	15,15	0,36
1C, 1 mm	15,89	15,64	0,26
Mean value	**16,49**	**16,26**	**0,23**
Standard deviation	**6,21**	**6,18**	**0,12**

The total and the electronic conductivity of the NCF and NCFC thin-films are very similar, the ionic conductivity seems to be significantly smaller for the NCFC sample. The standard deviations of the NCF sample are smaller because multiple measurements of the same electrode were included, and they do not deviate as much from each other in general as different microelectrodes. That does not have a huge impact on the conclusions though, since these measurements were mainly conducted to get qualitative results and it can be observed, that although the results for different geometries differ from each other, they are in the same order of magnitude and all geometries seem to yield reasonable results.

5.6.2. In-plane measurements in the micro/macro setup

After verifying that current collector geometry variations yield consistent results in terms of ion and electron conductivity, more detailed measurements were conducted in the micro/macro setup, which is less prone to artifacts and allows variation of H_2 and H_2O partial pressures. The impedance spectra of the in-plane measurements in the micro/macro setup were recorded in a range from 0.05 to 900000 Hz with ten points per decade and an AC amplitude of 10 mV at a temperature of 628°C. Different finger structure geometries of NCF

and NCFC thin-films were investigated in reducing and oxidizing atmospheres with several cycles from oxidizing to more reducing conditions and vice versa. These atmospheres were achieved by mixing the right amounts of oxygen nitrogen and ARCAL and then controlling the part of the gas mixture that should go through the humidifier to get to the desired oxygen partial pressure with a specifically for this task designed MFC setup. Figure 62 depicts representative impedance spectra for the measurements in oxidizing and reducing atmospheres. In oxidizing atmospheres only an ohmic resistance in the order of tens of ohms was observed instead of a semicircle. This is indicative for much higher electron conductivity in oxidizing conditions. The spectra in reducing atmospheres displayed a semicircle most of the time, sometimes a very clear one, as shown in Figure 62 b), and sometimes only a shoulder hinting to the semicircle shape. In contrast to the measurements in the micro setup by far less features hinting to non-stationary conditions could be observed.Figure 62: Representative impedance spectra for the in-plane measurements of NCF and NCFC samples in oxidizing (a) and reducing (b) atmospheres.

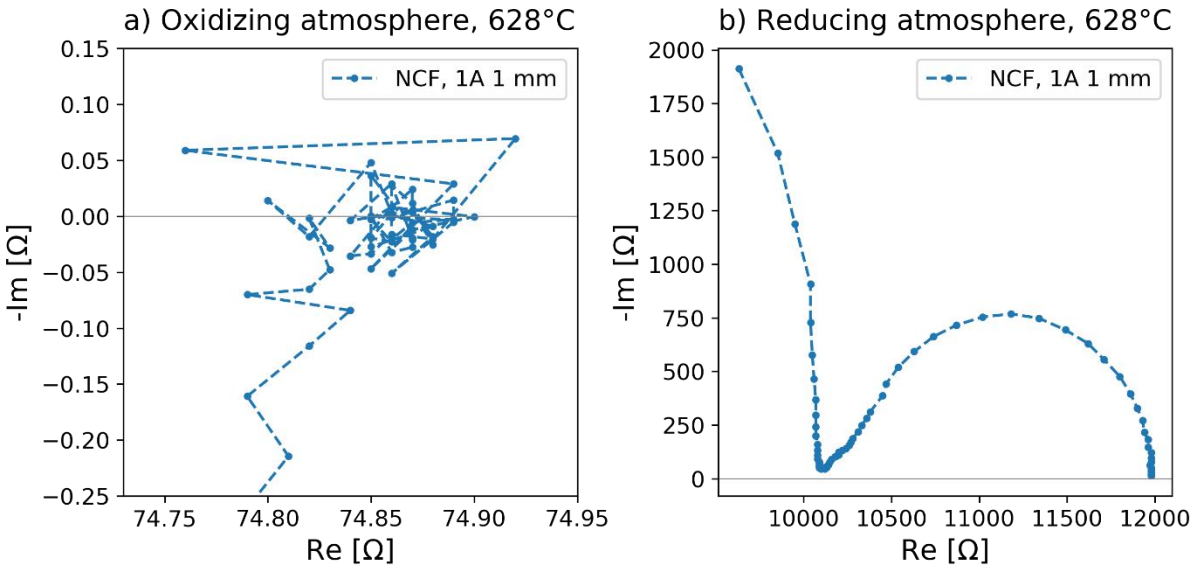

Figure 62: Representative impedance spectra for the in-plane measurements of NCF and NCFC samples in oxidizing (a) and reducing (b) atmospheres.

In Figure 63 the electronic and ionic conductivity, which were obtained by estimating the low frequency intercept on the x-axis as $1/\sigma_{eon}$ and the high frequency intercept as $1/\sigma_{total}$, allowing to calculate the ionic conductivity, are displayed for the more oxidizing and more reducing measured oxygen partial pressure range. Because no semicircle feature could be observed for the measurements in the oxidizing atmospheres, the ionic conductivity for these oxygen partial pressures could not be calculated. Moreover, the contacting resistance and the resistance associated with electron conduction within the finger-type current collectors may be much larger than the effect of the NCF/NCFC layer. Therefore, the calculated

conductivities are probably underestimated. This is most likely also the reason for the strong geometry dependence of the calculated conductivity. The electronic conductivities obtained in the oxidizing atmospheres are very high in comparison to the ones in reducing atmospheres and are rather constant in all measured oxidizing atmospheres. In the reducing atmospheres the NCF thin-film shows a higher electronic conductivity than the NCFC thin-film with a trend to a higher electronic conductivity in more reducing conditions, that can be explained by more electronic defects occurring in more reducing atmospheres. However, the electronic conductivity scales with $p(O_2)^{-0.17}$ and not $p(O_2)^{-0.25}$, which would be expected according to the defect chemistry.

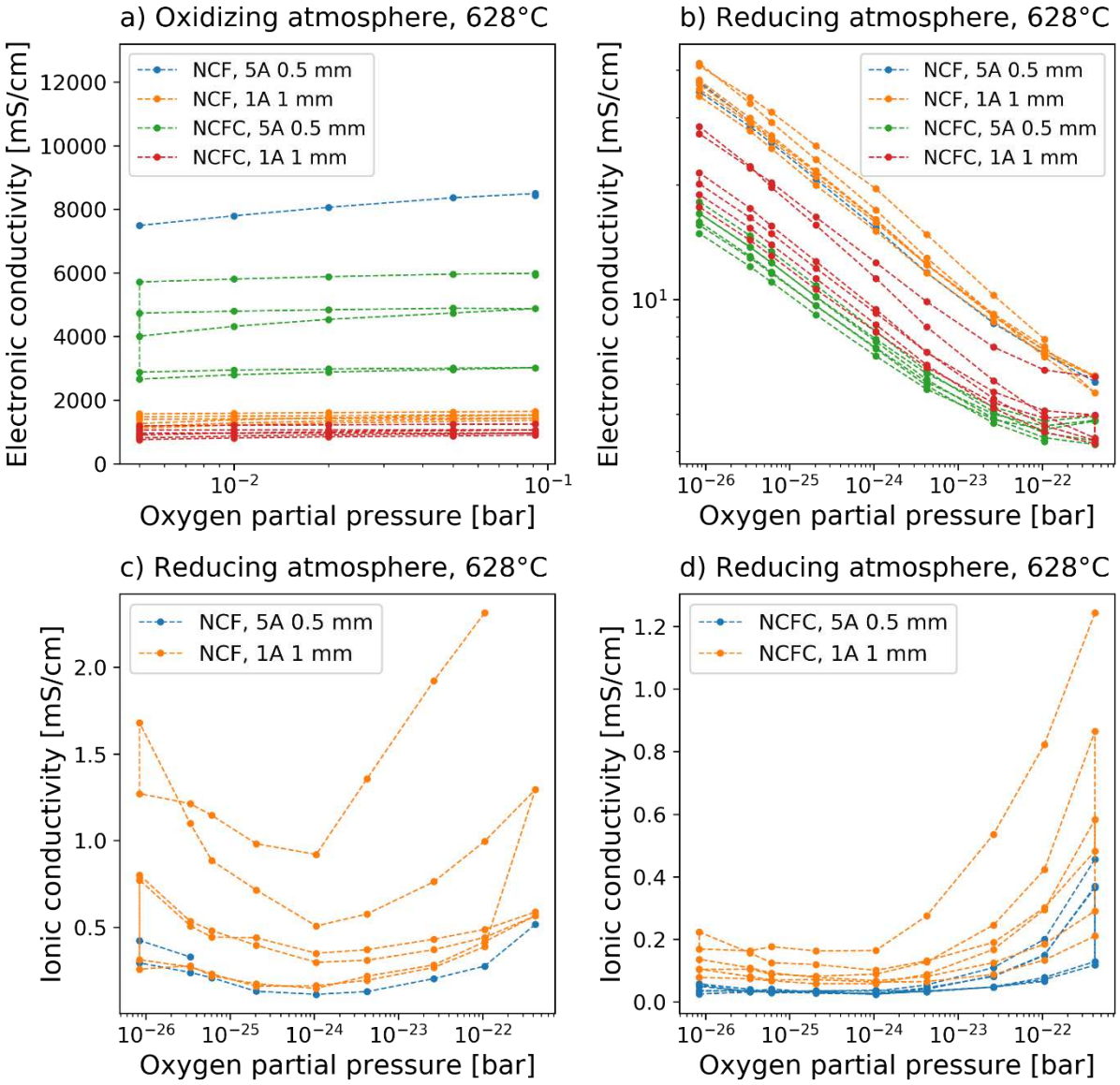

Figure 63: Electronic conductivity of the different electrode geometries of NCF and NCFC thin-films over the oxygen partial pressure in oxidizing (a) and reducing (b) atmospheres and ionic conductivity over oxygen partial pressure in reducing atmospheres (c, d).

In comparison to the measurements in the micro setup the electronic conductivity of the NCF samples is very similar with 15.40 mS/cm at the same oxygen partial pressure of approximately 10^{-24} bar while the electronic conductivity of the NCFC sample is lower with 7.88 mS/cm. The geometry does not seem to have a huge impact. Moreover, the electrode geometry 1A of the NCF and NCFC thin-films was measured before the 5A geometry and shows a higher electronic conductivity for the first cycles and a very similar one for the last cycles, indicating some form of degradation.

The ionic conductivity of the NCF thin-film in reducing atmospheres is higher than the one of the NCFC thin-film and the values are within the same order of magnitude as observed for the measurements in the micro setup. Furthermore, a degradation from the earlier measured 1A geometry to the later measured 5A geometry is clearly noticeable. A distinct tendency over the oxygen partial pressure cannot be observed. The ionic conductivity seems to increase in both more reducing and more oxidizing directions coming from an oxygen partial pressure of 10^{-24} bar, with a steeper increase to more oxidizing conditions. This trend is unexpected because the higher number of oxygen vacancies should theoretically lead to an increase in ionic conductivity in more reducing atmospheres. However, the minimum at approximately 10^{-24} bar oxygen partial pressure also marks the point where the method of adjusting the oxygen partial pressure to the desired value was changed from keeping the water partial pressure constant to keeping the hydrogen partial pressure constant. This indicates that not only the oxygen partial pressure but also the water and hydrogen partial pressures affect the behavior of the NCF and NCFC thin-films.

In summary, the electronic and ionic conductivities of NCF and NCFC behave qualitatively as expected and results gained in the micro and micro/macro setup are comparable: in oxidizing conditions, the electronic conductivity is quite high, due to electron holes that compensate the acceptor doping. Exact values can, however, not be given due to the strong contribution of the contacting resistance. In reducing conditions, the electron conductivities of NCF and NCFC are relatively similar, although both exhibit significant degradation during the time of the measurement (approx. 40 hours). The ion conductivity of NCF is much higher than that of NCFC, and an unexpected U-shaped curve with higher conductivities in H_2 and H_2O rich atmospheres is observed.

5.7. In-plane and electrochemical EIS measurements of NCF and NCFC electrode samples analyzed with a transmission line fit

The results explained in the following part were obtained from in-plane and electrochemical measurements of samples consisting of a single crystalline YSZ electrolyte, a three-layer GDC based counter electrode, a Ti/Pt finger structure current collector structured by

lithography and ion beam etching (equal to that used on the MgO substrates) and a PLD deposited thin-film electrode made of either NCF or NCFC. Impedance spectra were recorded in cycles at different oxidizing and reducing atmospheres achieved by the MFC setup with a flow of approximately 100 sccm in the micro/macro setup at 629°C. The samples were contacted with two needles on the contact pads of the finger structure electrodes and with a Pt mesh on the counter electrode. A software-controlled switch box allowed to switch from in-plane measuring mode to electrochemical mode without the need to open the test rod in between. The measurements were conducted in a frequency range from 0.05 to 900000 Hz with an AC amplitude of 10 mV. In contrast to the previous in-plane measurements the ionic and electronic conductivity were not only estimated by analyzing the intercepts on the x-axis, but also by a transmission line fit, as explained in 2.2, which considers the impedance spectra of the in-plane and electrochemical measurements with the same set of parameters leading to credible results if a good fit can be achieved. This was done by using the open source matlab code "Zfit[93]" with minor modifications, to allow simultaneous fitting of two spectra.

Figure 64 shows the impedance spectra and the real and imaginary part plotted over the frequency of the finger electrode 1A, 0.5 mm of the NCF sample measured in reducing atmosphere. The spectra for the in-plane measurements consist of a semicircle feature with an approximate 45° increase at high frequencies, the one of the electrochemical measurements of an elongated semicircle feature. Moreover, the data points of the transmission line fit are displayed and show a good match with the experimental data. The spectra of the measurements in oxidizing atmospheres are not shown, because the in-plane ones did not depict a semicircle feature and for the electrochemical measurements only a small part of a very big semicircle feature, which could not be fitted well, was noticeable. Consequently, a fit with the transmission line equivalent circuit was not possible. In addition to the transmission line fit and to validate these results the ASR and chemical capacitance of the electrochemical measurements in reducing atmospheres were obtained by fitting the features with two R, CPE parallel equivalent circuits, and normalizing the resistance to the electrode area. Transmission line fitting results are distinguished by using the addition "fit" for the corresponding curves in the figures.

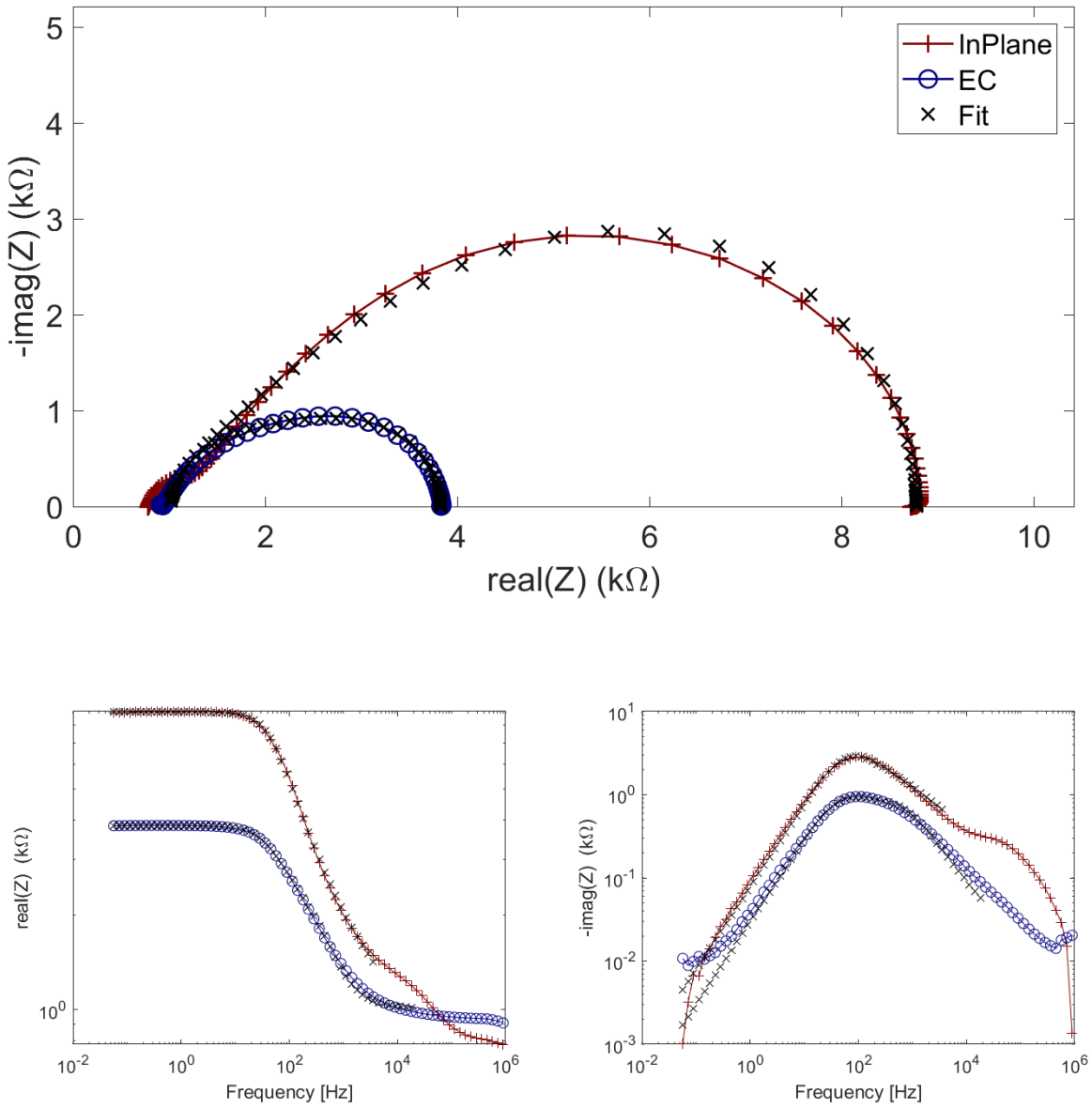

Figure 64: Representative impedance spectra of the in-plane and electrochemical (EC) measurements of the NCF and NCFC electrode samples, here NCF with finger geometry 1, 0.5 mm measured at a hydrogen to water ratio of 1:1.

In Figure 65 a) the electronic conductivity of the NCF and NCFC thin-films is displayed. It stays constant over the oxidizing oxygen partial pressure range and the values for different geometries deviate a lot from each other. However, the values are very similar to the ones of the in-plane measurements with MgO substrates and it can be observed that the finger geometry seems to have a bigger impact than the thin-film material variation of NCF and NCFC. In reducing atmosphere, as shown in Figure 65 b), the electronic conductivity increases for both NCF and NCFC thin-films with decreasing oxygen partial pressure, as expected due to more electronic defects in more reducing atmospheres. For the values obtained by analyzing the x-axis intercepts no difference between NCF and NCFC thin-film can be observed. The values obtained by the transmission line fit though show a slightly

smaller electronic conductivity of NCFC than that of NCF, the same trend as observed for the previous measurements of the thin-films on MgO substrates with overall very similar values, indicating good reproducibility. In general, the electronic conductivity values from the fit are marginally smaller than the ones estimated from the x-axis intercepts.

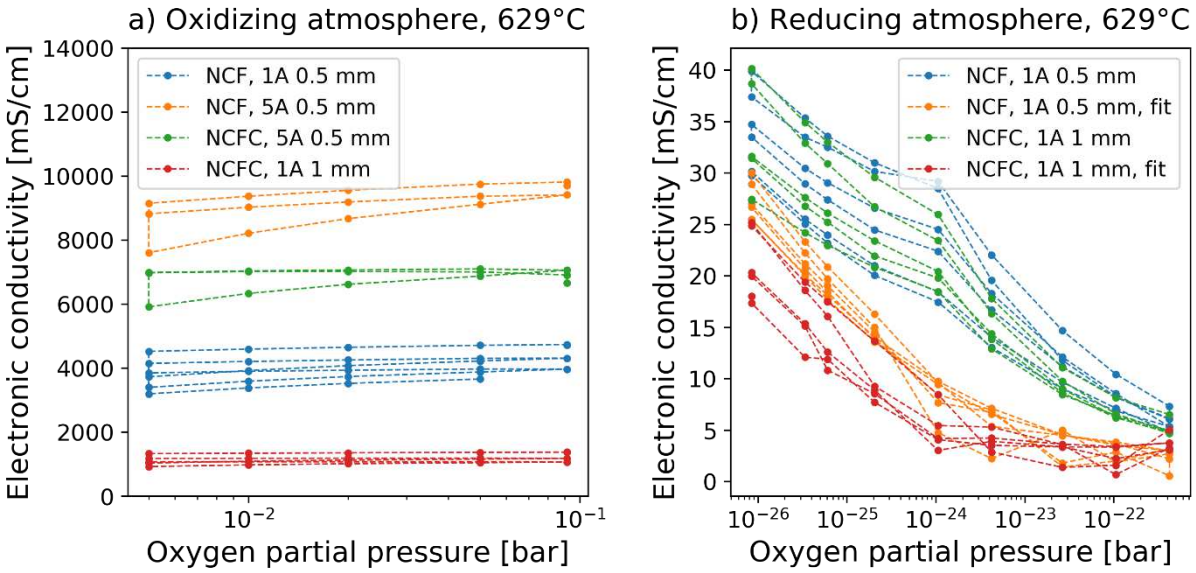

Figure 65: Electronic conductivity in oxidizing atmospheres (a) and reducing atmospheres (b) of the different finger geometries of NCF and NCFC thin-film samples plotted over the oxygen partial pressure and obtained from either the x-axis intercepts or the transmission line fit.

The ionic conductivity in reducing atmospheres could not so easily be quantified for those films because ion conduction within the YSZ substrates dominates in the in-plane measurements.

The ASR of the NCF and NCFC electrodes is displayed in Figure 66 a) and b) and it can be observed that it is generally smaller for the more reducing atmospheres than for the more oxidizing atmospheres, as expected due to more defects serving as reaction sites and more hydrogen molecules available for reaction. However, for the NCF electrode this trend is not continuous and a slight increase going to more reducing conditions from the minimum ASR at an oxygen partial pressure of approximately 10^{-24} bar can be noticed, hinting to an influence of the hydrogen and water partial pressure on the electrode behavior because this minimum is exactly at the point at which H_2 and H_2O partial pressures have both their maximum. The values obtained by the transmission line fit are marginally smaller than the ones obtained by fitting with R, CPE parallel circuit elements and the ASR of the NCFC electrodes is slightly smaller than that of the NCF electrodes, as previously observed for measurements of these thin-films, the absolute values are substantially lower though with an ASR of 3.3 Ωcm^2 for the NCF and 3.0 Ωcm^2 for the NCFC thin-film instead of approximately 30 Ωcm^2 which could not be reasonably explained by the available data.

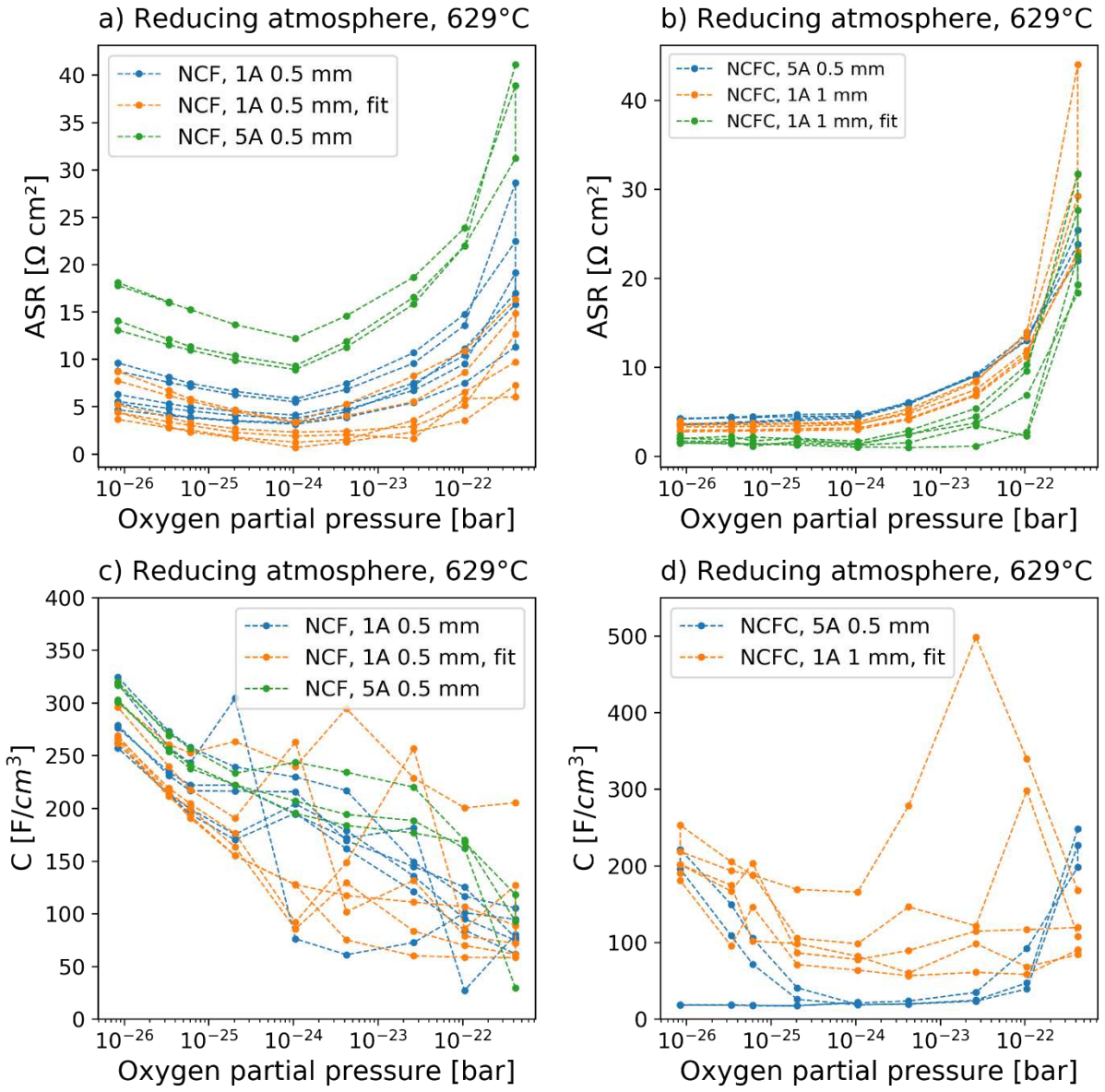

Figure 66: ASR over the oxygen partial pressure of NCF (a) and NCFC (b) samples and chemical capacitance over the oxygen partial pressure of NCF (c) and NCFC (d) samples measured in reducing atmospheres at 629°C.

The chemical capacitance of the thin-films, as depicted in Figure 66 c) and d), shows a tendency to higher values at more reducing conditions for the NCF electrodes, explained by more oxygen vacancies in more reducing atmospheres. For the NCFC electrodes this trend can only be observed for the lower measured oxygen partial pressures. The transmission line fit yields equal results and the values are very similar to previous results for NCF and NCFC thin-film electrodes, as shown in Figure 53 d) and Figure 55 c). However, the capacitance obtained from fitting at the higher measured oxygen partial pressure range shows a very high uncertainty and results varying substantially from cycle to cycle at the same conditions, indicating a poor fit in this oxygen partial pressure region. Overall, it can be concluded that the transmission line model describes the NCF and NCFC thin-films very well at reducing conditions and yields reasonable results for electronic and ionic conductivity, ASR and

chemical capacitance. Surprisingly, the ASR of these microelectrodes is roughly a factor of 10 lower, although all processing and measurement parameters were equal to macro-electrodes, except for current collector geometry.

5.8. Recycling of thin-film electrode samples

To investigate the possibility of recycling thin-film electrode samples, the thin-film of an NCFC electrode sample with grid current collector manufactured by lift-off lithography a YSZ electrolyte and a three-layer counter electrode was etched away with HCl and a new NCFC thin-film was deposited afterwards via PLD. Impedance spectra of the sample with the new thin-film were recorded in the micro/macro setup at 606°C in humidified ARCAL with a hydrogen to water ratio of 1:1. The frequency was varied from 0.05 to 900000 Hz and the AC amplitude set to 10 mV. Spectra were recorded in intervals of 20 minutes.

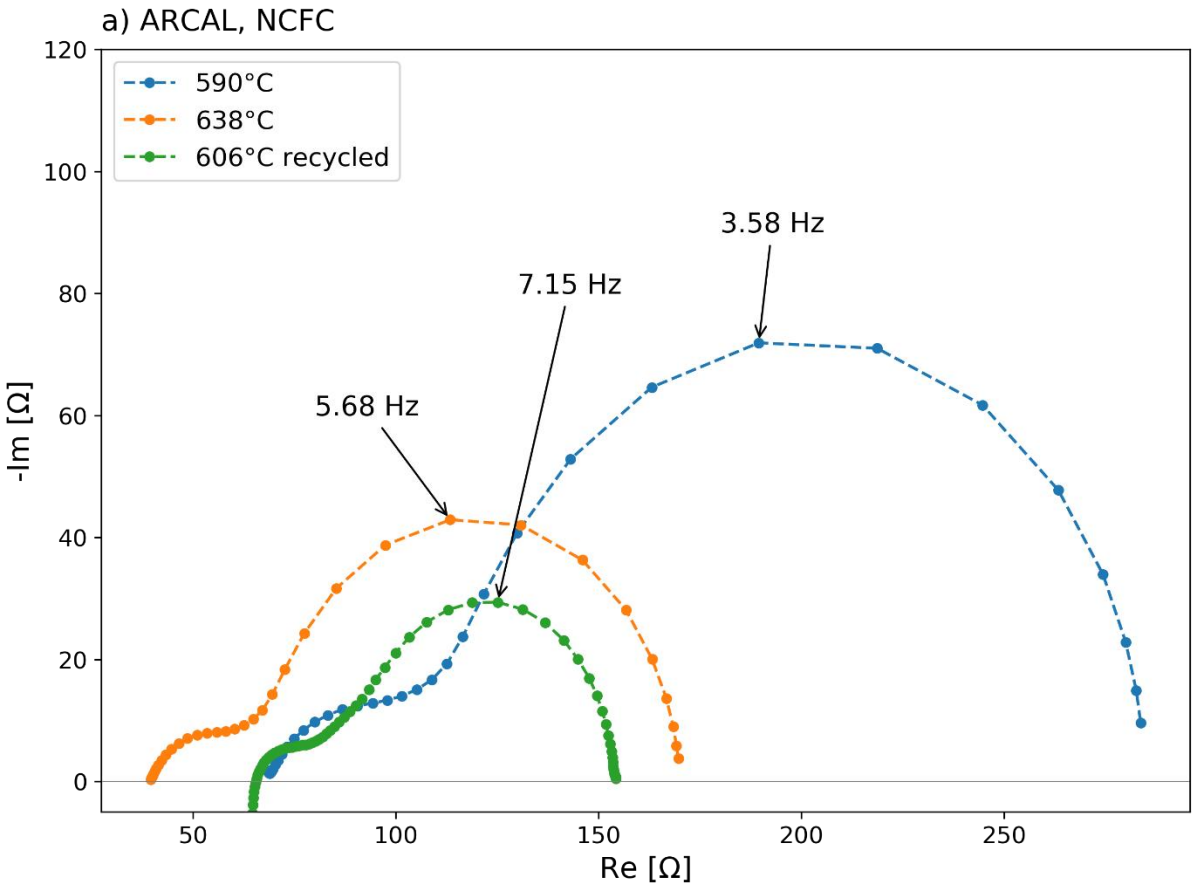

Figure 67: Impedance spectra of the NCFC thin-film sample before and after recycling and depositing a new NCFC thin-film, measured in humidified ARCAL with a hydrogen to water ratio of 1:1.

Figure 67 shows impedance spectra from the temperature cycles measured before recycling and a spectrum measured after recycling. The shape is pretty much identical with a big low frequency semicircle feature and a small high frequency feature and a similar peak frequency. That the high frequency feature, which could only be observed for this sample out

of all NCF and NCFC samples, is still present after depositing a new thin-film, further supports the assumption that this feature is an artifact due to the rather bad adhesion and many defects of the current collector caused by the lift-off lithography process. The temperatures where the spectra were recorded differ slightly from each other and the two closest to the one the recycled sample was measured at are shown. It can be observed that no major degradation occurred due to the recycling process and the spectra of the recycled sample shows an even smaller resistance that the one measured at higher temperature prior to recycling. However, this difference is well within the tolerance and could also be due to less degradation in the micro/macro setup compared to the wing setup, where the samples were measured before the recycling step.

Considering these results, reusing the three-layer counter electrode and current collector at least once and only depositing a new thin-film seems like a viable option without notable degradation due to the recycling procedure. This recycling process cannot be applied infinitely though, since the current collector already showed small signs of degradation under the optical microscope after the first time etching away the thin-film, due to the aggressive HCl treatment. That did not impact the performance after redepositing a thin-film, however, it could possibly lead to issues after repeatedly recycling the samples.

5.9. SEM images of NCF and NCFC thin-film electrodes

To confirm the exsolution of metal particles onto the surface of the thin-film electrodes, especially the NCFC ones, the surfaces of some samples after exposure to reducing conditions and cathodic bias was analyzed. Furthermore, samples that were measured at OCV and samples that were measured with applied bias are compared.

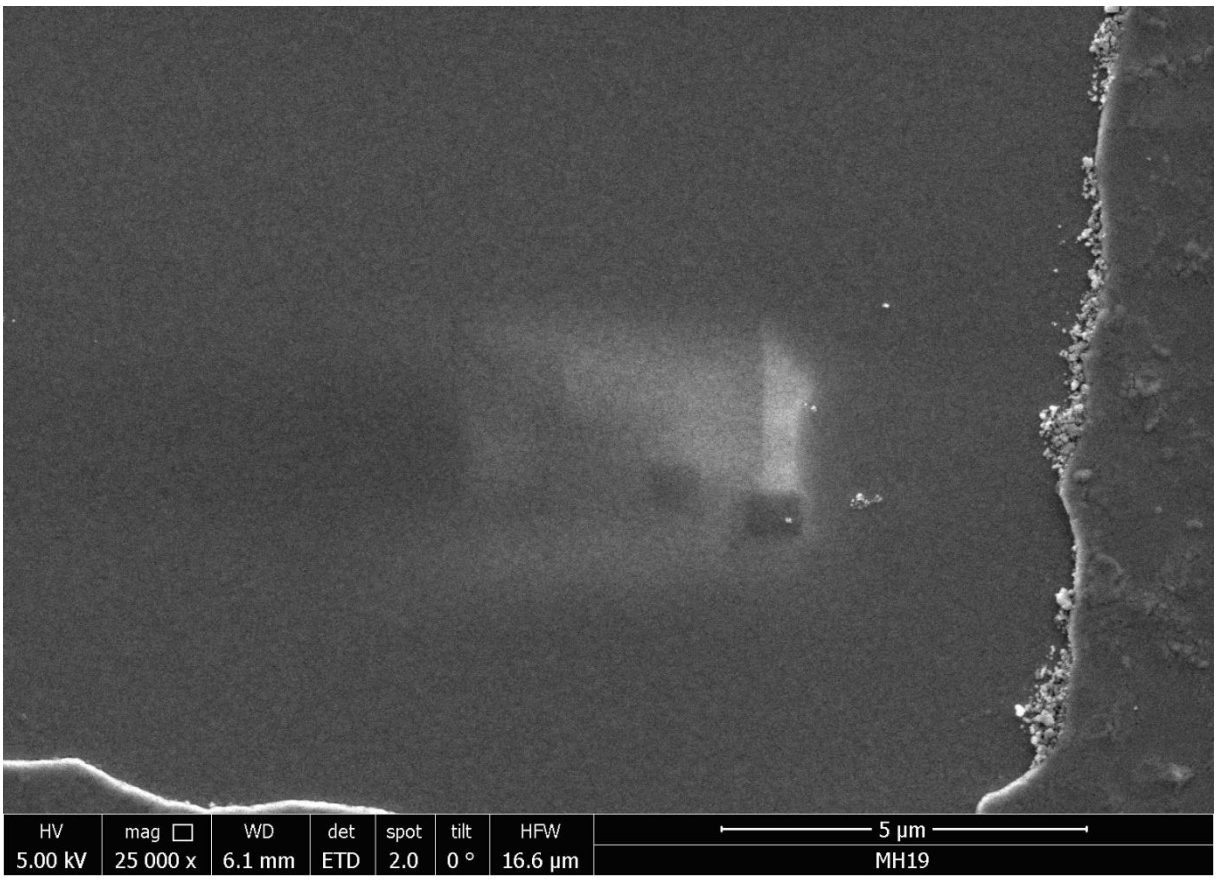

Figure 68: SEM images of the surface of an NCF electrode after exposure to reducing conditions.

In Figure 68 an SEM image of a NCF electrode after bias cycles in reducing atmosphere is displayed. The applied bias cycles and I-V curves are presented in 5.4.2. The surface only shows some irregularities near the edges of the current collector, these particles cannot be clearly identified as metal particles though and could also be impurities or other particles. The absence of exsolved metal particles fits well with the results of the measurements on NCF electrodes with down to -300 mV applied bias, where no characteristic jump indicating exsolutions could be observed. This indicates that NCF has a higher thermochemical stability than LSF.

Figure 69 shows the surface of an NCFC electrode after exposure to reducing conditions and cathodic bias up to -300 mV, with electrochemical measurements presented in 5.4.2. There are clearly particles visible, well dispersed on the whole surface. The darker area in the image on top is the current collector structure underneath the thin-film. The particles are

rather monodisperse with sizes ranging mostly from 40 to 60 nm. The presence of well dispersed metallic particles further indicates that the characteristic jump noticeable during the bias measurements shown in Figure 59 is in fact the reoxidation of exsolved metal particles and that they can be exsolved from a host perovskite by exposure to reducing conditions.

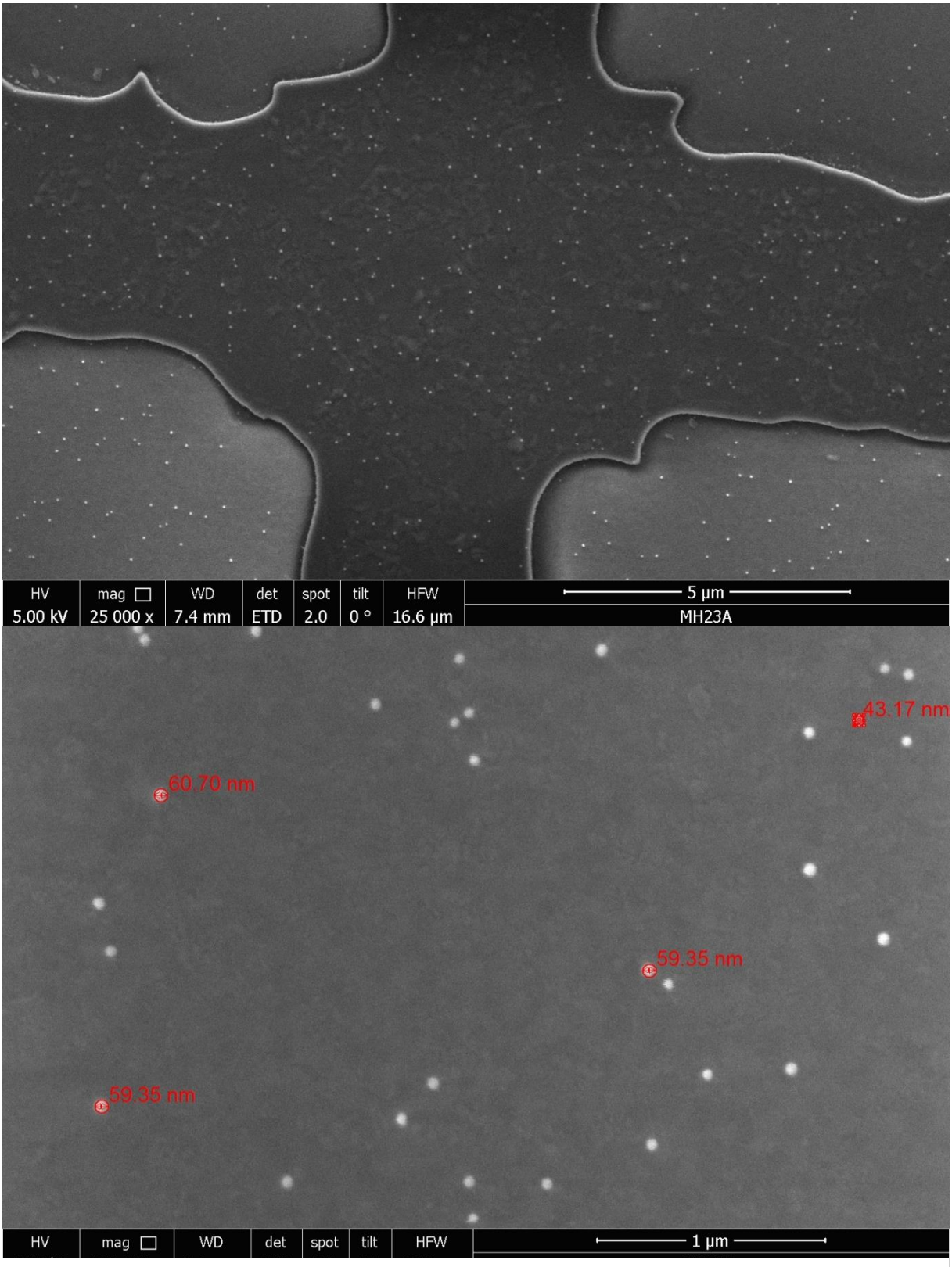

Figure 69: SEM images of an NCFC electrode surface after exposure to reducing conditions with applied bias.

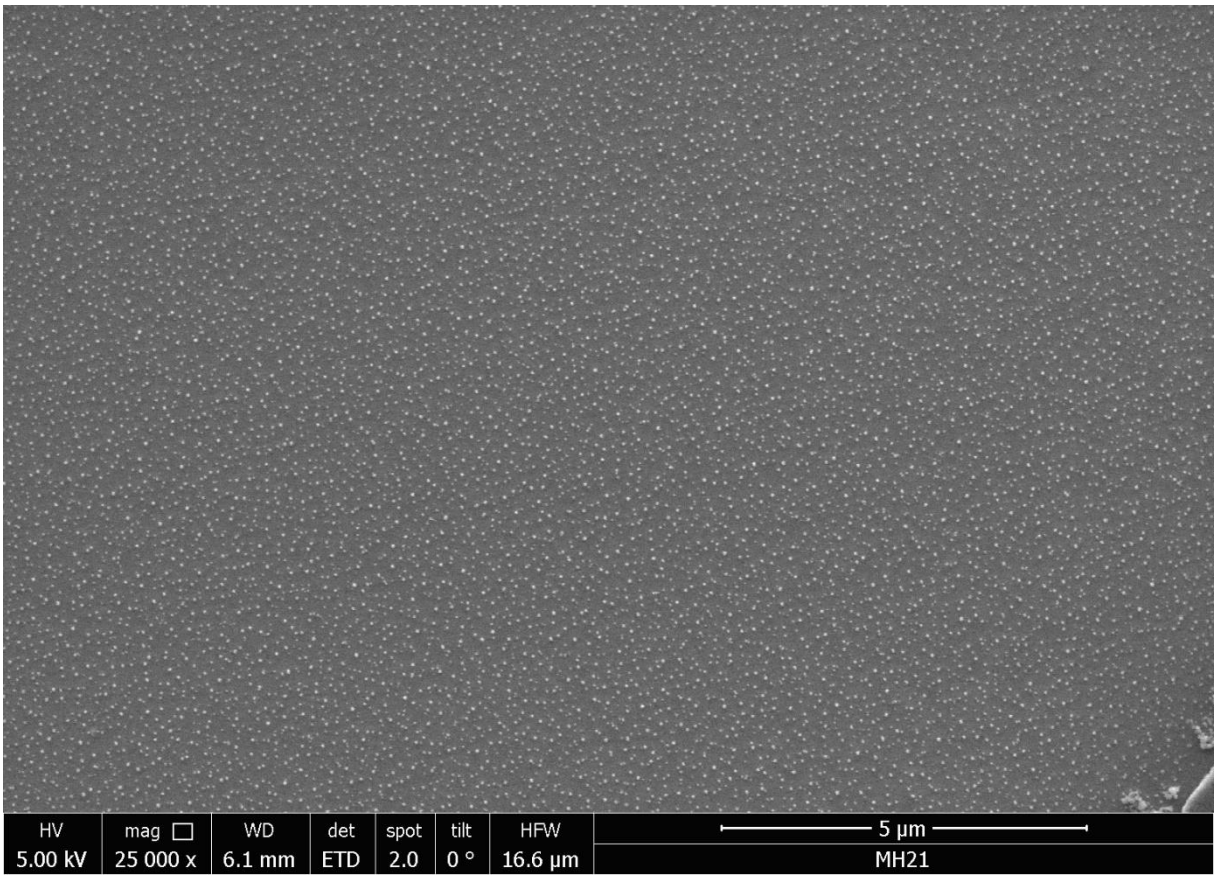

Figure 70: SEM image of an NCFC electrode surface after exposure to reducing conditions at OCV.

Furthermore, the exsolved particles on the NCFC samples could already be observed on samples after measurements in reducing atmospheres at OCV, as displayed in Figure 70, with even more exsolved particles on the surface compared to the sample measured with applied bias. For the exsolution of metal particles onto the surface of NCF electrodes, there are most likely more reducing conditions needed, which was not further investigated in this work but can be explained by the easier reducibility of cobalt compared to iron.

5.10. Results of the XPS measurements

Here, first results of ex-situ and in-situ XPS measurements shall be shortly presented. The focus lies therefore not on a detailed description but shall rather give an outline and motivation for further experiments in this direction.

XPS measurements were carried out in two different machines: a UHV setup and an ambient pressure analyzer. Both chambers contain a monochromated Al K_α X-ray source and a photoelectron analyzer by SPECS. The samples in the UHV setup were heated in vacuum to 400-500°C for 5 minutes to remove surface carbon species, whereas the APXPS samples were measured in a 1 mbar atmosphere, which consisted either of O_2, or a ~20:1 mixture of H_2 + H_2O. The temperature of the alumina back plate was ~600°C, measured by a thermocouple, and the sample temperature was ~520°C, according to the electrolyte

conductivity measured by electrochemical impedance spectroscopy. Elemental quantification was performed from survey spectra by normalizing the peak areas by Scofield photoionization cross sections[94] and effective photoelectron attenuation length. The atomic percentages were normalized so that Nd+Ca+Co+Fe = 100%.

Results are plotted in Figure 71. As expected, the elemental composition of the as deposited sample is similar in both analyzers (O_2, OCV vs. Pristine, UHV XPS). Generally, the sample surface is strongly enriched by Nd and Ca, and depleted in Fe content. The Co fraction is growing in the APXPS measurements in reducing conditions. On the other hand, the ex-situ degraded sample shows a dramatically altered surface composition, which mostly consists of Ca, Nd and Si. Commonly, Si impurities are found on all samples that were measured in reducing conditions, both in the APXPS setup and tube furnaces.

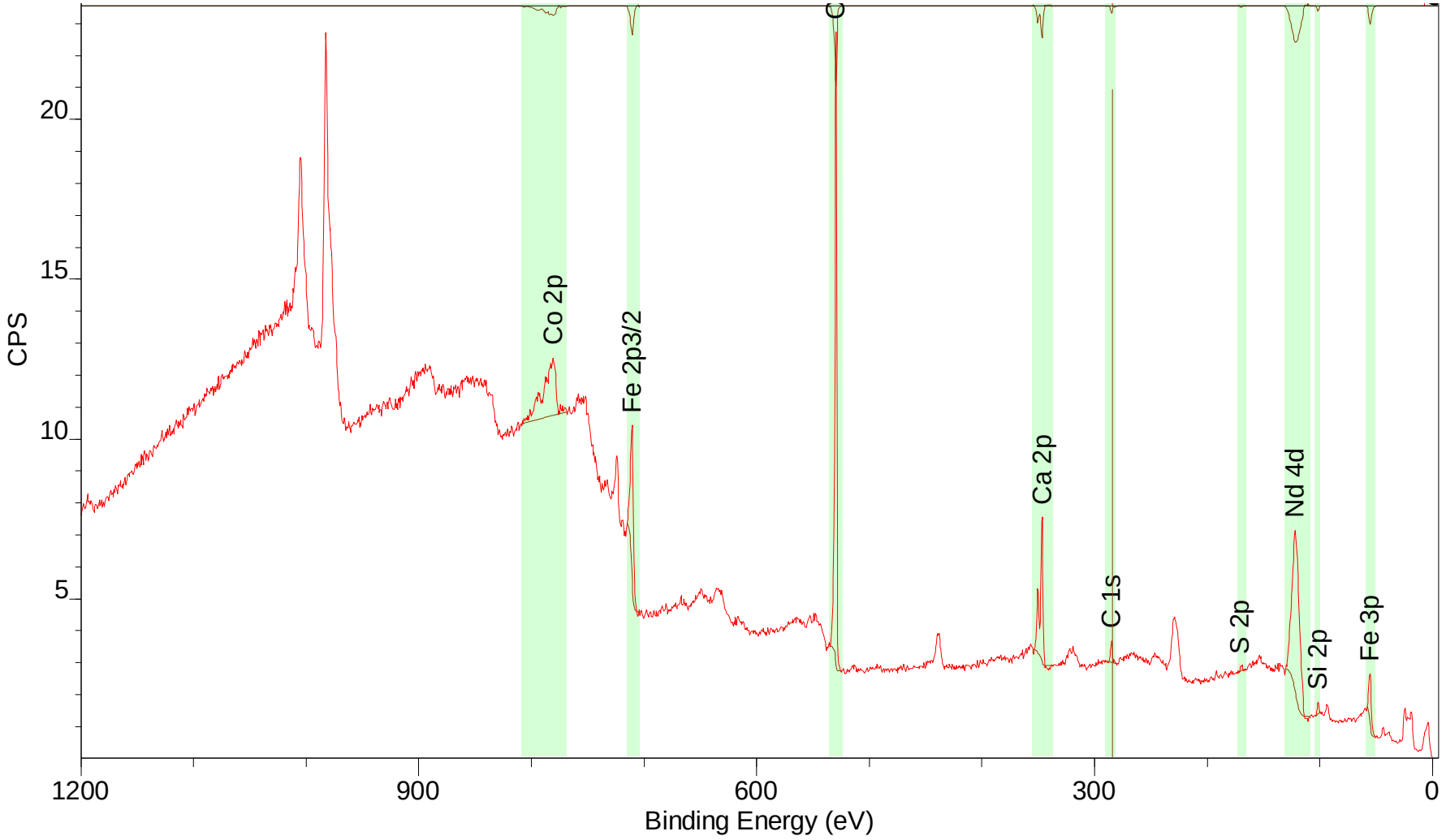

Figure 71: Exemplary XPS survey spectrum of an NCFC electrode in hydrogen/water atmosphere.

XPS detail spectra were recorded during the APXPS measurements to get an insight into oxidation states of Fe and Co and get direct information on the dynamics of the exsolution behavior.

In Figure 72 and Figure 73, Fe2p and Co2p spectra respectively are plotted. P-orbitals exhibit spin-orbit splitting of electrons with 1/2 and 3/2 total spin. Therefore, spectra consist of two peaks at ~710 and ~725 eV. For fitting, only the 2p3/2 region was considered, and fitted with two components for oxide and one for Fe metal by using CasaXPS. Fitting of the Co 2p spectra is more complex, due to a strong overlap of an Fe LMM auger peak with the Co 2p peaks. For a proper description of the Fe LMM shape, three peaks were used and fully constrained in their relative areas, positions and FWHM to avoid overparameterization. Co2p peaks were again fitted with two components for the oxide and one for the metal. By comparing the spectra in different conditions, it is clearly visible that Co metal exsolution happens already at OCV conditions, whereas significant amounts of Fe are only exsolved when an additional cathodic overpotential of -250 mV is applied. Oxidation of exsolved Co and Fe species occurs at at an anodic overpotential of +180 mV. In conclusion, it is possible to trigger and observe the exsolution of metallic species in ambient pressure XPS experiments, and the easier reducibility of Co, compared to Fe is visible.

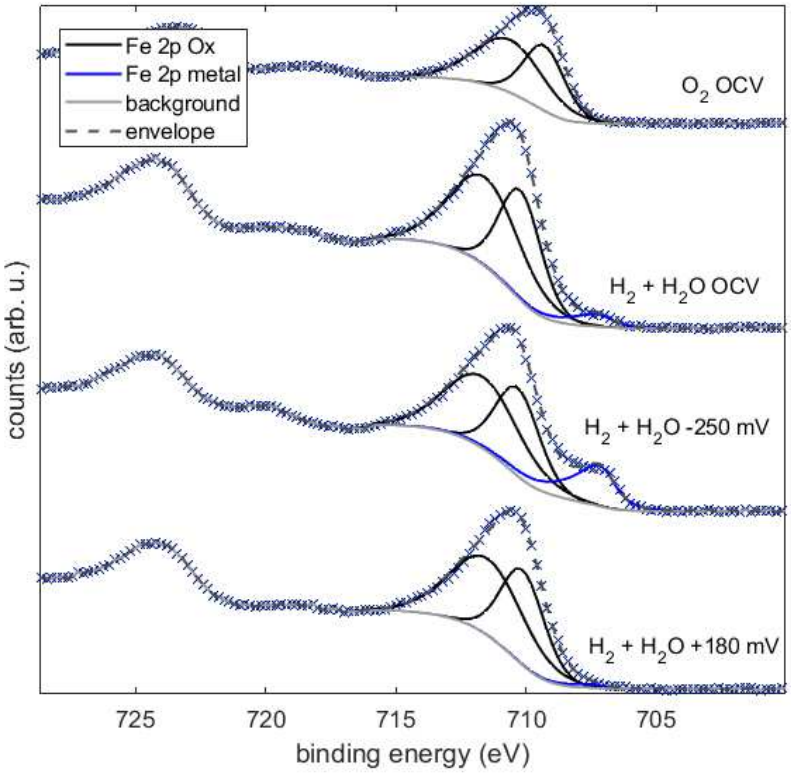

Figure 72: XPS detail spectra of Fe2p in different atmospheres at OCV and with applied bias.

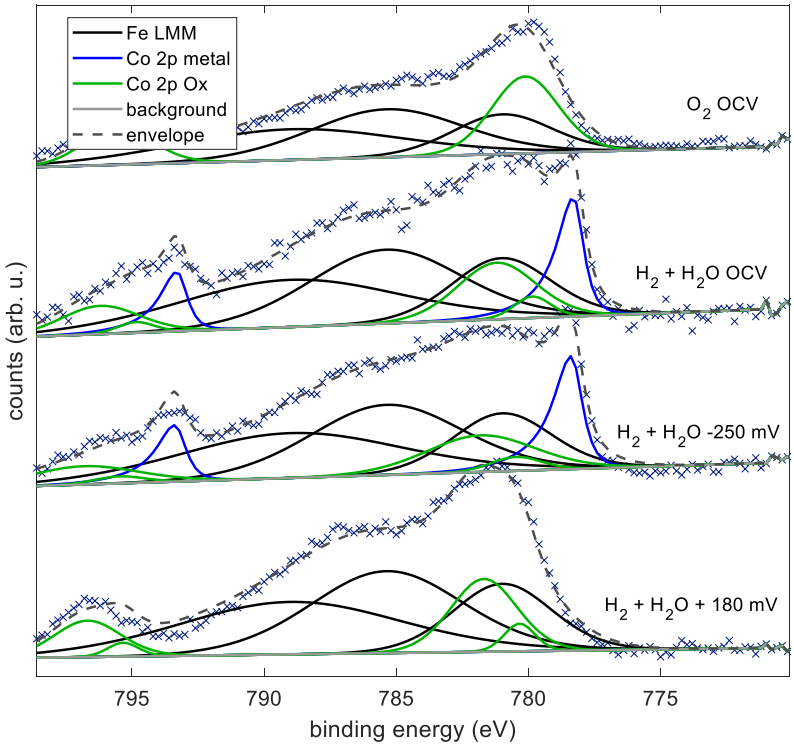

Figure 73: XPS detail spectra of Co2p in different atmospheres at OCV and with applied bias.

In Figure 74 the surface composition of NCFC thin-films as deposited and after measurements in the wing setup is displayed. For the sample degraded in the wing setup a substantial amount of Si impurities on the surface could be detected, which is most likely the cause for the high degradation of the electrodes in this measuring setup, as explained in 5.4.1. The impurities probably originate from the measuring setup, however, how exactly the degradation works and what kind of Si compounds are to blame needs further investigation.

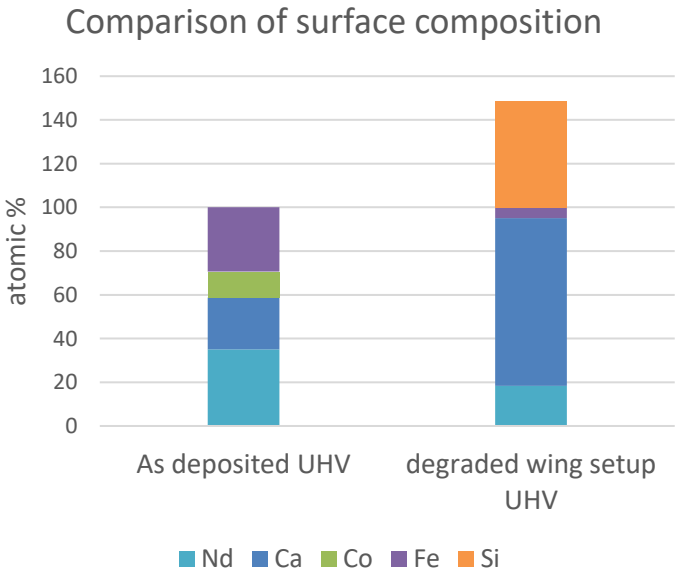

Figure 74: Surface composition of an NCFC thin-film as deposited and of an NCFC thin-film after measurements in the wing setup.

6. Conclusions

GDC based electrodes, more specifically single-layer PtGDC, dual-layer GDC|Pt and PtGDC|Pt as well as three-layer GDC|PtGDC|Pt electrodes were manufactured and characterized via EIS in mainly reducing atmospheres. Out of these, the GDC|Pt and GDC|PtGDC|Pt electrodes showed the best performance with a remarkably low ASR. Values as low as 0.05 Ωcm^2 at 600°C could be achieved. Moreover, it was found that due to the excellent kinetics at temperatures above 700°C gas diffusion becomes the limiting factor for the electrode reaction, even in the optimized setup where the gas diffusion ASR is in the order of 0.01 Ωcm^2. However, it was also found that the ohmic offset, which is usually ascribed to the electrolyte, has a contribution from the comparatively low electron conductivity of the GDC functional layer and this varies with the $p(O_2)$. By comparing the ohmic offset in oxidizing and reducing measurements, the effective ionic conductivity of the GDC electrode layer was estimated to be about one order of magnitude lower than that of bulk GDC, most likely due to the porosity and tortuosity of the GDC layer. In order to reduce losses resulting from electron conduction through the GDC layer, three-layer electrodes were successfully prepared. Those consist of a thinner GDC layer, due to spincoating instead of brushing, and an additional PtGDC layer between GDC and Pt to improve the mechanical interface. Moreover, those three-layer electrodes still showed the remarkably low ASR observed for GDC|Pt electrodes because the active thickness of the GDC layer was estimated to be 1 µm, while the spincoated GDC layer was 3 µm thick. The activation energy of the GDC|Pt and three-layer electrodes was approximately 1 eV, suggesting ion conduction through the YSZ-GDC interface as the limiting factor. Treatment of the electrodes with HCl inflicted degradation and a change in activation energy to ~0.6 eV, indicating a different limiting factor of the electrode reaction, likely ion conduction through the GDC layer or the surface reaction. The same lower activation energy could be observed for three-layer electrodes with an additional PLD deposited GDC interlayer to improve the YSZ-GDC interface. In CO + CO_2 atmosphere the kinetics were significantly slower with a resulting higher active film thickness compared to H_2 + H_2O and a different activation energy. The three-layer GDC electrodes were used as counter electrodes for the subsequent measurements on NCF and NCFC thin-film electrodes.

For these thin-film electrodes Ti/Pt current collectors structured by either lift-off lithography or lithography and ion-beam etching were prepared. The ones manufactured by ion-beam etching showed significantly better adhesion on the YSZ substrate and therefore also no artifacts in the impedance spectra. The NCF and NCFC thin-films were deposited by PLD. For characterization EIS measurements were carried out in reducing and oxidizing atmospheres and with applied bias. The NCFC electrodes showed a characteristic jump in

the current density-overpotential graph, indicating the oxidation of exsolved metal particles. The presence of these particles could be confirmed with SEM images and XPS data. For the NCF electrodes no signs of exsolved particles could be observed, most likely due to less reducibility of Fe compared to Co. Furthermore, the ASR was investigated in different measurement setups and for both NCF and NCFC electrodes a rather strong degradation, depending on the measurement setup could be noticed, indicating interaction with impurities originating from the measurement setups on the electrodes. However, after bias measurements, the ASR of most of the samples seemed to stabilize to a rather constant value with only minor degradation further on. The electronic and ionic conductivity of the thin-films was analyzed via in-plane EIS measurements on finger-structured microelectrodes. The electronic conductivity showed a trend to increasing values in more reducing conditions, due to the higher number of electronic defects in these conditions. For the ionic conductivity, however, no straightforward results were obtained from the measurements in different atmospheres because it seemed to depend not only on the oxygen partial pressure but also on the hydrogen and water partial pressure, which were varied in order to generate the desired oxygen partial pressures. Moreover, these microelectrodes exhibited a significantly smaller ASR than the macroelectrodes which could not be logically explained with the available data.

For future work on this topic the investigation of the electrochemical behavior of the NCF and NCFC electrodes in even more reducing conditions would be interesting to further characterize the exsolution behavior of NCFC and to obtain the less reducible Fe particles on NCF electrodes. Moreover, the performance of these materials in different fuels and the possibility of switching these electrodes from a more active to a less active state by targeted oxidation and reduction of the exsolved particles could be investigated.

List of figures

References

(1) Karl, T. R.; Arguez, A.; Huang, B.; Lawrimore, J. H.; McMahon, J. R.; Menne, M. J.; Peterson, T. C.; Vose, R. S.; Zhang, H.-M. Possible Artifacts of Data Biases in the Recent Global Surface Warming Hiatus. *Science* **2015**, *348* (6242), 1469–1472. https://doi.org/10.1126/science.aaa5632.

(2) Smalley, R. E. Future Global Energy Prosperity: The Terawatt Challenge. *MRS Bull.* **2005**, *30* (6), 412–417. https://doi.org/10.1557/mrs2005.124.

(3) Vitousek, P. M. Global Environmental Change: An Introduction. *Annu. Rev. Ecol. Syst.* **1992**, *23* (1), 1–14. https://doi.org/10.1146/annurev.es.23.110192.000245.

(4) Sun, Q.; Miao, C.; Hanel, M.; Borthwick, A. G. L.; Duan, Q.; Ji, D.; Li, H. Global Heat Stress on Health, Wildfires, and Agricultural Crops under Different Levels of Climate Warming. *Environment International* **2019**, *128*, 125–136. https://doi.org/10.1016/j.envint.2019.04.025.

(5) Raper, S. C. B.; Braithwaite, R. J. Low Sea Level Rise Projections from Mountain Glaciers and Icecaps under Global Warming. *Nature* **2006**, *439* (7074), 311–313. https://doi.org/10.1038/nature04448.

(6) Schiermeier, Q. Increased Flood Risk Linked to Global Warming. *Nature* **2011**, *470* (7334), 316–316. https://doi.org/10.1038/470316a.

(7) Panwar, N. L.; Kaushik, S. C.; Kothari, S. Role of Renewable Energy Sources in Environmental Protection: A Review. *Renewable and Sustainable Energy Reviews* **2011**, *15* (3), 1513–1524. https://doi.org/10.1016/j.rser.2010.11.037.

(8) Dresselhaus, M. S.; Thomas, I. L. Alternative Energy Technologies. *Nature* **2001**, *414* (6861), 332–337. https://doi.org/10.1038/35104599.

(9) Nehrir, M. H.; Wang, C.; Strunz, K.; Aki, H.; Ramakumar, R.; Bing, J.; Miao, Z.; Salameh, Z. A Review of Hybrid Renewable/Alternative Energy Systems for Electric Power Generation: Configurations, Control, and Applications. *IEEE Trans. Sustain. Energy* **2011**, *2* (4), 392–403. https://doi.org/10.1109/TSTE.2011.2157540.

(10) Siler-Evans, K.; Azevedo, I. L.; Morgan, M. G.; Apt, J. Regional Variations in the Health, Environmental, and Climate Benefits of Wind and Solar Generation. *Proceedings of the National Academy of Sciences* **2013**, *110* (29), 11768–11773. https://doi.org/10.1073/pnas.1221978110.

(11) Rao, K. R. Radioactive Waste: The Problem and Its Management. *Current Science* **2001**, *81*, 1534–1546.

(12) Chen, H.; Cong, T. N.; Yang, W.; Tan, C.; Li, Y.; Ding, Y. Progress in Electrical Energy Storage System: A Critical Review. *Progress in Natural Science* **2009**, *19* (3), 291–312. https://doi.org/10.1016/j.pnsc.2008.07.014.

(13) Baker, J. N.; Collinson, A. Electrical Energy Storage at the Turn of the Millennium. *Power Engineering Journal* **1999**, *13* (3), 107–112. https://doi.org/10.1049/pe:19990301.

(14) Denholm, P.; Kulcinski, G. L. Life Cycle Energy Requirements and Greenhouse Gas Emissions from Large Scale Energy Storage Systems. *Energy Conversion and Management* **2004**, *45* (13–14), 2153–2172. https://doi.org/10.1016/j.enconman.2003.10.014.

(15) Das, V.; Padmanaban, S.; Venkitusamy, K.; Selvamuthukumaran, R.; Blaabjerg, F.; Siano, P. Recent Advances and Challenges of Fuel Cell Based Power System Architectures and Control – A Review. *Renewable and Sustainable Energy Reviews* **2017**, *73*, 10–18. https://doi.org/10.1016/j.rser.2017.01.148.

(16) Mekhilef, S.; Saidur, R.; Safari, A. Comparative Study of Different Fuel Cell Technologies. *Renewable and Sustainable Energy Reviews* **2012**, *16* (1), 981–989. https://doi.org/10.1016/j.rser.2011.09.020.

(17) Sharaf, O. Z.; Orhan, M. F. An Overview of Fuel Cell Technology: Fundamentals and Applications. *Renewable and Sustainable Energy Reviews* **2014**, *32*, 810–853. https://doi.org/10.1016/j.rser.2014.01.012.

(18) Steele, B. C. H.; Heinzel, A. Materials for Fuel-Cell Technologies. *Nature* **2001**, *414* (6861), 345–352. https://doi.org/10.1038/35104620.

(19) Mahato, N.; Banerjee, A.; Gupta, A.; Omar, S.; Balani, K. Progress in Material Selection for Solid Oxide Fuel Cell Technology: A Review. *Progress in Materials Science* **2015**, *72*, 141–337. https://doi.org/10.1016/j.pmatsci.2015.01.001.

(20) da Silva, F. S.; de Souza, T. M. Novel Materials for Solid Oxide Fuel Cell Technologies: A Literature Review. *International Journal of Hydrogen Energy* **2017**, *42* (41), 26020–26036. https://doi.org/10.1016/j.ijhydene.2017.08.105.

(21) Yamamoto, O. Solid Oxide Fuel Cells: Fundamental Aspects and Prospects. *Electrochimica Acta* **2000**, *45* (15–16), 2423–2435. https://doi.org/10.1016/S0013-4686(00)00330-3.

(22) Shaikh, S. P. S.; Muchtar, A.; Somalu, M. R. A Review on the Selection of Anode Materials for Solid-Oxide Fuel Cells. *Renewable and Sustainable Energy Reviews* **2015**, *51*, 1–8. https://doi.org/10.1016/j.rser.2015.05.069.

(23) Guo, X.; Waser, R. Electrical Properties of the Grain Boundaries of Oxygen Ion Conductors: Acceptor-Doped Zirconia and Ceria. *Progress in Materials Science* **2006**, *51* (2), 151–210. https://doi.org/10.1016/j.pmatsci.2005.07.001.

(24) Jørgensen, M. J.; Primdahl, S.; Mogensen, M. Characterisation of Composite SOFC Cathodes Using Electrochemical Impedance Spectroscopy. *Electrochimica Acta* **1999**, *44* (24), 4195–4201. https://doi.org/10.1016/S0013-4686(99)00134-6.

(25) Huang, Q.-A.; Hui, R.; Wang, B.; Zhang, J. A Review of AC Impedance Modeling and Validation in SOFC Diagnosis. *Electrochimica Acta* **2007**, *52* (28), 8144–8164. https://doi.org/10.1016/j.electacta.2007.05.071.

(26) Hsieh, G.; Mason, T. O.; Pederson, L. R. Experimental Limitations in Impedance Spectroscopy: Part II — Electrode Artifacts in Three-Point Measurements on Pt/YSZ. *Solid State Ionics* **1996**, *91* (3–4), 203–212. https://doi.org/10.1016/S0167-2738(96)83020-7.

(27) Brahim, C.; Ringuedé, A.; Gourba, E.; Cassir, M.; Billard, A.; Briois, P. Electrical Properties of Thin Bilayered YSZ/GDC SOFC Electrolyte Elaborated by Sputtering. *Journal of Power Sources* **2006**, *156* (1), 45–49. https://doi.org/10.1016/j.jpowsour.2005.08.017.

(28) Kim, S. J.; Choi, G. M. Stability of LSCF Electrode with GDC Interlayer in YSZ-Based Solid Oxide Electrolysis Cell. *Solid State Ionics* **2014**, *262*, 303–306. https://doi.org/10.1016/j.ssi.2014.01.001.

(29) Tan, Y.; Wang, A.; Jia, L.; Yan, D.; Chi, B.; Pu, J.; Li, J. High-Performance Oxygen Electrode for Reversible Solid Oxide Cells with Power Generation and Hydrogen Production at Intermediate Temperature. *International Journal of Hydrogen Energy* **2017**, *42* (7), 4456–4464. https://doi.org/10.1016/j.ijhydene.2016.10.121.

(30) Nenning, A.; Bischof, C.; Fleig, J.; Bram, M.; Opitz, A. K. The Relation of Microstructure, Materials Properties and Impedance of SOFC Electrodes: A Case Study of Ni/GDC Anodes. *Energies* **2020**, *13* (4), 987. https://doi.org/10.3390/en13040987.

(31) Zhang, L.; Jiang, S. P.; He, H. Q.; Chen, X.; Ma, J.; Song, X. C. A Comparative Study of H_2S Poisoning on Electrode Behavior of Ni/YSZ and Ni/GDC Anodes of Solid Oxide Fuel Cells. *International Journal of Hydrogen Energy* **2010**, *35* (22), 12359–12368. https://doi.org/10.1016/j.ijhydene.2010.08.067.

(32) Kan, H.; Lee, H. Enhanced Stability of Ni–Fe/GDC Solid Oxide Fuel Cell Anodes for Dry Methane Fuel. *Catalysis Communications* **2010**, *12* (1), 36–39. https://doi.org/10.1016/j.catcom.2010.07.014.

(33) Hua, B.; Li, M.; Sun, Y.-F.; Li, J.-H.; Luo, J.-L. Enhancing Perovskite Electrocatalysis of Solid Oxide Cells Through Controlled Exsolution of Nanoparticles. *ChemSusChem* **2017**, *10* (17), 3333–3341. https://doi.org/10.1002/cssc.201700936.

(34) Burnat, D.; Kontic, R.; Holzer, L.; Steiger, P.; Ferri, D.; Heel, A. Smart Material Concept: Reversible Microstructural Self-Regeneration for Catalytic Applications. *J. Mater. Chem. A* **2016**, *4* (30), 11939–11948. https://doi.org/10.1039/C6TA03417A.

(35) Qi, H.; Xia, F.; Yang, T.; Li, W.; Li, W.; Ma, L.; Collins, G.; Shi, W.; Tian, H.; Hu, S.; Thomas, T.; Sabolsky, E. M.; Zondlo, J.; Hart, R.; Finklea, H.; Hackett, G. A.; Liu, X. In

Situ Exsolved Nanoparticles on $La_{0.5}Sr_{1.5}Fe_{1.5}Mo_{0.5}O_{6-\delta}$ Anode Enhance the Hydrogen Oxidation Reaction in SOFCs. *J. Electrochem. Soc.* **2020**, *167* (2), 024510. https://doi.org/10.1149/1945-7111/ab6a82.

(36) Opitz, A. K.; Nenning, A.; Rameshan, C.; Rameshan, R.; Blume, R.; Hävecker, M.; Knop-Gericke, A.; Rupprechter, G.; Fleig, J.; Klötzer, B. Enhancing Electrochemical Water-Splitting Kinetics by Polarization-Driven Formation of Near-Surface Iron(0): An In Situ XPS Study on Perovskite-Type Electrodes. *Angew. Chem. Int. Ed.* **2015**, *54* (9), 2628–2632. https://doi.org/10.1002/anie.201409527.

(37) Nenning, A.; Opitz, A. K.; Rameshan, C.; Rameshan, R.; Blume, R.; Hävecker, M.; Knop-Gericke, A.; Rupprechter, G.; Klötzer, B.; Fleig, J. Ambient Pressure XPS Study of Mixed Conducting Perovskite-Type SOFC Cathode and Anode Materials under Well-Defined Electrochemical Polarization. *J. Phys. Chem. C* **2016**, *120* (3), 1461–1471. https://doi.org/10.1021/acs.jpcc.5b08596.

(38) Nenning, A.; Fleig, J. Electrochemical XPS Investigation of Metal Exsolution on SOFC Electrodes: Controlling the Electrode Oxygen Partial Pressure in Ultra-High-Vacuum. *Surface Science* **2019**, *680*, 43–51. https://doi.org/10.1016/j.susc.2018.10.006.

(39) Götsch, T.; Schlicker, L.; Bekheet, M. F.; Doran, A.; Grünbacher, M.; Praty, C.; Tada, M.; Matsui, H.; Ishiguro, N.; Gurlo, A.; Klötzer, B.; Penner, S. Structural Investigations of $La_{0.6}Sr_{0.4}FeO_{3-\delta}$ under Reducing Conditions: Kinetic and Thermodynamic Limitations for Phase Transformations and Iron Exsolution Phenomena. *RSC Adv.* **2018**, *8* (6), 3120–3131. https://doi.org/10.1039/C7RA12309D.

(40) Thalinger, R.; Gocyla, M.; Heggen, M.; Klötzer, B.; Penner, S. Exsolution of Fe and SrO Nanorods and Nanoparticles from Lanthanum Strontium Ferrite $La_{0.6}Sr_{0.4}FeO_{3-\delta}$ Materials by Hydrogen Reduction. *J. Phys. Chem. C* **2015**, *119* (38), 22050–22056. https://doi.org/10.1021/acs.jpcc.5b06014.

(41) Papargyriou, D.; Miller, D. N.; Sirr Irvine, J. T. Exsolution of Fe–Ni Alloy Nanoparticles from (La,Sr)(Cr,Fe,Ni)O_3 Perovskites as Potential Oxygen Transport Membrane Catalysts for Methane Reforming. *J. Mater. Chem. A* **2019**, *7* (26), 15812–15822. https://doi.org/10.1039/C9TA03711J.

(42) Papargyriou, D.; Irvine, J. T. S. Nickel Nanocatalyst Exsolution from (La,Sr)(Cr,M,Ni)O_3 (M = Mn,Fe) Perovskites for the Fuel Oxidation Layer of Oxygen Transport Membranes. *Solid State Ionics* **2016**, *288*, 120–123. https://doi.org/10.1016/j.ssi.2015.11.007.

(43) Zhou, N.; Yin, Y.-M.; Chen, Z.; Song, Y.; Yin, J.; Zhou, D.; Ma, Z.-F. A Regenerative Coking and Sulfur Resistant Composite Anode with Cu Exsolution for Intermediate Temperature Solid Oxide Fuel Cells. *J. Electrochem. Soc.* **2018**, *165* (9), F629–F634. https://doi.org/10.1149/2.0841809jes.

(44) Sun, Y.; Li, J.; Zeng, Y.; Amirkhiz, B. S.; Wang, M.; Behnamian, Y.; Luo, J. A-Site Deficient Perovskite: The Parent for in Situ Exsolution of Highly Active, Regenerable Nano-Particles as SOFC Anodes. *J. Mater. Chem. A* **2015**, *3* (20), 11048–11056. https://doi.org/10.1039/C5TA01733E.

(45) Neagu, D.; Tsekouras, G.; Miller, D. N.; Ménard, H.; Irvine, J. T. S. In Situ Growth of Nanoparticles through Control of Non-Stoichiometry. *Nature Chemistry* **2013**, *5* (11), 916–923. https://doi.org/10.1038/nchem.1773.

(46) Han, H.; Park, J.; Nam, S. Y.; Kim, K. J.; Choi, G. M.; Parkin, S. S. P.; Jang, H. M.; Irvine, J. T. S. Lattice Strain-Enhanced Exsolution of Nanoparticles in Thin Films. *Nat. Commun.* **2019**, *10* (1), 1471. https://doi.org/10.1038/s41467-019-09395-4.

(47) Neagu, D.; Papaioannou, E. I.; Ramli, W. K. W.; Miller, D. N.; Murdoch, B. J.; Ménard, H.; Umar, A.; Barlow, A. J.; Cumpson, P. J.; Irvine, J. T. S.; Metcalfe, I. S. Demonstration of Chemistry at a Point through Restructuring and Catalytic Activation at Anchored Nanoparticles. *Nat. Commun.* **2017**, *8* (1), 1855. https://doi.org/10.1038/s41467-017-01880-y.

(48) Neagu, D.; Oh, T.-S.; Miller, D. N.; Ménard, H.; Bukhari, S. M.; Gamble, S. R.; Gorte, R. J.; Vohs, J. M.; Irvine, J. T. S. Nano-Socketed Nickel Particles with Enhanced Coking Resistance Grown in Situ by Redox Exsolution. *Nat. Commun.* **2015**, *6* (1), 8120. https://doi.org/10.1038/ncomms9120.

(49) Neagu, D.; Kyriakou, V.; Roiban, I.-L.; Aouine, M.; Tang, C.; Caravaca, A.; Kousi, K.; Schreur-Piet, I.; Metcalfe, I. S.; Vernoux, P.; van de Sanden, M. C. M.; Tsampas, M. N. *In Situ* Observation of Nanoparticle Exsolution from Perovskite Oxides: From Atomic Scale Mechanistic Insight to Nanostructure Tailoring. *ACS Nano* **2019**, *13* (11), 12996–13005. https://doi.org/10.1021/acsnano.9b05652.

(50) Kim, K. J.; Han, H.; Defferriere, T.; Yoon, D.; Na, S.; Kim, S. J.; Dayaghi, A. M.; Son, J.; Oh, T.-S.; Jang, H. M.; Choi, G. M. Facet-Dependent *in Situ* Growth of Nanoparticles in Epitaxial Thin Films: The Role of Interfacial Energy. *J. Am. Chem. Soc.* **2019**, *141* (18), 7509–7517. https://doi.org/10.1021/jacs.9b02283.

(51) Larminie, J.; Dicks, A. *Fuel Cell Systems Explained*, 2nd ed.; J. Wiley: Chichester, West Sussex, 2003.

(52) Timurkutluk, B.; Timurkutluk, C.; Mat, M. D.; Kaplan, Y. A Review on Cell/Stack Designs for High Performance Solid Oxide Fuel Cells. *Renewable and Sustainable Energy Reviews* **2016**, *56*, 1101–1121. https://doi.org/10.1016/j.rser.2015.12.034.

(53) Nechache, A.; Cassir, M.; Ringuedé, A. Solid Oxide Electrolysis Cell Analysis by Means of Electrochemical Impedance Spectroscopy: A Review. *Journal of Power Sources* **2014**, *258*, 164–181. https://doi.org/10.1016/j.jpowsour.2014.01.110.

(54) Fundamentals of Electrochemical Impedance Spectroscopy. In *Impedance Spectroscopy*; John Wiley & Sons, Inc.: Hoboken, NJ, USA, 2012; pp 1–21. https://doi.org/10.1002/9781118164075.ch1.

(55) Choi, W.; Shin, H.-C.; Kim, J. M.; Choi, J.-Y.; Yoon, W.-S. Modeling and Applications of Electrochemical Impedance Spectroscopy (EIS) for Lithium-Ion Batteries. *J. Electrochem. Sci. Technol.* **2020**, *11* (1), 1–13. https://doi.org/10.33961/jecst.2019.00528.

(56) Park, S.-M.; Yoo, J.-S. Peer Reviewed: Electrochemical Impedance Spectroscopy for Better Electrochemical Measurements. *Anal. Chem.* **2003**, *75* (21), 455 A-461 A. https://doi.org/10.1021/ac0313973.

(57) Lasia, A. Electrochemical Impedance Spectroscopy and Its Applications. In *Modern Aspects of Electrochemistry*; Conway, B. E., Bockris, J. O., White, R. E., Eds.; Kluwer Academic Publishers: Boston, 2002; Vol. 32, pp 143–248. https://doi.org/10.1007/0-306-46916-2_2.

(58) Jorcin, J.-B.; Orazem, M. E.; Pébère, N.; Tribollet, B. CPE Analysis by Local Electrochemical Impedance Spectroscopy. *Electrochimica Acta* **2006**, *51* (8–9), 1473–1479. https://doi.org/10.1016/j.electacta.2005.02.128.

(59) Lai, W.; Haile, S. M. Impedance Spectroscopy as a Tool for Chemical and Electrochemical Analysis of Mixed Conductors: A Case Study of Ceria. *J. American Ceramic Society* **2005**, *88* (11), 2979–2997. https://doi.org/10.1111/j.1551-2916.2005.00740.x.

(60) Jamnik, J.; Maier, J. Generalised Equivalent Circuits for Mass and Charge Transport: Chemical Capacitance and Its Implications. *Phys. Chem. Chem. Phys.* **2001**, *3* (9), 1668–1678. https://doi.org/10.1039/b100180i.

(61) Lee, J.-S.; Jamnik, J.; Maier, J. Generalized Equivalent Circuits for Mixed Conductors: Silver Sulfide as a Model System. *Monatsh. Chem.* **2009**, *140* (9), 1113–1119. https://doi.org/10.1007/s00706-009-0130-x.

(62) Nenning, A.; Opitz, A. K.; Huber, T. M.; Fleig, J. A Novel Approach for Analyzing Electrochemical Properties of Mixed Conducting Solid Oxide Fuel Cell Anode Materials by Impedance Spectroscopy. *Phys. Chem. Chem. Phys.* **2014**, *16* (40), 22321–22336. https://doi.org/10.1039/C4CP02467B.

(63) Mogensen, M. Physical, Chemical and Electrochemical Properties of Pure and Doped Ceria. *Solid State Ionics* **2000**, *129* (1–4), 63–94. https://doi.org/10.1016/S0167-2738(99)00318-5.

(64) Nakayama, M.; Martin, M. First-Principles Study on Defect Chemistry and Migration of Oxide Ions in Ceria Doped with Rare-Earth Cations. *Phys. Chem. Chem. Phys.* **2009**, *11* (17), 3241. https://doi.org/10.1039/b900162j.

(65) Bishop, S. R.; Duncan, K. L.; Wachsman, E. D. Defect Equilibria and Chemical Expansion in Non-Stoichiometric Undoped and Gadolinium-Doped Cerium Oxide. *Electrochimica Acta* **2009**, *54* (5), 1436–1443. https://doi.org/10.1016/j.electacta.2008.09.026.

(66) Steele, B. Appraisal of $Ce_{1-y}Gd_yO_{2-y/2}$ Electrolytes for IT-SOFC Operation at 500°C. *Solid State Ionics* **2000**, *129* (1–4), 95–110. https://doi.org/10.1016/S0167-2738(99)00319-7.

(67) Chueh, W. C.; Lai, W.; Haile, S. M. Electrochemical Behavior of Ceria with Selected Metal Electrodes. *Solid State Ionics* **2008**, *179* (21–26), 1036–1041. https://doi.org/10.1016/j.ssi.2007.12.087.

(68) Chueh, W. C.; Hao, Y.; Jung, W.; Haile, S. M. High Electrochemical Activity of the Oxide Phase in Model Ceria–Pt and Ceria–Ni Composite Anodes. *Nature Materials* **2012**, *11* (2), 155–161. https://doi.org/10.1038/nmat3184.

(69) Gerstl, M.; Hutterer, A.; Fleig, J.; Bram, M.; Opitz, A. K. Model Composite Microelectrodes as a Pathfinder for Fully Oxidic SOFC Anodes. *Solid State Ionics* **2016**, *298*, 1–8. https://doi.org/10.1016/j.ssi.2016.10.013.

(70) Richter, J.; Holtappels, P.; Graule, T.; Nakamura, T.; Gauckler, L. J. Materials Design for Perovskite SOFC Cathodes. *Monatsh. Chem.* **2009**, *140* (9), 985–999. https://doi.org/10.1007/s00706-009-0153-3.

(71) Wang, Y.; Wang, Y.; Ren, W.; Liu, P.; Zhao, H.; Chen, J.; Deng, J.; Xing, X. Improved Conductivity of $NdFeO_3$ through Partial Substitution of Nd by Ca: A Theoretical Study. *Phys. Chem. Chem. Phys.* **2015**, *17* (43), 29097–29102. https://doi.org/10.1039/C5CP03941J.

(72) Peña, M. A.; Fierro, J. L. G. Chemical Structures and Performance of Perovskite Oxides. *Chem. Rev.* **2001**, *101* (7), 1981–2018. https://doi.org/10.1021/cr980129f.

(73) Yin, J.-W.; Yin, Y.-M.; Lu, J.; Zhang, C.; Minh, N. Q.; Ma, Z.-F. Structure and Properties of Novel Cobalt-Free Oxides $Nd_xSr_{1-x}Fe_{0.8}Cu_{0.2}O_{3-\delta}$ ($0.3 \leq x \leq 0.7$) as Cathodes of Intermediate Temperature Solid Oxide Fuel Cells. *J. Phys. Chem. C* **2014**, *118* (25), 13357–13368. https://doi.org/10.1021/jp500371w.

(74) Abdel-Latif, I. A. Crystal Structure and Electrical Transport of Nano-Crystalline Strontium-Doped Neodymium Ortho-Ferrites. *J. Nanopart. Res.* **2020**, *22* (5), 111. https://doi.org/10.1007/s11051-020-04846-2.

(75) Chen, Y.; Wei, Y.; Zhong, H.; Gao, J.; Liu, X.; Meng, G. Synthesis and Electrical Properties of $Ln_{0.6}Ca_{0.4}FeO_{3-\delta}$ (Ln = Pr, Nd, Sm) as Cathode Materials for IT-SOFC. *Ceramics International* **2007**, *33* (7), 1237–1241. https://doi.org/10.1016/j.ceramint.2006.03.035.

(76) Yo, C. H.; Jung, I. Y.; Ryu, K. H.; Ryu, K. S.; Choy, J. H. A Study of the Nonstoichiometry and Physical Properties of the Perovskite $Nd_{1-x}Ca_xFeO_{3-y}$ System. *Journal of Solid State Chemistry* **1995**, *114* (1), 265–270. https://doi.org/10.1006/jssc.1995.1038.

(77) Kuhn, M.; Hashimoto, S.; Sato, K.; Yashiro, K.; Mizusaki, J. Oxygen Nonstoichiometry, Thermo-Chemical Stability and Lattice Expansion of $La_{0.6}Sr_{0.4}FeO_{3-\delta}$. *Solid State Ionics* **2011**, *195* (1), 7–15. https://doi.org/10.1016/j.ssi.2011.05.013.

(78) Schmid, A.; Fleig, J. The Current-Voltage Characteristics and Partial Pressure Dependence of Defect Controlled Electrochemical Reactions on Mixed Conducting Oxides. *J. Electrochem. Soc.* **2019**, *166* (12), F831–F846. https://doi.org/10.1149/2.1031912jes.

(79) Zhou, J.; Shin, T.-H.; Ni, C.; Chen, G.; Wu, K.; Cheng, Y.; Irvine, J. T. S. *In Situ* Growth of Nanoparticles in Layered Perovskite $La_{0.8}Sr_{1.2}Fe_{0.9}Co_{0.1}O_{4-\delta}$ as an Active and Stable Electrode for Symmetrical Solid Oxide Fuel Cells. *Chem. Mater.* **2016**, *28* (9), 2981–2993. https://doi.org/10.1021/acs.chemmater.6b00071.

(80) Lai, K.-Y.; Manthiram, A. Evolution of Exsolved Nanoparticles on a Perovskite Oxide Surface during a Redox Process. *Chem. Mater.* **2018**, *30* (8), 2838–2847. https://doi.org/10.1021/acs.chemmater.8b01029.

(81) Lindenthal, L.; Rameshan, R.; Summerer, H.; Ruh, T.; Popovic, J.; Nenning, A.; Löffler, S.; Opitz, A. K.; Blaha, P.; Rameshan, C. Modifying the Surface Structure of Perovskite-Based Catalysts by Nanoparticle Exsolution. *Catalysts* **2020**, *10* (3), 268. https://doi.org/10.3390/catal10030268.

(82) Jamnik, J.; Maier, J.; Pejovnik, S. A Powerful Electrical Network Model for the Impedance of Mixed Conductors. *Electrochimica Acta* **1999**, *44* (24), 4139–4145. https://doi.org/10.1016/S0013-4686(99)00128-0.

(83) Schmid, A.; Rupp, G. M.; Fleig, J. Voltage and Partial Pressure Dependent Defect Chemistry in $(La,Sr)FeO_{3-\delta}$ Thin Films Investigated by Chemical Capacitance Measurements. *Phys. Chem. Chem. Phys.* **2018**, *20* (17), 12016–12026. https://doi.org/10.1039/C7CP07845E.

(84) Pechini, M. P.; Adams, N. Method of Preparing Lead and Alkaline Earth Titanates and Niobates and Coating Method Using the Same to Form a Capacitor. 3330697, July 11, 1967.

(85) Water https://webbook.nist.gov/cgi/inchi/InChI%3D1S/H2O/h1H2 (accessed Oct 21, 2020).

(86) Oxygen https://webbook.nist.gov/cgi/inchi/InChI%3D1S/O2/c1-2 (accessed Oct 21, 2020).

(87) Hydrogen https://webbook.nist.gov/cgi/inchi/InChI=1S/H2/h1H (accessed Oct 21, 2020).

(88) Chueh, W. C.; Haile, S. M. Electrochemical Studies of Capacitance in Cerium Oxide Thin Films and Its Relationship to Anionic and Electronic Defect Densities. *Phys. Chem. Chem. Phys.* **2009**, *11* (37), 8144. https://doi.org/10.1039/b910903j.

(89) Wang, S.; Kobayashi, T.; Dokiya, M.; Hashimoto, T. Electrical and Ionic Conductivity of Gd-Doped Ceria. *J. Electrochem. Soc.* **2000**, *147* (10), 3606. https://doi.org/10.1149/1.1393946.

(90) Gonzalez-Cuenca, M.; Zipprich, W.; Boukamp, B. A.; Pudmich, G.; Tietz, F. Impedance Studies on ChromiteTitanate Porous Electrodes under Reducing Conditions. *Fuel Cells* **2001**, *1* (3–4), 256–264.

(91) Udomsilp, D.; Rechberger, J.; Neubauer, R.; Bischof, C.; Thaler, F.; Schafbauer, W.; Menzler, N. H.; de Haart, L. G. J.; Nenning, A.; Opitz, A. K.; Guillon, O.; Bram, M. Metal-Supported Solid Oxide Fuel Cells with Exceptionally High Power Density for Range Extender Systems. *Cell Reports Physical Science* **2020**, *1* (6), 100072. https://doi.org/10.1016/j.xcrp.2020.100072.

(92) Lee, J.; Fleig, J.; Maier, J.; Chung, T.; Kim, D. Microcontact Impedance Spectroscopy in Nitrogen-Graded Zirconia. *Solid State Ionics* **2005**, *176* (19–22), 1711–1716. https://doi.org/10.1016/j.ssi.2005.04.036.

(93) Dellis, J.-L. Zfit https://www.mathworks.com/matlabcentral/fileexchange/19460-zfit) (accessed Oct 18, 2020).

(94) Scofield, J. H. Hartree-Slater Subshell Photoionization Cross-Sections at 1254 and 1487 EV. *Journal of Electron Spectroscopy and Related Phenomena* **1976**, *8* (2), 129–137. https://doi.org/10.1016/0368-2048(76)80015-1.